

Experimental Investigation of
Micro Channel Heat Pipes (MCHP)
for Battery Cooling

Experimental Investigation of Micro Channel Heat Pipes (MCHP) Battery Pack Cooling

By MAHMOUD AL AKCHAR, B.Sc.

A Thesis

Submitted to the School of Graduate Studies

McMaster University

In Partial Fulfillment of the Requirement

For the Degree of Master of Applied Sciences

January 2025

McMaster University © Copyright by Mahmoud Al Akchar, January 2025

M.A.Sc. Thesis - M. Al Akchar; McMaster University - Mechanical Engineering.

McMaster University MASTER OF APPLIED SCIENCE (2025) Hamilton, Ontario (Mechanical Engineering)

TITLE: Experimental Investigation of Micro Channel Heat Pipes (MCHP) Battery Pack Cooling

AUTHOR: Mahmoud Al Akchar, B.Sc. (York University, Toronto, Canada)

SUPERVISOR: Dr. Saeid Habibi

NUMBER OF PAGES: xviii, 155

Abstract

The battery thermal management system (BTMS) of lithium-ion battery packs remains a critical challenge in advancing electric vehicle (EV) technologies, particularly during fast charging. As EV adoption increases, the demand for faster charging times and higher energy capacities grows, necessitating larger battery packs. Inadequate heat dissipation can lead to severe performance degradation, reduced battery lifespan, and increased safety risks.

This study explores the implementation of Micro Channel Heat Pipes (MCHPs) as an innovative cooling solution, aiming to enhance battery safety, performance, and longevity. The research focuses on evaluating the thermal performance of a six-cell prismatic battery module under three thermal management configurations: a baseline without active cooling, a traditional bottom cold plate cooling system, and the proposed MCHP cooling setup.

A standardized series of experimental tests were conducted, including the Hyundai Ioniq fast charging protocol and a 10-second 400A pulse fast charging protocol at 25°C, to assess the thermal performance, temperature uniformity, and cooling effectiveness of each setup. The Bottom Cooling demonstrated the highest localized cooling effectiveness at the cell's bottom, achieving up to 21.02% effectiveness. However, its performance diminished significantly at distant thermocouple locations, with negative effectiveness values of -3.43%, indicating localized heat accumulation. MCHP cooling, in contrast, provided more uniform cooling, achieving up to 13.58% effectiveness at the cell's bottom and notably outperforming Bottom cooling at distant points with 13.42% effectiveness, demonstrating its ability to distribute heat more evenly throughout the cells.

The results demonstrate that MCHP cooling excels in providing consistent and distributed cooling, effectively mitigating thermal hotspots, and adequate cooling performance compared to

Bottom cooling. The MCHP system presents a promising BTMS solution for next-generation EVs. Further optimization of the MCHP design and integration is required for improved cooling efficiency, supporting the growing demands for faster charging, enhanced safety, and prolonged battery life in electric vehicles.

Acknowledgments

In the name of Allah, the Most Gracious, the Most Merciful. I begin by expressing my deepest gratitude and praise to Almighty Allah for His endless blessings, guidance, and strength, which have enabled me to undertake and complete this thesis.

I am sincerely grateful to my supervisor, Dr. Saeid Habibi, for his constant guidance, support, and encouragement throughout this journey. The opportunities I was given under his mentorship profoundly shaped me as both a scientist and an individual. I am especially thankful for being involved in diverse projects that enriched my understanding of engineering management and research. I am also deeply appreciative of the incredible opportunity to intern in Europe—a chance that allowed me to fulfill lifelong dreams, from witnessing the Eiffel Tower to strolling along the canals of Amsterdam and finally visiting Granada, a place I had longed to see since I was 10 years old.

I would like to extend my heartfelt gratitude to everyone at CMHT for their support and friendship throughout my master's journey. Special thanks to Dr. Ryan Ahmed for offering invaluable life advice that helped me transition from academia to the professional world. I am thankful to Dr. Peyman Setoodeh for his generosity in grading my first-year assignments. I am sincerely grateful to Farzaneh Ebrahimi for patiently answering all my questions about batteries, teaching me how to operate the cell cycler, and guiding me through ECM modeling in MATLAB. I especially appreciate your kindness in introducing me to so many lifelong friends. My deepest thanks to Lewis Gross for helping me become a better manager, designer, and engineer—you will always be the best trainee I've had the privilege to mentor. I am also grateful to Nick Kosmal for providing critical technical support and invaluable manufacturing guidance. Lastly, a special

thanks to Zeina Tawakol for encouraging me to join CMHT, which has been an incredibly enriching experience.

I am truly thankful to Dana Incorporated and Calyos for trusting our team with the testing and development of their MCHP technology and for the invaluable internship opportunity at Dana, France. Special thanks to Ibrahim Zaaroura for his guidance and friendship during my work and travels in France. I also sincerely appreciate the technical expertise and timely support from Deenadhayalan Somasundaram at Dana, and Olivier de Laet and Christian Popper at Calyos, in every aspect of the MCHP project.

To my friends who have been by my side throughout this journey, I am deeply grateful. A special thank you to Dr. Kanan Idris for encouraging me to pursue my master's degree and supporting me through the application process—and for not convincing me to pursue a PhD; I probably would have if you had. Thank you, Dr. Daphne Archonta, for teaching me so much during my undergraduate studies and continuing to support me throughout graduate school. I am also deeply thankful to Dr. Riyam and Abdul Madani for making this journey easier and consistently motivating me to explore new career opportunities.

Lastly, I am eternally grateful to my family for their steadfast support. To my parents, who have stood by me in every decision and life path I've chosen—I owe everything to you. Your sacrifices, especially moving overseas to provide better opportunities for me and my siblings, have shaped who I am today. Without your love and dedication, I could have never imagined reaching this point. A heartfelt thank you to my little brother, Omar, whose curiosity and excitement for my research and 3D printing brought joy and inspiration to this journey.

Table of Contents

1	Introduction.....	1
1.1	Problem Statement.....	2
1.2	Thesis Outline.....	3
2	Literature Review.....	5
2.1	Batteries operation	5
2.1.1	Battery Types	6
2.1.2	Electrical Energy Storage Devices.....	7
2.1.3	The format of Lithium-Ion cells: Cylindrical, prismatic, pouch.....	8
2.2	Background on Cell Characterization.....	12
2.2.1	Terminologies	13
2.2.2	Open Circuit Voltage (OCV) test.....	19
2.2.3	Static Capacity test.....	21
2.2.4	Hybrid Pulse Power Characterization (HPPC) Test.....	22
2.3	Battery Thermal Management	24
2.3.1	Air Cooling	25
2.3.2	Liquid Cooling.....	27
2.3.3	Two Phase Cooling	30
2.3.4	Heat Pipes	31

3	Cell Characterization	34
3.1	CALB 3.7V 113Ah cell specifications.....	34
3.2	Cycler / Thermal Chamber Specifications	36
3.3	Testing Setup (thermal placement, cell holder)	37
3.4	Test Procedure.....	39
3.4.1	OCV Test Procedure	39
3.4.2	Static Capacity Test Procedure	40
3.4.3	HPPC Test Procedure.....	40
3.4.4	Fast Charging Tests Procedure.....	42
3.5	Results and Discussion (Capacity, Resistance).....	44
3.5.1	Static Capacity Test Results	44
3.5.2	OCV Test Results	47
3.5.3	HPPC Test Results	50
3.5.4	Fast Charging Tests Results	54
4	Battery Module Design Methodology	62
4.1	Micro Channel Heat Pipe Technology (MCHP).....	64
4.2	Dana Cold Plate	67
4.3	Busbar Design.....	68
4.4	No Cooling Testing Module.....	71
4.4.1	No Cooling Setup Thermocouple placement	72

4.5	Bottom Cold Plate Cooling Testing Module.....	73
4.5.1	Bottom Cold Plate Setup Thermocouple Placement.....	77
4.6	MCHP Testing Module	81
4.6.1	MCHP Setup Thermocouple Placement	86
4.7	Governing Thermal Equations for Battery and Cooling Configurations.....	88
4.7.1	Cell based.....	89
4.7.2	Testing Setups	90
4.8	Battery Management System Setup	92
4.8.1	Orion BMS: Features and Configuration.....	92
4.8.2	System Integration	93
5	Testing Procedure.....	95
5.1	Testing equipment.....	95
5.2	Testing Global Parameters	99
5.3	Fast charging protocols	102
6	Results and Discussion	103
6.1	No Cooling Module testing results	103
6.1.1	Hyundai Fast Charging Test.....	103
6.1.2	Pulse Fast charging	106
6.2	Bottom Cooling module test results.....	109
6.2.1	Hyundai Fast charging	109

6.2.2	Pulse fast charging	114
6.3	MCHP Cooling	119
6.3.1	Hyundai.....	119
6.3.2	Pulse.....	125
6.4	Cooling Methods Comparison Analysis	130
6.4.1	Hyundai Fast charging	131
6.4.2	Pulse.....	135
7	Future Work	140
8	Conclusion	143
9	References.....	145
10	Appendices.....	163
10.1	New Design Dimensioning.....	163
10.1.1	MCHP.....	163
10.1.2	Body Center Part.....	164
10.1.3	MCHP Testing Top Part	165
10.1.4	Enclosed Top Part	166
10.1.5	Bottom Cooling Lower Part.....	167
10.1.6	Enclosed Lower Part.....	168

Lists of Figures

Figure 1 Electrochemical setup of a battery cell while discharging.	6
Figure 2 Power and Energy comparison for common energy storage devices [15].	8
Figure 3 Cylindrical Cell internal structure [18].....	9
Figure 4 Prismatic Cell internal structure [25].	11
Figure 5 Pouch Cell internal structure [19].....	12
Figure 6 SoC – DoD relation [41].....	14
Figure 7 Internal resistance of various cells chemistries at different cell temperatures under 1C load [53].	17
Figure 8 example of a Li-Ion Cell Internal Resistance Vs SoC [55].	18
Figure 9 Illustration of the CCCV charging protocol profile [59].	19
Figure 10 Relationship between OCV and SoC during discharge, charge, and static voltage in low-current OCV test [63].	20
Figure 11 Voltage vs. Capacity curves for Samsung 50E cells during static capacity tests conducted at varying temperatures, and discharge rates of C/5 and 1C.	22
Figure 12 U.S.D.O.E. Standard HPPC test sequence [67].	24
Figure 13 Second-order equivalent circuit battery model (ECM) [69].	24
Figure 14 Air Cooled BTMS in a 2004 Second generation Toyota Prius hybrid with a 1.3Kwh NiMh battery pack [83], [89].	27
Figure 15 Hyundai Ioniq 5 battery pack extruded view [93].	29
Figure 16 Different cold plate serpentine channel designs [96].	29
Figure 17 Zig-Zag serpentine 13-channel cold plate design [97].	30
Figure 18 U shaped Heat Pipe with a side cold plate [105].	32
Figure 19 U shaped Heat pipe with bottom cooling [106].	33
Figure 20 CALB L221N113A Cell with M6 stud terminals.	35

Figure 21 ESPEC BTZ-133 thermal chamber.	37
Figure 22 Thermocouple placement on the cell for single-cell testing.	38
Figure 23 Single-cell fixture inside the BTZ-133 thermal chamber.	39
Figure 24 The current (A) profile of the Hyundai Ioniq fast charging at 25°C.	43
Figure 25 400A pulse charging current profile.	44
Figure 26 Static Capacity Voltage, Current discharge vs Time at 0,25,45°C ambient testing conditions.	46
Figure 27 Rise Over Ambient Average Temperatures of the Static Capacity Tests. It is noted that the measurements at 25°C exhibit more noise compared to the other test conditions.	47
Figure 28 OCV-SoC curves at 25°C. The mean OCV is used in SoC estimation applications. ...	49
Figure 29 Mean OCV-SoC curves at 0°C, 25°C and 45°C.	50
Figure 30 HPPC test Voltage Response Curve at 25°C.	52
Figure 31 CALB cell internal resistance based on HPPC tests.	53
Figure 32 Hyundai fast charging test Voltage response.	55
Figure 33 Hyundai fast charging test cell temperature response at 15 locations.	56
Figure 34 Hyundai fast charging test, cell temperature response grouped by cell facing.	57
Figure 35 400A Pulse fast charging test Voltage response.	58
Figure 36 400A Pulse fast charging test cell temperature response at 15 locations.	59
Figure 37 400A Pulse fast charging test, cell temperature response grouped by cell facing.	60
Figure 38 Layout of the 6-cell prototypes with cell labeling and positioning.	63
Figure 39 Calyos MCHP operation diagram [117].	66
Figure 40 Calyos MCHP different cells use cases example [117].	67
Figure 41 Dana Cold Plate, used in the bottom cooling and MCHP cooling.	68
Figure 42 Three types of copper busbars are used during testing.	69
Figure 43 No Cooling Test Module CAD design, showing the cover and busbar installation.	72
Figure 44 Cell C of the No Cooling testing module thermocouple placement and labelling.	73

Figure 45 Cell D of the No Cooling testing module thermocouple placement and labelling.....	73
Figure 46 Bottom Cooling test setup CAD design with a breakdown of the components.	75
Figure 47 Bottom Cooling setup TIM installation.....	76
Figure 48 Bottom Cooling Setup final assembly.....	76
Figure 49 Bottom Cooling Setup final assembly with the top removed.....	77
Figure 50 Bottom Cooling setup TIM material deflection measurements after applying cell compression pressure.....	77
Figure 51 Cell A of the Bottom Cooling testing module thermocouple placement and labelling.	78
Figure 52 Cell B of the Bottom Cooling testing module thermocouple placement and labelling of the cell and each thermocouple.....	79
Figure 53 Cell C of the Bottom Cooling testing module thermocouple placement and labelling.	79
Figure 54 Cell D of the Bottom Cooling testing module thermocouple placement and labelling.	80
Figure 55 Cell E of the Bottom Cooling testing module thermocouple placement and labelling.	80
Figure 56 Cell F of the Bottom Cooling testing module thermocouple placement and labelling.	81
Figure 57 MCHP Test Module CAD design concept.....	82
Figure 58 MCHP dimensions with tolerances.	82
Figure 59 Corner view of the complete MCHP testing module.	84
Figure 60 MCHP testing module, illustrating the condenser support plates and the thermocouple placement on the condenser.	85
Figure 61 MCHP testing module, showing the busbar adaptation cut.....	85
Figure 62 Cell A of the MCHP testing module thermocouple placement and labelling,.....	86
Figure 63 Cell B of the MCHP testing module thermocouple placement and labelling,	87
Figure 64 Cell C of the MCHP testing module thermocouple placement and labelling,	87
Figure 65 Cell D of the MCHP testing module thermocouple placement and labelling,	87
Figure 66 Cell E of the MCHP testing module thermocouple placement and labelling,.....	88
Figure 67 Cell F of the MCHP testing module thermocouple placement and labelling,	88

Figure 68 Orion 2 BMS system integration with the testing module.	94
Figure 69 AVL E-Storage BTE 160 Battery tester and emulator.	96
Figure 70 Tenny Environmental TC20 thermal chamber.	97
Figure 71 Testing setup showing the unit under testing, thermal chamber, chiller to the cold plate, and DAQ connections.	100
Figure 72 No Cooling, Hyundai fast charging Voltage response curve.	104
Figure 73 No Cooling, Hyundai fast charging cell C temperature response.	105
Figure 74 No Cooling, Hyundai fast charging cell D temperature response.	106
Figure 75 No Cooling, Pulse fast charging Voltage curve response.	107
Figure 76 No Cooling, Pulse fast charging cell C temperature response.	108
Figure 77 No Cooling, Pulse fast charging cell D temperature response.	108
Figure 78 Bottom Cooling, Hyundai Ioniq fast charging Voltage response curve.	110
Figure 79 Bottom Cooling, Hyundai Ioniq fast charging cell A temperature response.	111
Figure 80 Bottom Cooling, Hyundai Ioniq fast charging cell B temperature response.	111
Figure 81 Bottom Cooling, Hyundai Ioniq fast charging cell C temperature response.	112
Figure 82 Bottom Cooling, Hyundai Ioniq fast charging cell D temperature response.	112
Figure 83 Bottom Cooling, Hyundai Ioniq fast charging cell E temperature response.	113
Figure 84 Bottom Cooling, Hyundai Ioniq fast charging cell F temperature response.	113
Figure 85 Bottom Cooling, Pulse fast charging Voltage response curve.	115
Figure 86 Bottom Cooling, Pulse fast charging cell A temperature response.	116
Figure 87 Bottom Cooling, Pulse fast charging cell B temperature response.	117
Figure 88 Bottom Cooling, Pulse fast charging cell C temperature response.	117
Figure 89 Bottom Cooling, Pulse fast charging cell D temperature response.	118
Figure 90 Bottom Cooling, Pulse fast charging cell E temperature response.	118
Figure 91 Bottom Cooling, Pulse fast charging cell F temperature response.	119
Figure 92 MCHP Cooling, Hyundai Ioniq fast charging Voltage response curve.	120

Figure 93 MCHP Cooling, Hyundai Ioniq fast charging cell A temperature response.	122
Figure 94 MCHP Cooling, Hyundai Ioniq fast charging cell B temperature response.....	122
Figure 95 MCHP Cooling, Hyundai Ioniq fast charging cell C temperature response.....	123
Figure 96 MCHP Cooling, Hyundai Ioniq fast charging cell D temperature response.	123
Figure 97 MCHP Cooling, Hyundai Ioniq fast charging cell E temperature response.	124
Figure 98 MCHP Cooling, Hyundai Ioniq fast charging cell F temperature response.	124
Figure 99 MCHP Cooling, Pulse fast charging Voltage response curve.....	126
Figure 100 MCHP Cooling, Pulse fast charging cell A temperature response.	127
Figure 101 MCHP Cooling, Pulse fast charging cell B temperature response.	128
Figure 102 MCHP Cooling, Pulse fast charging cell C temperature response.	128
Figure 103 MCHP Cooling, Pulse fast charging cell D temperature response.	129
Figure 104 MCHP Cooling, Pulse fast charging cell E temperature response.	129
Figure 105 MCHP Cooling, Pulse fast charging cell F temperature response.....	130
Figure 106 Cells C and D mutual thermocouple locations across the three testing setups.	131
Figure 107 Mutal thermocouples, Hyundai fast charging cell C temperature response.	133
Figure 108 Mutal thermocouples, Hyundai fast charging test: Bottom and MCHP cooling cell C effectiveness relative to No Cooling.....	134
Figure 109 Mutal thermocouples, Hyundai fast charging cell D temperature response.....	134
Figure 110 Mutal thermocouples, Hyundai fast charging test: Bottom and MCHP cooling cell D effectiveness relative to No Cooling.....	135
Figure 111 Mutal thermocouples, Pulse fast charging cell C temperature response.	137
Figure 112 Mutal thermocouples, Pulse fast charging test: Bottom and MCHP cooling cell C effectiveness relative to No Cooling.....	138
Figure 113 Mutal thermocouples, Pulse fast charging cell D temperature response.....	138
Figure 114 Mutal thermocouples, Pulse fast charging test: Bottom and MCHP cooling cell D effectiveness relative to No Cooling.....	139
Figure 115 New testing setup with the MCHP Top attachment to be bonded to the cold plate.	141

Figure 116 New testing setup with the Bottom Cooling attachment to be bonded to the cold plate.	142
Figure 117 Optimized MCHP dimensions.	163
Figure 118 Body middle part left side.	164
Figure 119 The MCHP testing fixture top part.	165
Figure 120 Enclosed top cover utilized in both No Cooling and Bottom Cooling setups.	166
Figure 121 Bottom Cooling lower part attachment.	167
Figure 122 Enclosed Lower cover utilized in both No Cooling and MCH Cooling setups.	168

Lists of Tables

Table 1 Key specifications of CALB prismatic cells from the manufacturer’s datasheet [109]. .	35
Table 2 Highlighted results of the Static Capacity tests.	46
Table 3 Internal Resistance of the CALB cell based on the HPPC tests at 0,25, & 45°C.	53
Table 4 Summary of the specifications at each stage, from individual cells to the battery pack..	63
Table 5 Calyos MCHP’s specification sheet [116].	65
Table 6 TIM material comparison for the Bottom cooling application.	74
Table 7 Hyundai Fast Charging Effectiveness Values based on the last 300 S of testing.....	131
Table 8 Pulse Fast Charging Effectiveness Values based on the last 300 S of testing.....	136

List of Abbreviations

Abbreviation	Definition
Ah	Ampere-hour
AVL	An automotive engineering and testing systems provider
BMS	Battery Management System
BTMS	Battery Thermal Management System
CALB	China Aviation Lithium Battery
CCCV	Constant Current/Constant Voltage
DAQ	Data Acquisition
DoD	Depth of Discharge
ECM	Equivalent Circuit Model
EIS	Electrochemical Impedance Spectroscopy
EV	Electric Vehicle
HPPC	Hybrid Pulse Power Characterization
IC	Internal Combustion
ICEV	Internal Combustion Engine Vehicle
kWh	Kilowatt-hour
LIB	Lithium-Ion Battery
MCHP	Micro-Channel Heat Pipe
MTBF	Mean Time Between Failures
NMC	Nickel Manganese Cobalt
OCV	Open Circuit Voltage
PETG	Polyethylene Terephthalate Glycol
Q	Heat Transfer Rate
RMS	Root Mean Square
RTD	Resistance Temperature Detector
SoC	State of Charge
ZEV	Zero-Emission Vehicle

Chapter 1

Introduction

The global transition from conventional internal combustion engine vehicles (ICEVs) to electric vehicles (EVs) is being driven by the urgent need for sustainable energy solutions in the transportation sector. Governments worldwide have set ambitious targets to accelerate the adoption of zero-emission vehicles (ZEVs). In Canada, the government aims to achieve 100% ZEV sales for new light-duty vehicles by 2035, with interim milestones of 20% by 2026 and 60% by 2030. Federal initiatives such as purchase incentives, investments in charging infrastructure, and the Electric Vehicle Availability Standard have been instrumental in this transition, resulting in a steady increase in ZEV market share from 3.1% in 2019 to 11.7% in 2023 [1]. This commitment underscores the need to address key technical barriers, particularly in battery charging efficiency and thermal management, which are critical to scaling EV adoption.

From a consumer standpoint, range anxiety and prolonged charging times remain significant concerns, often limiting EV competitiveness compared to the quick refuelling process of ICEVs. Addressing these challenges requires advancements in high-density energy storage systems and fast-charging technologies.

Lithium-ion batteries (LIBs) have become the dominant energy storage solution for EVs due to their superior energy density, long cycle life, and low self-discharge rates. These attributes make LIBs more reliable and efficient than legacy battery technologies, such as lead-acid systems, which are primarily used for auxiliary power in ICEVs [2].

Fast-charging systems are designed to minimize EV downtime by significantly reducing the time required to recharge batteries. However, this approach often results in increased thermal instability, primarily due to the heat generated by internal resistance and electrochemical reactions. Excessive heat buildup can lead to thermal runaway, reduced efficiency, and accelerated battery degradation, while low temperatures exacerbate issues such as lithium plating and reduced power output, further compromising safety and performance. To mitigate these risks, effective Battery Thermal Management Systems (BTMS) are essential for maintaining safe operating temperatures and ensuring the longevity and reliability of battery systems during fast charging [3], [4], [5].

Liquid cooling has emerged as the most common BTMS due to its superior heat transfer capabilities. However, active liquid cooling systems are not without risks; leakage remains a critical issue, often caused by poor sealing, material degradation, or design flaws. Leakage can lead to inadequate cooling, increasing the risk of thermal runaway in lithium-ion batteries [6].

Therefore, there is a need for a safe and effective BTMS solution for lithium-ion battery systems that can isolate active liquid cooling systems from battery modules, minimizing risks of leakage or failure while maintaining optimal temperature control during fast charging and normal operation.

1.1 Problem Statement

This thesis focuses on the thermal management of lithium-ion batteries, specifically exploring the use of Micro-Channel Heat Pipe (MCHP) technology as an innovative and scalable cooling solution for EV battery packs. The study addresses key challenges in EV battery systems, including thermal runaway, degradation due to uneven temperature distribution, and the limitations of conventional cooling strategies such as bottom cold plate cooling.

The core objective of this project is to design, test, and validate MCHP technology for battery cooling and benchmark its performance against traditional bottom cold plate systems. The research comprises three primary cooling setups: a control module with no active cooling, a module cooled using a bottom cold plate, and a module integrated with MCHP technology. These setups are tested under high-stress charging protocols, including the Hyundai Ioniq fast charging profile and a 400A pulse charging profile, to evaluate thermal performance, temperature uniformity, and effectiveness under realistic operational conditions.

1.2 Thesis Outline

The thesis is structured into seven chapters, beginning with foundational concepts for each discussion topic and ending with a comprehensive analysis of the effectiveness and limitations of the proposed BTMS.

Chapter One: An introduction of the motivations behind the research and its significance in current EV development. An overview of the project goals and the thesis outline are listed to guide the reader through the individual topics.

Chapter Two: A comprehensive review of the background and concepts necessary to understand the research is provided. Topics include the fundamentals of lithium-ion battery systems, their thermal behavior, and the impact of temperature on performance and safety. Existing cooling methods, including bottom cold plates and Heat pipes BTMS are discussed, are reviewed.

Chapter Three: Individual cell characterization, emphasizing capacity and internal resistance at different SoC levels. These parameters are critical for ensuring accurate SoC estimation and effective cell balancing in battery module and pack design. The CALB L221N113A cell's performance is analyzed against manufacturer specifications to provide insights into

capacity, thermal stability, and degradation behaviour.

Chapter Four: Provides a detailed explanation of the cooling technologies used in this project. Then, the experimental design and methodology used to evaluate a battery module's performance under three distinct BTMS configurations: No Cooling, Bottom Cold Plate Cooling, and Micro-Channel Heat Pipe (MCHP) Cooling.

Chapter Five: Details the equipment, methodologies, and parameters employed to conduct fast-charging experimental tests on the different battery module configurations. It aims to ensure consistent and comparable results across the three testing setups, enabling a comprehensive evaluation and validation of the different cooling methods.

Chapter Six: Presents the results of the experimental tests conducted using the three setups. Key findings include temperature distributions, voltage and current response curves, and the cooling performance of each method under fast charging conditions. In addition to effectiveness comparison of the cooling strategies is analyzed, and the limitations of each setup are discussed in detail.

Chapter Seven: Concludes with a summary of the research findings and their significance. The advantages and limitations of MCHP cooling technology are highlighted, along with actionable recommendations for future work.

The MCHP's is a promising technology that can provide consistent, distributed cooling through phase-change mechanisms, enhancing heat transfer efficiency with minimal external input. This makes it a viable solution for improving thermal management and safety during fast charging.

Chapter 2

Literature Review

2.1 Batteries operation

A battery cell is an energy storage device that converts chemical energy into electrical energy through electrochemical reactions. Cells are composed of three main components: Anode (negative electrode), Cathode (positive electrode) electrolyte, and separator.

During discharge, the anode undergoes oxidation, releasing electrons into the external circuit. These electrons flow through the load to the cathode, which undergoes reduction by gaining the electrons. This electron flow powers the load, creating electricity. Simultaneously, the electrolyte facilitates ion movement within the battery, allowing cations (positive ions) to migrate from the anode to the cathode, while the separator prevents direct electrical contact between the electrodes, ensuring safe operation. This ion movement maintains charge balance as the electrochemical reactions proceed.

During charging, an external electrical current reverses the flow of electrons through the circuit and ions through the electrolyte. The difference in electrochemical potential between the anode and cathode determines the battery's voltage and drives the movement of electrons and ions during both discharge and charge processes, as shown in Figure 1 [7].

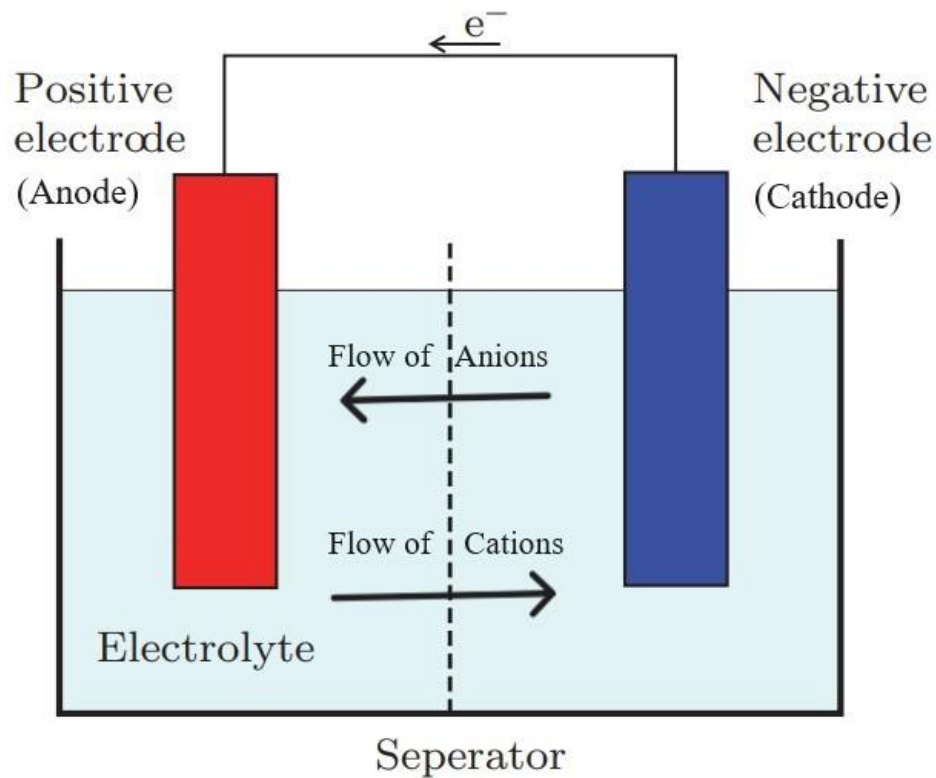


Figure 1 Electrochemical setup of a battery cell while discharging.

2.1.1 Battery Types

The main two types of batteries are primary which is non-rechargeable and secondary which is rechargeable.

In primary batteries, the chemical reactions are irreversible, leading to a finite lifespan. These batteries are designed for single use and are commonly found in household devices such as remote controls, flashlights, and toys.

In secondary batteries, the chemical reactions are reversible. These batteries can be recharged and used repeatedly until they cannot hold charge. They are widely used in household devices such as phones, laptops, as well as EVs, and on a large industrial scale in power generation and storage, heavy machinery [8].

Primary batteries usually have higher energy density than secondary batteries. The inability of recharge prevents primary batteries from being used in EVs. Moving on when batteries are mentioned, it is assumed that it is a secondary battery unless labeled as a primary battery.

2.1.2 Electrical Energy Storage Devices

There are many options for energy storage and not a correct answer for all cases. Each use case is analyzed for a balance between power and energy. Specific energy refers to the energy density of the cell or how much energy the battery cell can store per weight. This determines how long a battery can run. Specific power refers to how much power a battery cell can provide per its weight. This determines how quickly the cell energy can be released.

In EVs, balancing energy and power is critical, as it determines the size and performance of the battery pack. While capacitors can technically power an EV and deliver rapid acceleration, achieving a reasonable driving range would require an impractically large number of capacitors.

Figure 2 shows the common energy storage devices and their relative specific powers and energies. The optimum battery cell will be closer to the top right corner as that minimizes the size and weight of the battery pack while maintaining high efficiency.

Lithium-Ion Batteries (LIB) provide good power and energy in addition to a high life cycle. This makes them desirable in EV applications. Lead Acid cells on the other hand are used in most Internal Combustion (IC) vehicles due to their lower price (US \$240 per kWh) and relatively good power and energy supply [9]. However, their life cycle is much lower with around 300-500 cycles [10].

Supercapacitors have higher energy density than regular capacitors making them better for EV applications. Their specific power ranges from 0.5 to 10 kW/kg and their specific energy

densities are from 1 to 10 Wh/kg [11]. They have a longer life cycle of 500–10,000. However, they come at a very high price (US \$10,000 per kWh) making them not suitable for common EV use [9]. Supercapacitors have self-discharge issues and high fabrication costs [12].

Fue Cells utilize an electrochemical reaction to convert chemical energy to electrical energy directly. They have high specific energy making them suitable for long-duration applications. However, their low specific power makes them less effective for rapid power applications. Their cost to run is about US \$180 – US \$230 kWh [14].

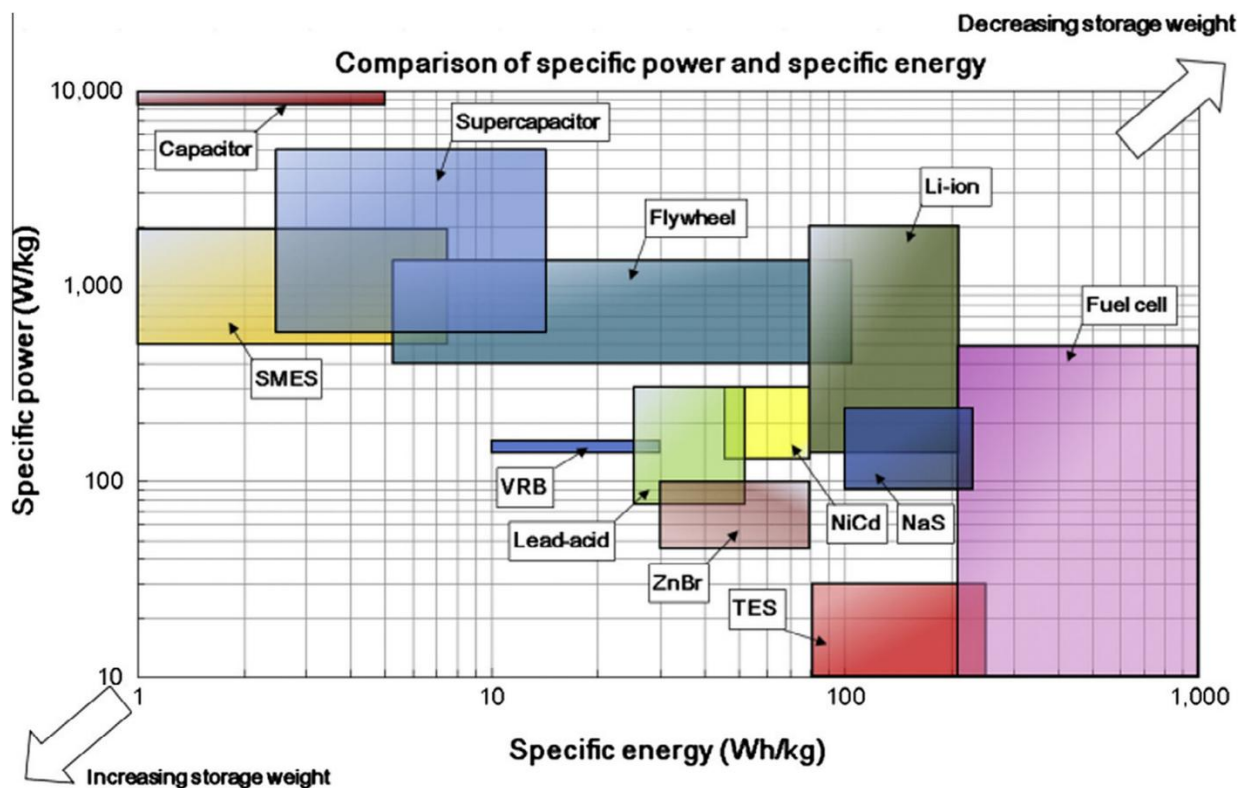


Figure 2 Power and Energy comparison for common energy storage devices [15].

2.1.3 The format of Lithium-Ion cells: Cylindrical, prismatic, pouch.

Lithium-ion cells come in different form factors as follows:

Cylindrical Lithium-Ion Cells: They are the most common commercially, introduced by

Sony in 1992 with the 18650 meaning a cell size of 18 mm in diameter and 65 mm in length [16]. As shown in Figure 3, the anode, cathode, and separator are arranged in thin sheets that are layered together and then rolled into a jelly-roll configuration. These are then fit within the cylindrical metal casing, which provides mechanical support. The manufacturing technology of cylindrical cells reached a point of maturity where their cost at large scale is significantly lower than other cells. They are used in most hand-held devices such as power bank batteries, laptops to electric cigarettes. They are constantly scaled up in size for higher energy density (26650, and 21700 cells). The 21700 cells introduced by Tesla have a 50% increase in energy content per cell during 0.5C discharging compared to the 18650 cells using the same materials [17]. However, the cylindrical shape provides low cell packing density, in addition to harder cooling methods as traditional cold plates cannot cover the surface area. The low nominal voltage and capacity of cylindrical cells necessitate combining thousands of them in parallel and series configurations to achieve the necessary power and energy levels for EVs. This requirement significantly increases the complexity of the structural design in EVs.

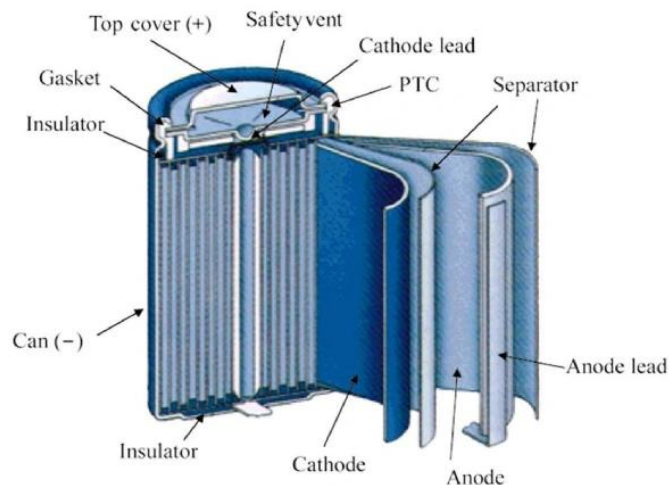


Figure 3 Cylindrical Cell internal structure [18].

Prismatic Lithium-Ion Cells: These have become a prominent option for EVs and energy storage systems. Unlike cylindrical cells, which feature a round shape and jelly-roll design, prismatic cells are constructed in rectangular or square formats, as seen in Figure 4. This design allows for more efficient space utilization, maximizing packing density within battery packs [19]. Inside the cell, the electrode materials are arranged in stacked or z-fold configurations, providing greater electrode surface area, which enhances the battery's overall energy capacity [20]. The prismatic casing is typically hard, offering robust mechanical support and protecting against issues such as swelling, a common concern with lithium-ion cells. One of the key benefits of prismatic cells is their ability to distribute current more uniformly across the electrodes, reducing the inefficiencies caused by curvature in cylindrical designs. This improved current distribution enhances the utilization of active materials and supports the use of thinner electrodes, further increasing energy density. However, despite achieving a higher packing density, prismatic cells generally have about 20% lower energy density compared to cylindrical cells, which may limit their use in applications where space constraints and maximum energy density are critical [19]. Additionally, their larger surface area allows for more straightforward thermal management, making cooling easier through systems like direct liquid cooling [21], [22]. While traditional views may favour cylindrical cells for their lower upfront costs, emerging research indicates that prismatic cells can offer competitive or even lower costs per kWh when considering factors such as material efficiency, manufacturing processes, and economies of scale [23], [24].

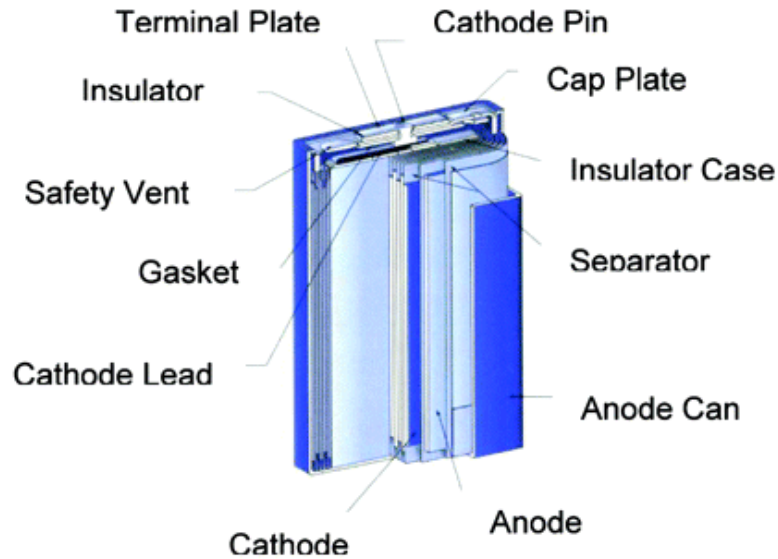


Figure 4 Prismatic Cell internal structure [25].

Pouch Lithium-Ion Cells: They are one of the newest advancements in energy storage technology, favoured for their lightweight design and high energy density. As shown in Figure 5, these cells are constructed using a soft polymeric film that encloses the internal components [26], [27]. Inside the pouch, the anode, cathode, and separator are layered, flattened, and stacked, making more efficient use of space. This arrangement maximizes the surface area for electrochemical reactions, enhances thermal management, and minimizes the risk of internal short circuits [28]. The structure of pouch cells can also be tailored by adjusting the thickness and composition of each layer to optimize performance characteristics like energy density and cycle life [29]. Pouch cells can achieve impressive energy densities, with some lithium-sulfur (Li-S) models exceeding 436 Wh/kg [30]. They are also versatile in supporting various chemistries, including lithium-ion and lithium-sulfur systems, broadening their applicability in different energy storage needs [31]. However, pouch cells face challenges in mechanical stability and thermal management. The flexible packaging can swell during charge and discharge cycles, potentially

compromising structural integrity and long-term performance [32]. Additionally, cooling systems may be less effective due to the lack of a rigid casing, requiring new approaches to thermal management [26], [33]. Researchers are working on new materials and designs to improve the robustness and thermal properties of pouch cells to ensure reliability in demanding applications [34]. Pouch cells offer a cost advantage due to their simpler construction, and their total cost of ownership—including factors such as energy density, cycle life, and safety—can be lower than that of cylindrical and prismatic cells [35]. As the industry continues to push for higher performance at lower costs, pouch cells are poised to play a vital role in the future of electric mobility and renewable energy storage [31], [36]

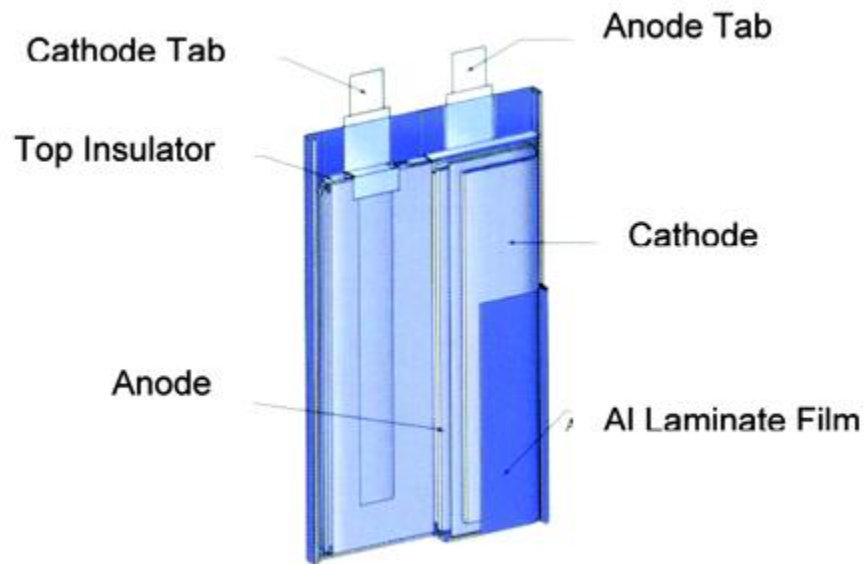


Figure 5 Pouch Cell internal structure [19].

2.2 Background on Cell Characterization

Cell characterization is the process of evaluating a cell's electrochemical behavior by linking its chemical properties to measurable parameters. This is achieved by monitoring voltage, current, and temperature responses under various operating conditions. Through a series of tests,

key performance metrics such as capacity, internal resistance, and thermal behavior are assessed. Understanding these properties enables optimization of battery design and performance, while addressing challenges related to efficiency, safety, and lifespan. This section will examine the methods and metrics used in cell characterization and their role in advancing battery technologies.

2.2.1 Terminologies

State of Charge (SoC): SoC of a cell is defined as the percentage of capacity a cell has relative to its maximum capacity. It is an indication of how much capacity is left before it fully discharges. It can be calculated as shown in Equation (2.1).

$$SOC = \frac{\text{Current Capacity (Ah)}}{\text{Maximum Capacity (Ah)}} \cdot 100\% \quad (2.1)$$

The challenge in measuring the State of Charge (SoC) lies in the inherently chemical nature of battery cells, which prevents direct measurement through purely physical means. One of the simplest techniques for estimating SoC is Coulomb Counting, where the current entering or leaving the battery is integrated over time to estimate the charge level. However, this method is prone to errors, as it requires continuous tracking of current, and any inaccuracies can accumulate over time. Additionally, factors like self-discharge and cell aging impact capacity, further complicating SoC estimation. A more reliable approach would be to link SoC to a specific chemical or physical phenomenon that reflects the cell's state more directly [37].

State of Health (SoH): The SoH of a cell quantifies its current performance relative to its original condition. At 100% SoH, the cell operates with optimal internal resistance and energy storage capacity. However, when SoH declines to 80%, it is typically regarded as end-of-life (EOL), as the battery may no longer deliver sufficient energy and power to support adequate driving range. Additionally, reduced SoH increases internal resistance, leading to higher cell

temperatures and potentially necessitating alternative cooling solutions to maintain safe operation [38], [39].

Depth of Discharge: DoD measures how much capacity in Ampere-hours (Ah) is removed during a discharge. It is essentially the inverse of SoC as shown in Figure 6. A 0% DoD indicates a fully charged battery, while a 100% DoD indicates a fully discharged battery. DoD has a direct impact on a battery's cycle life; frequent deep discharges accelerate the degradation of battery materials, ultimately reducing the total number of charge-discharge cycles the battery can sustain before experiencing significant capacity loss [40].

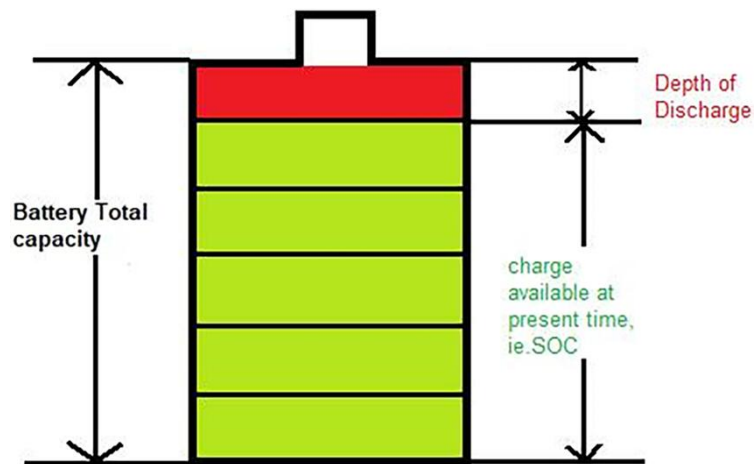


Figure 6 SoC – DoD relation [41].

C-Rate: C-Rate defines the rate at which a battery charges or discharges relative to its nominal capacity, expressed in units of “C.” For instance, if a cell has a nominal capacity of 4.6 Ah, charging it at 2C means it will be charged at 9.2 A, reaching 100% SoC from 0% in half an hour. Conversely, discharging at 0.5C would draw 2.3 A, discharging the cell over two hours [42].

Cycle life: Cycle life indicates the number of full charge-discharge cycles a battery can sustain before its capacity falls below 80% of its original level [43]. Cycle life is influenced by

DoD, C-rate, temperature, and the chemistry of cells. High DoD and faster C-rates increase degradation, while moderate levels enhance longevity. High temperatures accelerate chemical reactions, and low temperatures hinder ion mobility [44], [45].

Open Circuit Voltage (OCV): OCV is the electrical potential difference between a device's two terminals when disconnected from any circuit, representing its maximum potential output without current flow. OCV is a key indicator of a battery's SoC; as a battery discharges, its OCV decreases, reflecting reduced available energy, while a fully charged battery shows a peak OCV determined by its electrochemical materials [46].

Operating Voltage: Operating voltage, also called discharge or load voltage, is the potential difference between battery terminals when current flows through an external circuit. It is always lower than the open-circuit voltage due to the need to overcome internal polarization and ohmic resistance as current passes through the battery [47]. The relationship between operating voltage and OCV can be found using Equation (2.2) [48].

$$V_{Open\ Voltage} = OCV - I_{Active} * R_{Internal} \quad (2.2)$$

Standard Charging / Discharging: This refers to the standard charging/ discharging currents the manufacturer recommends. Usually in terms of C-rates and cut-off voltages. Standard charging starts with a constant current until reaching an upper voltage limit, then switches to constant voltage, allowing the current to taper to a low threshold. Standard discharging follows a constant current until reaching a setpoint lower voltage limit [49].

Internal Resistance: Refers to the opposition to current flow within a battery, leading to energy losses in the form of heat during charging and discharging. Battery internal resistance can be divided into two main components: ohmic resistance and polarization resistance. Ohmic resistance is primarily determined by the physical properties of the battery materials and

connections, while polarization resistance arises from electrochemical reactions at the electrodes during charge and discharge [50]. The internal resistance is influenced by factors such as temperature, SoC, and battery age.

Lower running temperature conditions result in higher cell resistance, this is mainly due to the reduced ionic conductivity of the electrolyte and restricted lithium-ion mobility resulting in impeding ion movement and slowing electrochemical reactions during battery operation. At higher temperatures, the ion kinetic energy increases, facilitating faster charge transfer reactions at the electrodes [50], [51]. However, higher temperatures can also pose risks of thermal runaway and accelerated aging of battery components [50], [52]. Figure 7 shows the temperature dependence of internal resistance for lithium-based batteries (LiFePO₄, Li-PO, Li-Ion) and lead-acid batteries at 1-C load [53].

SoC also affects the internal resistance of li-ion cells. The resistance often increases at higher SoCs closer to 100% and at low SoCs closer to 0% as shown in Figure 8 [54], [55]. At 100% SoC, lithium-ion concentration in the electrolyte peaks, causing increased internal resistance. This rise is primarily due to the thickening of the SEI layer on the anode, which increases charge transfer resistance, and side reactions from overcharging that degrade electrode materials and generate gas [56]. Additionally, polarization resistance increases at full charge, impeding lithium-ion movement [50].

At 0% SoC, when fully discharged, internal resistance also peaks due to lithium-ion depletion in the electrolyte, limiting intercalation at the electrodes [57]. Low SoC further raises polarization and ohmic resistance as electrolyte conductivity declines, restricting ion mobility [51], [52].

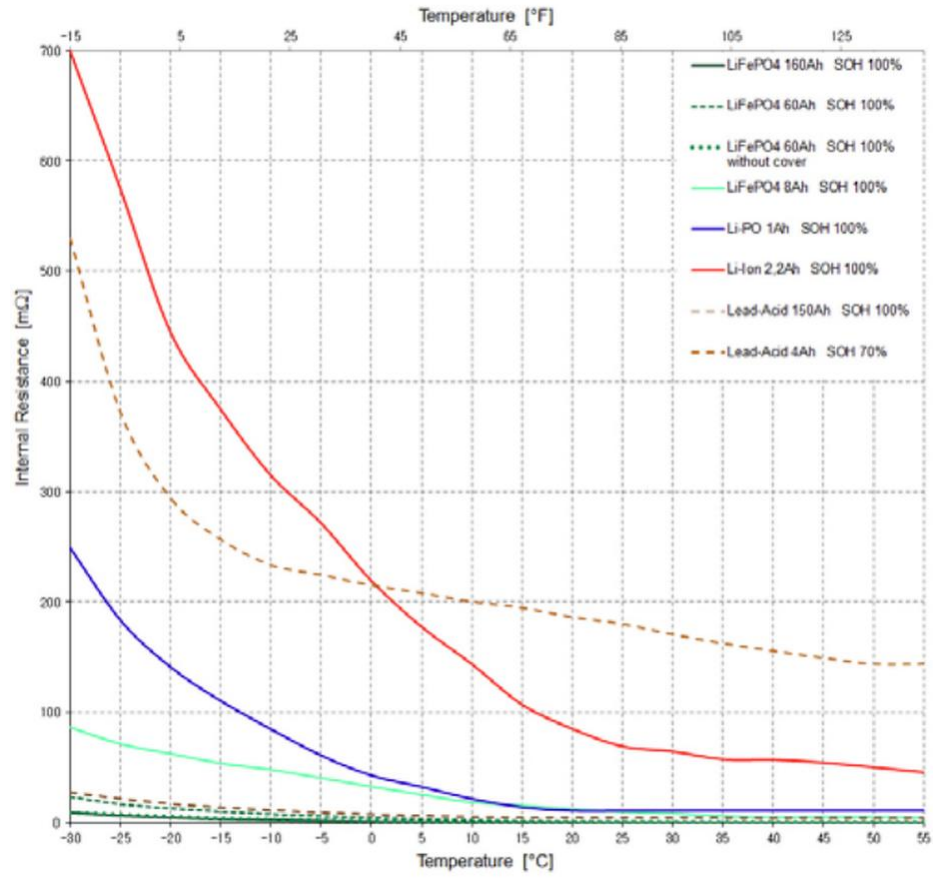


Figure 7 Internal resistance of various cells chemistries at different cell temperatures under 1C load [53].

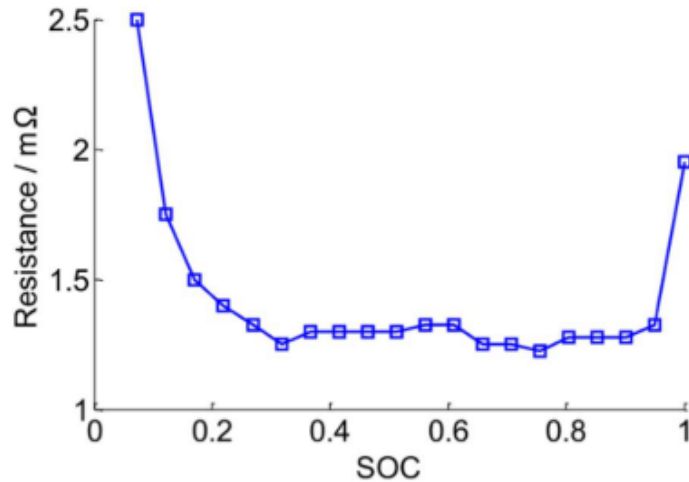


Figure 8 example of a Li-Ion Cell Internal Resistance Vs SoC [55].

Constant Current/ Constant Voltage (CCCV) protocol: The CCCV charging protocol is a conservative method for charging a cell to its maximum capacity. As illustrated in Figure 9, the charging profile begins with a constant current (CC) phase, typically at a moderate current level. Once the cell reaches a predefined cutoff voltage, the protocol transitions to the constant voltage (CV) phase, where the voltage remains steady as the current gradually decreases. Charging continues until the current drops to a specified cutoff value, indicating that the maximum capacity has been reached [58].

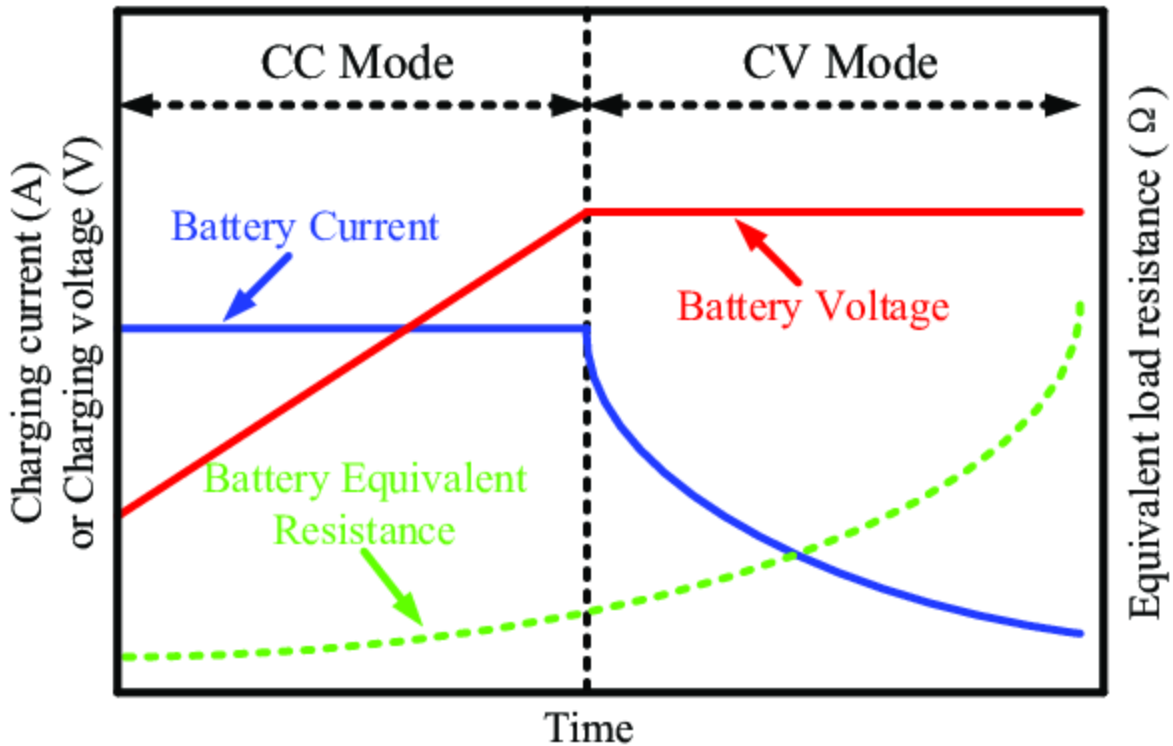


Figure 9 Illustration of the CCCV charging protocol profile [59].

2.2.2 Open Circuit Voltage (OCV) test

The OCV test is used to obtain the OCV-SoC curve, as mentioned in section **Error! Reference source not found.** the OCV increases as the SoC increases. This direct relationship allows SoC estimation based on OCV measurements when the battery is in a relaxed state. However, OCV can vary with temperature and cell aging or SoH, so tests are performed under different operating conditions to create comprehensive OCV-SoC curves covering a range of SoH values [60].

There are two primary methods for measuring the OCV-SoC relationship: the incremental pulse test and the low current charge/discharge test. In the incremental pulse test, the battery is charged or discharged in 10% SoC increments, followed by extended rest periods, allowing the

voltage to stabilize. This is a measurement of the true OCV at the specific SoC level. In the low current test, cells are charged or discharged at very low C-rates, typically below $C/20$. This minimizes the voltage drop from internal resistance and polarization, allowing the resulting OCV measurement to closely approximate the true value [61], [62].

The OCV-SoC curves often differ between charging and discharging due to hysteresis and polarization effects, with charge OCV generally being higher than discharge OCV. To address this, data from both processes are typically averaged. As shown in Figure 10, the true static OCV curve closely represents an average of the charge and discharge curves [63]. Although the incremental pulse test yields more accurate OCV measurements across SoC levels, it requires longer rest times and strict environmental control for optimal accuracy [64].

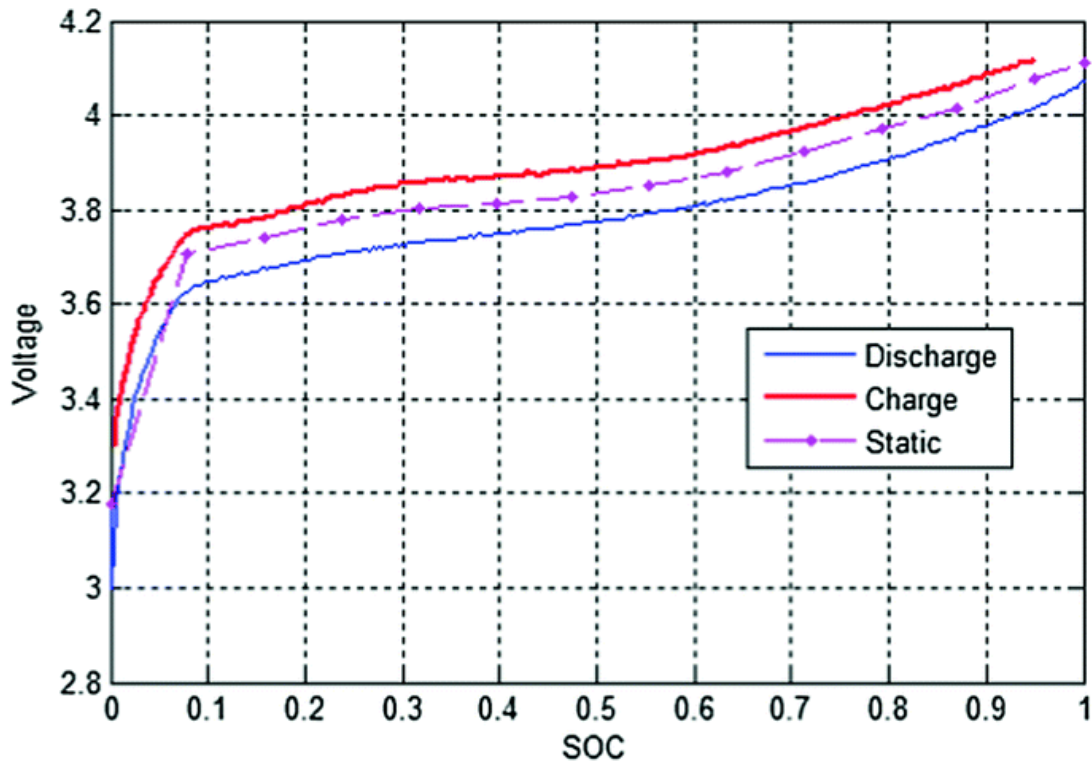


Figure 10 Relationship between OCV and SoC during discharge, charge, and static voltage in low-current OCV test [63].

2.2.3 Static Capacity test

The static capacity test assesses a cell's actual energy storage capacity and validates it against the manufacturer's datasheet, also serving as an indicator of the State of Health (SoH) relative to its original capacity. The test should be conducted under constant, controlled conditions, this test evaluates cell capacity across different SoC ranges based on the maximum and minimum operating voltages.

The constant current (CC) discharge test is the most common method, where the battery is fully charged using a constant current/constant voltage (CCCV) protocol, then discharged at a fixed current until reaching its cut-off voltage. The total discharge, measured in ampere-hours (Ah) or milliampere-hours (mAh), provides a direct indication of the battery's capacity [65], [66].

Factors such as temperature, discharge rate, and battery age impact capacity test results. Higher temperatures can increase ionic conductivity, enhancing capacity, while high discharge rates may reduce effective capacity due to internal resistance and kinetic constraints [49], [51]. Standardized conditions are essential for consistent and comparable results across cells. Figure 11 shows a static capacity test on Samsung 50E cylindrical cells shows that the maximum cell capacity can be reached at lower C-rates discharge and higher temperatures.

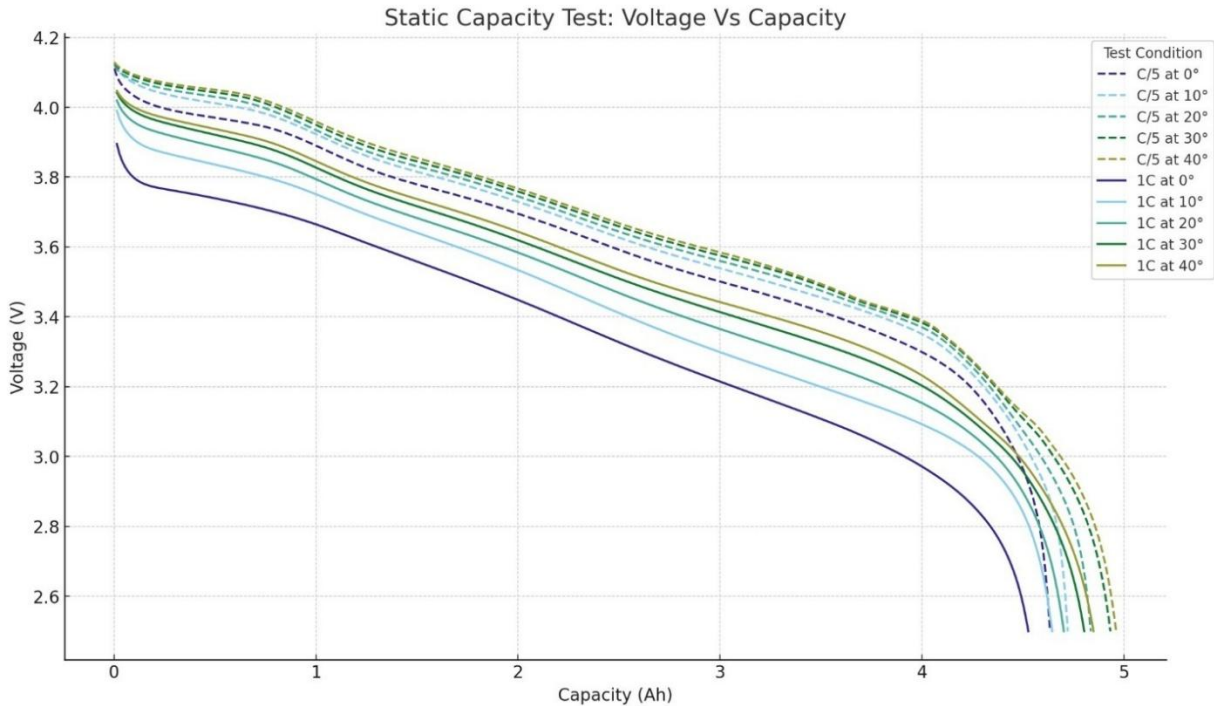


Figure 11 Voltage vs. Capacity curves for Samsung 50E cells during static capacity tests conducted at varying temperatures, and discharge rates of C/5 and 1C.

2.2.4 Hybrid Pulse Power Characterization (HPPC) Test

According to the U.S. Department of Energy Battery Test Manual for Electric Vehicles, the Hybrid Pulse Power Characterization (HPPC) test assesses a cell's dynamic power capability across its voltage limits using a test profile with both discharge and charge (regeneration) pulses. Initially, it measures the minimum voltage pulse discharge power after a 30-second discharge pulse and the maximum voltage pulse charge power after a 10-second charge pulse. These measurements determine key performance metrics, such as Peak Power and Available Energy [67]. Figure 12 illustrates a standard HPPC test sequence in which the cell is fully discharged and rested for 1 hour, then fully charged and rested for another hour. Pulses are then applied at 10% DoD increments, with a 1-hour rest in between each discharge/ charge pulse sequence.

Different HPPC profiles are used based on test requirements and desired data, with adjustments in rest periods, C-rates, and cell temperatures. For high-power applications, a high-current HPPC profile assesses cell performance under extreme load conditions. This involves setting discharge and charge C-rates to the maximum limits recommended by the cell's manufacturer to evaluate the battery's capacity and internal resistance to withstand high power demands.

The HPPC data includes voltage response curves, which allow for calculating the internal resistance based on capacity removed across SoC ranges. This data is crucial for evaluating resistance degradation in life testing and developing hybrid battery performance models for vehicle systems analysis [67]. The ohmic resistance can be estimated by measuring the instantaneous voltage drop at the start of the discharge and charge pulses. The polarization resistance can be estimated by measuring the voltage change throughout the discharge and charge pulses [68]. The Equivalent Circuit Model (ECM) is a mathematical model that represents the cell's electrical performance as an electrical circuit with resistors and capacitors. These parameters can be derived through voltage drop calculations (Equation (2.2)) or advanced curve-fitting methods, such as genetic algorithms, particularly for higher-order ECMs. While higher-order ECMs require additional data and testing, they typically enhance estimation accuracy. The second-order ECM shown in Figure 13 offers a balanced approach, optimizing both accuracy and computational efficiency, while minimizing over-parameterization [69].

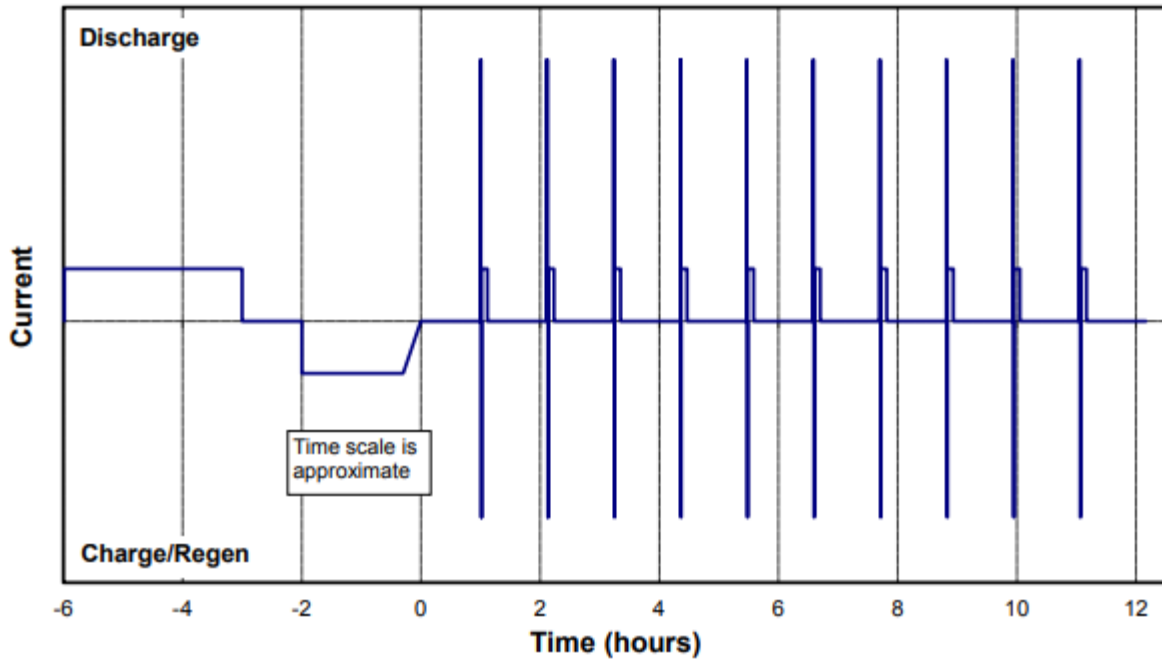


Figure 12 U.S.D.O.E. Standard HPPC test sequence [67].

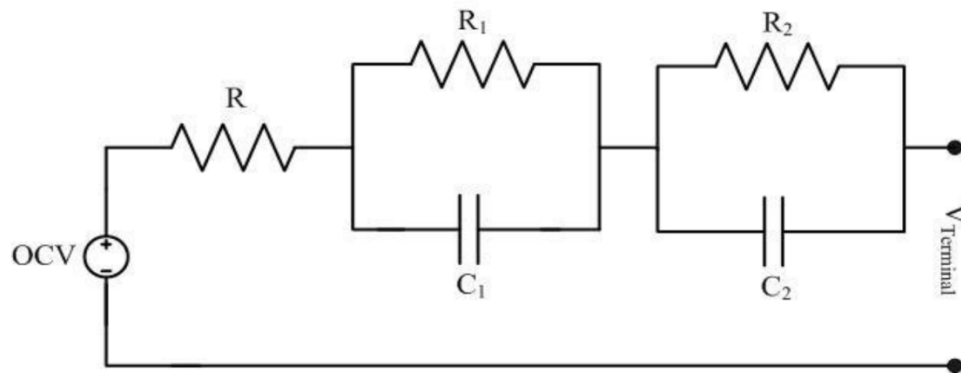


Figure 13 Second-order equivalent circuit battery model (ECM) [69].

2.3 Battery Thermal Management

There is a direct relation between temperature and cell performance. Studies found that the optimal operating temperatures of Li-Ion cells usually lie between 0°C to 40°C, anything lower or higher would affect the cell's efficiency and cycle life [70]. The heat generation of Li-Ion cells is greater at high current loads, this leads to an increase in the cells operating temperatures [71]. Excessive temperatures affect the electrochemical reactions life cycle, and safety of batteries [72].

The extreme increase in Li-ion cell temperatures triggers exothermic reactions within the cell, caused by electrolyte decomposition or internal short circuits. Those reactions are self-sustainable causing uncontrollable rise in temperature, and gas release within the cells [73]. As the temperature rises, the internal pressure increases, causing cells ruptures, fires or even explosions. In a battery pack, the risk of thermal propagation between adjacent cells can lead to large-scale fires [74].

The uniformity of cell temperature also affects the performance. Within a cell, the electrochemical reactions proceed at different rates causing instability, and a non-uniform energy utilization [75]. As discussed before, the internal resistance of cells varies according to temperatures [57]. This can be extended to be within the cell itself, making some parts overcharged or discharged than others. The non-uniformity of temperatures across cells in a battery pack causes further uneven voltages across the pack. Research shows that cells internally and across the pack should be kept at under 5°C to prevent capacity loss and to enhance the safety of the cell or pack [76].

Different Battery Thermal Management Systems (BTMS) are used within the industry to maintain ideal operating temperatures and temperature uniformity across cells. The main cooling approaches can be categorized into Active cooling, Passive cooling and a combination of both. In active cooling. Active cooling relies on an external energy source to operate, while passive cooling utilizes the natural heat dissipation mechanism of the system [77], [78]. This section will discuss BTMS technologies and advancements such as air cooling, liquid cooling, two-phase cooling, and heat pipes.

2.3.1 Air Cooling

Passive air cooling relies on the natural air convection heat dissipation to the surrounding

air volume. Aluminum fins are usually attached to the heating unit to increase the surface area and improve the cooling efficiency [79]. While being a simple solution, it is not currently used in any automotive production battery packs as it is not suitable for high-power applications where high heat generation is expected due to its low thermal conductivity rate.

Active air cooling relies on forced air convection heat dissipation using a mechanical component like a fan or a blower to circulate the air surrounding the heating unit. Those BTMS components have low cost, require less maintenance, and have fewer components than other BTMS used in EVs. Studies show that reciprocating airflow achieves better cooling uniformity and efficiency than unidirectional airflow by disturbing the boundary layers on the heating unit [80], [81]. This can be achieved with a reversible fan where the direction of rotation changes periodically.

Active air cooling is mainly used in low-capacity EVs and hybrid vehicles that require less power than larger EVs because air cooling is limited by the low thermal conductivity of air [82]. Figure 14 shows an example of a suction-based BTMS, highlighting the inlet, air circulation path around the battery unit and hot air outlet [83]. Some hybrid electric vehicles that utilize forced air cooling with fans in their battery packs include the 2020 Ford Fusion SE Hybrid, which features a 1.4 kWh battery pack [84]. The 2023 Toyota Prius with a 0.91 kWh battery pack, while its plug-in version is equipped with a larger 13.1 kWh pack [85], [86]. EVs employing air cooling systems include the 2025 Nissan Leaf with a 40 kWh pack and the 2024 Renault Zoe with a 52 kWh pack [87], [88].

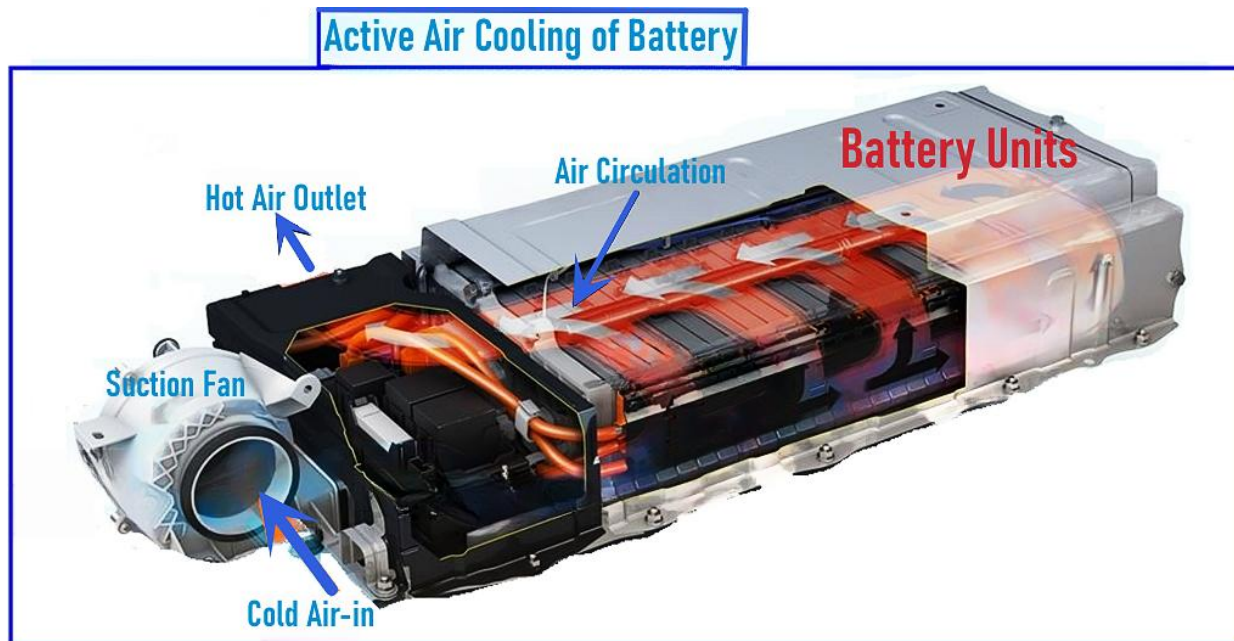


Figure 14 Air Cooled BTMS in a 2004 Second generation Toyota Prius hybrid with a 1.3Kwh NiMh battery pack [83], [89].

2.3.2 Liquid Cooling

Liquid cooling is mostly done under an active mechanism. In immersion cooling, the heating unit is sunken inside a liquid tank; pumps usually recirculate the liquid around the heating unit. In indirect cooling, a medium mechanism is used to carry the liquid such as cold plates or circumferential serpentine manifold. Immersion cooling has better heat conductance, as there is no extra resistance between the heating unit and the liquid. This leads to better thermal performance and lower cell temperatures at high currents. However, in electrical devices, a dielectric liquid is used. The issue with dielectric fluids is that they have a higher rate of heat rejection and poor thermal properties leading to a non-uniform heat dissipation across the cells [90].

Indirect cooling is the standard in industry. Serpentine cooling which is used by Tesla

provides greater surface area contact with cylindrical cells and therefore better temperature uniformity across the cells [91]. However, they require more space, and higher pumping power due to the increased liquid volume and pressure [92]. They also introduce more complexity into the battery pack design. Cold Plates are widely used in industry, Figure 15 shows the Hyundai Ioniq 5 BTMS which utilizes a large cold plate that has a serpentine path from the inlet from one side to the outlet on the other side of the battery pack to cool down all the battery modules [93]. Rivian on the other hand uses a cold plate sandwiched between each two modules [94]. Cold plate channel shape and size can be optimized based on the system requirements. A higher number of channels can improve the heating and cooling uniformity but it comes at the cost of a more complex design and larger pressure drops [95]. As shown in Figure 16 serpentine-shaped dual inlet and outlet micro-channel cold plate systems have high-temperature uniformity and energy efficiency. A micro-channel thickness of 1.0 mm and width of 4–5 mm ensures efficient heat dissipation and minimal pressure drop, reducing pump power requirements [96]. Figure 17 shows a novel zig-zag serpentine flow pattern within 13 rectangular profile channels that maximizes coolant coverage over the cold plate's surface area [97].

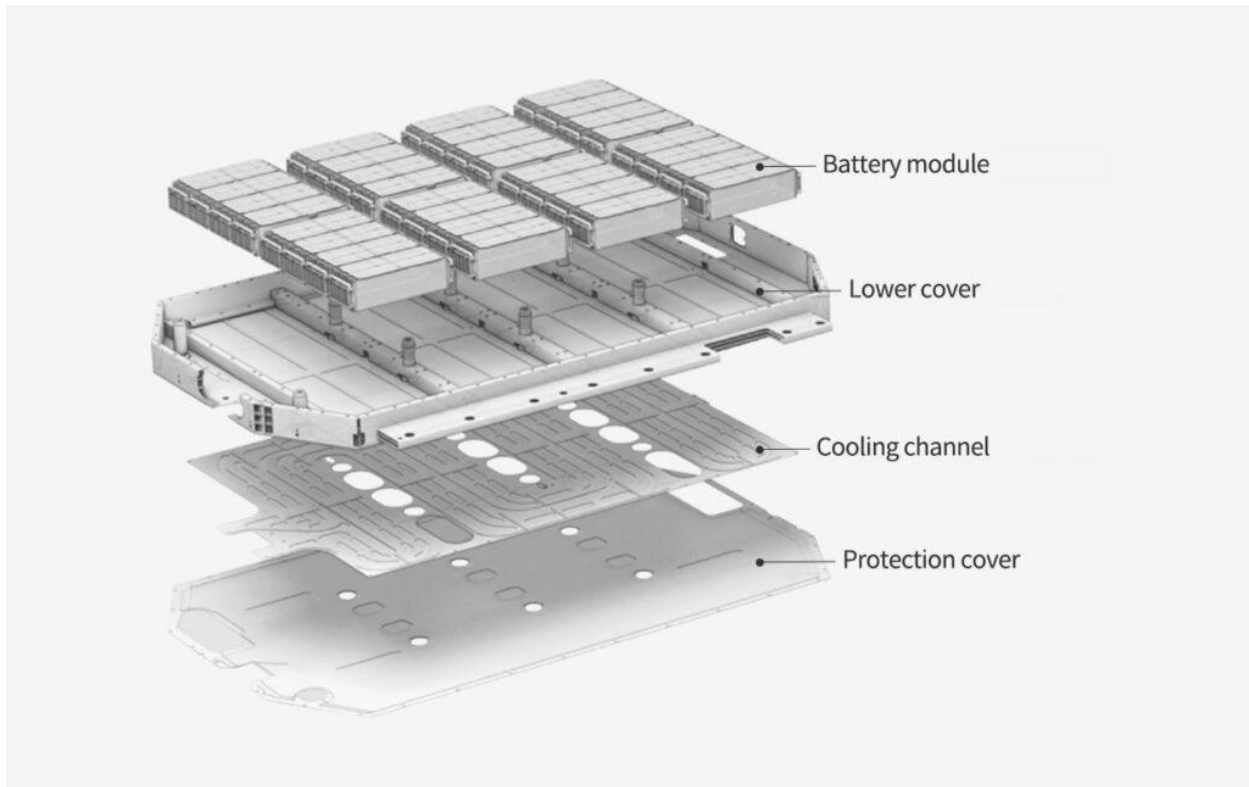


Figure 15 Hyundai Ioniq 5 battery pack extruded view [93].

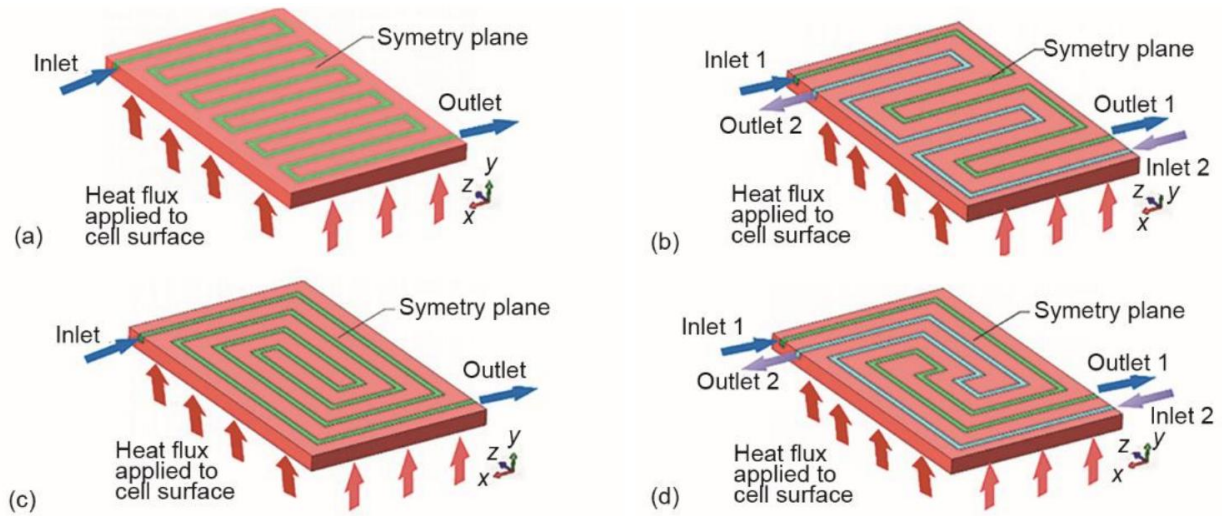


Figure 16 Different cold plate serpentine channel designs [96].



Figure 17 Zig-Zag serpentine 13-channel cold plate design [97].

2.3.3 Two Phase Cooling

Two-phase cooling utilizes the phase change from liquid to vapor with high thermal conductivity to efficiently absorb heat from the battery surface. Two-phase cooling can achieve good thermal uniformity within the battery pack. This will allow for constant and longer operation of the pack as the variance in temperature will affect the cell's chemistry causing imbalances in performance and degradation rates [98]. Two Phase Cooling technology also reduces coolant usage due to the high thermal conductivity, making the system lighter. The enhanced temperature control facilitates ultra-fast charging, even under high C-rates [99]. Hong et al. studied direct two-phase cooling in a lithium-ion EV battery pack. During aging, the two-phase refrigerant cooling system demonstrated a 16.1% increase in battery capacity and a 15.0% reduction in internal resistance when compared to liquid cooling under harsh environmental conditions [100]. Two-phase immersion cooling consistently achieved remarkable thermal uniformity, maintaining a 1°C temperature difference during 10C discharges [101]. In contrast, it outperformed single-phase liquid immersion and natural convective air cooling by 69% and 99%, respectively. Additionally,

this performance extended to cell charging at rates of up to 4C, a category considered fast charging, where temperature rise remained around 1°C, with a 0.3°C maximum axial temperature difference across the cell [101].

2.3.4 Heat Pipes

Heat pipes are passive thermal management solutions designed to transport heat from a hot spot to a cooler region using a vacuum-sealed pipe filled with a working fluid, typically a refrigerant [102]. At the evaporator end, heat from the source is absorbed through the pipe wall, causing the working fluid to vaporize. The vaporized fluid then moves toward the cooler condenser end, where it releases the absorbed heat, condenses back into liquid form, and is returned to the evaporator via capillary action within a wick structure or through gravitational forces. This cyclic process enables continuous heat transfer with no external energy input, offering a reliable means of temperature regulation [103]. On the condensation side, depending on the application, natural convection can be used to maintain the system as completely passive, or forced convection, using a fan or cold plate, can be applied, resulting in a hybrid system [104].

A study on a U-shaped flat microchannel heat pipe array with a side cold plate at the condensation section, Figure 18, demonstrated a 16% reduction in cell temperatures and a 60% improvement in temperature uniformity, keeping the cells within a 5°C difference [105]. Another study evaluating a 3D vapor chamber, Figure 19, with a 120% filling ratio showed superior performance compared to a 60% filling ratio, reducing thermal resistance from 0.4 K/W at 10W to 0.18 K/W at 60W while maintaining a temperature difference within 5°C. Orientation tests (0°, 90°, and 180°) revealed negligible performance impact due to the sintered wick structure, confirming the system's reliability under varying vehicle inclinations [106]. Therefore, Heat Pipes

demonstrate a promising solution for BTMS due to their ability to maintain good temperature uniformity.

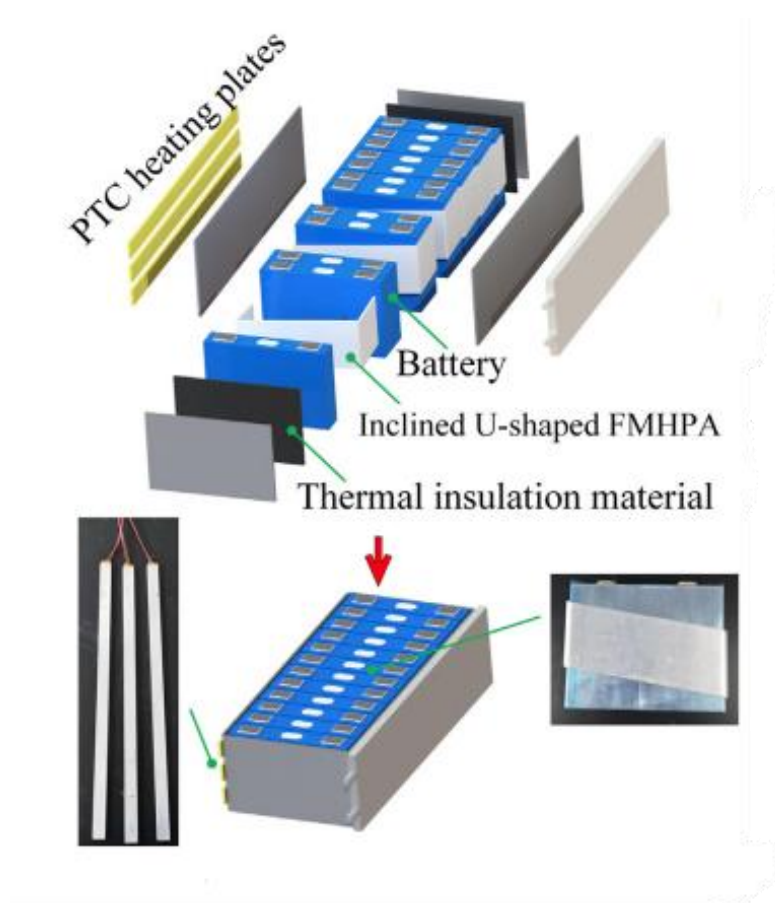


Figure 18 U shaped Heat Pipe with a side cold plate [105].

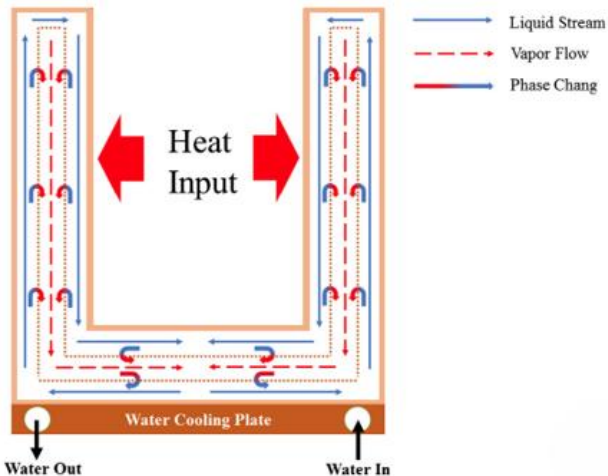
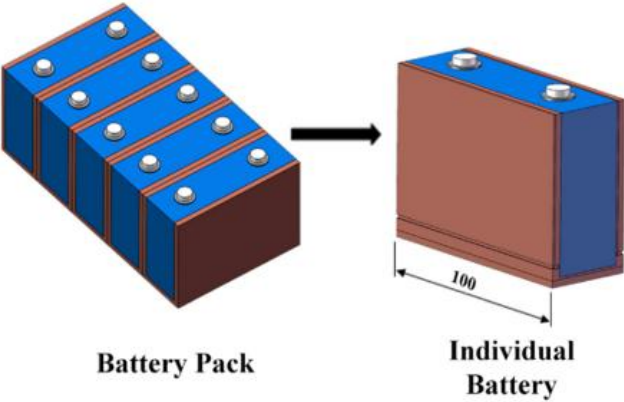


Figure 19 U shaped Heat pipe with bottom cooling [106].

Chapter 3

Cell Characterization

This section will examine the individual cell characterization, which is important for assessing performance relative to the manufacturer's specifications. The CALB L221N113A are chosen by the project partner for their high capacity, fast charging capability, and their geometrical dimension. Analyzing the CALB cell's behaviour under various conditions provides valuable insights into its capacity, thermal stability, and degradation rates. However, in this project, the primary focus is on capacity and internal resistance at different SoC levels. These parameters are critical for battery module or pack design, as they support the Battery Management System (BMS) in SoC estimation and cell balancing.

3.1 CALB 3.7V 113Ah cell specifications

The L221N113A cells are manufactured by China Aviation Lithium Battery (CALB), ranked as the 7th largest EV battery supplier in 2023 [107]. These prismatic cells use NMC 811 chemistry, comprising Nickel (80%), Manganese (10%), and Cobalt (10%). The high nickel content provides high energy density, while manganese and cobalt contribute to thermal stability and structural integrity, respectively. The combination of high energy density and reduced cobalt content makes NMC 811 cells ideal for EV applications, where efficiency and range are crucial [108]. Table 1 presents the key specifications of the CALB cells, as outlined in the manufacturer's datasheet [109]. The product used in testing was purchased from a 3rd party supplier and had m6 studs welded on the cell's terminals as shown in Figure 20.

Table 1 Key specifications of CALB prismatic cells from the manufacturer's datasheet [109].

Manufacturer	China Aviation Lithium Battery (CALB)
Model Number	L221N113A
Type	Prismatic
Chemistry	Lithium Nickel Manganese Cobalt Oxide (NMC811)
Nominal Voltage	3.67 V
Operating Voltages	2.8-4.35V $T \geq 0^{\circ}\text{C}$ 2.2-4.35V $-30^{\circ}\text{C} \leq T < 0^{\circ}\text{C}$
Nominal Capacity	113.5 Ah
Internal Resistance	0.4~0.6 m Ω
Recommended SOC Window	5%~97%
Charging Temperature	-20~55 $^{\circ}\text{C}$
Discharging Temperature	-30~55 $^{\circ}\text{C}$
Dimension	220.8 \pm 0.2(W) x 33.36 \pm 0.2(T) x 105.88 \pm 0.3(H)mm
Weight	1800 \pm 25g
Shell Material	Aluminum alloy



Figure 20 CALB L221N113A Cell with M6 stud terminals.

3.2 Cyclor / Thermal Chamber Specifications

A controlled testing environment, utilizing high-precision equipment, is essential for accurate cell performance assessment. This study uses the following devices:

- 1- Arbin BT-2000: This unit supports six completely independent channels, allowing multiple simultaneous tests with no cross-interference. It offers accuracy up to 0.02% for low power, and 0.05% for high power, with current rise times as fast as 10 μ s for reliable testing. Features include Potentiostatic/Galvanostatic functionality, four-point Kelvin probe connection for main channels, channel paralleling to increase current handling, and multiple current ranges for enhanced accuracy across various testing conditions. It offers expansion options through plug-and-play channels and auxiliary modules [110].
- 2- ESPEC BTZ-133 Thermal Chamber: This environmental chamber, shown in Figure 21, has an interior volume of 1.5 cu. ft. (42 litres) and operating temperature range of -70°C to 180°C. It supports average heating and cooling rates of 3.5°C/min and 3°C/min, respectively, with a temperature fluctuation of $\pm 0.5^\circ\text{C}$ at the control sensor, ensuring stable environmental conditions [111].



Figure 21 ESPEC BTZ-133 thermal chamber.

3- AVL Compact I/O Cubes: This device manages control and data acquisition across the cyclers, and thermal chambers, integrating data from testing devices. It includes 16 universal measurement channels, 24 thermocouple channels, and 8 RTD channels for temperature measurements, along with 8 analog and 16 digital outputs. It has acquisition rates up to 100 Hz with good noise-resistance [112].

These devices are managed by a central PC using AVL Lynx and Puma system integration, which configures the testing procedures and reads the data collected.

3.3 Testing Setup (thermal placement, cell holder)

Fifteen T-type thermocouples were installed on the cell and one ambient thermocouple was

in the chamber for the single-cell testing. As shown in Figure 22, three thermocouples are placed on the cell's sides, where the Micro Channel Heat Pipes (MCHP) cooling technology will be positioned in the module design phase. Three thermocouples are positioned on the front and back of the cells, and one at the bottom. This arrangement provides comprehensive coverage of the cell's heat distribution and helps in identifying key heating zones, which is important information that can be used in cooling system design.

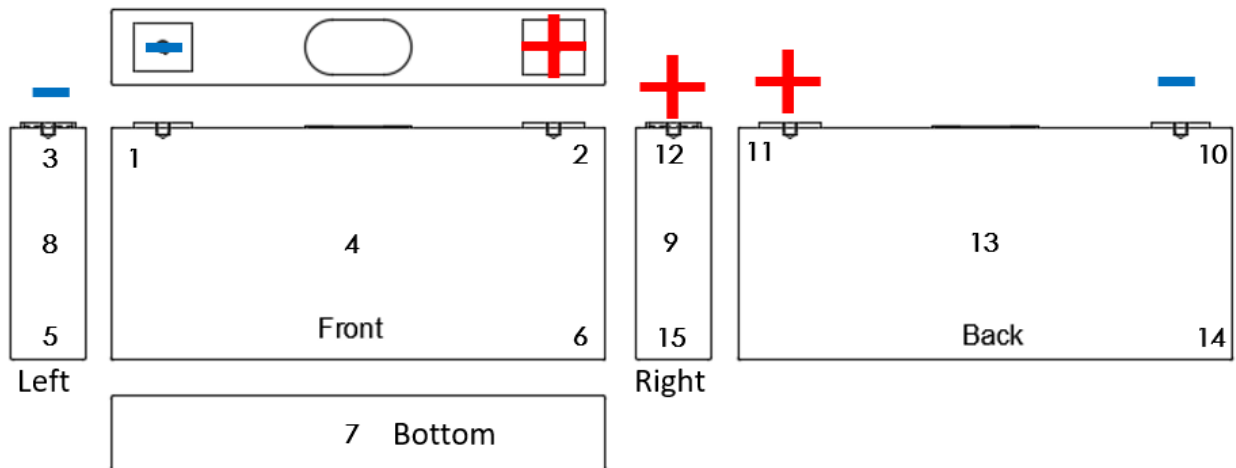


Figure 22 Thermocouple placement on the cell for single-cell testing.

The cell is secured inside the thermal chamber using a fixture, as shown in Figure 23. The setup evaluates the cell's performance without active cooling, relying solely on adiabatic cooling. Although the chamber includes a small fan positioned in the corner, its effect is considered negligible.



Figure 23 Single-cell fixture inside the BTZ-133 thermal chamber.

3.4 Test Procedure

To extract key insights about the cell's behavior, five testing procedures were implemented. The Static Capacity test evaluates the cell's performance against the datasheet specifications. The Open Circuit Voltage (OCV) test maps the voltage response across the SOC range at different temperatures, providing essential data for SOC estimation and integration into the module's BMS. The Hybrid Pulse Power Characterization (HPPC) test determines the cell's internal resistance, which is critical for BMS implementation at the module level. Finally, the Hyundai Ioniq fast charging and 400A pulse fast charging profiles assess the cell's performance and thermal response under high-current charging conditions.

3.4.1 OCV Test Procedure

The charge and discharge OCV tests are done at 0.05C-rate which equates to 6.75 A. It was done at ambient temperatures of 0°C, 25°C and 45°C. The OCV test procedure for battery cells is as follows:

- 1- Soak at 25°C for 4 hours.

- 2- Charge using CCCV mode at a 0.5 C rate, with a cutoff voltage of 4.35 V and a cutoff current of 5.6 A.
- 3- Rest for an hour.
- 4- Soak at the desired temperature for 4 hours.
- 5- Discharge at 0.05 C rate with the cut-off voltage of 2.8 V.
- 6- Rest for an hour.
- 7- Charge at 0.05 C rate with the cut-off voltage of 4.35 V.
- 8- Rest for an hour.

3.4.2 Static Capacity Test Procedure

The static capacity test is done at 1 C-rate discharge, and ambient temperature of 0°C, 25°C and 45°C. 1 C-rate was chosen based on the nominal discharge rate the cell's datasheet recommended [109]. The test procedure for battery cells is as follows:

- 1- Soak at 25 °C for 4 hours.
- 2- Charge using CCCV mode at a 1 C rate, with a cutoff voltage of 4.35 V and a cutoff current of 5.6 A.
- 3- Rest for an hour.
- 4- Soak at the desired temperature for 1 hour.
- 5- Discharge at 1 C rate with the cut-off voltage of 2.8 V.
- 6- Rest for an hour.

3.4.3 HPPC Test Procedure

A modified version of the standard HPPC test as explained in section 2.2.4 is used for the

tests. The tests are done at 1 C-rate, and ambient temperatures of 0°C, 25°C and 45°C. The HPPC test procedure for battery cells is as follows:

- 1- The battery is soaked at 25°C for 1 hour.
- 2- Charge using CCCV mode at a 1 C rate, with a cutoff voltage of 4.35 V and a cutoff current of 5.6 A.
- 3- Rest for an hour.
- 4- The battery is soaked at the desired temperature for 1 hour.
- 5- Discharge the battery at 1/4C for 100 seconds.
- 6- Rest for 200 seconds.
- 7- Charge at 1/20 C for 100 seconds.
- 8- Rest for 200 seconds.
- 9- Discharge the battery at 1/2C for 100 seconds.
- 10- Rest for 200 seconds.
- 11- Charge at 1/10 C for 100 seconds.
- 12- Rest for 200 seconds.
- 13- Discharge the battery at 3C/4 for 100 seconds.
- 14- Rest for 200 seconds.
- 15- Charge at 1/5 C for 100 seconds.
- 16- Rest for 200 seconds.
- 17- Discharge the battery at 1C for 100 seconds.
- 18- Rest for 200 seconds.
- 19- Charge at 1/4 C for 100 seconds.
- 20- Rest for 1 hour.

21- Discharge the battery at 1C to reach 10% of capacity removal and allow for one hour rest after each discharge.

22- Repeat steps 5-21 for SOCs from 100-0% with 10 % intervals with cut-off voltage of 2.8 V.

3.4.4 Fast Charging Tests Procedure

Two fast-charging profiles are used based on the project partner's requirements. The first one is the Hyundai Ioniq fast charging at 25°C and the second is Pulse fast charging at 25°C. Those two profiles are used as a benchmark to evaluate the cell's thermal performance under high charging loads. Before running any fast-charging test, the cells are discharged at 1C, rested for an hour, and then soaked at 25°C. With the Pulse charge, the cell is flipped so the front side of the cell is closer to the chamber fan. This is to eliminate the effect of the fan on both sides without the need to repeat the tests twice.

The Hyundai Ioniq at 25°C fast charging profile, illustrated in Figure 24, starts with a peak current of 303.4 A at 9.2 minutes and sustains a current above 300 A for approximately 6 minutes during the CC phase. After this, the current begins to decrease gradually but remains above 180 A for around 7.5 minutes before transitioning into the CV phase. By the end of the profile, at around 46 minutes, the current tapers to 11 A. It is worth noting that the anomalies observed near the end of the profile may stem from measurement errors, as the data was likely recorded during a live test. However, these discrepancies are not expected to impact the testing outcomes significantly.

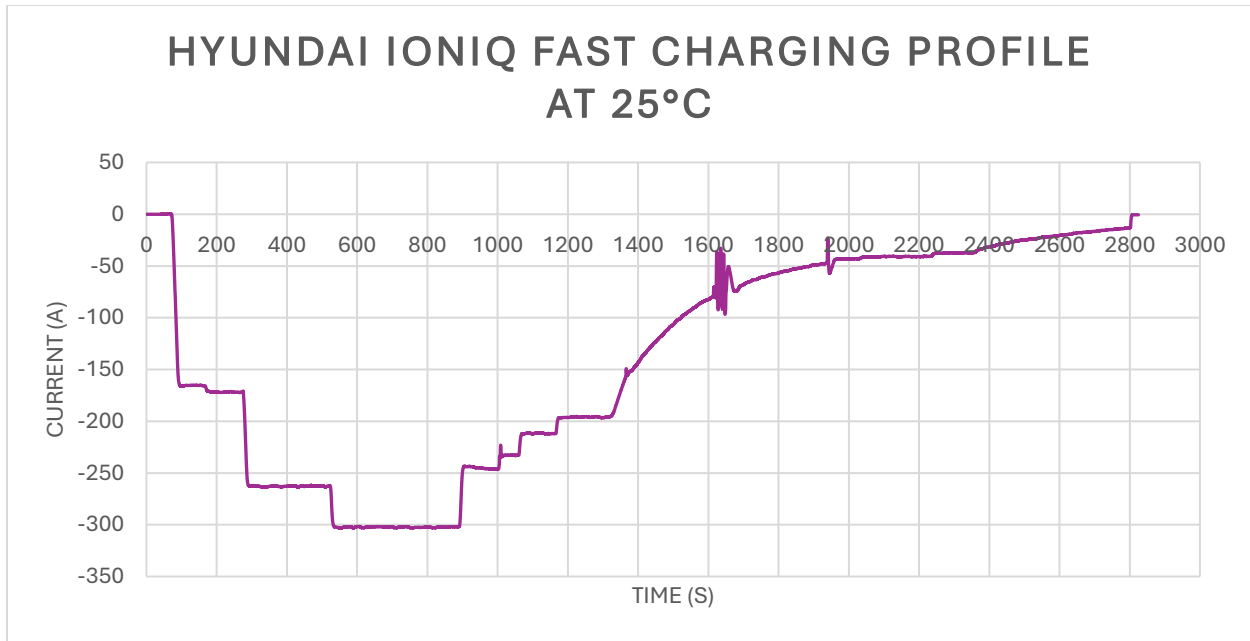


Figure 24 The current (A) profile of the Hyundai Ioniq fast charging at 25°C.

Pulse Fast Charging employs short bursts of high current interspersed with brief relaxation periods, enabling effective heat dissipation compared to traditional constant current (CC) charging. The intermittent pulses allow the cell to dissipate heat during rest intervals, mitigating thermal buildup [113]. Additionally, studies indicate that pulsating currents enhance charge acceptance by optimizing the cell's electrochemical response [114].

Figure 25 illustrates the current pulse charging profiles used in this study. The test begins with 400A pulses for 10 seconds, followed by 10-second rest periods, sustained for approximately 22 minutes. It then transitions to 340A pulses for around 6 minutes, and finally to 227A pulses, continuing until the current tapers at the end of the profile. The 400A pulses were selected based on the cell's datasheet, which specifies this value as the maximum acceptable current for pulse fast charging [109].

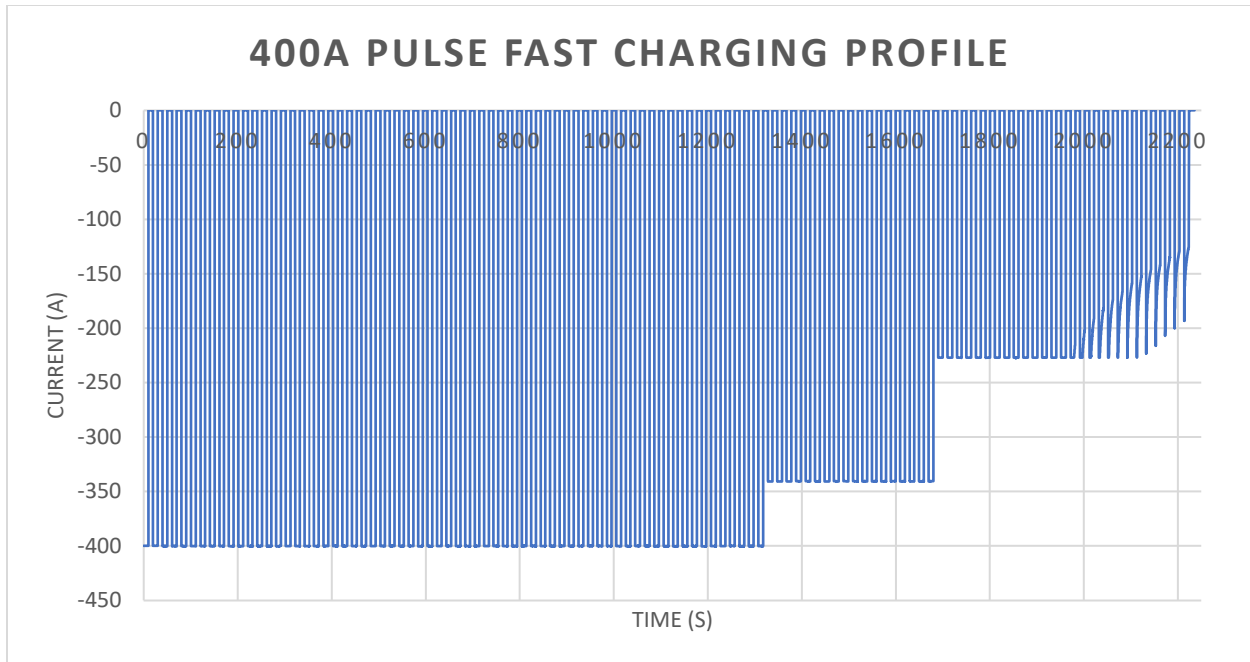


Figure 25 400A pulse charging current profile.

3.5 Results and Discussion (Capacity, Resistance)

3.5.1 Static Capacity Test Results

The static capacity discharge test at 1C was conducted at 0°C, 25°C, and 45°C, revealing two key findings: the capacities of the cells and the temperature rise during constant current discharge. As shown in Figure 26, the voltage drop across the three test temperatures highlights distinct differences in performance. At 0°C, the cell reached the cutoff voltage in 54.5 minutes, whereas at 25°C and 45°C, it took 61.21 minutes and 62.5 minutes, respectively. This indicates that the energy extracted from the cell at 0°C was less than its nominal capacity, while at 25°C and 45°C, the cell delivered more energy than its nominal rating. The total energy capacities were 103.1 Ah, 115.7 Ah, and 118.1 Ah, respectively. The voltage curves for the tests at 25°C and 45°C are almost identical, whereas at 0°C, the voltage drop was significantly higher. These observations confirm that cell performance improves at higher temperatures, although the relative improvement

diminishes beyond a certain point. The results of the Static Capacity tests are summarized in Table 2.

Figure 27 demonstrates the temperature rise during the discharge process. At 0°C, the cell's average temperature increased by 11°C, while at 25°C and 45°C, the increases were 8°C and 5°C, respectively. At 0°C, the cell's temperature rose to an average of 11°C, compared to 33°C and 50°C at 25°C and 45°C. The observed temperature deltas indicate that the cells produce more heat at lower ambient temperatures, likely due to increased internal resistance. This correlation underscores the impact of temperature on the cell's thermal behavior and internal losses, with colder conditions amplifying heat generation and reducing efficiency. The temperature readings at 25°C showed significant noise due to the use of a different DAQ device, introducing a higher margin of error. Despite this, the average temperature and overall trend remained accurate and aligned with expected behavior.

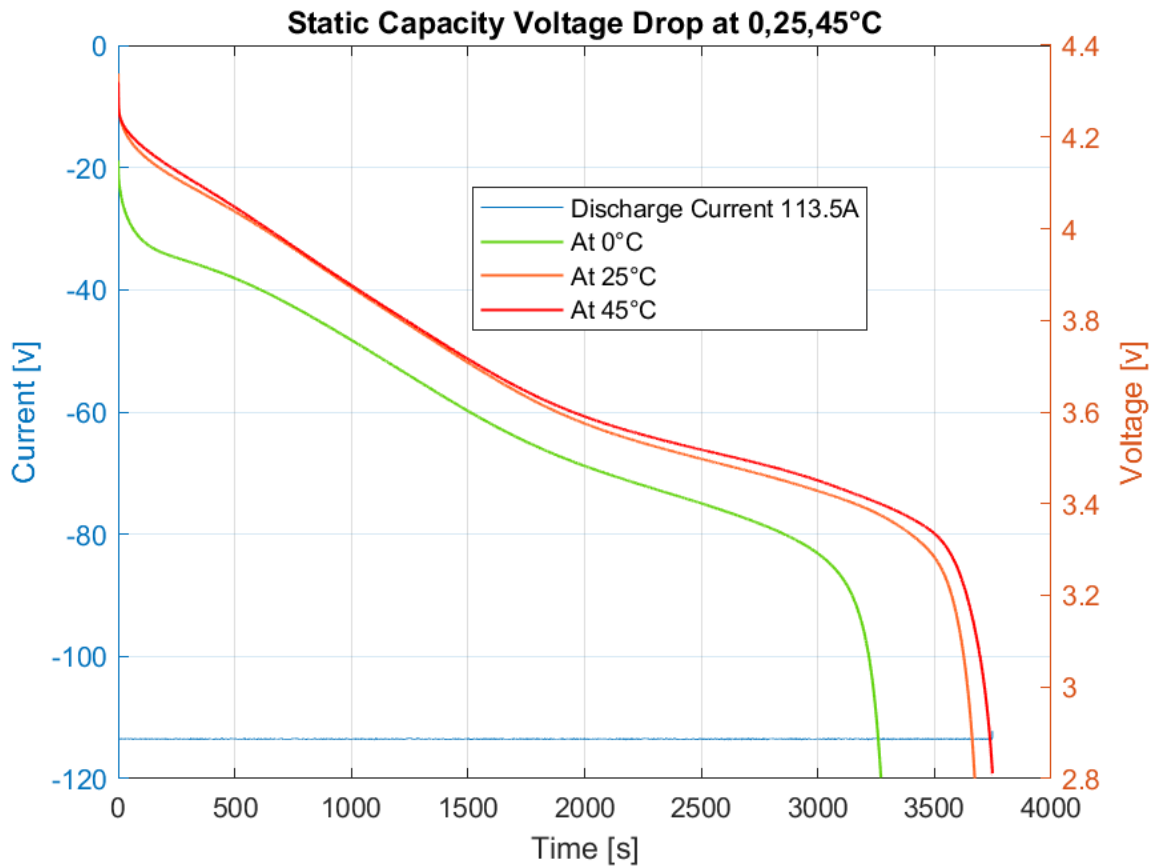


Figure 26 Static Capacity Voltage, Current discharge vs Time at 0,25,45°C ambient testing conditions.

Table 2 Highlighted results of the Static Capacity tests.

Ambient Temperature Testing Case (°C)	Removed Capacity (Ah)	Test Time (s)	Max Temperature Increase (°C)
At 0°C	103.1	3270.5	10.5
At 25°C	115.7	3672.6	6.9
At 45°C	118.1	3748.6	4.9

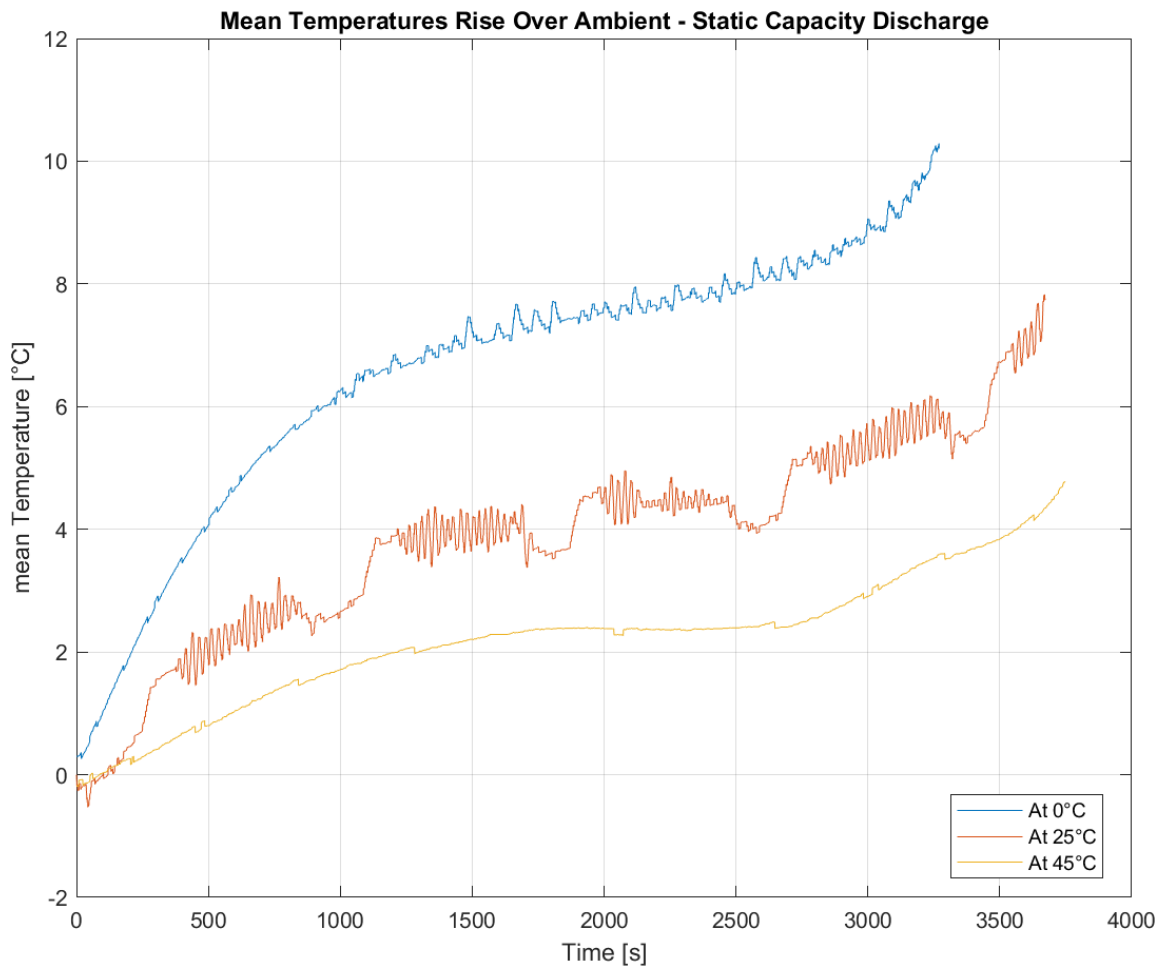


Figure 27 Rise Over Ambient Average Temperatures of the Static Capacity Tests. It is noted that the measurements at 25°C exhibit more noise compared to the other test conditions.

3.5.2 OCV Test Results

The OCV-SoC curve at 25°C (Figure 28) exhibits a clear hysteresis between the charge and discharge profiles. This hysteresis arises from irreversible thermodynamic and electrochemical processes, which are discussed further in Section 2.2.2. The mean OCV curve mitigates the hysteresis effect and serves as a practical baseline for SoC estimation. At low SoC, the curve shows

a steep voltage rise, indicative of significant shifts in lithium-ion concentration within the active material. In the 20%–80% SoC range, the voltage response is relatively linear, making this region particularly suitable for SoC estimation due to its reduced sensitivity to small variations. At higher SoC values, the slope becomes steeper, suggesting that the cell still has ongoing electrochemical activity.

The mean OCV-SoC curves at 0°C, 25°C and 45°C (Figure 29) demonstrate the impact of temperature on equilibrium voltage. At 0°C, the OCV values are consistently lower due to increased internal resistance and reduced ionic mobility, both of which hinder the electrochemical processes. At 45°C, the OCV values are slightly elevated compared to those at 25°C, reflecting enhanced ion transport and reduced polarization at higher temperatures (lower internal resistance). These temperature effects are most pronounced at lower SoC levels, where the electrochemical limitations are more significant. However, at mid-range and higher SOC levels, the OCV values tend to converge, indicating that temperature variations have less influence in this range. This suggests that for this cell, OCV-SOC estimations are more straightforward and reliable at SOC levels above 20%.

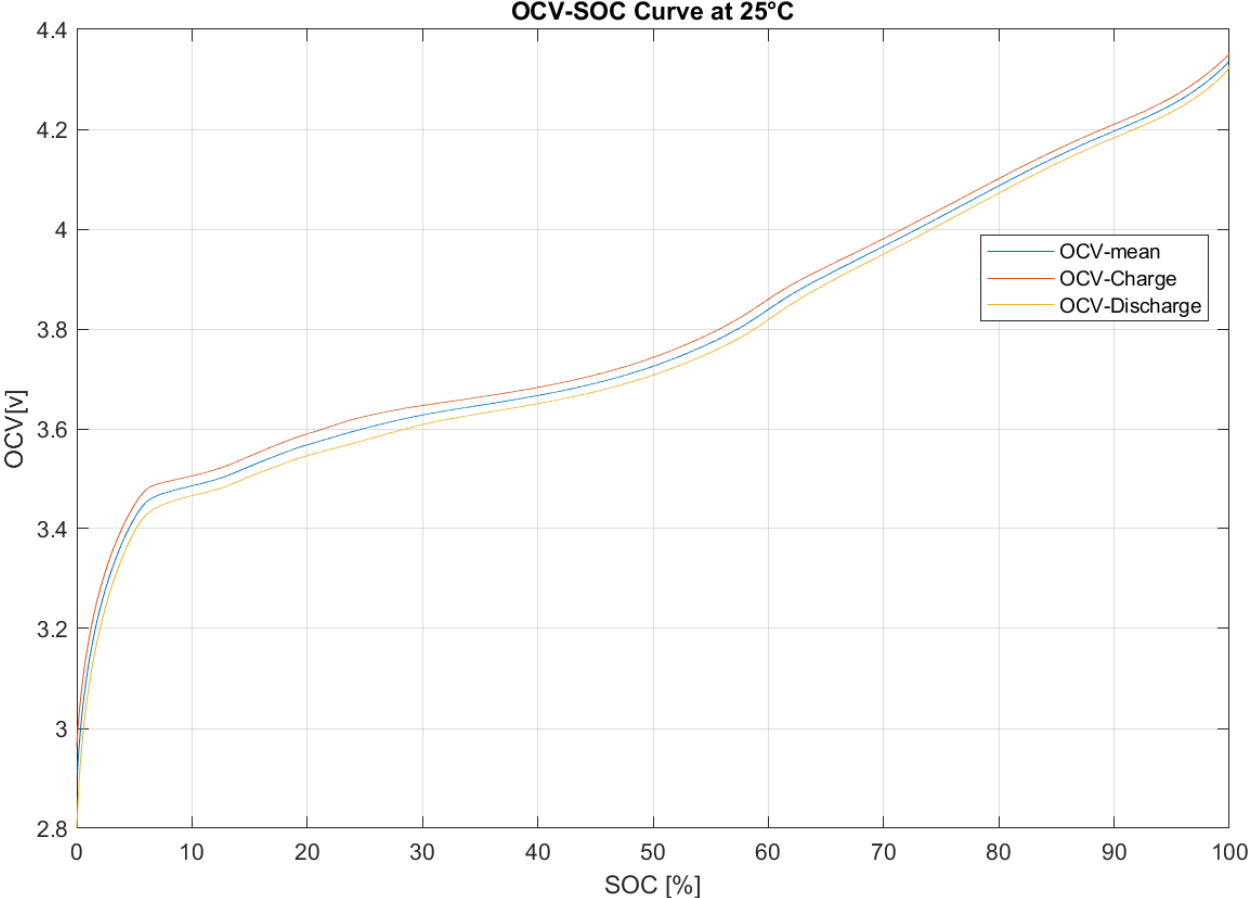


Figure 28 OCV-SoC curves at 25°C. The mean OCV is used in SoC estimation applications.

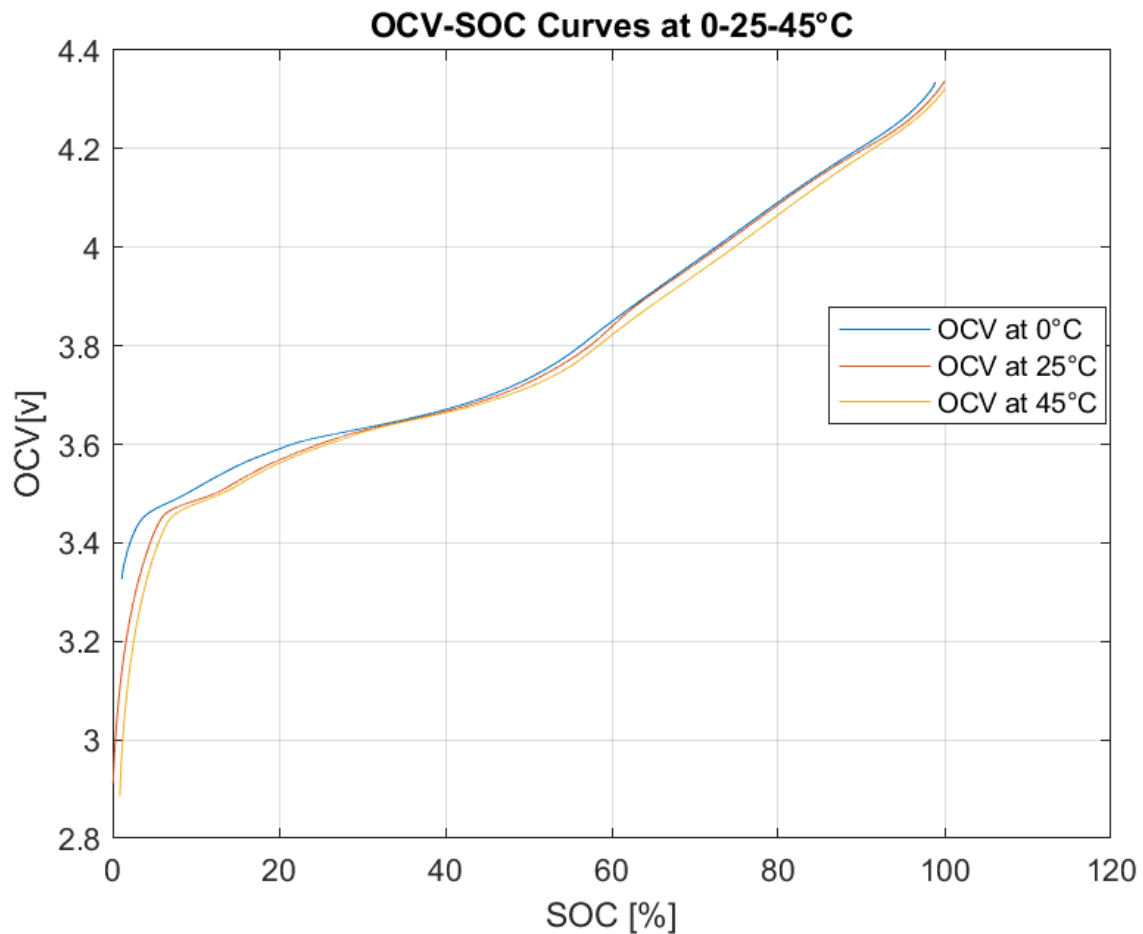


Figure 29 Mean OCV-SoC curves at 0°C, 25°C and 45°C.

3.5.3 HPPC Test Results

The HPPC test results for the CALB cell provides characterization of its internal resistance components, including ohmic resistance, polarization resistance, and total internal resistance. According to the datasheet, the internal resistance is 0.4 - 0.6 m Ω at 1 kHz and 70% SoC. This most likely refers to the ohmic resistance, which is commonly measured using electrochemical impedance spectroscopy (EIS) at high frequencies (e.g., 1 kHz).

Figure 30 presents the HPPC test voltage response at 25 °C, which is comparable across all tested temperatures. The figure captures the distinct pulses employed in the HPPC tests, as outlined

in Section 3.4.3, consisting of alternating discharge and charge steps interspersed with rest periods. The voltage response during these pulses demonstrates the immediate ohmic drop and the slower polarization recovery, both of which are influenced by SOC and temperature.

The internal resistance values derived in this section are based on the first discharge pulse in the HPPC test, calculated using the voltage drop Equation (2.2) described in Section 2.2.4. This simplified approach was chosen because off-the-shelf BMS solutions typically require only an average internal resistance value for SoC estimation and thermal management. Nevertheless, additional pulses were incorporated into the test protocol to enable future developments of better state estimation.

At 0°C, the internal resistance is highest across all SoC ranges, as shown in Figure 31 and Table 3. The total internal resistance peaks at 3.76mΩ in the 90%–100% SoC range and remains elevated at 3.14 mΩ in the 0%–10% SOC range. These high values are driven by polarization resistance, with $R_{\text{Polarization}}$ reaching 1.90mΩ in the 90%–100% SOC range and 1.47mΩ in the 0%–10% SoC range. The 50%–60% SOC range exhibits a distinct spike, where R_{Internal} reaches 3.32mΩ, primarily due to a polarization resistance of 1.89mΩ. In contrast, the SoC ranges from 30% to 50% are comparatively more stable, with R_{Internal} around 2.70 mΩ.

At 25°C, there is a significant reduction in internal resistance. The total resistance ranges from 1.68mΩ in the 90%–100% SOC range to 1.53mΩ at 0%–10% SOC, with ohmic resistance remaining consistent between 0.57mΩ and 0.62mΩ, closely matching datasheet specifications. The mid-SOC spike persists, with R_{Internal} reaching 1.71mΩ in the 50%–60% range, driven by $R_{\text{Polarization}}$ of 1.13mΩ. The 30%–50% SOC range demonstrates the lowest resistance, with R_{Internal} as low as 1.23mΩ in the 40%–30% range.

At 45°C, results highlight the lowest internal resistance values across all SOC ranges.

R_{Internal} ranges from $1.37 \text{ m}\Omega$ in the 90%–100% SoC range and $1.28 \text{ m}\Omega$ at 0%–10% SOC. The mid-SoC spike is still present but less pronounced, with R_{Internal} peaking at $1.43 \text{ m}\Omega$ in the 50%–60% SoC range, driven by $R_{\text{Polarization}}$ of $0.92 \text{ m}\Omega$. The 30%–50% SOC range continues to exhibit the lowest resistance, with R_{Internal} around $1.10 \text{ m}\Omega$.

The results demonstrate that higher temperatures significantly reduce internal resistance, due to improved ionic conductivity and reduced polarization effects improving cell performance. However, elevated temperatures accelerate degradation and increase the risk of thermal runaway, making 25°C the optimal operating temperature for balancing resistance and safety. The mid-SOC spike observed consistently across all temperatures suggests intrinsic electrochemical phenomena linked to the CALB cell's chemistry. Further studies incorporating more advanced resistance characterization methods are necessary to better understand this behavior and refine battery models.

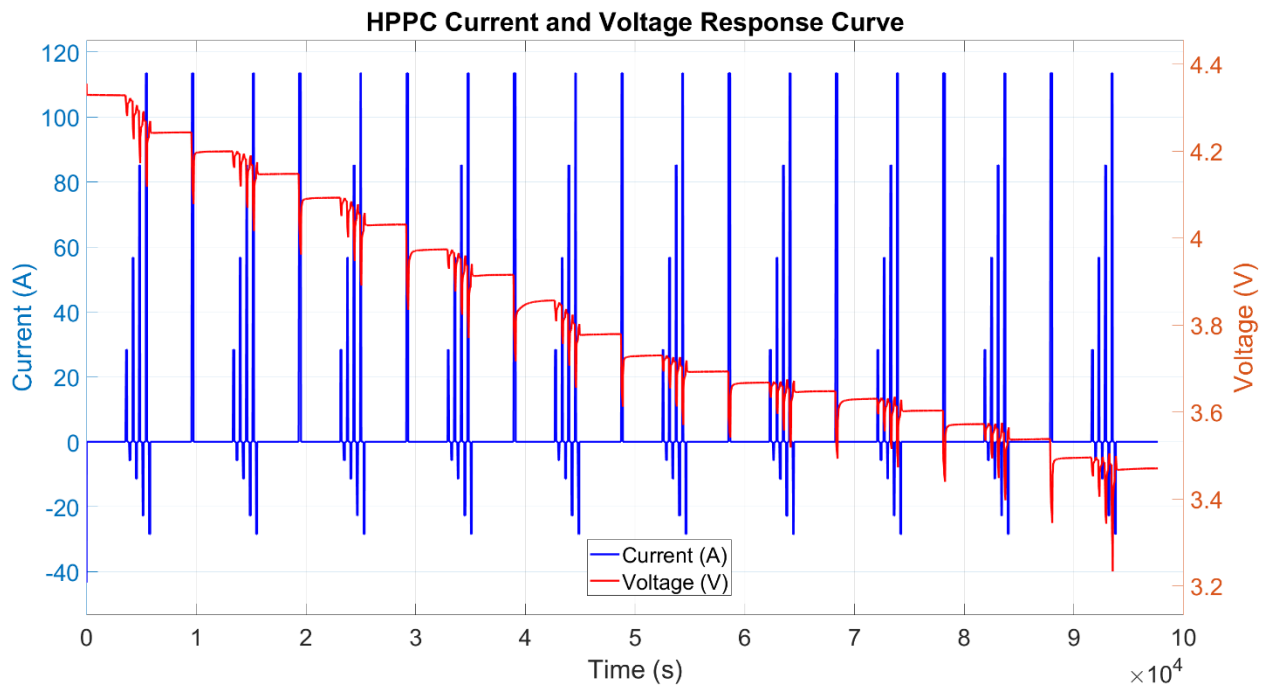


Figure 30 HPPC test Voltage Response Curve at 25°C .

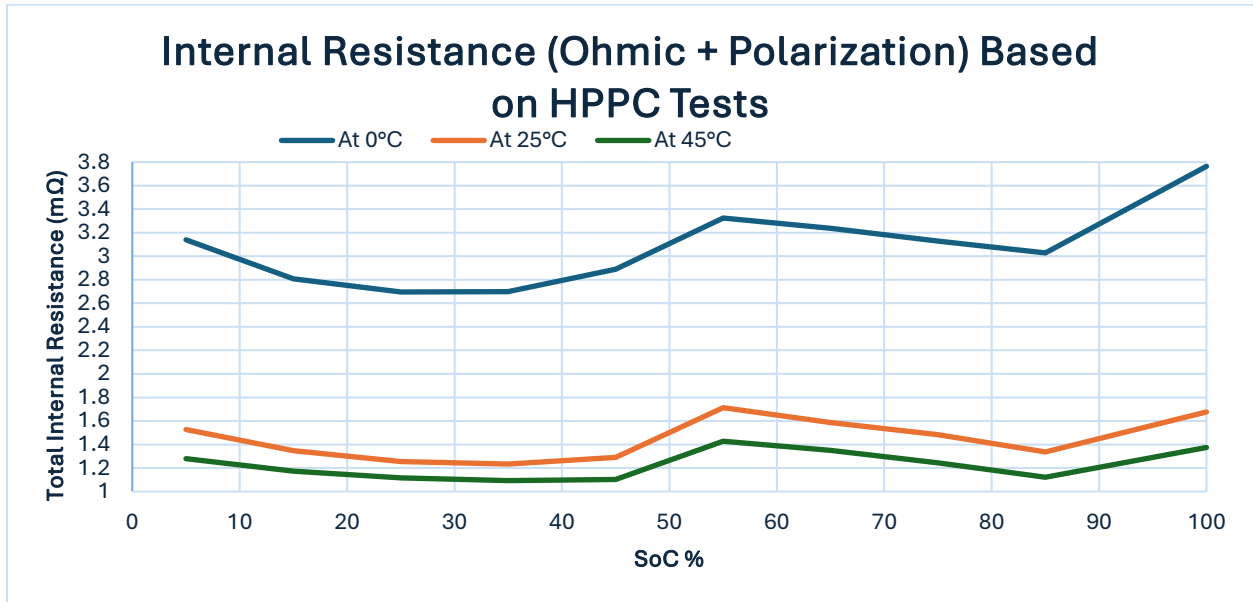


Figure 31 CALB cell internal resistance based on HPPC tests.

Table 3 Internal Resistance of the CALB cell based on the HPPC tests at 0, 25, & 45°C.

At 0°C			
SoC %	R_Ohmic (mΩ)	R_Polarization (mΩ)	R_Internal (mΩ)
100-90	1.87	1.90	3.76
90-80	1.69	1.34	3.03
80-70	1.54	1.59	3.13
70-60	1.49	1.75	3.24
60-50	1.44	1.89	3.32
50-40	1.53	1.36	2.89
40-30	1.56	1.13	2.70
30-20	1.56	1.13	2.70
20-10	1.58	1.23	2.81
10-0	1.67	1.47	3.14

At 25°C			
SoC %	R_Ohmic (mΩ)	R_Polarization (mΩ)	R_Internal (mΩ)
100-90	0.62	1.06	1.68

90-80	0.61	0.72	1.34
80-70	0.57	0.92	1.48
70-60	0.59	1.00	1.59
60-50	0.58	1.13	1.71
50-40	0.59	0.70	1.29
40-30	0.57	0.66	1.23
30-20	0.59	0.66	1.25
20-10	0.60	0.74	1.35
10-0	0.62	0.91	1.53

At 45°C

SoC %	R_Ohmic (mΩ)	R_Polarization (mΩ)	R_Internal (mΩ)
100-90	0.55	0.82	1.37
90-80	0.51	0.61	1.12
80-70	0.52	0.72	1.24
70-60	0.53	0.82	1.35
60-50	0.51	0.92	1.43
50-40	0.54	0.57	1.10
40-30	0.52	0.57	1.09
30-20	0.54	0.57	1.12
20-10	0.53	0.64	1.17
10-0	0.55	0.73	1.28

3.5.4 Fast Charging Tests Results

The Hyundai Ioniq fast charging profile charges the cell from 0% SoC to 94% SoC with a total charge capacity of 106.4 Ah. The voltage response curve, shown in Figure 32 illustrates a rapid voltage rise from 3.24V to 4.24V. At the initial stage, a sharp voltage spike occurs as the cell is excited with high C-rates, during the transition from no current to +150A. The spike diminishes in magnitude at higher current stages, such as +200A and +300A, as the cell stabilizes under load. A slight voltage drop follows the +300A phase due to a reduction in current, but the voltage continues to rise steadily as the cell approaches higher SoC. Finally, during the CV phase, the voltage increase becomes more gradual, although some minor irregularities are observed between

1500 and 2000 seconds, due to current profile fluctuations. The profile achieves an 80% SoC charge in approximately 23 minutes, with the remaining 20% SoC taking an additional 23 minutes, resulting in a total charge time of 46 minutes.

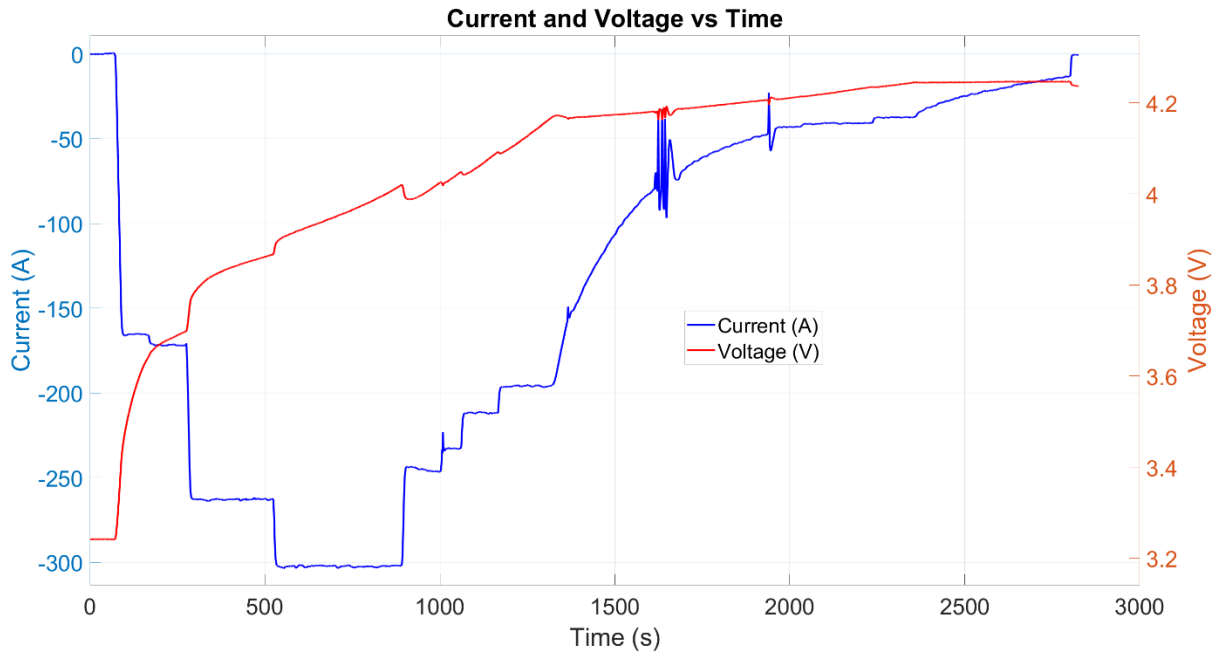


Figure 32 Hyundai fast charging test Voltage response.

Temperature data, shown in Figure 33, indicates a steep thermal rise during the fast-charging process, particularly as the current increases to +300A, with the maximum temperature reaching 47°C at the Front Center of the cell. This peak is approximately 21°C above the ambient temperature and occurs around the 1700-second mark, after which the temperature begins to gradually decrease as the current drops. Thermocouples positioned near the positive terminals (TC 2 and TC 12) consistently recorded higher temperatures than those near the negative terminals (TC 1 and TC 10). This temperature disparity is attributed to the material properties of the electrodes, as the cathode (NMC811) exhibits higher thermal resistance and lower thermal conductivity

compared to the graphite anode. The localized heating at the positive terminal is significant and primarily results from ohmic heating due to the cathode's higher resistivity, polarization losses during charging, and the inherent thermal characteristics of the NMC811 material [115]. Figure 34, which shows averaged temperatures based on cell faces, reflects similar trends, with the front, bottom, and right sides exhibiting the highest temperatures due to their positioning within the thermal chamber. The back side, which is positioned closer to the chamber fan, experiences enhanced cooling and remains significantly cooler than the front, even though they should be thermally similar under ideal conditions.

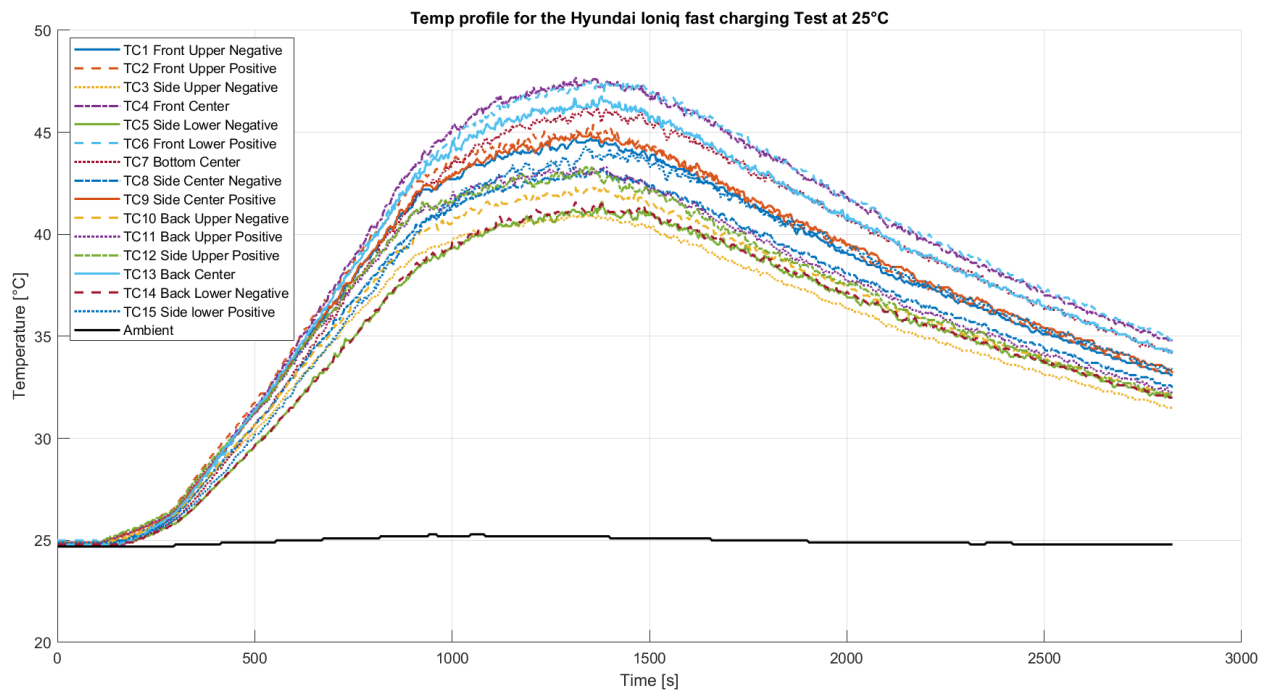


Figure 33 Hyundai fast charging test cell temperature response at 15 locations.

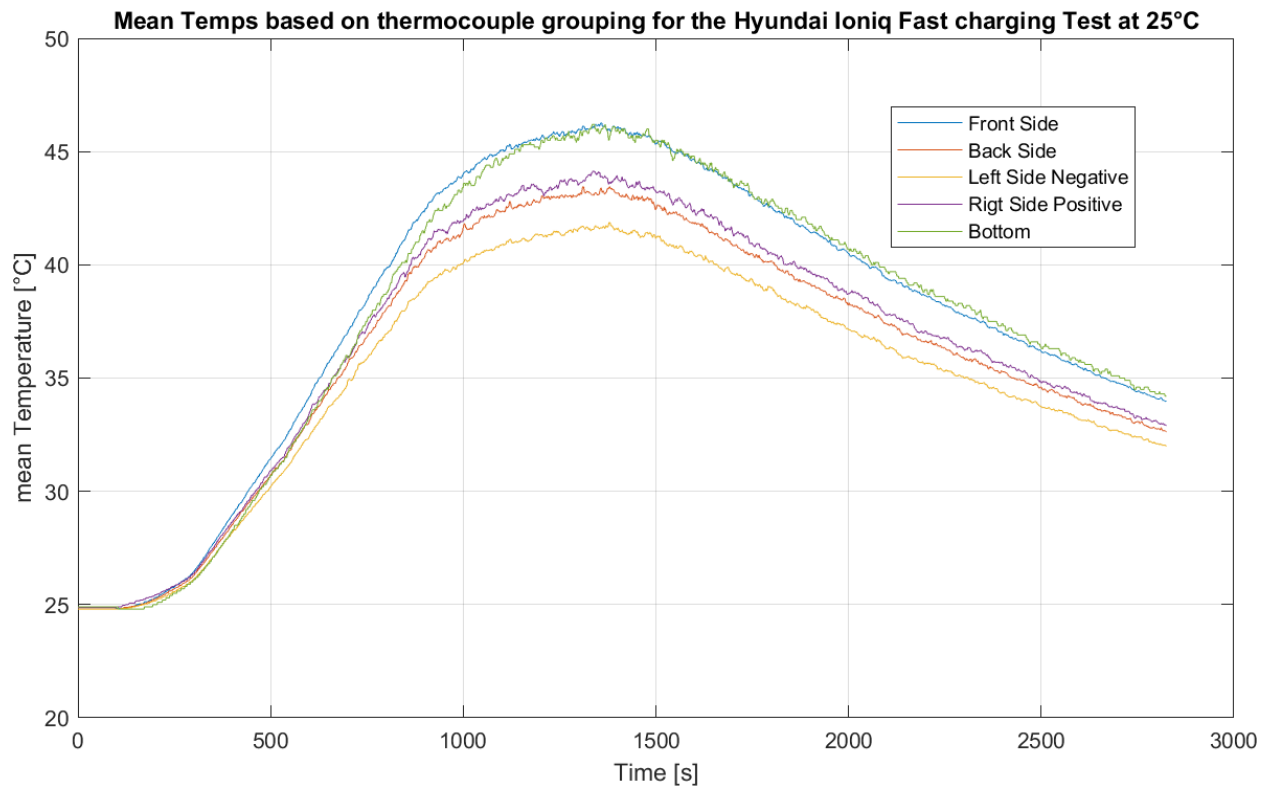


Figure 34 Hyundai fast charging test, cell temperature response grouped by cell facing.

The 400A 10-second pulse fast charging profile charges the cell from 0% SoC to 94% SoC with a total charge capacity of 106.5 Ah. The voltage response curve, illustrated in Figure 35, displays a pulsating voltage increase throughout the test. The voltage spikes during each pulse are primarily due to ohmic resistance, with a smaller contribution from polarization resistance, due to the pulse short time. The 400A pulses result in significantly higher voltage spikes compared to the 340A and 227A pulses, highlighting the amplified effects of internal resistance at higher currents. At the end of the test, beyond the 2000-second mark, the cycler begins to taper the current slightly to prevent the cell from exceeding the specified cutoff voltage. The profile achieves a 65% SoC charge within 22 minutes during the 400A phase, transitions to 80% SoC in an additional 6 minutes during the 340A phase, and completes the charge to 94% SoC in a further 9 minutes during the

227A phase, with a total charge time of 37 minutes.

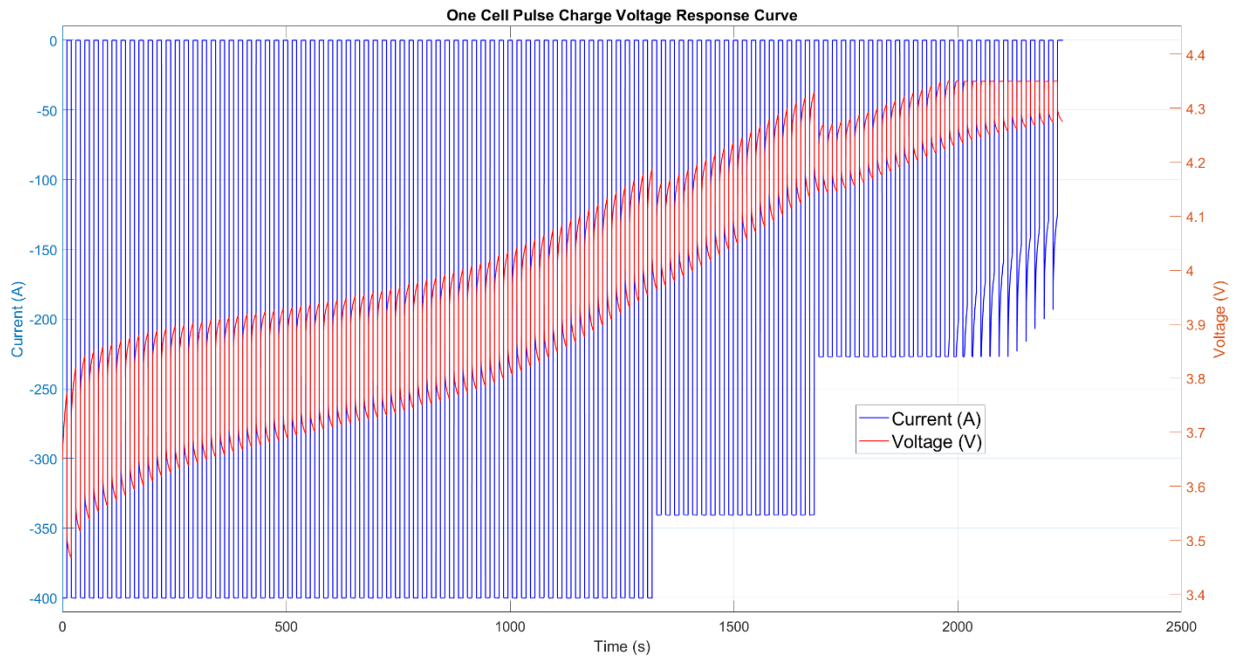


Figure 35 400A Pulse fast charging test Voltage response.

Thermal data, presented in Figure 36, shows a steady temperature increase throughout the charging process, with sharp rises during the initial 400A phase. The temperature slope becomes less steep as the current transitions to 340A pulses, eventually plateauing before reaching a peak temperature of 48°C at the Back Center of the cell. During the 227A phase, the temperature begins to decline as the current reduces. Similar to the Hyundai test, thermocouples near the positive terminals (TC 11 and TC 2) record higher temperatures than those near the negative terminals (TC 10 and TC 1). Figure 37 shows the mean temperatures grouped by cell faces. The back sides exhibit the highest average temperatures due to the repositioning of the cell within the chamber. The front and right sides, now closer to the chamber fan, experience more effective cooling.

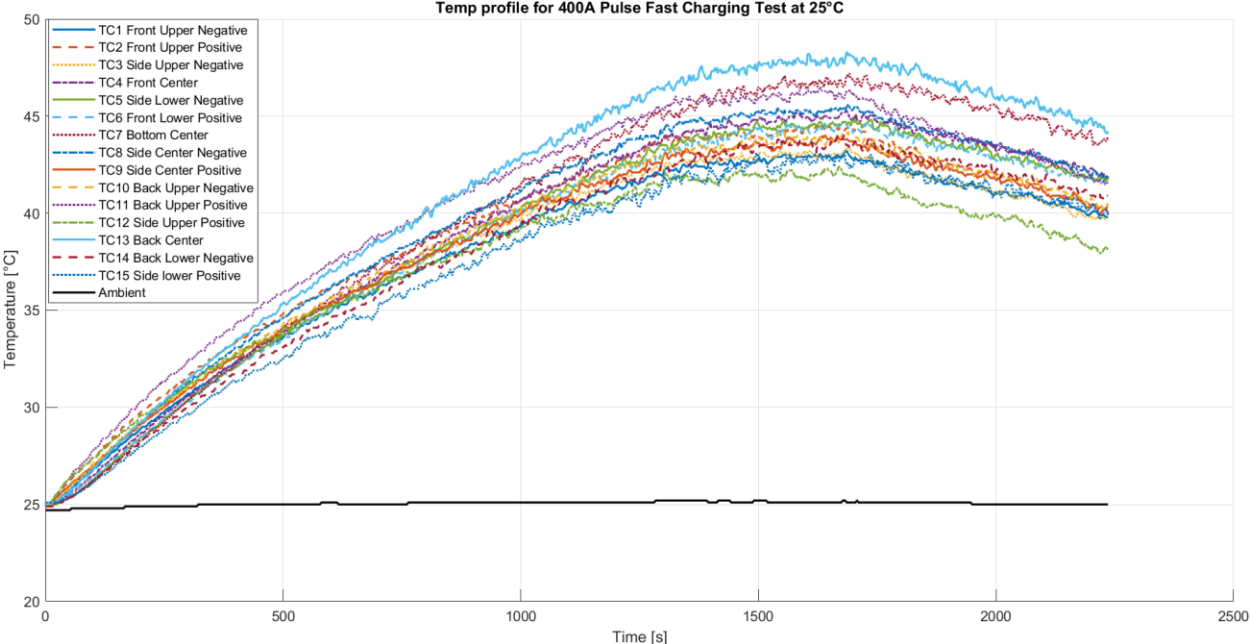


Figure 36 400A Pulse fast charging test cell temperature response at 15 locations.

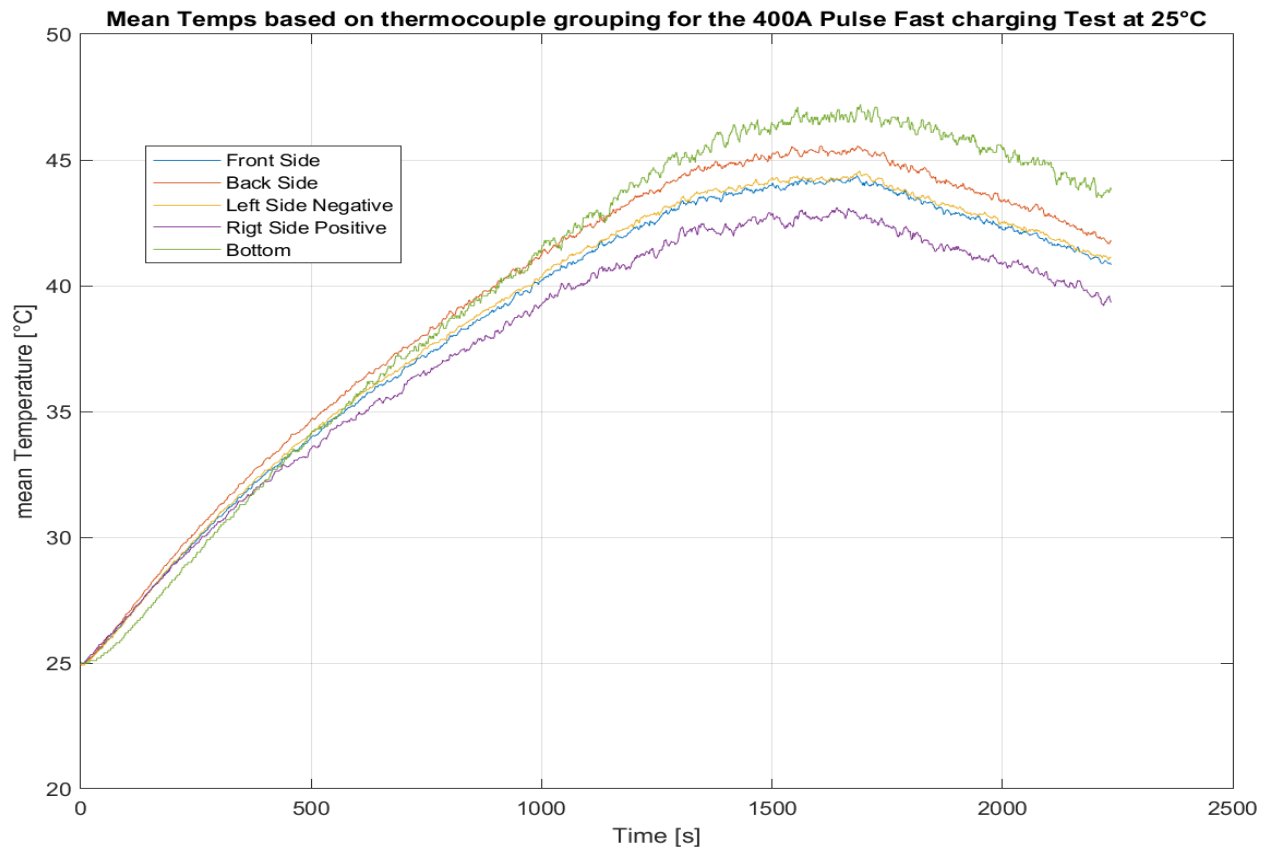


Figure 37 400A Pulse fast charging test, cell temperature response grouped by cell facing.

A comparison between the Hyundai fast charging profile and the pulse fast charging profile highlights their respective strengths. The Hyundai profile reaches 80% SoC approximately 5 minutes faster, while the pulse profile achieves 94% SoC 9 minutes earlier. While the pulse profile exhibits slightly higher maximum temperatures due to the 400A pulses, its thermal behavior shows a more controlled and gradual heat generation compared to the Hyundai profile. In both tests, thermocouples near the anode (negative terminal) consistently recorded lower temperatures than those near the cathode (positive terminal), reflecting the higher thermal resistance of NMC compared to graphite. The reorientation of the cell with respect to the fan location confirms that heat distribution is strongly influenced by chamber airflow, with minimal impact from cell design, as both tests show similar thermal patterns for the front and back sides. These results emphasize

the importance of effective thermal management. A hybrid charging strategy that combines the Hyundai profile for rapid early-stage charging with the pulse profile after 80% SoC could balance faster charging with reduced thermal stress. Such an approach, combined with robust cooling solutions, can improve charging efficiency, cell safety, and long-term performance.

Chapter 4

Battery Module Design Methodology

The goal of this project is to validate and compare the performance of Micro-Channel Heat Pipe (MCHP) cooling against conventional bottom cold plate cooling. The objective is to isolate active cooling from the module and develop a scalable reliable thermal management solution. This is achieved through the design and testing of three distinct setups:

1. No Cooling: A simple enclosure without cooling is used to establish control thermal performance, identify hotspots, and evaluate cell-to-cell heating. This configuration also informs the placement of thermocouples for subsequent setups.
2. Bottom Cooling: A cold plate is attached to the bottom of the cells, representing a conventional active cooling strategy.
3. MCHP Cooling: MCHPs are integrated into the module, with the cold plate attached to the condensing side of the MCHPs to facilitate heat dissipation.

To ensure systematic evaluation and efficient resource utilization, development begins with a 6-cell prototype module. This serves as a testing platform for optimizing thermal and electrical performance before scaling to a 44 V full module. Ultimately, the final battery pack will consist of 20 modules, each rated at 44 V, resulting in a 100kWh system. Table 4 summarizes the specifications at each stage of scaling, from individual cells to the final battery pack.

Table 4 Summary of the specifications at each stage, from individual cells to the battery pack.

Specification	Cell	Testing Module	Full Module	Battery Pack
Nominal Voltage	3.67 V	22 V	44 V	880 V
Nominal Capacity	113.5 Ah	113.5 Ah	113.5 Ah	113.5 Ah
Energy	417 Wh	2.5 kWh	5 kWh	100 kWh
Ohmic Resistance	0.4~0.6mΩ	2.4~3.6mΩ	4.8~7.2mΩ	96~144mΩ
Cells in Series	-	6	12	240
Cells in Parallel	-	1	1	1

Each prototype module is designed with consistent cell labelling and positioning, as shown in Figure 38, to allow for accurate comparisons across configurations. Specific details of the mechanical design, thermocouple placements, and other module-specific features will be addressed in the subsequent sections.

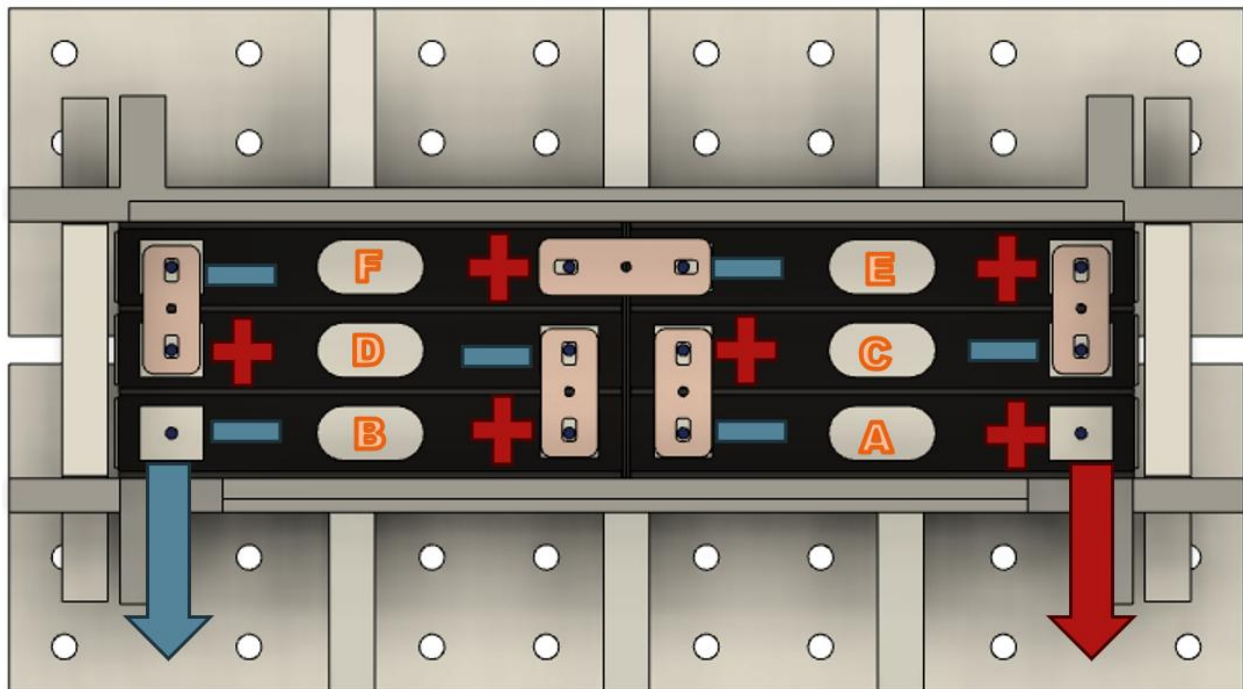


Figure 38 Layout of the 6-cell prototypes with cell labeling and positioning.

4.1 Micro Channel Heat Pipe Technology (MCHP)

Micro-Channel Heat Pipes (MCHPs) offer a passive thermal management solution specifically designed for high-energy-density systems like battery packs. These systems utilize phase change and capillary action, and gravity to transfer heat efficiently, eliminating the need for external power or mechanical components. When heat is applied to the evaporator section, the working fluid absorbs thermal energy and vaporizes. The vapor then moves through the adiabatic region, a thermally insulated section that prevents heat loss and facilitates energy-efficient transport while allowing two-phase mixing. At the condenser section, the vapor releases its heat, condenses back into liquid form, and is returned to the evaporator, enabling a continuous heat transfer cycle [102].

The Calyos MCHP, as illustrated in Figure 39, operates similarly but relies primarily on gravity-assisted flow to circulate the working fluid between the heat source and cold source. For this system to function effectively, the heat source must always be positioned below the cooling source, ensuring gravity-driven flow. Table 5 Shows the specifications of Calyos MCHPs. The system uses dielectric refrigerants as the working fluid, minimizing risks such as electrical short circuits and ensuring safe operation. With a typical thermal resistance of 0.035 K/W, the capacity to handle up to 150 W per component, and an operational range of 0°C to +120°C for heat sources, the MCHP demonstrates high thermal efficiency. Calyos reports a lifespan exceeding 200,000 hours, making the system reliable and maintenance-free for applications like electric vehicles battery pack cooling [116], [117].

Calyos innovation lies in the high customizability of their MCHP, enabling seamless integration into diverse battery pack designs as shown in Figure 40. The flexibility includes adjustable bends, where the angle and location can be tailored to fit specific battery geometries,

and the ability to modify length, width, and thickness to fit cell dimensions and spatial constraints. Calyos also offer customizable cross-sectional profiles, including unique shapes such as triangular designs, to meet specific application requirements. This level of flexibility ensures that Calyos' MCHPs address both thermal management and structural integration challenges in advanced battery systems [117].

Table 5 Calyos MCHP's specification sheet [116].

Calyos MCHP System Information	
Typical Thermal Resistance	0.035 K/W
Working Fluids	R1233zd(E)
Typical Cold Source	Air – Liquid Cold Plate – Conductive Plate
Power per Component	< 150 W
Max. Average Heat Flux	< 7.5 W/cm ²
Max. Hotspot Heat Flux	< 15 W/cm ²
Max. Temperature	< 120 °C
HP Material	Aluminum
Bonding Method	Welded or Brazed
Operating Heat Source Temperature	0 °C to +120 °C
Operating Cold Source Temperature	-40 °C to +60 °C
Storage Temperature	-60 °C to +90 °C
MTBF	> 200,000 h

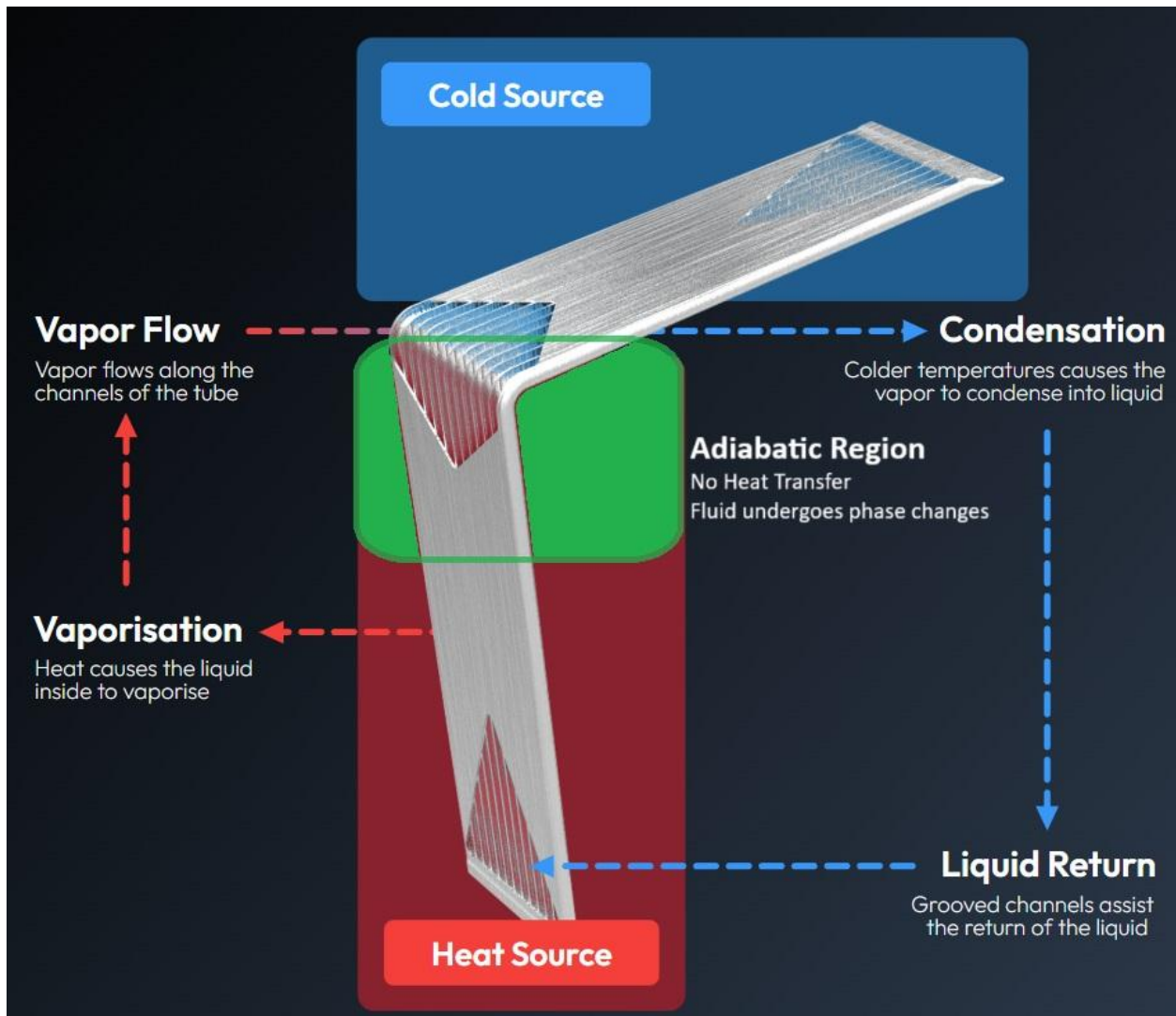


Figure 39 Calyos MCHP operation diagram [117].

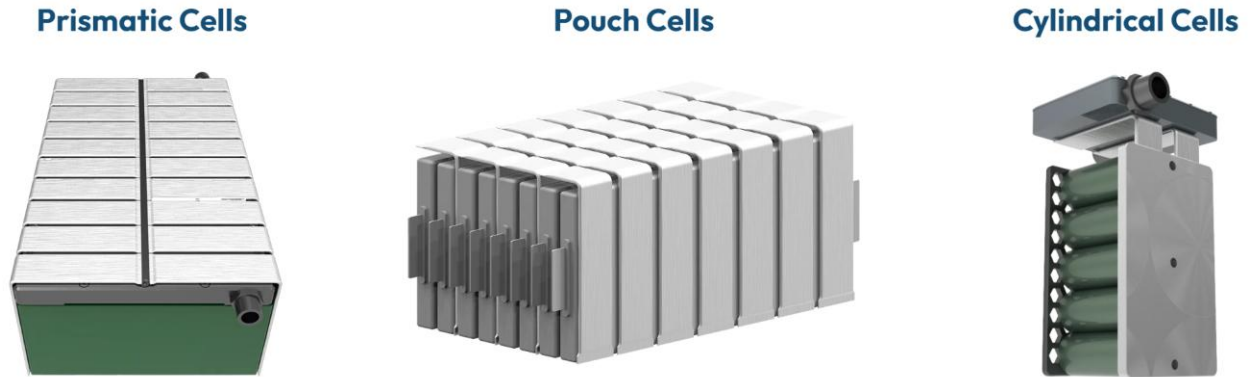


Figure 40 Calyos MCHP different cells use cases example [117].

4.2 Dana Cold Plate

The cold plate used across the designs was provided by Dana Inc. and is a production-grade unit that is implemented in EVs. This cold plate, shown in Figure 41, features a powder-coated surface and offers a thermal resistance of $0.013^{\circ}\text{C}/\text{W}$ at the beginning of life. It operates within a nominal pressure range of 180 kPa, with a maximum operating pressure of 250 kPa, and has a burst pressure of 500 kPa. The plate supports a nominal flow rate of 2.2 LPM, with a maximum flow rate of 3.33 LPM, aligning with its cooling specifications. Designed for 1000 W heat dissipation applications, it provides cooling from both sides; however, only one side is utilized in this study. The effective cooling/heating dimensions of the cold plate are 341 mm x 538 mm.



Figure 41 Dana Cold Plate, used in the bottom cooling and MCHP cooling.

4.3 Busbar Design

Busbar sizing is a critical step in module design to ensure safe and efficient operation under high-current conditions. For this study, the busbars are designed to handle the 400A pulse charging profile, which represents the maximum expected current. Copper was selected for its high conductivity and low resistivity, minimizing power loss and ensuring efficient heat dissipation.

$$I_{\text{eff}} = \sqrt{\frac{\sum I_i^2 \cdot t_i \cdot \text{Duty Cycle}}{\sum t_i}} \quad (4.1) \quad [118]$$

I_{eff} : Effective (RMS) current (A),

I_i : Current during each phase (A),

t_i : Duration of each phase (s).

Duty Cycle: The charge-to-rest ratio is 50% or 0.5.

The effective RMS current during the pulse profile is calculated using Equation (4.1), which averages the current over the three phases of the charging profile:

- Phase 1: 400 A pulses for 22 minutes.
- Phase 2: 340 A pulses for 6 minutes.
- Phase 3: 227 A pulses for 9 minutes.

This results in an RMS current (I_{eff}) of 252 A. The cross-sectional area (A) of the busbar is determined based on the current density (J) using Equation (4.2). A safe J value for copper at air cooling can be between 1.2 to 1.6 A/mm^2 [119]. A conservative current density (J) of 1.2 A/mm^2 based on air cooling is selected. Therefore, a minimum required cross-sectional area is calculated to be 210 mm^2 , sufficient to handle the current without excessive heat generation.

$$A = \frac{I}{J} \quad (4.2)$$

[120]

Figure 42 illustrates the three types of copper busbars designed for various testing setups. Busbars A and B share the same cross-sectional area of 242 mm^2 , differing only in length to suit specific configurations. Busbar C, custom-designed for the MCHP testing setup, features a larger cross-sectional area of 403 mm^2 to accommodate the MCHP placement.

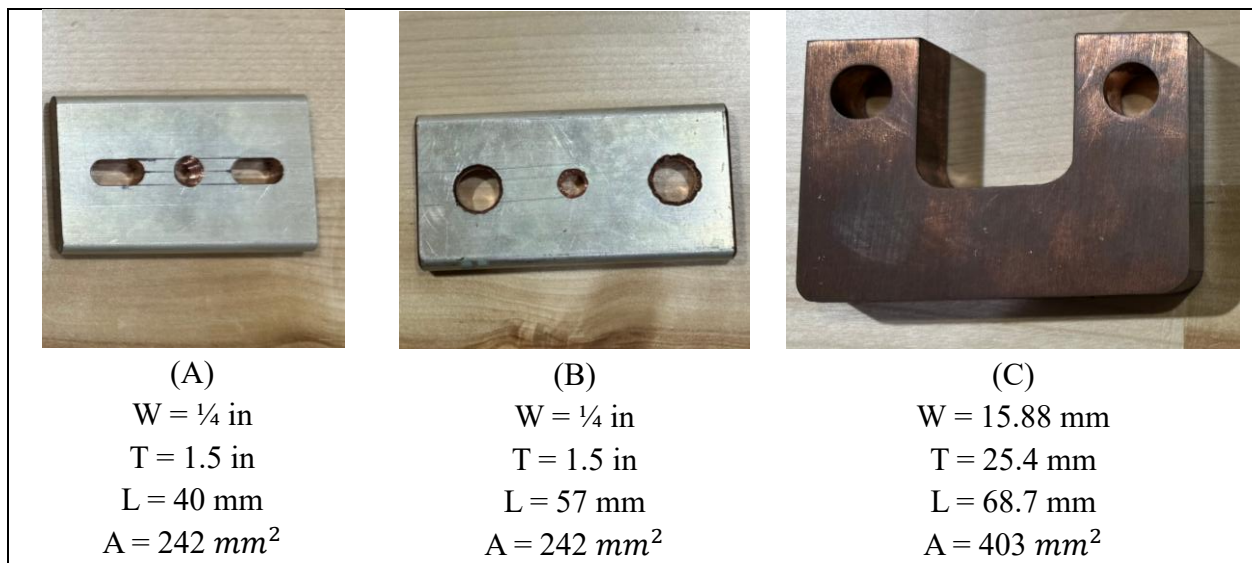


Figure 42 Three types of copper busbars are used during testing.

The busbars are integrated into the module designs as follows:

- Busbar A connects all cells within the testing modules across all configurations.
- Busbar B connects cells E and F for the No Cooling and Bottom Cooling setups.
- Busbar C, a custom design, replaces Busbar B in the MCHP Cooling setup to accommodate the MCHP geometry.

At the module terminals:

- The No Cooling and Bottom Cooling setups use busbars for terminal connections.
- The MCHP Cooling system connects directly to the terminals via cables to align with the MCHP design.

The resistance of each busbar is calculated using Equation (4.3), and the corresponding power loss (P) is determined using Equation (4.4).

$$R = \rho \cdot \frac{L}{A} \quad (4.3)$$

[120]

ρ : The resistivity of the material.

$$P = I^2 \cdot R \quad (4.4)$$

[120]

The resistivity of copper at 20°C is $1.7241 \cdot 10^{-8} \Omega\text{m}$ [120]. The resistance and the power loss over the pulse fast charging profile for each busbar are approximated as follows:

- Busbar A: $R_A = 2.85 \cdot 10^{-6} \Omega$, $P_A = 0.18 \text{ W}$.
- Busbar B: $R_B = 4.06 \cdot 10^{-6} \Omega$, $P_B = 0.26 \text{ W}$.
- Busbar C: $R_C = 2.94 \cdot 10^{-6} \Omega$, $P_C = 0.19 \text{ W}$.

Thermal behavior was assessed using Equation (4.5), which estimates the transient

temperature rise during the fast charging at 400A.

$$Q = mC_p\Delta T \quad (4.5)$$

$$m = \rho_{copper} \cdot A \cdot L$$

$$Q = P \cdot Time$$

C_p : Specific heat capacity of copper is 385 J/kg°C.

ρ_{copper} : Density of copper is 8960 kg/m³.

Based on steady-state thermal conductivity, uniform current distribution, adiabatic conditions, and transient heat accumulation, and the pulse testing lasting 2220 seconds. The estimated busbar temperature rise without any cooling during the pulse test should be around:

- Busbar A: $\Delta T_A = 12^\circ C$
- Busbar B: $\Delta T_B = 12.1^\circ C$
- Busbar C: $\Delta T_C = 4.4^\circ C$

Therefore, those busbars should be sufficient to test the 6 cells prototypes without excessive heating caused by their resistance at fast charging with extreme currents.

4.4 No Cooling Testing Module

The No Cooling system, illustrated in Figure 43, is a simple enclosure with a detachable top and openings for the positive and negative terminals, as well as sensor routing. This design serves as a benchmark to evaluate cell heating with minimal heat dissipation to the surroundings. It is used to assess the impact of cell-to-cell heating and provides a baseline for determining thermocouple placements in subsequent setups.

The enclosure is 3D-printed with PETG material. A 0.5 mm insulation fiberboard epoxy sheet is placed between each pair of cells to prevent short-circuiting in case of scratches on the cell's protective surface. Additionally, this layer acts as a buffer to accommodate cell expansion during cycling, reducing stress on adjacent cells and maintaining structural integrity.

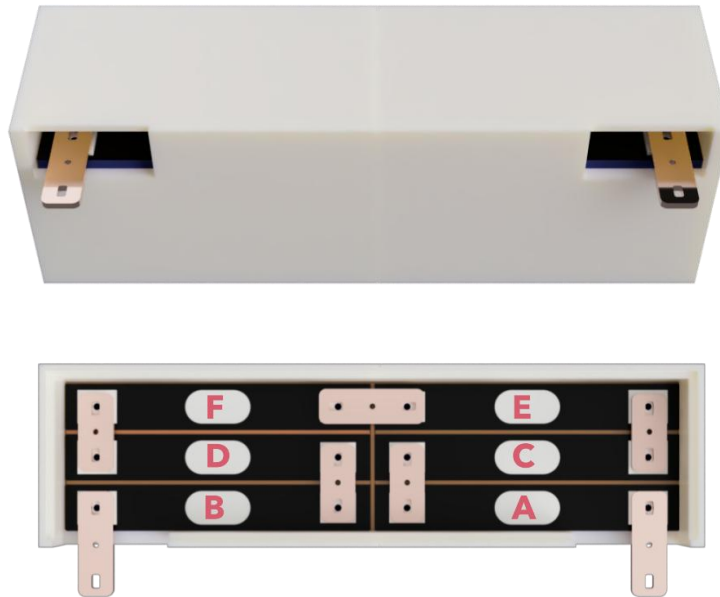


Figure 43 No Cooling Test Module CAD design, showing the cover and busbar installation.

The cells

4.4.1 No Cooling Setup Thermocouple placement

The No Cooling thermocouple placement was focused on cells C and D, Figure 43, as limited thermocouples were available. These two cells were selected because their central position, surrounded by other cells, is expected to experience the worst heating conditions. The thermocouple placement and labeling for cells C and D are illustrated in Figure 44 and Figure 45. All Type T thermocouples were secured and affixed to the cells using Kapton tape to ensure reliable thermal contact.

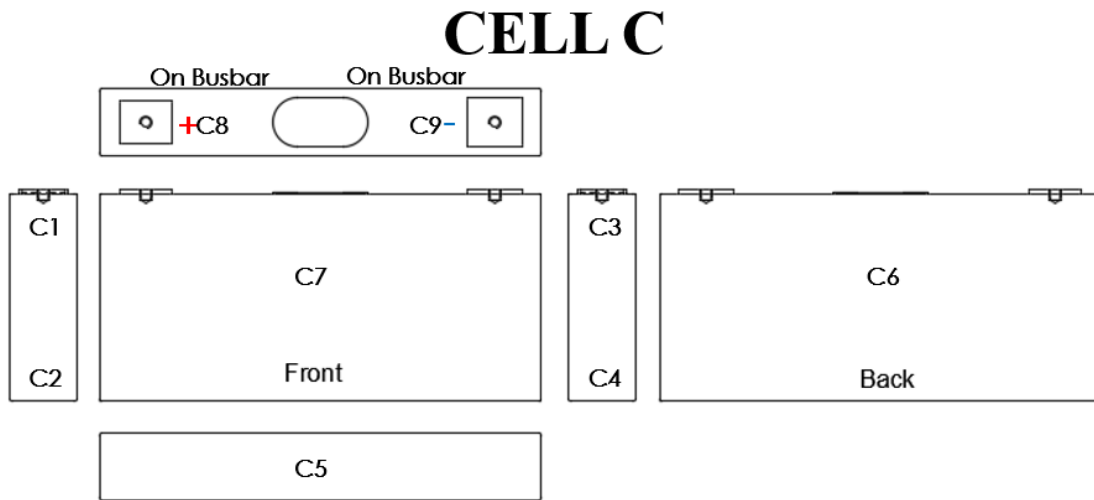


Figure 44 Cell C of the No Cooling testing module thermocouple placement and labelling.

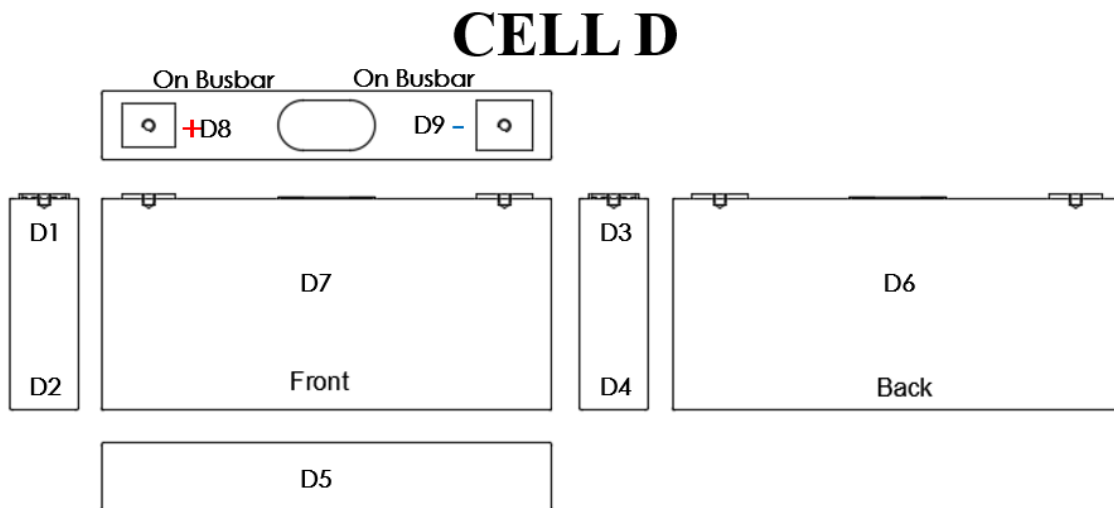


Figure 45 Cell D of the No Cooling testing module thermocouple placement and labelling.

4.5 Bottom Cold Plate Cooling Testing Module

Most EV's prismatic cell battery packs are cooled with bottom cooling via cold plates, such as the BMW ix and the Hyundai Ioniq series [121], [122]. Bottom cold plate testing was chosen to represent existing cooling technologies, using the Dana cold plate described in Section 4.2 as the

foundation. In industrial applications, thermally conductive gap fillers are commonly used to ensure full contact between cells and cold plates. These fillers are applied with robotic arms for consistent layering, and the modules are placed under pressure for curing, which typically takes more than seven days. However, once cured, the filler acts as a strong adhesive, making it nearly impossible to remove cells without damaging them. Due to the destructive nature of this process, gap fillers were deemed unsuitable for rapid lab testing requiring frequent module changes.

An alternative was considered in the form of paste-type TIMs, which would better mimic the performance of gap fillers. However, the challenge of achieving consistent layer thickness persisted. Consequently, a thermal pad with a 2 mm thickness and a thermal conductivity of 3.5 W/m·K was selected. The thermal pad offers a non-destructive, repeatable, and efficient solution, providing sufficient thermal conductivity while ensuring ease of application. The breakdown of the three TIMs considered is shown in Table 6.

Table 6 TIM material comparison for the Bottom cooling application.

	Bergquist Gap Filler TGF 2025APS	Thermal Paste S- Putty-100	Thermal Pad TG- A3500-2mm
Thermal Conductivity (W/m.K)	2.0	3.5	3.5
Operating Temperature (°C)	-40 to 80	-60 to 180	-50 to 180
Volume Resistivity (Ω.m)	10 ⁶	10 ¹³	8 x 10 ¹²
Voltage Resistance (KV/mm)	>5	>12	>13
Cure Time	7 days at 25°C	NA	NA

The final design, shown in Figure 46, consists of three 3D-printed PETG components: a top cover, a sleeve, and a hollow base. The base is adhered directly to the cold plate using an epoxy adhesive with a maximum strength of 3900 psi. The base design accounts for controlled

compression of the TIM through structural deflection, allowing for reprinting and adjustments if necessary. The sleeve incorporates rigid cross members to evenly distribute the load across the cells, ensuring uniform pressure. Six toggle latches are mounted on the sleeve and baseplate to achieve a compression ratio of 63% for the TIM material. The latches are secured using threaded inserts to maintain structural integrity during testing. On the cells side, 2 mm sheets of 3D-printed TPU were inserted between cells to provide electrical insulation in case of scratches, and mechanical isolation in case of cell expansion.

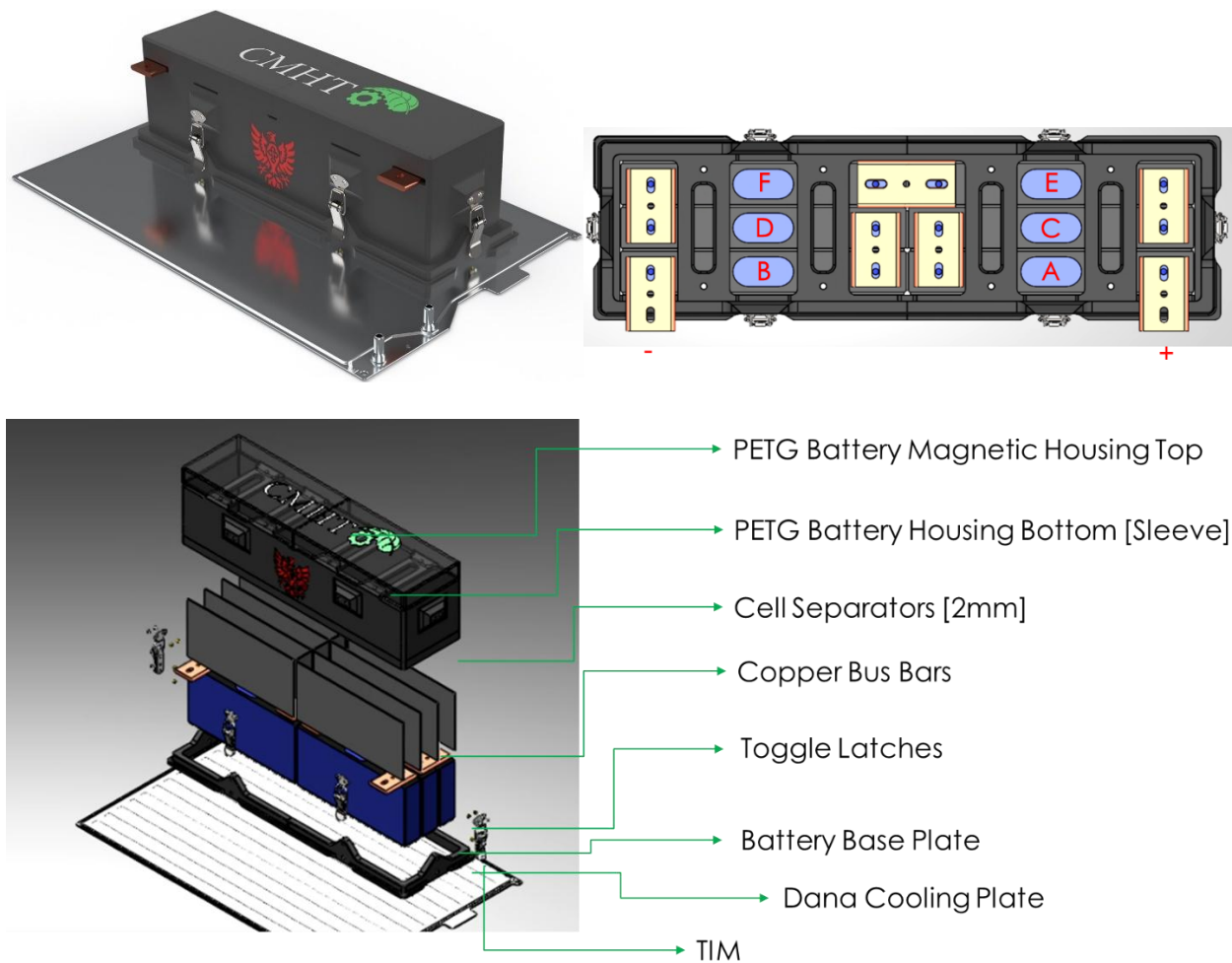


Figure 46 Bottom Cooling test setup CAD design with a breakdown of the components.

Thermal pads are adhered to the bottom of each cell and thermocouples, as shown in Figure

47. Wiring holes are integrated into the design to route thermocouples and voltage sensors, while the top cover includes cutouts for the positive and negative terminals. The top cover is magnetically attached, providing easy access to the cells and sensors while protecting the module during testing.



Figure 47 Bottom Cooling setup TIM installation.

The final assembly is shown in Figure 48 and Figure 49. Testing investigation showed that the compression achieved on the cells, Figure 50, was measured at an average of 1.67 mm of the 2 mm TIM thickness, resulting in an 83% compression ratio. This value was interpolated with the TIM material datasheet, yielding an estimated thermal impedance of approximately $1.3 \text{ K}\cdot\text{m}^2/\text{W}$.

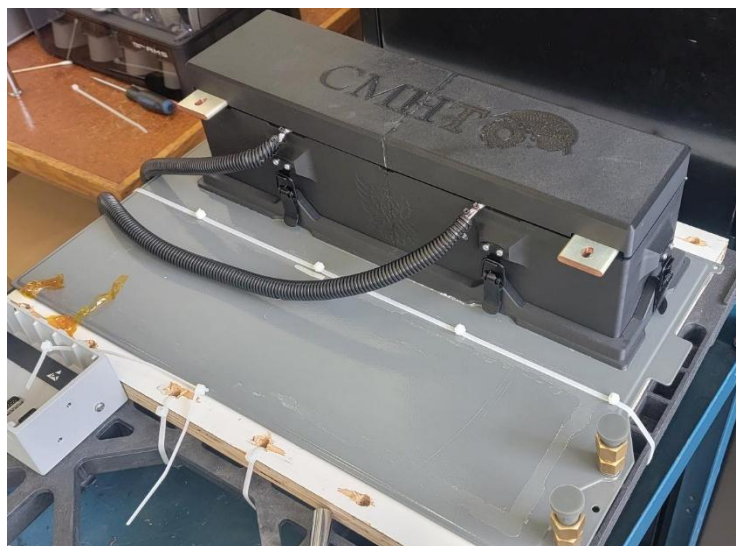


Figure 48 Bottom Cooling Setup final assembly.



Figure 49 Bottom Cooling Setup final assembly with the top removed.

Post Test TIM Measurements

1.65	1.67	1.70	1.69	1.64	1.69	1.68	1.70
F				E			
1.68	1.64	1.68	1.64	1.68	1.64	1.64	1.67
D				C			
1.68	1.67	1.68	1.68	1.67	1.68	1.67	1.66
B				A			
1.70	1.69	1.65	1.64	1.66	1.68	1.68	1.65

Notes: All measurements are in mm
Average measurement is 1.67 mm

Figure 50 Bottom Cooling setup TIM material deflection measurements after applying cell compression pressure.

4.5.1 Bottom Cold Plate Setup Thermocouple Placement

The thermocouple placement for the Bottom Cold Plate cooling module was designed to ensure repeatability with the MCHP setup, facilitated by additional data acquisition devices.

Critical measurement points for the bottom cooling configuration are at the cell bottoms, where three thermocouples are positioned, and sandwiched between the TIM and the cells. The 0.5 mm diameter of the thermocouples and the 2 mm thickness of the TIM ensure minimal contact loss while maintaining reliable thermal measurements. Each cell side is equipped with one or two thermocouples, depending on its position within the module. Thermocouples were not placed on the front or back faces of the cells due to the limited number of thermocouple channels and because these locations were deemed less critical for meeting the project objectives.

The thermocouple placement and labelling for each cell are detailed in Figure 51 to Figure 56. All thermocouples were secured with Kapton tape and attached to the cells using electrical tape.

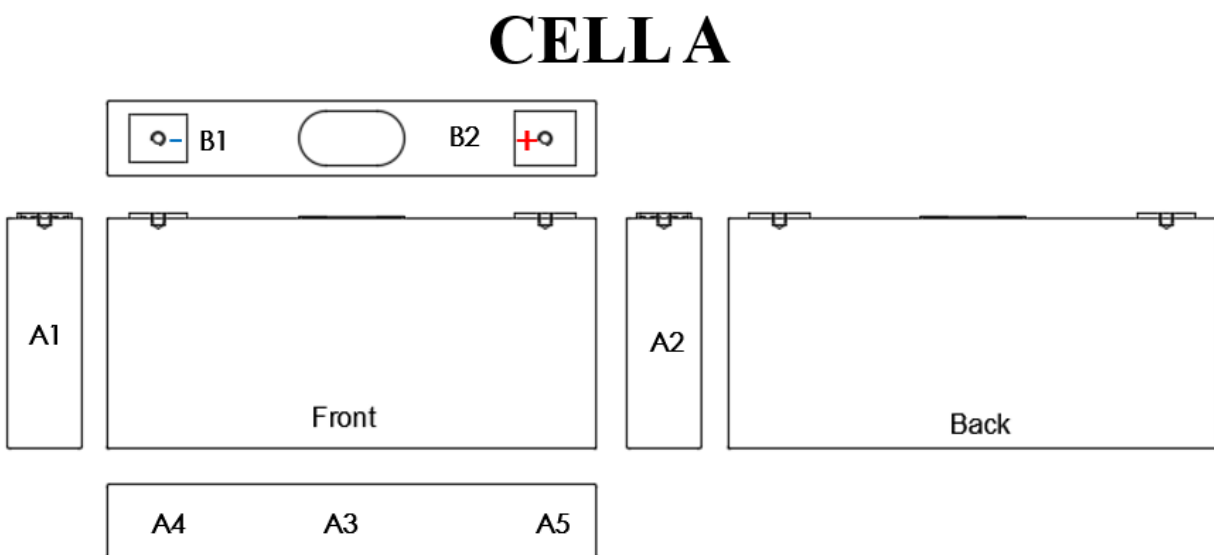


Figure 51 Cell A of the Bottom Cooling testing module thermocouple placement and labelling.

CELL B

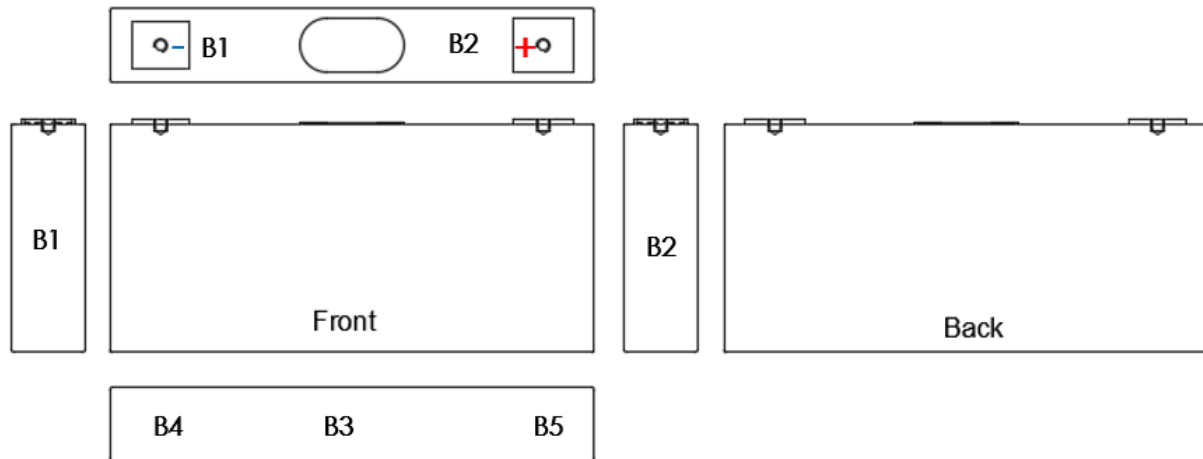


Figure 52 Cell B of the Bottom Cooling testing module thermocouple placement and labelling of the cell and each thermocouple.

CELL C

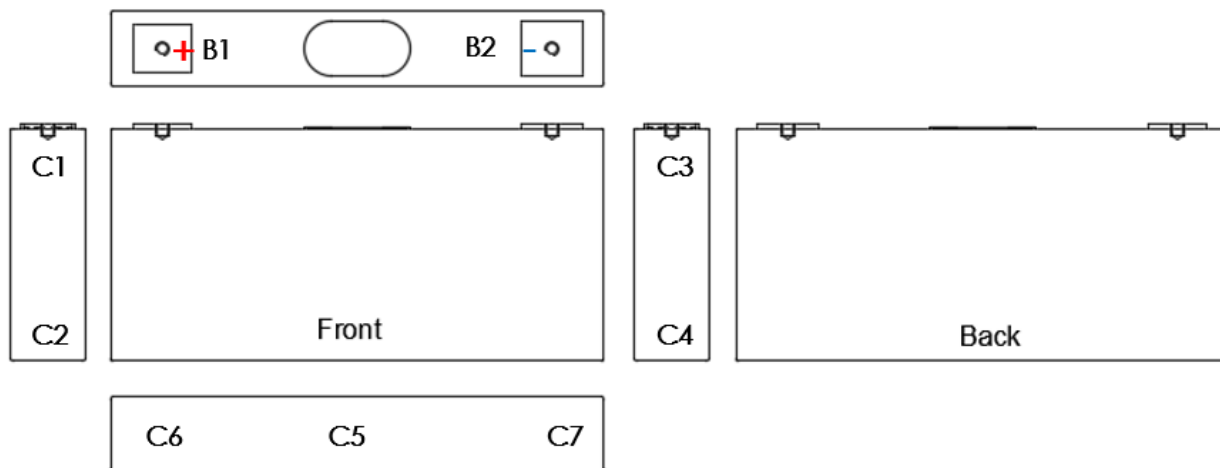


Figure 53 Cell C of the Bottom Cooling testing module thermocouple placement and labelling.

CELL D

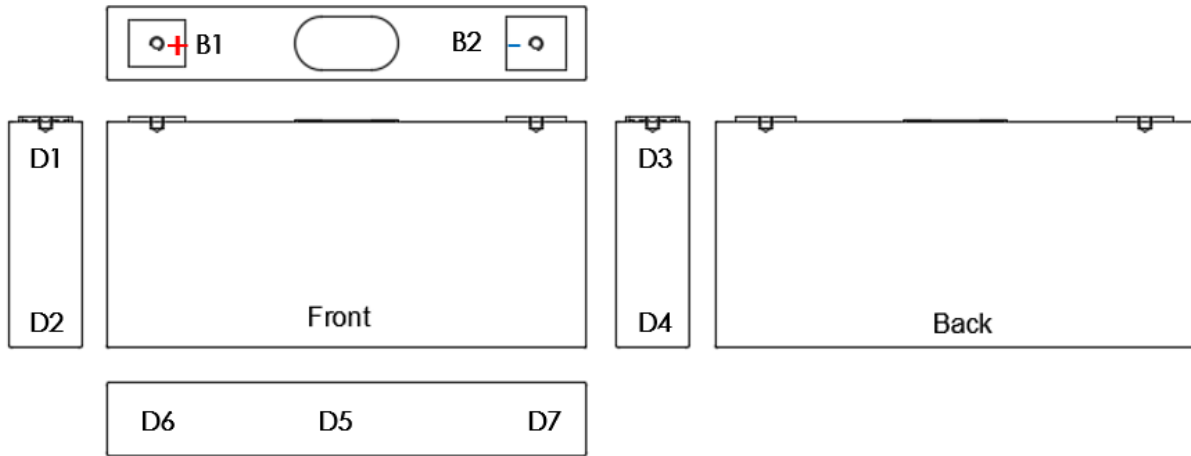


Figure 54 Cell D of the Bottom Cooling testing module thermocouple placement and labelling.

CELL E

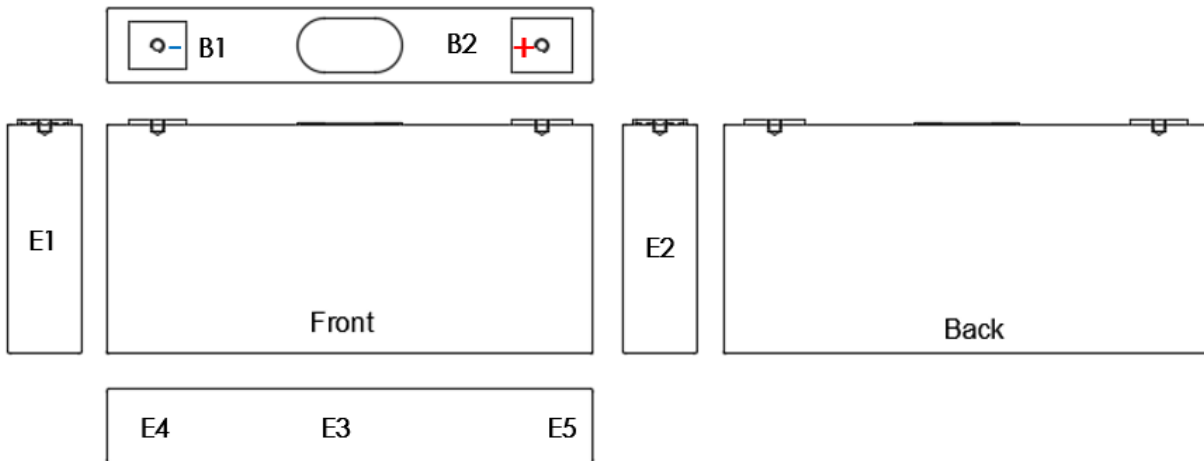


Figure 55 Cell E of the Bottom Cooling testing module thermocouple placement and labelling.

CELL F

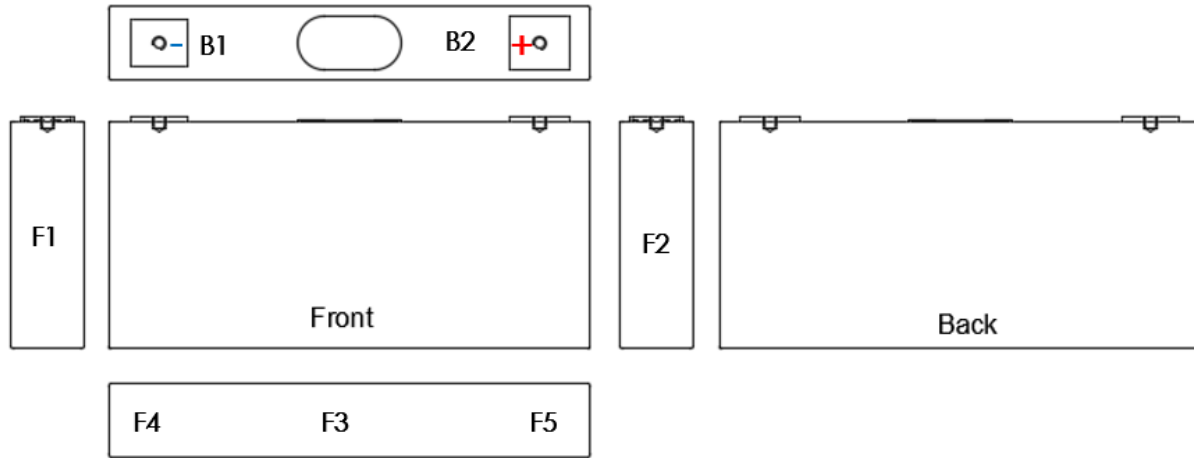


Figure 56 Cell F of the Bottom Cooling testing module thermocouple placement and labelling.

4.6 MCHP Testing Module

The MCHP test module, illustrated in Figure 57, was designed to support versatile configurations for testing MCHPs while maintaining adaptability for additional cells in future tests. The design is centered around the MCHP dimensions shown in Figure 58, ensuring compatibility and structural integrity. All custom parts in the module were 3D printed using PETG material.



Figure 57 MCHP Test Module CAD design concept.

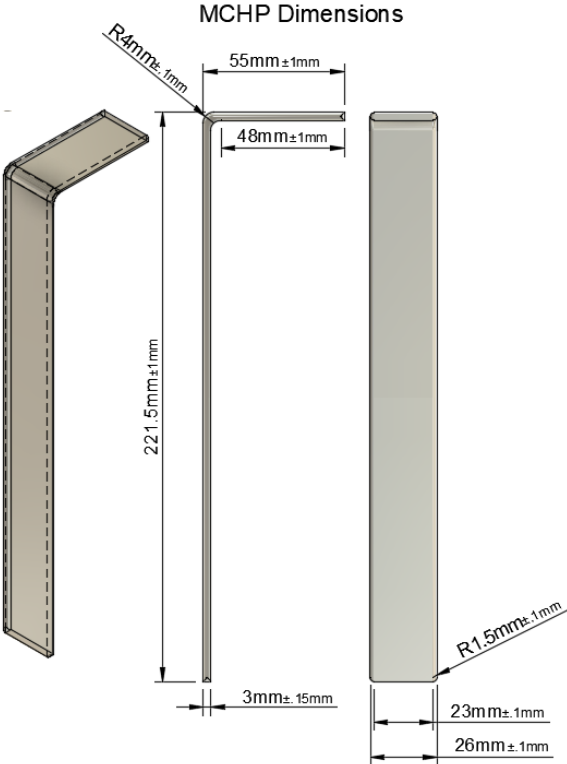


Figure 58 MCHP dimensions with tolerances.

To provide adequate compression and alignment, the module incorporates M6 threaded rods to apply X- and Y-axis pressure, ensuring proper contact between the MCHP evaporator side and the cells. The condenser section is supported by a 10 mm thick board designed to stabilize the MCHP and distribute compression forces uniformly. On top of the MCHP, a cold plate is installed and compressed using two 1-inch high-density MDF boards. These boards, torqued via the 3/8" threaded rods, provide Z-axis compression and allow for adjustable pressure between the MCHP condenser section and the cold plate.

The MCHPs are equipped with pre-installed thermal interface materials (TIM): a 0.1 mm graphite TIM (28 W/mK) on the condenser side and a 0.3 mm silicone-based thermal insulator (5 W/mK) on the evaporator side. Additionally, a 2 mm electrical and thermal insulator on the back prevents heat leakage. As in the Bottom Cold Plate setup, 2 mm sheets of 3D-printed TPU were inserted between cells to provide electrical insulation in case of scratches, and mechanical isolation in case of cell expansion.

Calyos recommended around 100 kPa and higher compression values on all of the MCHP contacts. For this test, the torque was set at 1.5 Nm because it was observed that torques above 1.7 Nm caused bending in the MDF boards and cold plate. Pressure calculations Equations (4.6 & (4.7) indicate an applied pressure of approximately 97 kPa per MCHP, factoring in an additional 17 kg weight placed on the module.

$$Force = \frac{Torque}{Nut\ Radius} \quad (4.6)$$

$$Pressure = \frac{Force}{Contact\ Surface\ Area} \quad (4.7)$$

The final assembly, shown in Figure 59, Figure 60, Figure 61, highlights the integration of the MCHP supporting board, MDF compression system, and cold plate. Due to a design modification, a rectangular cut was made in the back panel to accommodate the U-shaped Busbar C. Thermocouples are routed through the positive and negative terminal openings.

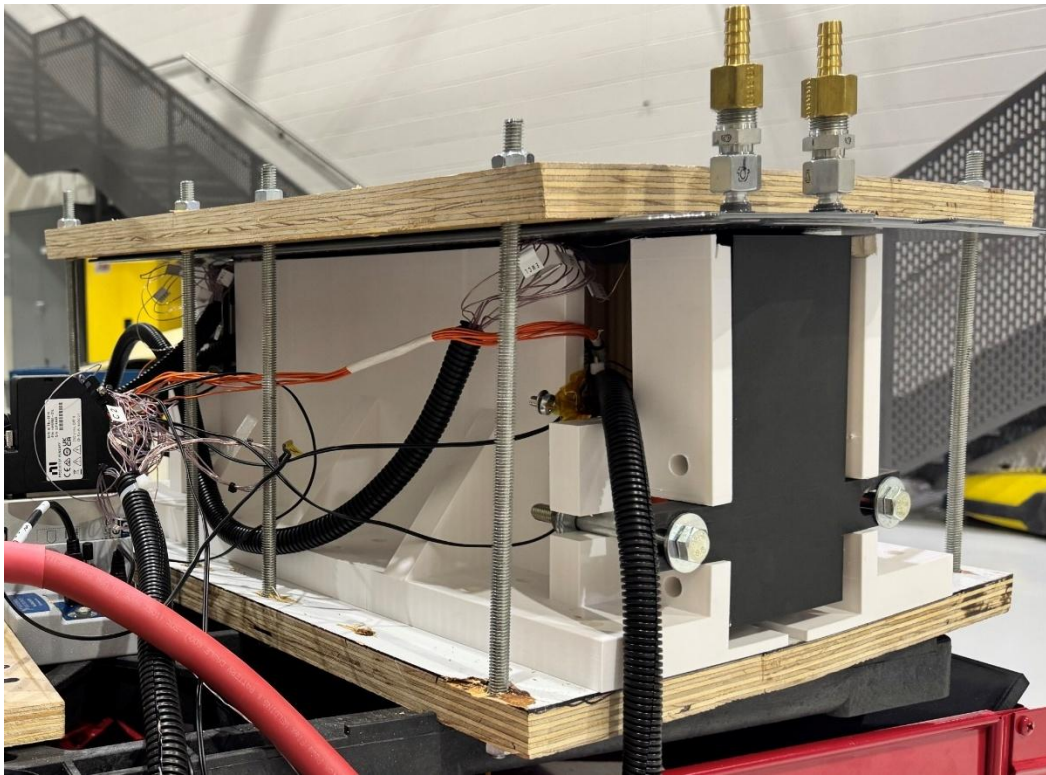


Figure 59 Corner view of the complete MCHP testing module.

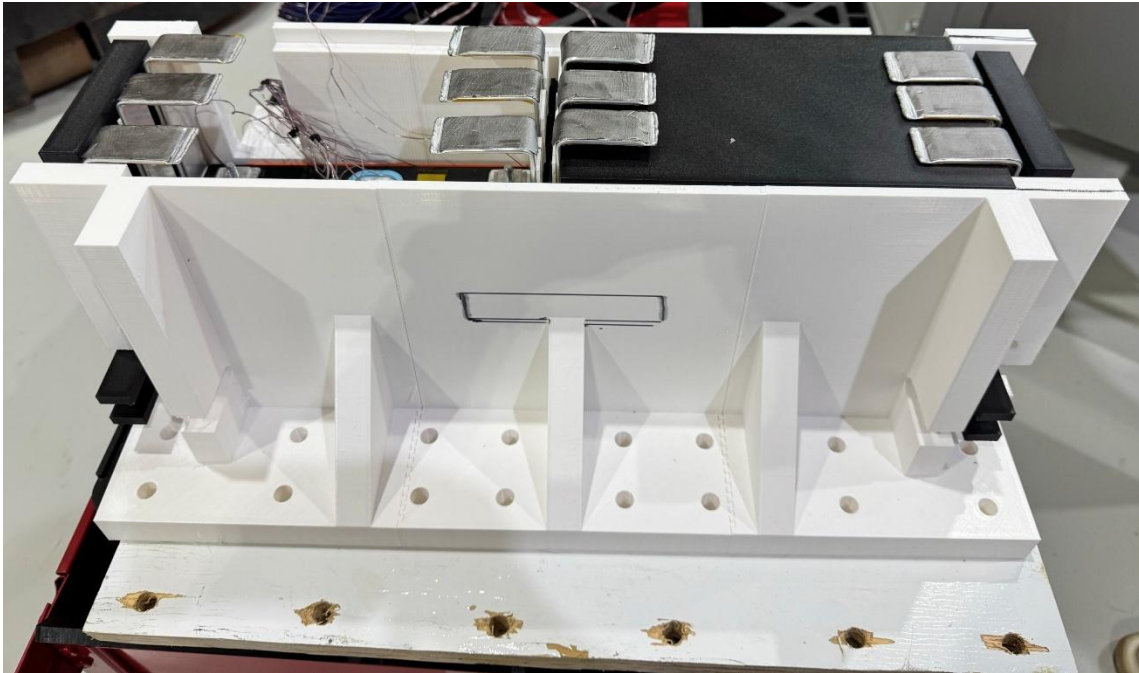


Figure 60 MCHP testing module, illustrating the condenser support plates and the thermocouple placement on the condenser.

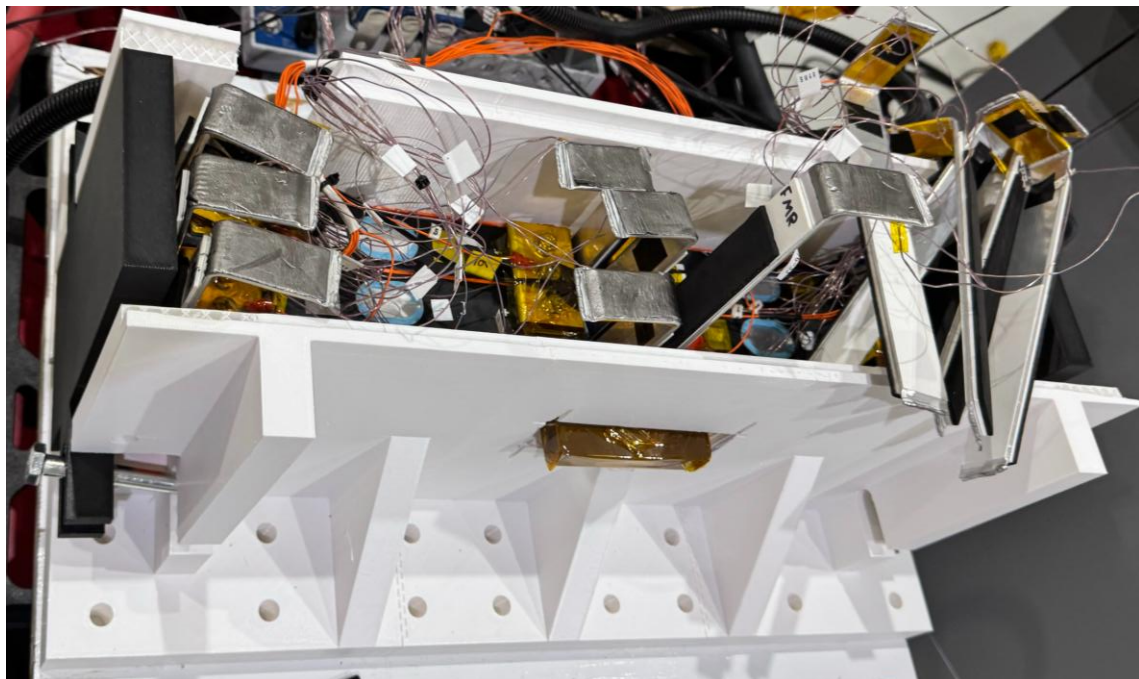


Figure 61 MCHP testing module, showing the busbar adaptation cut.

4.6.1 MCHP Setup Thermocouple Placement

The thermocouple placement for the MCHP setup followed a similar approach to the Bottom Cold plate testing module. The thermocouples used are 0.5 mm diameter Type T. The side thermocouples were repositioned from the center to the corners to allow full contact between the MCHP evaporator and the cell surface. One thermocouple was added to the adiabatic region, and another was placed below the condenser region to avoid obstructing contact between the MCHP and the cold plate.

The thermocouple placement and labelling for each cell are shown in Figure 62 to Figure 67. All thermocouples were secured with Kapton tape and affixed to the cells using electrical tape.

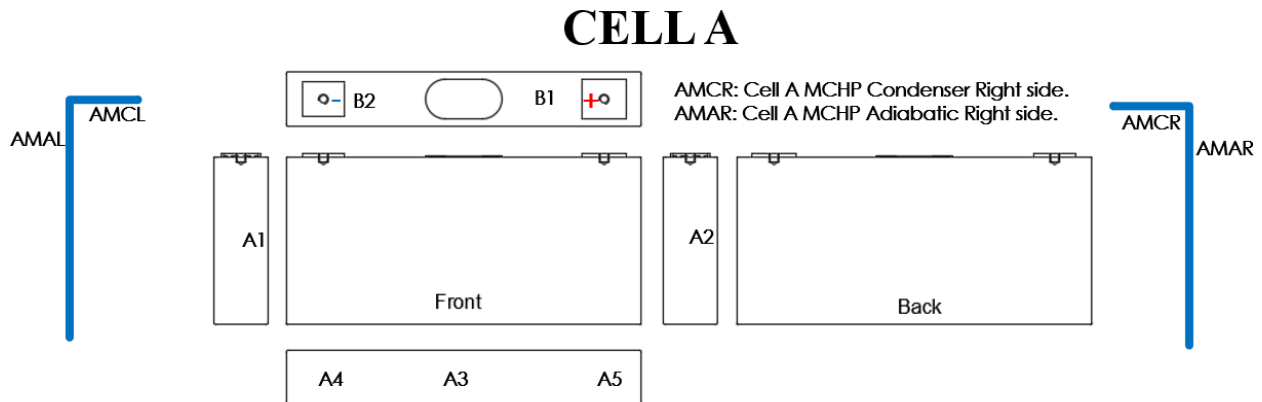


Figure 62 Cell A of the MCHP testing module thermocouple placement and labelling.

CELL B

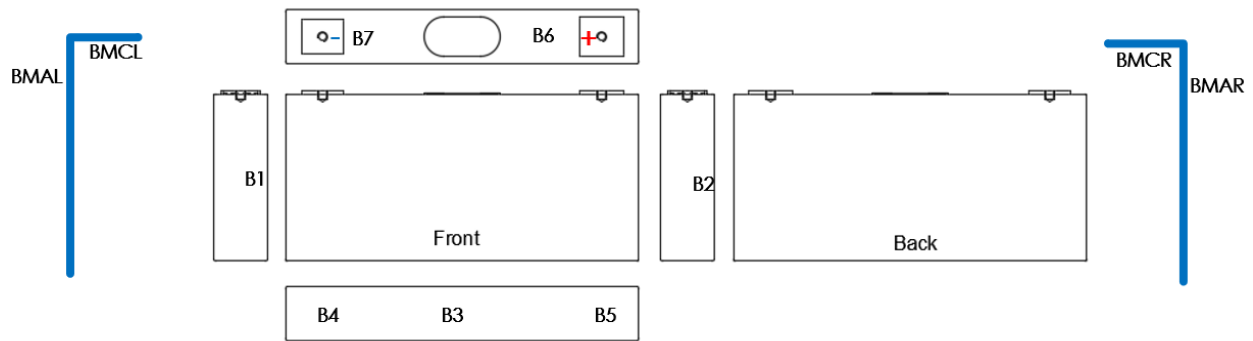


Figure 63 Cell B of the MCHP testing module thermocouple placement and labelling,

CELL C

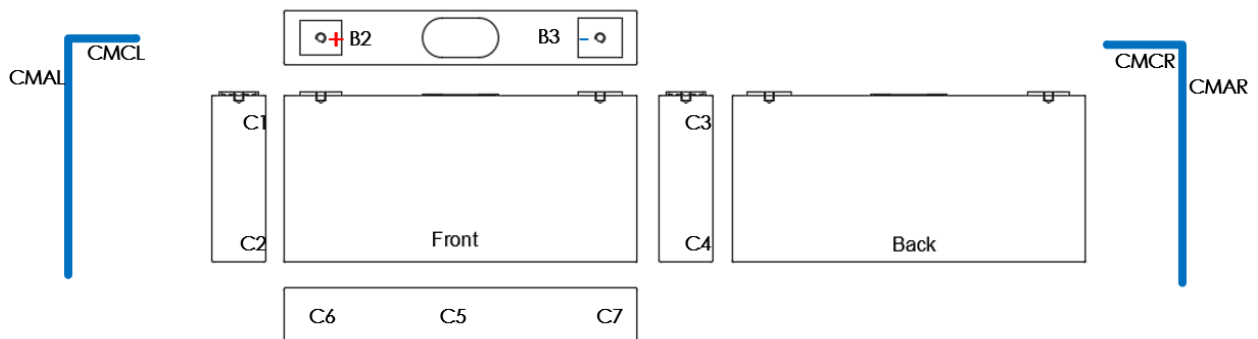


Figure 64 Cell C of the MCHP testing module thermocouple placement and labelling,

CELL D

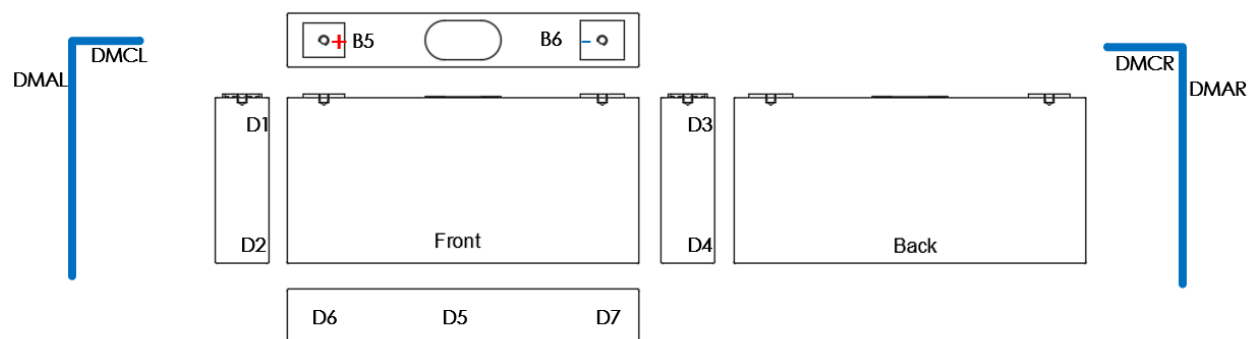


Figure 65 Cell D of the MCHP testing module thermocouple placement and labelling,

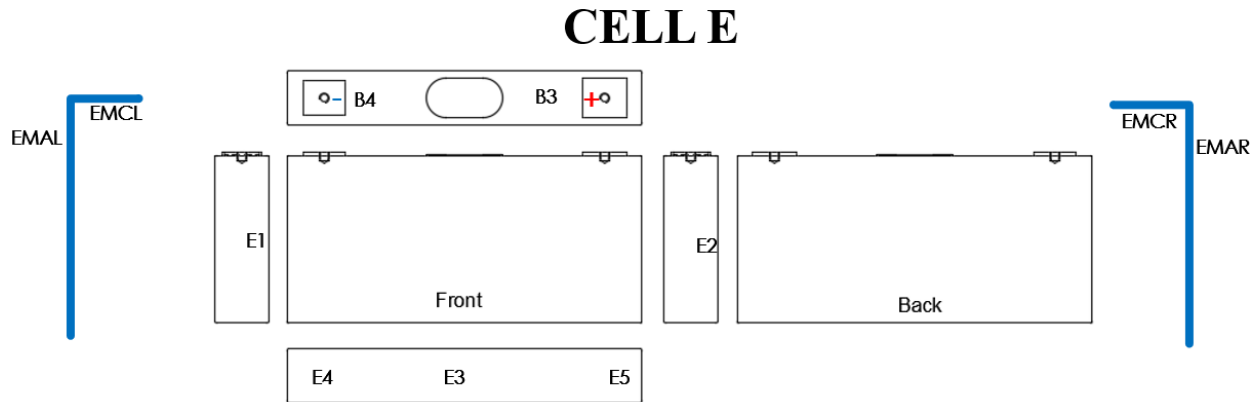


Figure 66 Cell E of the MCHP testing module thermocouple placement and labelling,

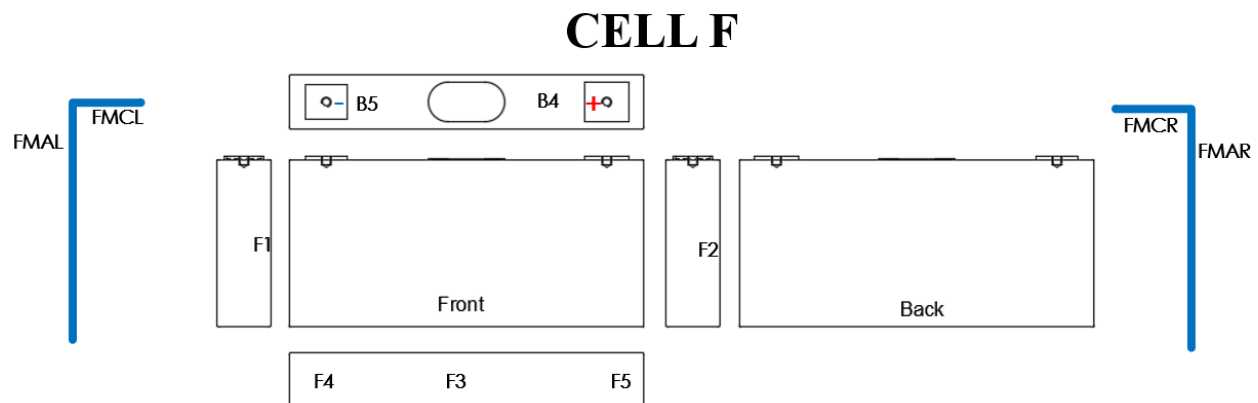


Figure 67 Cell F of the MCHP testing module thermocouple placement and labelling,

4.7 Governing Thermal Equations for Battery and Cooling Configurations

This section outlines the fundamental thermal equations relevant to the battery cells and the implemented cooling systems. The key equations governing heat generation within the cells and heat dissipation through the No Cooling, Bottom Cooling, and MCHP Cooling methods are presented. These equations provide the theoretical foundation for understanding the thermal behaviour of the battery module under various cooling configurations, highlighting the principles behind each thermal management strategy.

4.7.1 Cell based

The heat transfer rate (Q) of a cell during operation is governed by the heat generated due to internal resistance, electrochemical reactions, and how this heat is dissipated.

The Ohmic heating of a cell can be estimated using Equation (4.8), this equation calculates the heat generated due to resistive (ohmic) losses inside the cell. This method assumes that all resistive losses convert directly to heat.

$$Q_{ohmic} = I^2 \cdot R_{Internal} \quad (4.8)$$

The Entropic Heat Generation due to the electrochemical reactions in the cell can be estimated using Equation (4.9). The entropic coefficient is specific to the cell chemistry and is typically obtained experimentally.

$$Q_{Entropic} = I \cdot T \cdot \frac{dU}{dT} \quad (4.9)$$

T is the absolute temperature (K)

$\frac{dU}{dT}$ is the entropic coefficient (V/K)

The total heat generation in the cell is the sum of the Ohmic heat generation and the Entropic heat generation as shown in Equation (4.10). At high current loads, the entropic heat generation is very minimal compared to the ohmic and therefore it can be neglected.

$$Q_{cell} = Q_{ohmic} + Q_{Entropic} \quad (4.10)$$

An experimental approach is usually taken for heat generation estimation of battery cells using heat generation based on Equation (4.5). This approach utilizes the temperature data during a time period. The specific heat is found either experimentally by studying the material of the cell

or analytically by solving for it via Equation (4.11). The latter is more common for its simplicity. The specific heat (C_p) of the L221N113A cells according to the manufacturer is 1300 (J/kg.k).

$$C_p = \frac{Q_{cell}}{m \cdot \Delta T} \quad (4.11)$$

4.7.2 Testing Setups

In the No Cooling setup, the main heat dissipation method is natural convection from the top side of the cell, which is exposed to air. The convective heat transfer rate (Q) can be calculated with Equation (4.12). The heat conduction into the plastic casing can be neglected due to the insulative properties of PETG.

$$Q_{convective} = h \cdot A \cdot \Delta T \quad (4.12)$$

The main heat dissipation in the Bottom Cooling and MCHP is through the cold plate working fluid. This can be simplified by the thermal mechanisms for both cooling methodologies.

For Bottom cooling:

- 1- Heat Conduction between the Cells and the TIM.
- 2- Heat Conduction between the TIM and the Cold plate.
- 3- Heat Convection between the Cold plate and the working fluid.

For the MCHP cooling system.

- 1- Heat Conduction between the Cells and the TIM.
- 2- Heat Conduction between the Cells and the MCHP evaporation section.
- 4- Two phase mixed vapour Heat Convection between the MCHP evaporation section and the working fluid.
- 5- Two phase mixed vapour Heat Convection between the working fluid and MCHP

condensation section.

- 6- Heat Conduction between the MCHP condensation section and the TIM.
- 7- Heat Conduction between the TIM and the Cold plate.
- 8- Heat Convection between the Cold plate and the working fluid.

As observed, the MCHP cooling system involves multiple heat transfer mechanisms which introduces additional thermal resistance compared to the more direct conduction and convection mechanisms in the Bottom cooling system. This complexity results in lower overall cooling efficiency for the MCHP system. However, due to its larger contact surface area and the cell's heat dissipation rate to the sides more than the bottom, the MCHP system remains competitive with traditional cold plate cooling.

The heat conduction can be calculated using Equation (4.13). Where k is the Thermal conductivity of the material ($\text{W/m}\cdot\text{K}$), A is the contact Area (m^2), ΔT is the temperature difference across the material (K), and L is the thickness of the material (m).

$$Q_{\text{conduction}} = \frac{k \cdot A \cdot \Delta T}{L} \quad (4.13)$$

The most straightforward method to compare the heat dissipation performance between the MCHP cooling and the Bottom Cooling system is by calculating the heat removed by the working fluid in the cold plate. This can be achieved by measuring the temperature difference between the inlet and outlet of the cold plate, using a known working fluid with an established specific heat capacity and a precisely measured flow rate. By assuming that all the heat absorbed by the fluid originates solely from the battery cells without any heat losses and steady-state conditions existing, the heat dissipation can be determined using the energy balance in Equation (4.5).

4.8 Battery Management System Setup

Battery Management Systems (BMS) are essential for ensuring the safe, efficient, and reliable operation of lithium-ion battery packs. They monitor critical parameters such as cell voltage, State of Charge (SoC), State of Health (SoH), and temperature, while also regulating charge and discharge currents to prevent conditions like overcharging or overheating. A key function of the BMS is cell balancing, which equalizes voltages across all cells to maximize usable capacity and maintain long-term performance [123].

4.8.1 Orion BMS: Features and Configuration

The Orion 2 BMS is a versatile and advanced system designed for lithium-ion battery applications. It provides real-time monitoring of individual cell voltages, pack voltage, current, and temperature points. This project uses the Orion 2 BMS primarily for cell balancing and safety management. The system integrates OCV-SoC curves and resistance values derived in Sections 3.5.1 and 3.5.2 for SoC estimation and current limitations.

The BMS employs passive cell balancing, which dissipates excess energy from higher-voltage cells as heat through resistors. This method maintains voltage imbalances within 5 mV, ensuring consistent performance across all cells. For safety, the Orion 2 BMS dynamically controls relays to activate or deactivate contactors, disconnecting the battery pack in case of overvoltage, undervoltage, overcurrent, or high-temperature conditions [124]. These safety thresholds are configured based on the cell specifications provided in the datasheet.

4.8.2 System Integration

The Orion 2 BMS is integrated with key safety and monitoring components to ensure robust performance. Additionally, the system is set on an external board for easy testing module replacement. An Anderson connection is used to connect the system to the battery cyclers. The system configuration, as illustrated in Figure 68 includes:

- 2 x 500 A Fuses: These fuses protect the pack from overcurrent conditions, breaking the circuit to prevent damage.
- 2 x 500 A, 800V Contactors: Controlled by relays, these contactors manage the connection and disconnection of the pack from external systems.
- 2 x Relays: The relays act as switches controlled by the BMS to activate or deactivate the contactors based on real-time voltage, current, and temperature fault conditions.
- 7 x Voltage Sensors: Positioned between each pair of cells, these sensors provide measurement up to 1mV for each cell in which the BMS uses for pack voltage measurement.
- Current Sensor: Located at the negative terminal of the pack, the sensor monitors the flow of current during charging and discharging cycles.
- Thermistors: Eight thermistors that comes with the Orion are used to measure the temperature of the busbars and ambient environment.

This configuration ensures precise monitoring and control of voltage, current, and temperature parameters, enabling safe operation and optimal performance of the battery pack during fast-charging tests.

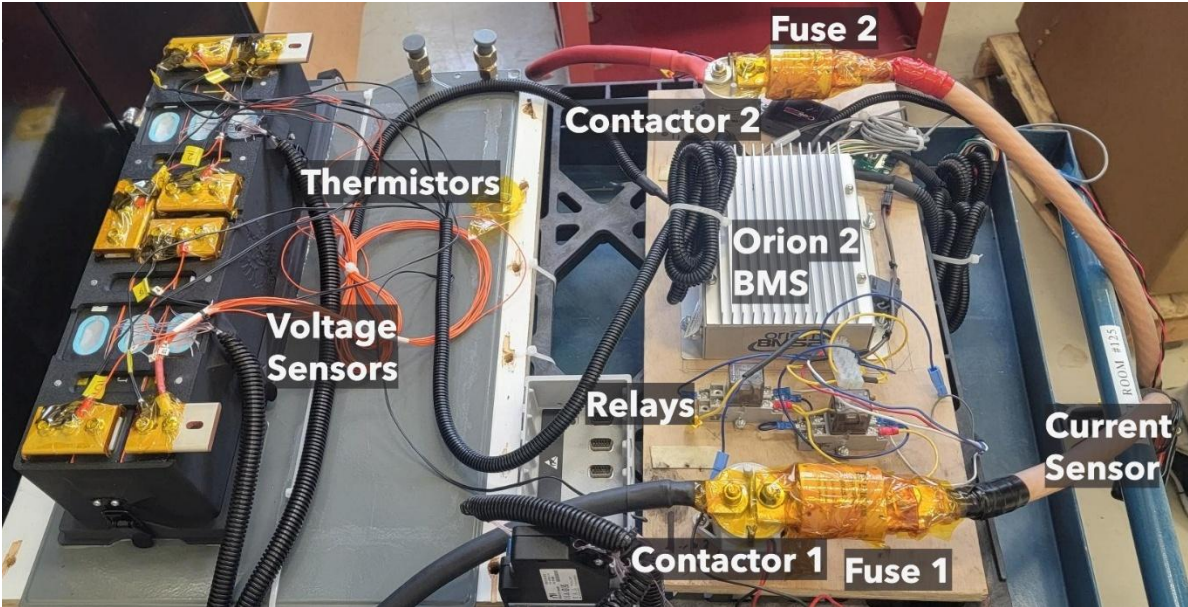


Figure 68 Orion 2 BMS system integration with the testing module.

Chapter 5

Testing Procedure

This chapter outlines the equipment, methodologies, and parameters used to conduct fast charging tests on battery modules presented in Chapter 4. The goal is to achieve comparable results across the three testing modules which allows for validating the different cooling methods.

5.1 Testing equipment

A controlled testing environment utilizing high-precision equipment is critical for accurate cell performance assessment and thermal analysis. The following devices were employed in this study:

1. **AVL E-Storage BTE 160 Battery Cyclers:** This unit, shown in Figure 69, operates as a battery cycler, emulator, and fast charger. It supports a voltage range of 8–800 V, a current limit of 600 A, and a power capacity of 160 kW, with an operational accuracy of $\pm 0.1\%$. The cycler is equipped with 22 thermocouple inputs, offering a measurement accuracy of $\pm 2^\circ\text{C}$, enabling detailed thermal monitoring alongside electrical performance evaluation [125].



Figure 69 AVL E-Storage BTE 160 Battery tester and emulator.

2. **Tenney TC20 Thermal Chamber:** Shown in Figure 70, this environmental chamber provides a capacity of 20 cubic feet and supports a temperature range of -68°C to 180°C . It ensures a temperature accuracy of $\pm 1^{\circ}\text{C}$, delivering stable and repeatable environmental conditions for testing [126].



Figure 70 Tenny Environmental TC20 thermal chamber.

3. **VWR 1171PD chiller:** This chiller features a 1/4 HP positive displacement pump with a cooling capacity of 800 W at 20°C. It operates within a temperature range of -10°C to 40°C, with a stability of $\pm 0.1^\circ\text{C}$. The chiller includes a 4.2-liter reservoir, a flow rate of 1 GPM (3.75 LPM), and pressure ranges between 20–100 PSI. A return valve and an analog flow meter were installed to control the flow rate [127].
4. **NI 9213 and NI 9214:** 16-channel thermocouple input modules designed for reliable thermal measurement. Both modules support Type T thermocouples over a wide range of -

270°C to +1372°C with 24-bit resolution, ensuring accurate and consistent data acquisition. The NI 9213 offers an accuracy of $\pm 0.36^\circ\text{C}$ at 70°C and a sampling rate of up to 75 Hz, while the NI 9214 provides enhanced accuracy of $\pm 0.24^\circ\text{C}$ at 70°C in high-resolution mode, with a maximum sampling rate of 100 Hz. Both modules include built-in cold-junction compensation (CJC) sensors for stable measurements under varying ambient conditions, along with features like open thermocouple detection and noise immunity, making them well-suited for dynamic and high-precision applications [128], [129].

5. **NI 9205:** 32-channel analog input module designed for high-channel-density applications, with a ± 10 V measurement range, 16-bit resolution, and a maximum sampling rate of 250 kHz. It supports both differential and single-ended measurements, with overvoltage protection up to ± 30 V for reliability [130]. In this project, the NI 9205 was used as a thermocouple input module without cold-junction compensation, which resulted in noisy data and a typical accuracy range of $\pm 3^\circ\text{C}$. While not suitable for precise temperature measurements, the module provided sufficient temperature monitoring capabilities to observe general thermal trends across the test setup.
6. **Type T thermocouples:** Composed of a copper-positive leg and a constantan-negative leg, operate from -270°C to 370°C with an accuracy of $\pm 1.0^\circ\text{C}$ [131]. In this study, the junctions were spot welded in-house and tested for accuracy before use, ensuring reliable thermal contact and precise measurements.

This combination of high-precision equipment ensured reliable and accurate data acquisition for both thermal and electrical performance assessments. The integration of these tools provided a controlled and repeatable testing environment, enabling a comprehensive evaluation of

the battery modules under various cooling strategies and fast-charging conditions.

5.2 Testing Global Parameters

The tests were conducted inside the Tenney TC 20 thermal chamber at a controlled ambient temperature of 25°C. The cold plate temperature was regulated by the VWR chiller, set to 25°C. Water was selected as the cooling fluid as no extreme temperatures were anticipated during testing. The flow rate, controlled via a flow meter and return valve attached to the chiller, was set between 2.2–2.4 LPM to align with the cold plate's nominal specifications, ensuring consistent and efficient thermal performance. A type K thermocouple was added at the inlet and outlet of the cold plate to measure the fluid temperature rise. The chiller was run for at least an hour before testing to ensure thermal equilibrium and to eliminate air bubbles from the liquid cooling loop, including the cold plate and hoses. Figure 71 highlights the testing setup configuration inside the thermal chamber with all the connections surrounding it.

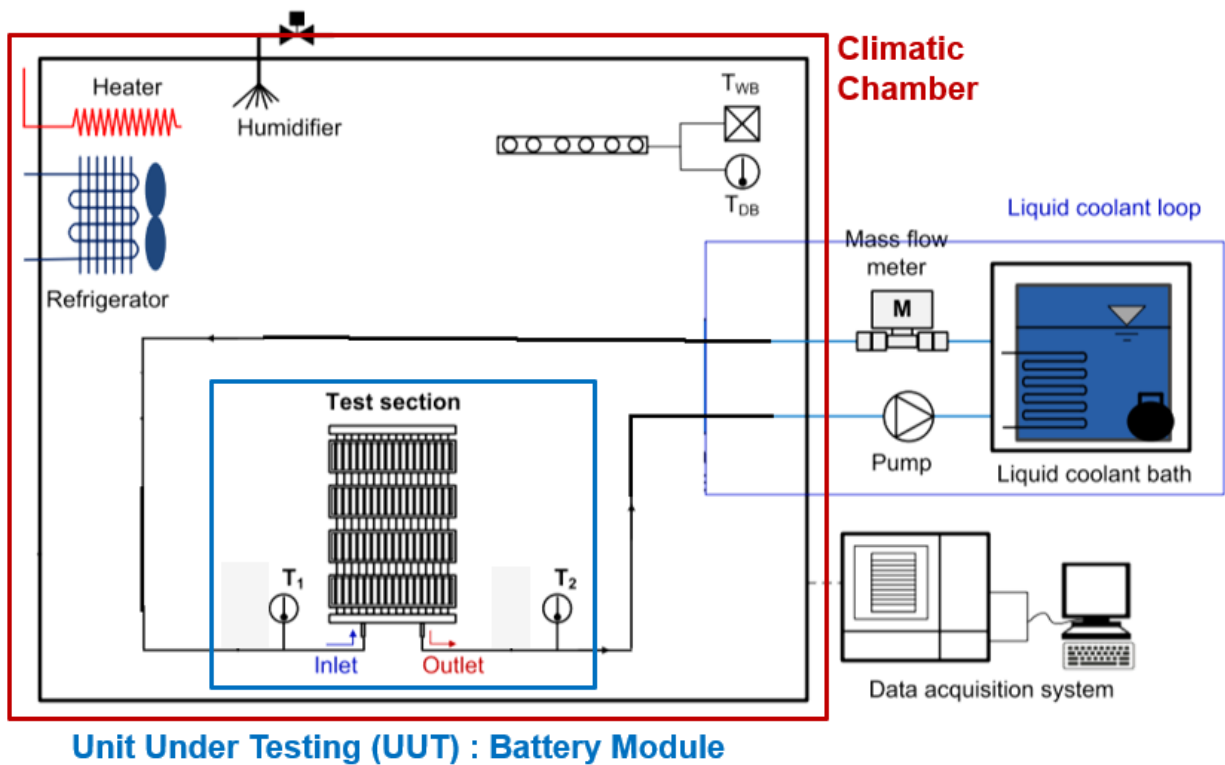


Figure 71 Testing setup showing the unit under testing, thermal chamber, chiller to the cold plate, and DAQ connections.

Data acquisition was conducted at 10 Hz to capture rapid transients in temperature and current, providing high-resolution measurements critical for analyzing thermal and electrical behavior during the tests. Each thermocouple acquisition system included an ambient sensor placed at the chamber's center to monitor and validate the ambient temperature during testing. Thermal data from the NI modules was monitored via LabVIEW, operating externally to the AVL system.

Voltage and current limits were configured on both the AVL cycler and Orion BMS to comply with the cell's operating specifications. The module voltage was limited to a range of 16.8 V to 26.1 V, reflecting the safe operating limits of the cells. Current limits were set at 120 A for

discharge and 405 A for charge, with some allowance to accommodate occasional current and voltage overshoots.

Temperature limits were set on the AVL cyclers and the Orion BMS to ensure the safety of the cells and busbars during testing. The cells were limited to a maximum temperature of 55°C per the datasheet specifications. For the No Cooling test, the busbar temperature was capped at 60°C. However, this limit was relaxed to 65°C for the Bottom Cooling and MCHP setups after discussions with faculty advisors, as copper busbars can safely operate up to 90°C [132]. The No Cooling test was not repeated under the revised conditions.

The Orion BMS is set to maintain cell balancing between cells within 5 mV. However, testing was permitted with deviations up to 50 mV, as the cell's wide voltage range ensures minimal impact on capacity measurements with this level of imbalance.

The NI 9213 was used to capture the temperatures of cells C and D for the Bottom cooling and MCHP testing setups. The NI 9123 is the most accurate DAQ used and those cells exhibit the worst-case heating scenario. Therefore, it is important to have accurate temperature readings.

The NI 9214 was used to capture the temperatures of cells A, B, and E for the Bottom cooling and MCHP testing setups.

The NI 9205 was used to capture the temperatures of the MCHPs installed on cells A, C, and E.

The AVL cycler built-in thermocouple data acquisition device was used to capture the temperatures on cells C and D for the no-cooling setup. Then it was used to capture the temperatures on cell F and the cold plate inlet and outlet for the Bottom cooling and MCHPs testing setups. Finally, it was used to capture the temperatures of the MCHPs installed on cells B, D, and F on the MCHP testing setup.

5.3 Fast charging protocols

The same testing procedure was applied to each of the three setups (No Cooling, Bottom Cold Plate, and MCHP Cooling). Each test began with the module charged to 100% SoC (or maximum voltage limit) and then discharged at 1C to 0% SoC (or minimum voltage limit).

After discharge, the modules were left to rest and balance for at least 4 hours, ensuring thermal equilibrium and voltage alignment between cells. Testing was typically conducted the following day to allow sufficient cooling and stabilization.

The Hyundai Ioniq and the 400A Pulse fast charging profiles are detailed in Section 3.4.4, were implemented for all setups. For the No Cooling test, the test was stopped once the busbar temperature reached 60°C, as natural cooling was insufficient for prolonged testing. For the Bottom Cooling and MCHP Cooling setups, testing paused once the cells reached 55°C or the busbar reached 65°C. Testing resumed only after temperatures dropped below 50°C for both the cells and busbars and repeated until the charging profile was done. This method ensured safety while allowing for accurate thermal performance comparisons between setups.

Chapter 6

Results and Discussion

The evaluation of cooling performance in the No Cooling, Bottom Cooling, and MCHP Cooling setups were conducted using two primary metrics: cooling effectiveness and temperature distribution within individual cells and across the module. The analysis first focuses on the performance of each setup independently, followed by a comparative assessment to highlight the strengths and limitations of each cooling method. It should be noted that due to inaccuracies in the K-type thermocouple measurements at the cold plate inlet and outlet, these values are excluded from this discussion.

6.1 No Cooling Module testing results

The No Cooling module served as a baseline for assessing thermal behavior in the absence of active cooling. Results were obtained under the Hyundai Ioniq fast charging profile and the 400A Pulse fast charging profile. Temperature readings were recorded for Cells C and D, which were selected due to their central position in the module and exposure to the highest heat accumulation from neighbouring cells.

6.1.1 Hyundai Fast Charging Test

The Hyundai fast charging test for the No Cooling module was completed up to 90% of the +300A current region, which accounts for 62% of the fast-charging phase and 31% of the total test duration. The voltage response, shown in Figure 72, exhibited a steep rise at the beginning due

to ohmic resistance, followed by a progressive increase as the charging current reached higher C-rates. The module voltage increased from a relaxed state of 19.27 V (3.2 V per cell) to a peak of 23.93 V (3.99 V per cell) over 14.35 minutes before the test was terminated due to the busbar temperature reaching 60°C. Coulomb counting indicated that 55.1 Ah of charge was delivered, corresponding to an estimated 50% SoC, assuming the cells were fully discharged and relaxed prior to testing.

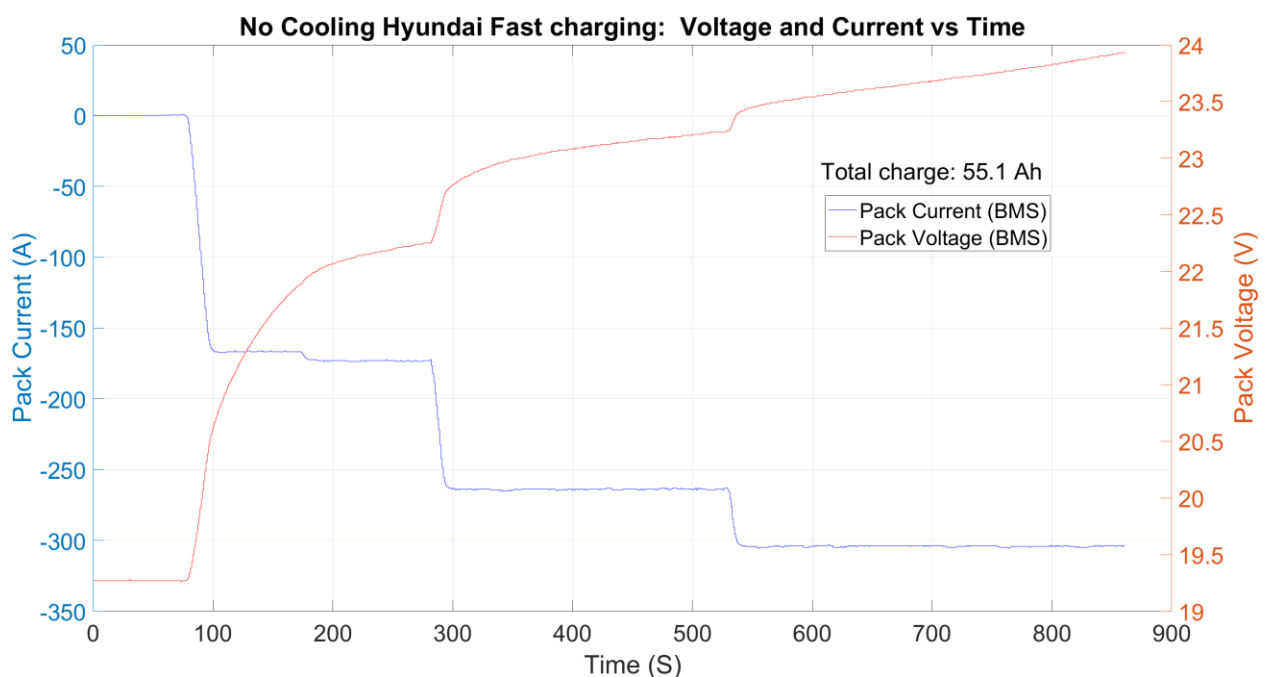


Figure 72 No Cooling, Hyundai fast charging Voltage response curve.

The temperature rise of cells C and D are presented in Figure 73 and Figure 74, showing a steady increase that becomes more pronounced as the charging current rises. Slight deviations from the 25°C starting point suggest minor inaccuracies in thermocouple calibration or insufficient soaking time, though these differences are negligible. The highest temperatures are observed on the sides where the cells are adjacent, indicating significant cell-to-cell heating. For cell D, the

upper sides consistently exhibit higher temperatures than the lower sides, while a malfunction in the upper positive thermocouple on cell C limits direct comparison. However, lower side readings suggest that cell C's upper positive side likely exceeds cell D's upper side temperature. The front and back faces of both cells display similar temperatures, slightly higher than the bottoms. Cell C shows a narrower temperature range of 2.1°C, while cell D's broader range of 7.07°C is attributed to the anomalously high temperature recorded at the upper negative side of cell D and the missing thermocouple data from cell C.

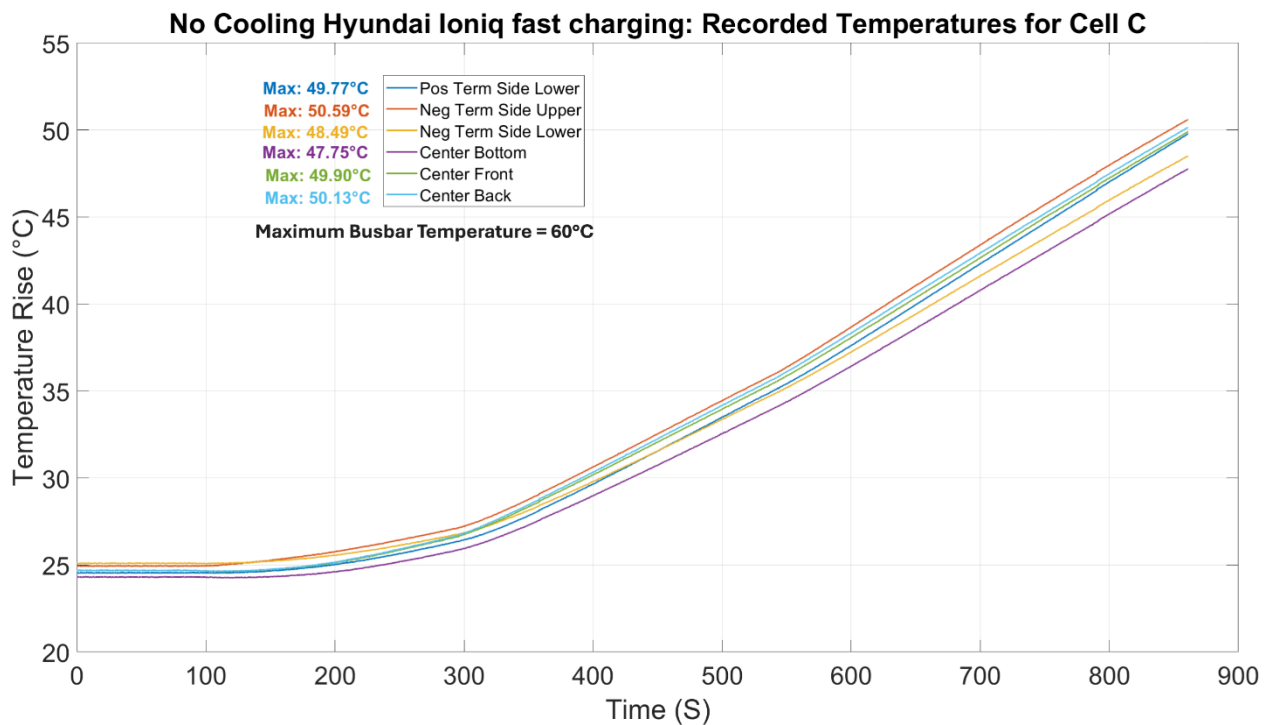


Figure 73 No Cooling, Hyundai fast charging cell C temperature response.

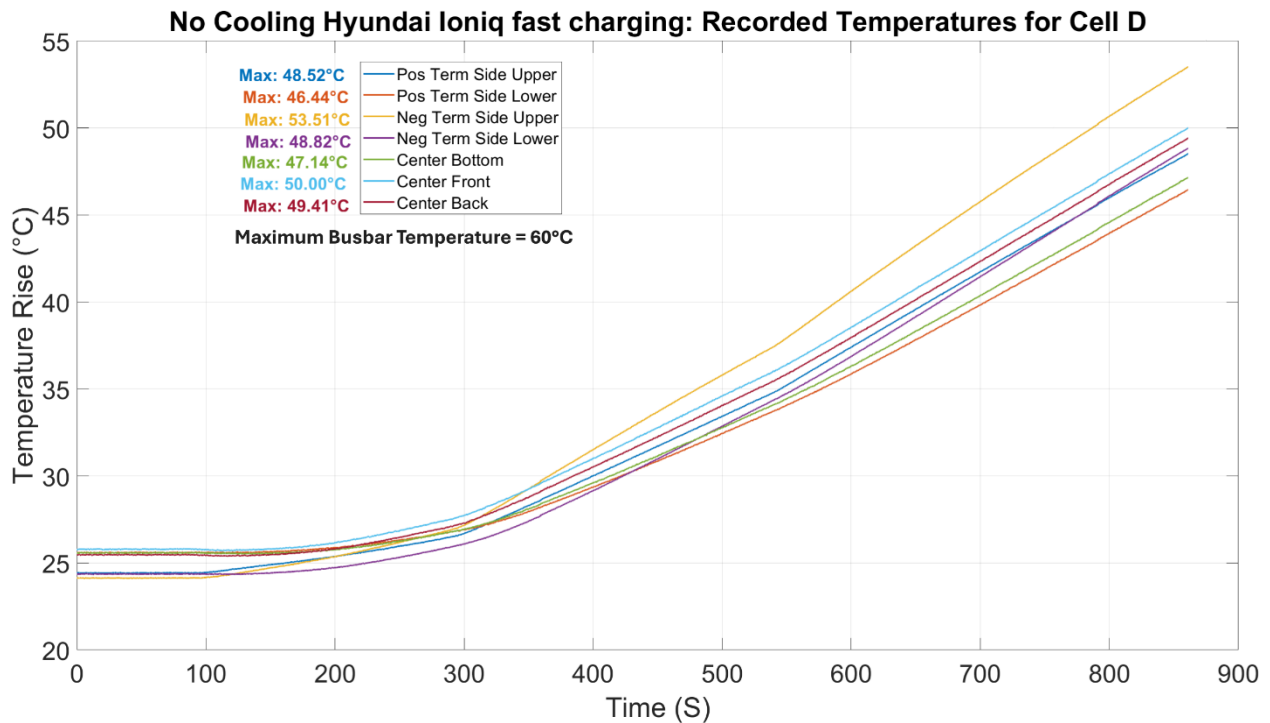


Figure 74 No Cooling, Hyundai fast charging cell D temperature response.

6.1.2 Pulse Fast charging

The 400A 10-second pulse fast charging profile was partially completed, covering 60% of the 400A region and 35% of the entire profile. The test lasted 13.1 minutes before being halted due to the busbar temperature reaching 60°C. During this time, 44Ah of charge was delivered to the cells, corresponding to 39% SoC. The voltage response curve, shown in Figure 75, mirrors the trend observed in single-cell testing. The module began at a relaxed voltage of 19.19V (3.2V per cell), peaked at 23.72V (3.95V per cell), and settled at 22.4V (3.7V per cell) during the no-current resting phase. The initial voltage spike reflects the ohmic resistance, followed by an increase during each pulse due to polarization resistance. A sharp voltage drop occurs immediately after the pulse ends. The overall rise in voltage is attributed to both the charging process and the excitation of ions, stabilizing progressively as the voltage curve transitions into the more linear OCV region

of the cells.

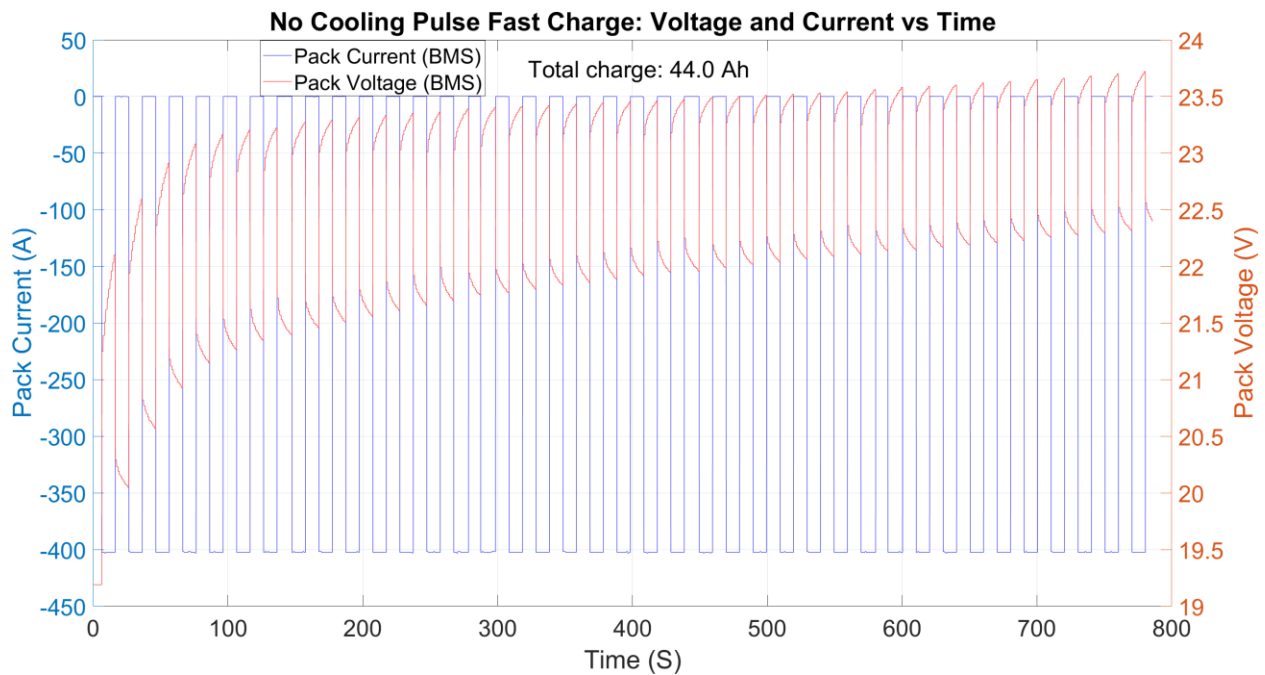


Figure 75 No Cooling, Pulse fast charging Voltage curve response.

The temperature rise of cells C and D above the 25°C ambient baseline is shown in Figure 76 and Figure 77. The curves exhibit a steady increase, with minimal dips observed during the brief rest periods between each pulse. Initial temperatures below 25°C highlight the need for extended soaking times to ensure thermal equilibrium before testing. As observed in previous tests, the highest temperatures are recorded near the upper sides adjacent to the terminals, where the cells are in close proximity. The lowest temperatures are consistently observed at the bottom, while the fronts and backs exhibit similar thermal behavior. The temperature range for cell C is 3.55°C, while for cell D, it is 6.97°C, indicating a larger thermal variation likely due to the increased heating effect at specific positions within the module.

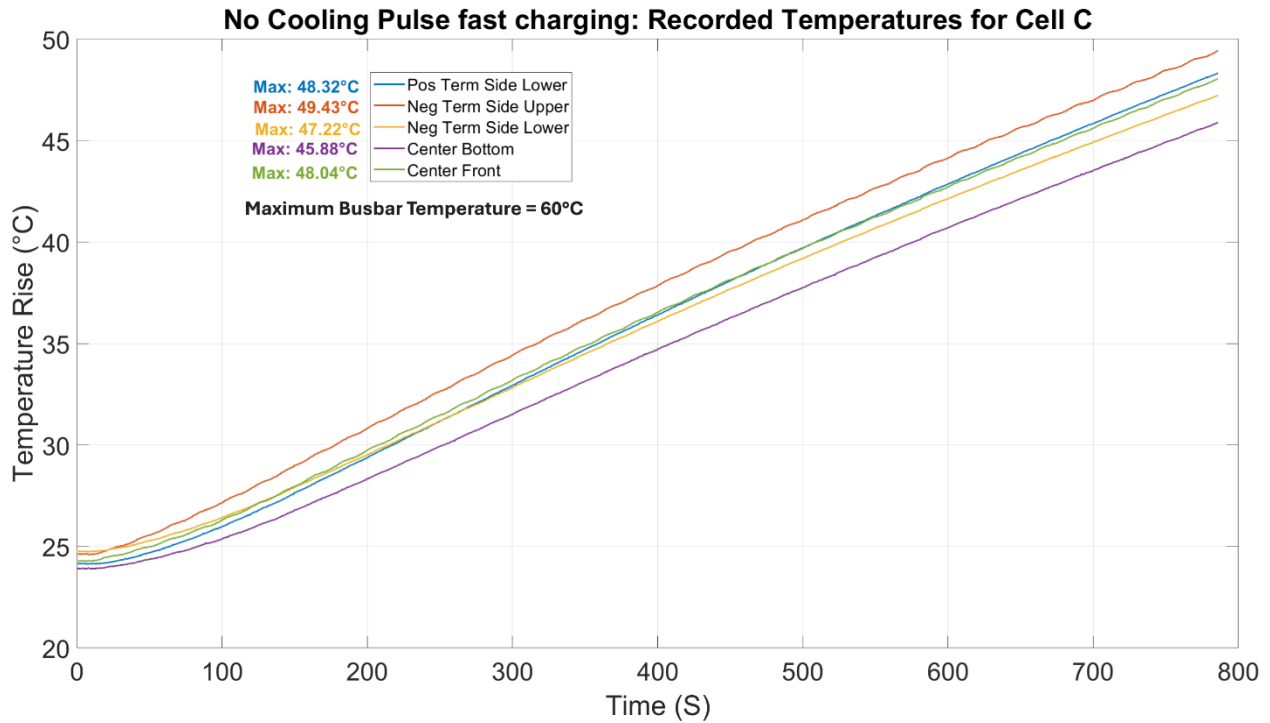


Figure 76 No Cooling, Pulse fast charging cell C temperature response.

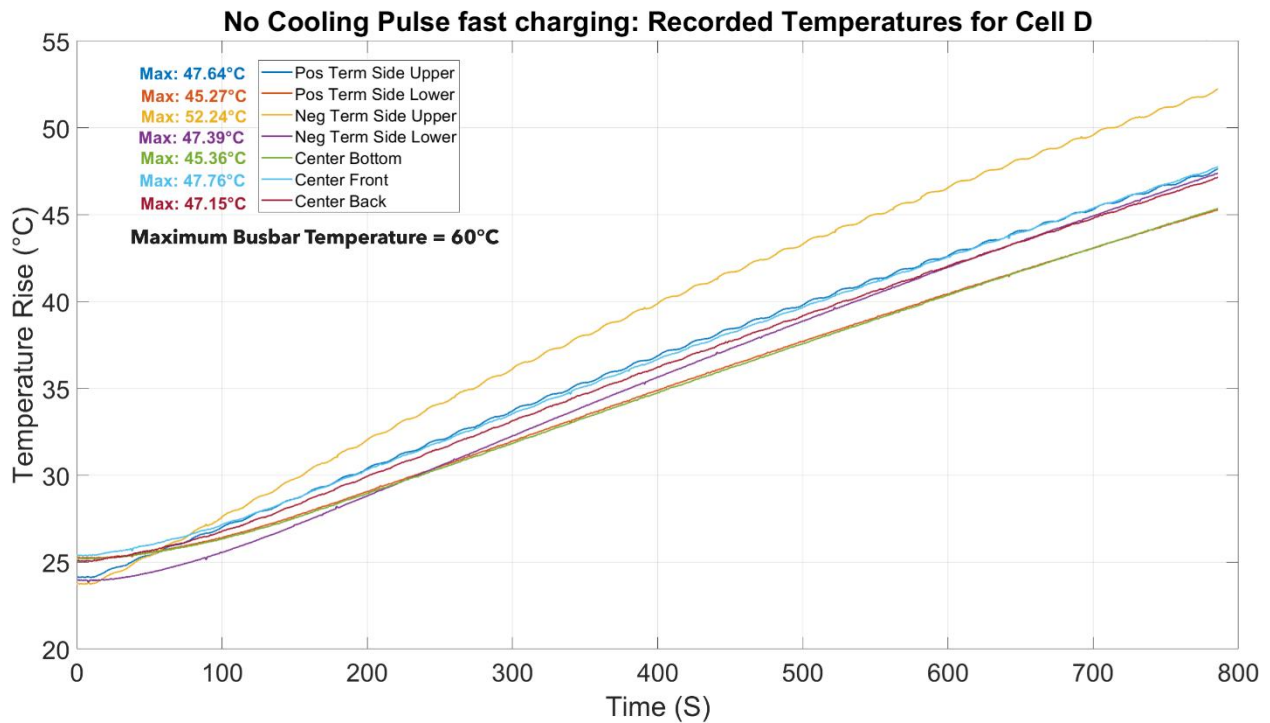


Figure 77 No Cooling, Pulse fast charging cell D temperature response.

6.2 Bottom Cooling module test results

The Bottom Cooling module aimed to assess the thermal management capabilities of a production-grade cold plate. Results from the Hyundai fast charging and Pulse fast charging profiles are discussed below.

6.2.1 Hyundai Fast charging

The Hyundai Ioniq fast charging profile was conducted in three parts, interrupted twice as the busbar temperature reached the 65°C threshold. The voltage response curve, shown in Figure 78, highlights the test segments and the rest periods between them. Initially, the voltage spiked due to ion excitation, continuing to rise with increasing current. The first segment lasted 12.85 minutes, covering approximately 58% of the fast-charging region and delivering 48.5Ah to the cells. After 4.5 minutes of cooling to 50°C, the test resumed, but the busbar reheated to the threshold within 4.75 minutes during the second segment. The voltage increase was less pronounced as the cells entered the near-linear portion of their OCV curve and were not fully relaxed. The third segment began after a 4.35-minute cooling period, completing the fast-charging and CV phases. In total, the three segments delivered 106.8Ah, achieving 94% SoC over 56 minutes, including rest periods, with the voltage increasing from 18.93V to 25.8V (3.16V to 4.3V per cell).

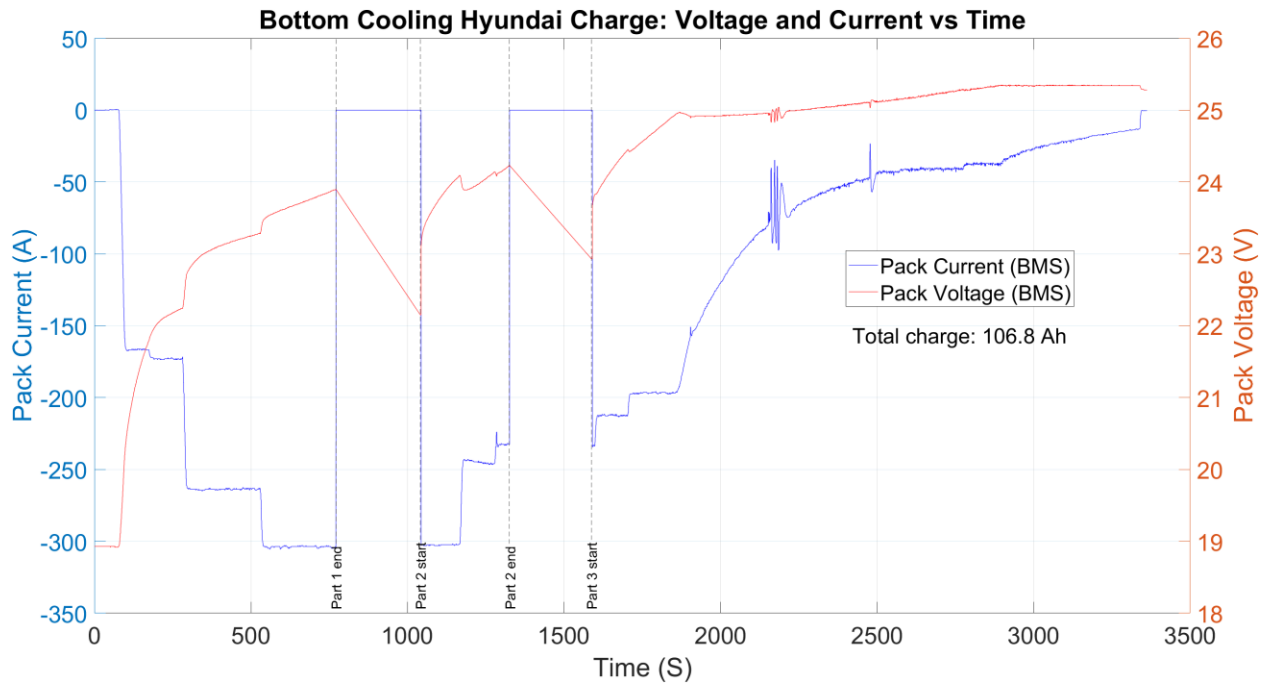


Figure 78 Bottom Cooling, Hyundai Ioniq fast charging Voltage response curve.

The temperature profiles for the cells are presented in Figure 79 to Figure 84. During the first part of the test, the highest recorded temperature was 48°C on cell C at the upper-side positive terminal. By the end of the second part, all cells reached their peak temperatures, with the highest measured at 52.98°C, again at cell C’s upper-side positive terminal. The effects of cell-to-cell heating were evident across all cells, particularly in cells C and D, which were exposed to heating from three adjacent sides. Consistently, the sides adjacent to other cells exhibited the highest temperatures, with temperatures decreasing toward the bottom of the cells. The bottom regions also displayed signs of cell-to-cell heating, with temperatures ranging from 34.6°C to 37.86°C, where middle cells were at the higher end of the range. The temperature variation within each cell ranged from 12.8°C to 17.53°C which is an unacceptably high range, as thermal uniformity is critical for safety and performance, typically limited to a 5°C difference.

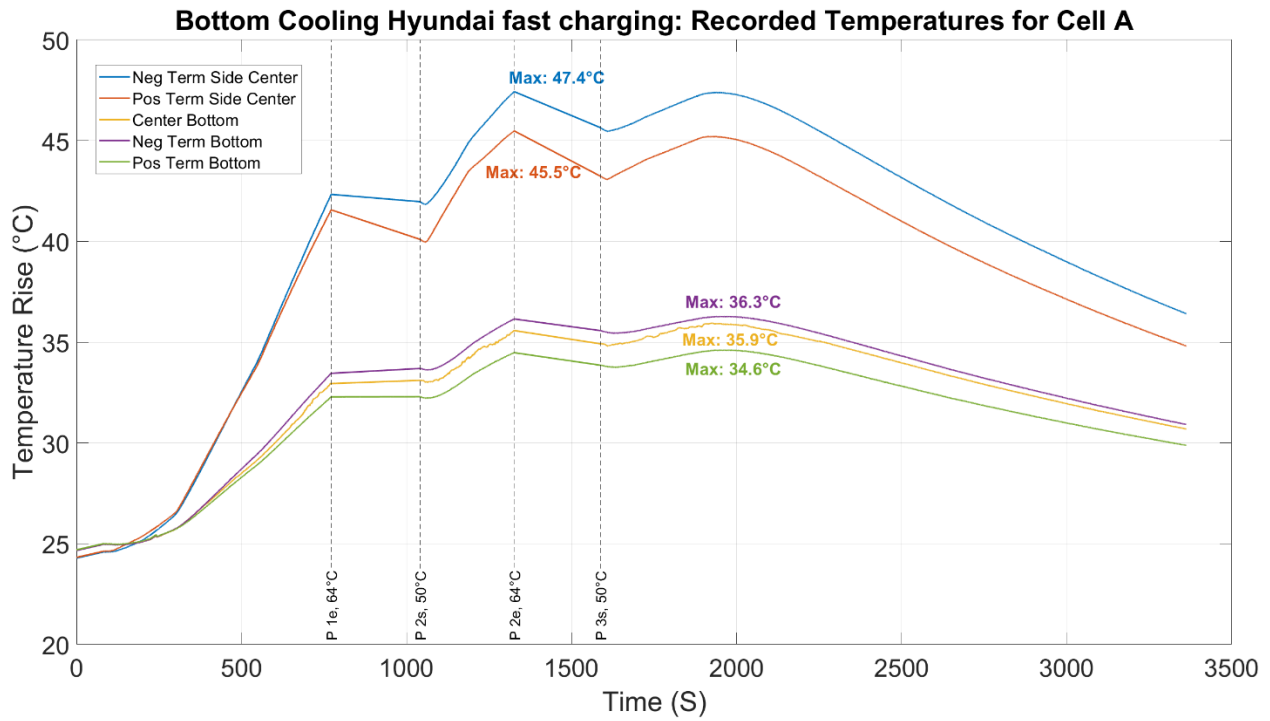


Figure 79 Bottom Cooling, Hyundai Ioniq fast charging cell A temperature response.

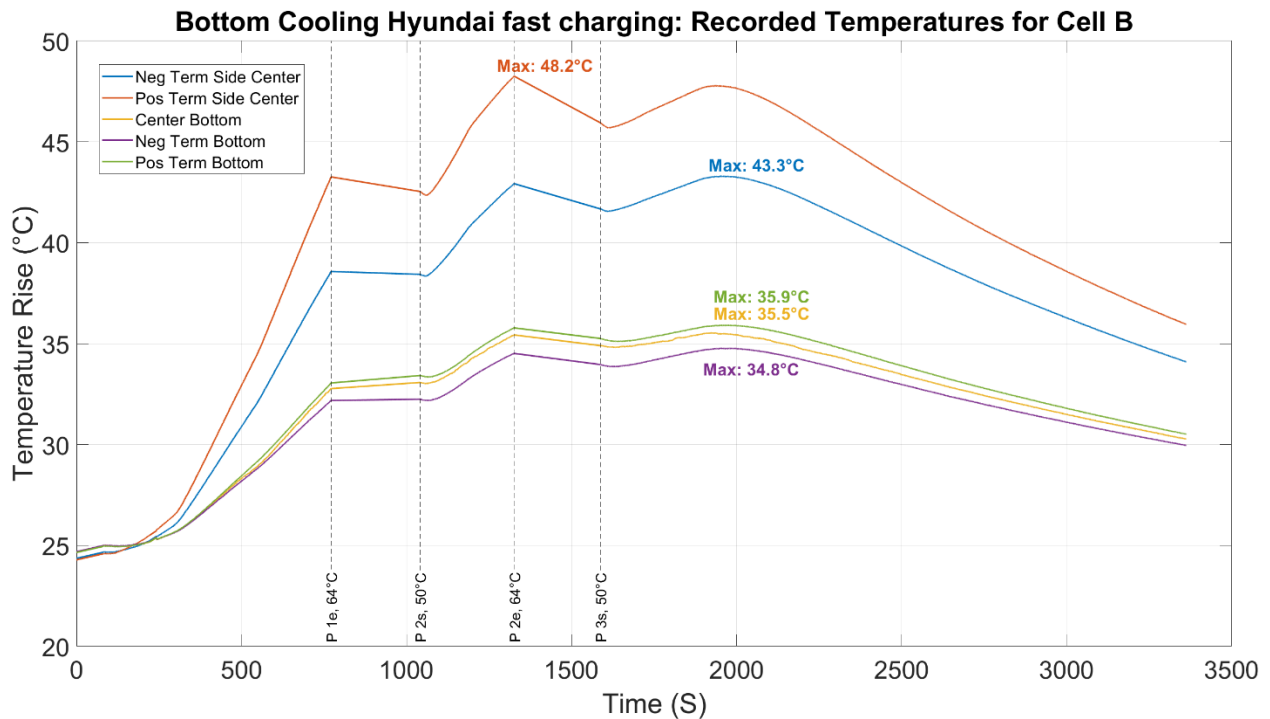


Figure 80 Bottom Cooling, Hyundai Ioniq fast charging cell B temperature response.

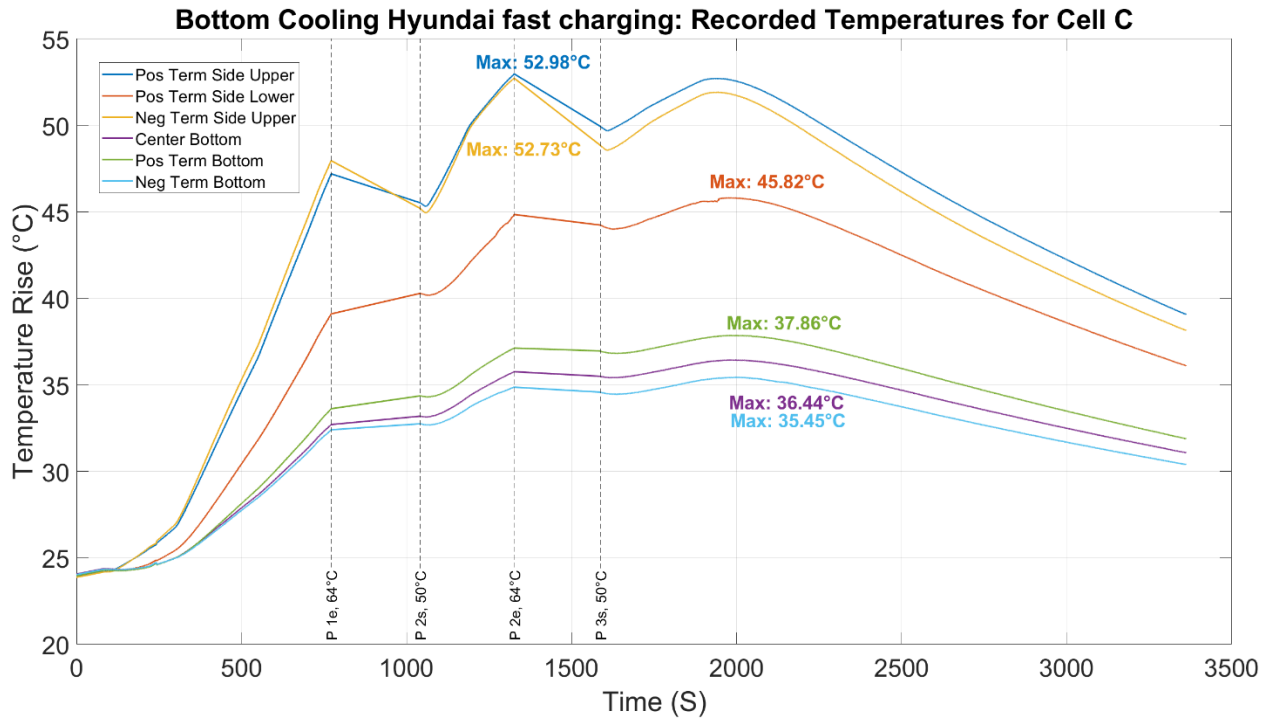


Figure 81 Bottom Cooling, Hyundai Ioniq fast charging cell C temperature response.

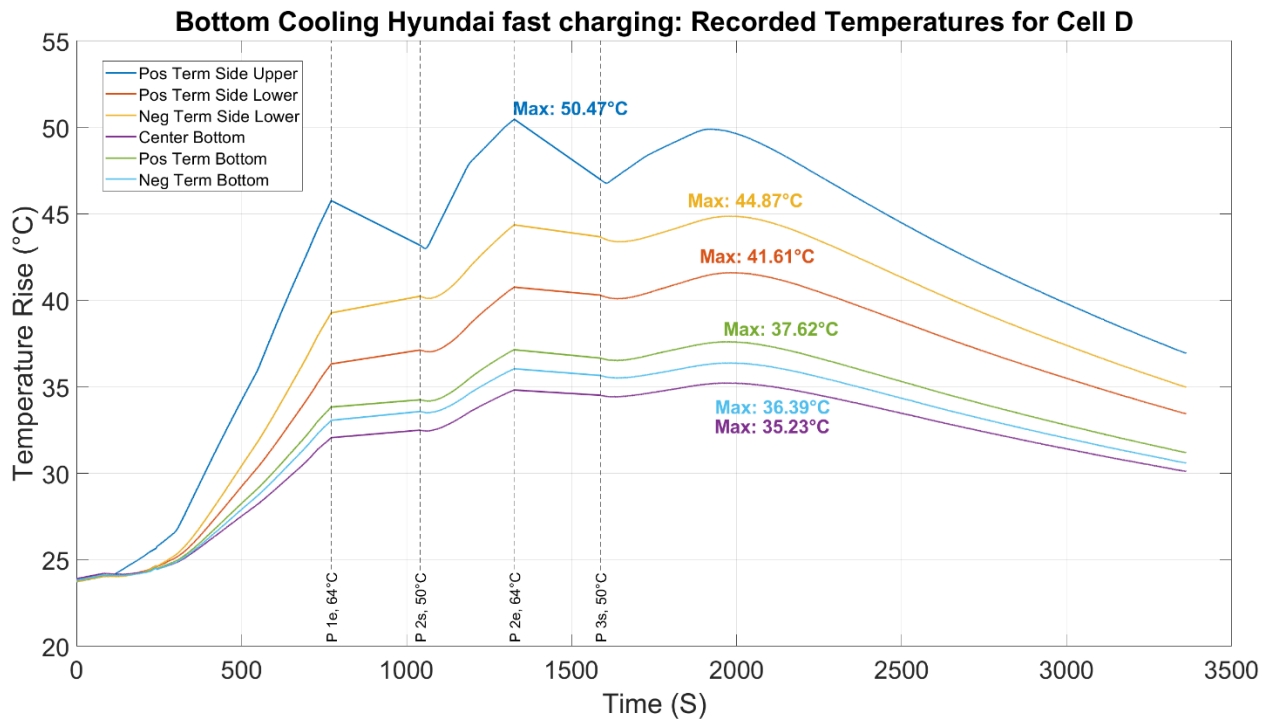


Figure 82 Bottom Cooling, Hyundai Ioniq fast charging cell D temperature response.

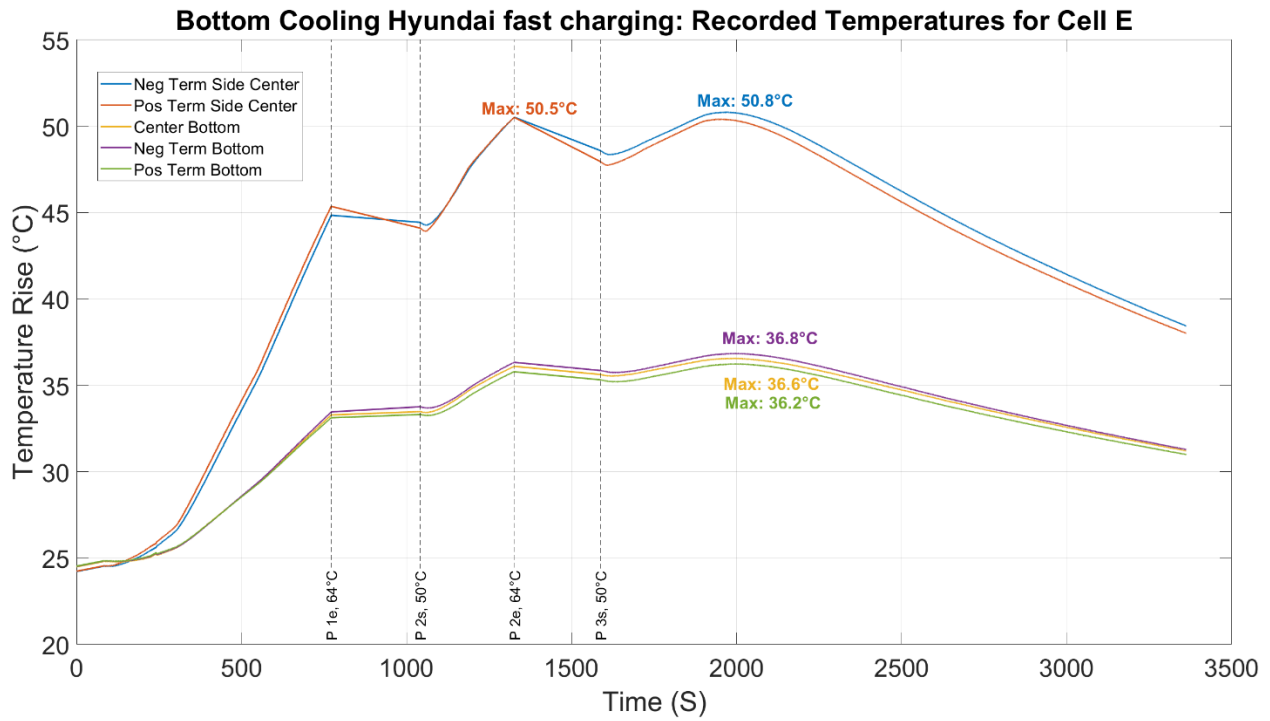


Figure 83 Bottom Cooling, Hyundai Ioniq fast charging cell E temperature response.

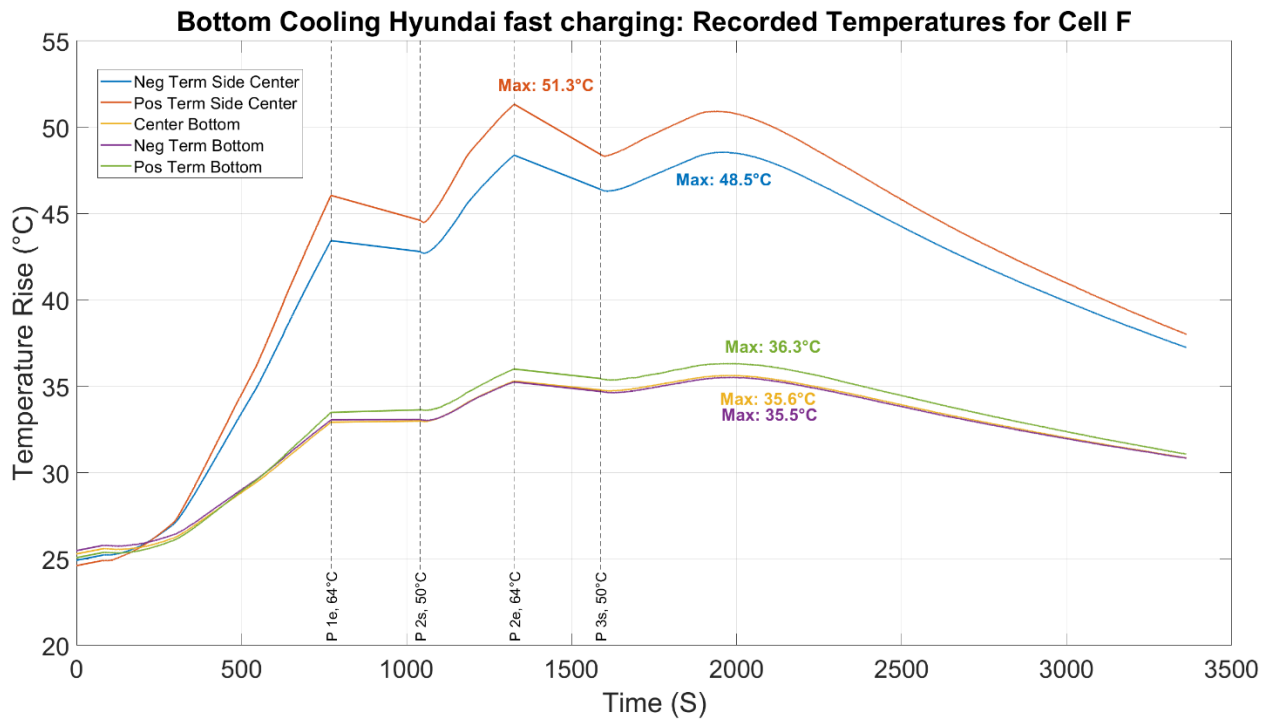


Figure 84 Bottom Cooling, Hyundai Ioniq fast charging cell F temperature response.

6.2.2 Pulse fast charging

The 10-second 400A Pulse fast charging profile was completed in eight segments, primarily interrupted by the busbar temperature reaching the 65°C limit. Exceptions occurred during parts 5 and 7, where the test was halted due to cycler errors, likely caused by frequent profile pauses. The voltage response curve, shown in Figure 85, highlights the segmented test progression and corresponding rest periods. In the first segment, the cells were charged with 30.5 Ah, reaching 27% SoC in 9.12 minutes, approximately 25% of the full profile. The busbar required 3.1 minutes to cool down after this segment, with an average cooldown time of 3.8 minutes across all segments, which was shorter than observed in the Hyundai profile. This suggests that the heating was predominantly concentrated on the busbar's outer layers.

The voltage curve exhibited a similar trend to the no-cooling test, with an initial sharp spike caused by ohmic resistance, followed by a reduced voltage difference as the SoC increased. This behavior is attributed to the excitation of non-relaxed cells. The total energy delivered to the cells was 104.9 Ah, equating to 92% SoC in 61.8 minutes. This value is slightly lower than expected, likely due to the cycler misreading some currents during the frequent pauses and resumptions. The voltage ranged from 18.75V to 25.21V (3.13V to 4.2V per cell). The lower initial voltage indicates that the cells were either more deeply discharged or insufficiently relaxed before the test. However, this deviation is not expected to affect the electrical and thermal performance for the purposes of this project.

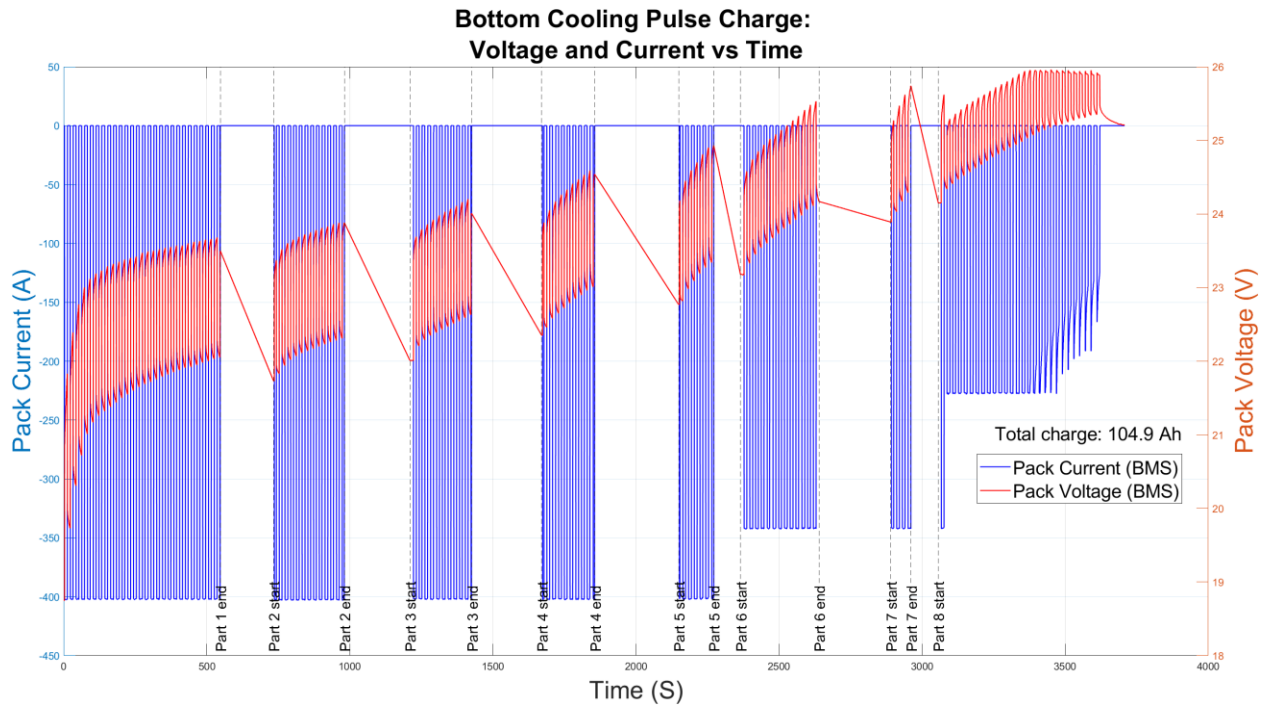


Figure 85 Bottom Cooling, Pulse fast charging Voltage response curve.

The temperature profiles during the pulse fast charging test, shown in Figure 86 to Figure 91, revealed a maximum temperature of 42°C on cell C at the negative terminal side by the end of the first charging segment, with a slightly lower value at the positive terminal side. This indicates that cell-to-cell heating had not fully developed at this stage. Overall, the temperature rise was less prominent compared to the Hyundai profile and the no-cooling test. After each rest period, the cells exhibited a brief cooling phase before resuming their temperature increase, suggesting that the outer surface temperatures lagged behind the core temperatures as heat transfer occurred. The highest temperatures were observed at the sides adjacent to other cells, confirming the ongoing influence of cell-to-cell heating, albeit less significant than in previous tests. The bottom of the cells maintained the lowest temperatures, while the fronts and backs exhibited similar values. Bottom temperatures ranged from 34.0°C to 37.99°C , with the middle cells showing slightly higher

readings. Temperature variation within each cell ranged from 12.6°C to 17.4°C, closely resembling trends observed in the Hyundai test.

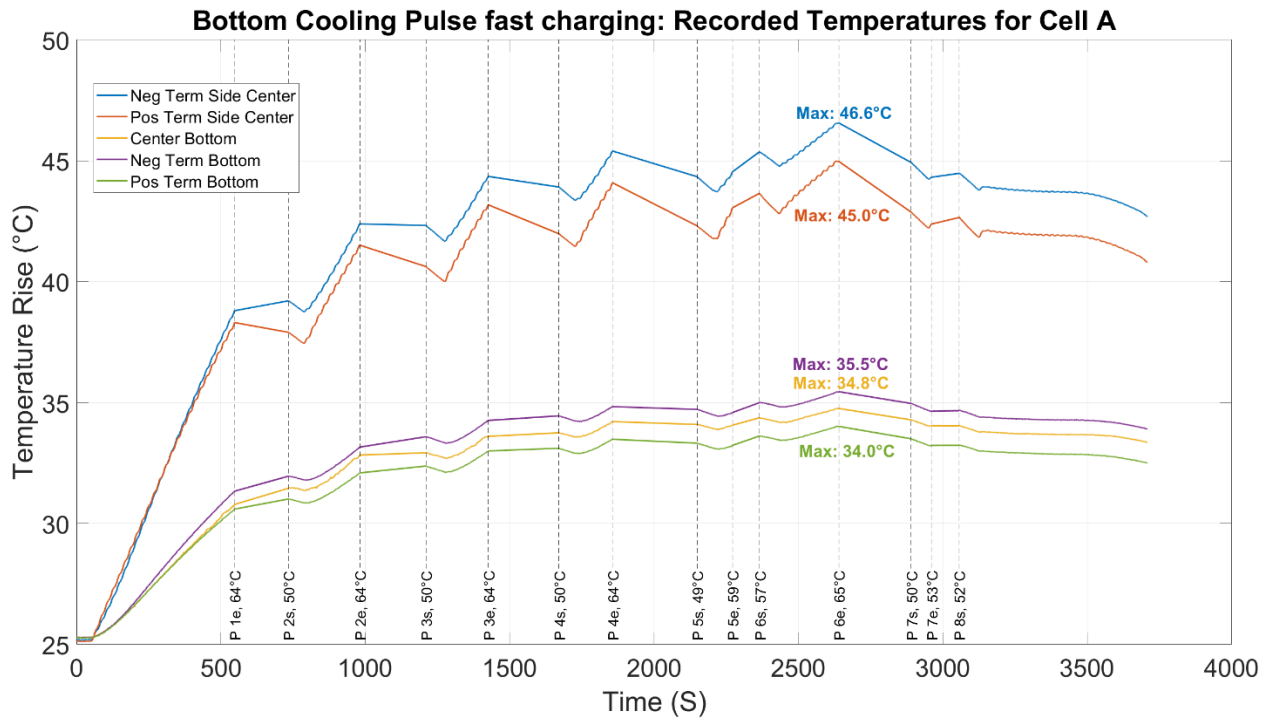


Figure 86 Bottom Cooling, Pulse fast charging cell A temperature response.

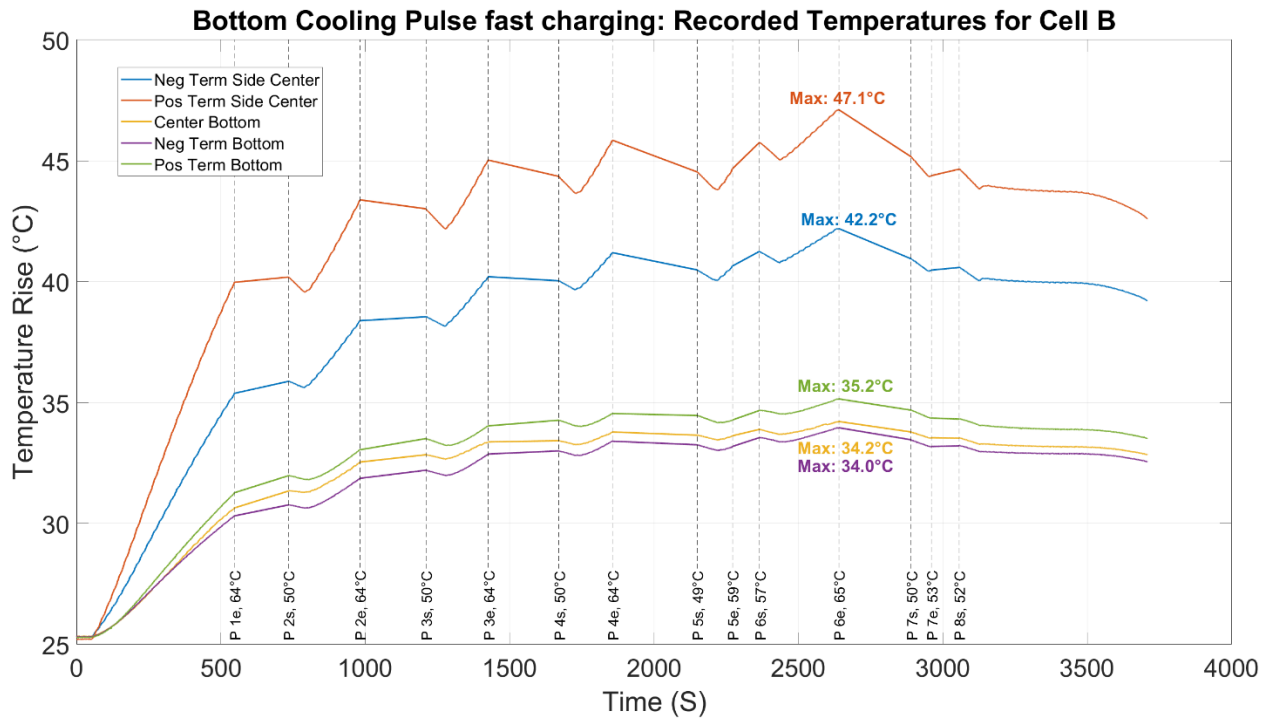


Figure 87 Bottom Cooling, Pulse fast charging cell B temperature response.

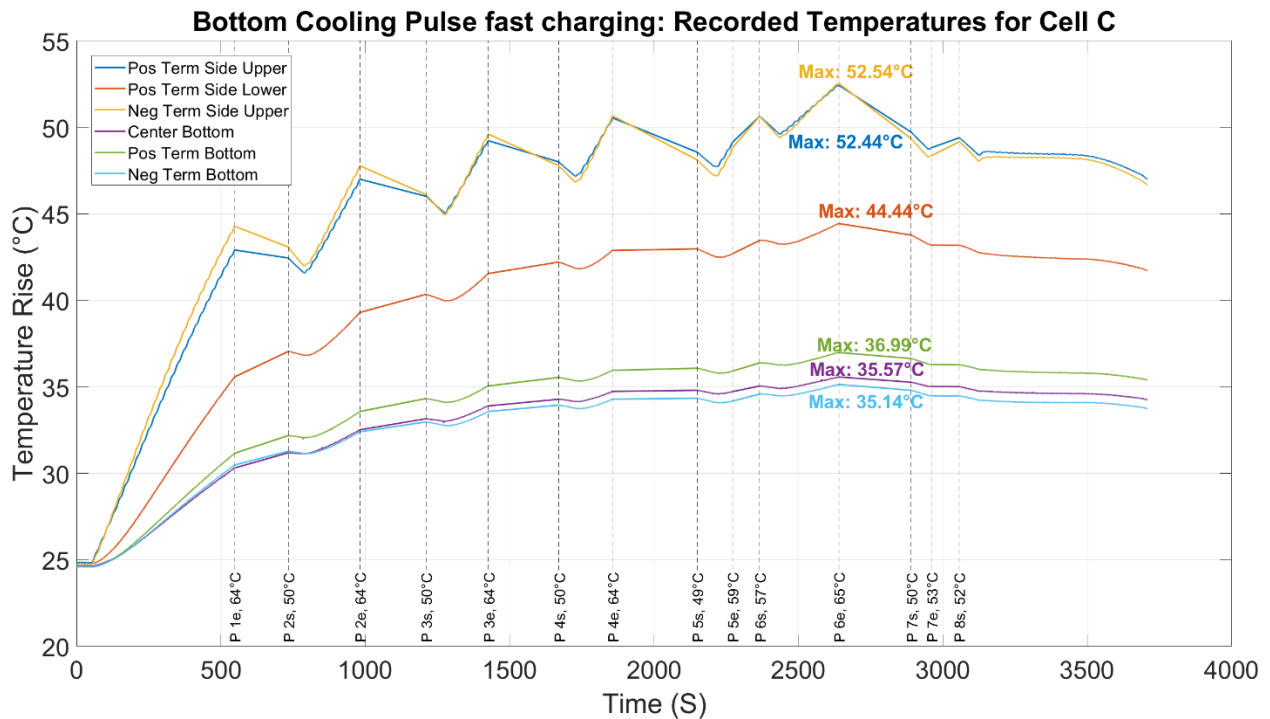


Figure 88 Bottom Cooling, Pulse fast charging cell C temperature response.

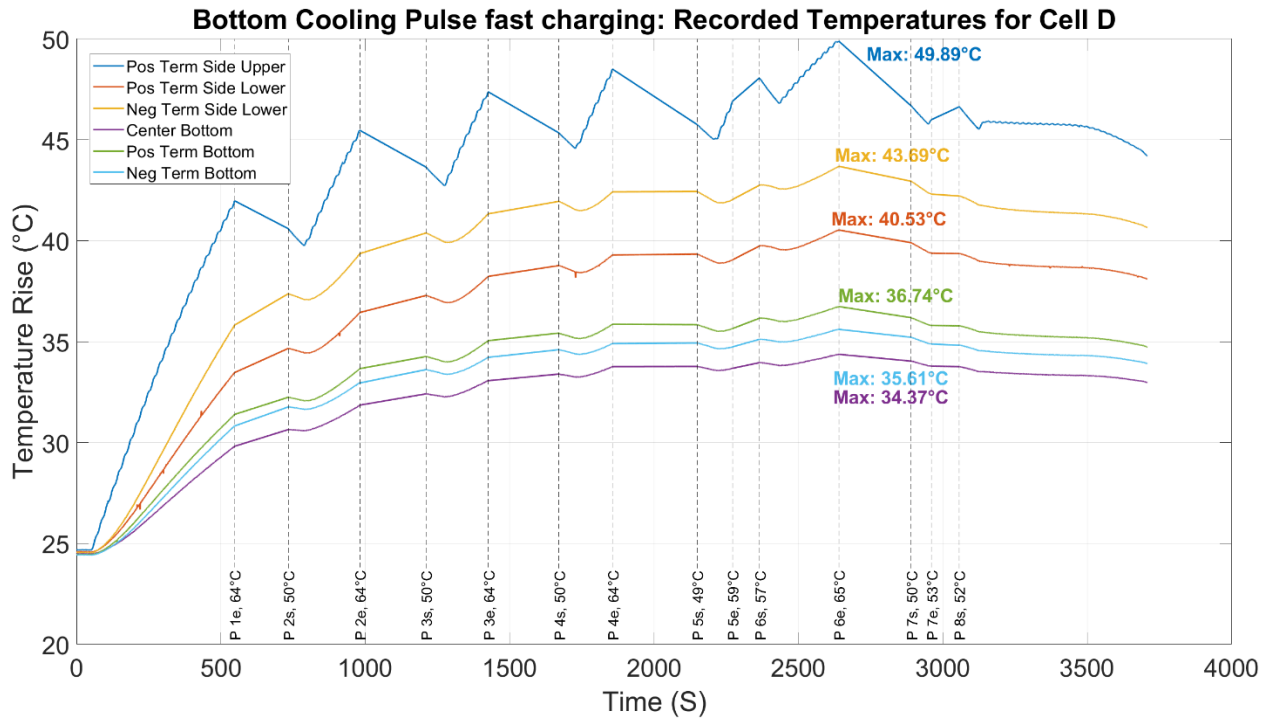


Figure 89 Bottom Cooling, Pulse fast charging cell D temperature response.

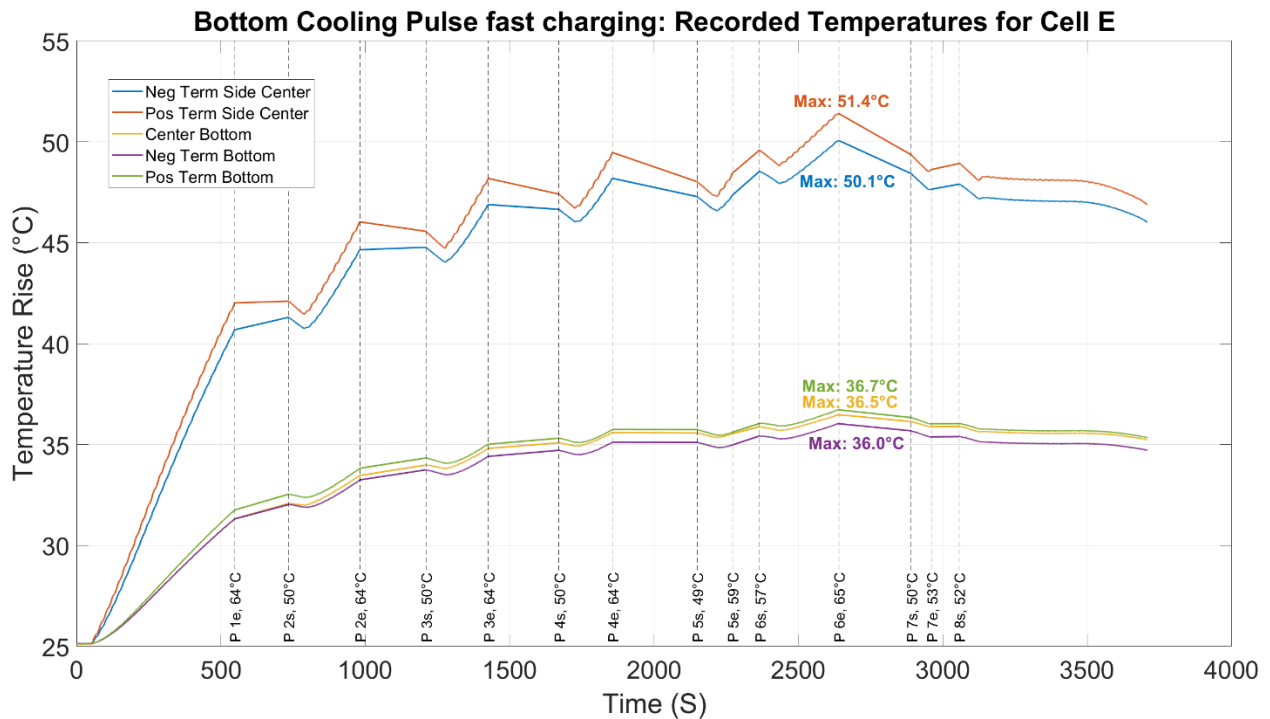


Figure 90 Bottom Cooling, Pulse fast charging cell E temperature response.

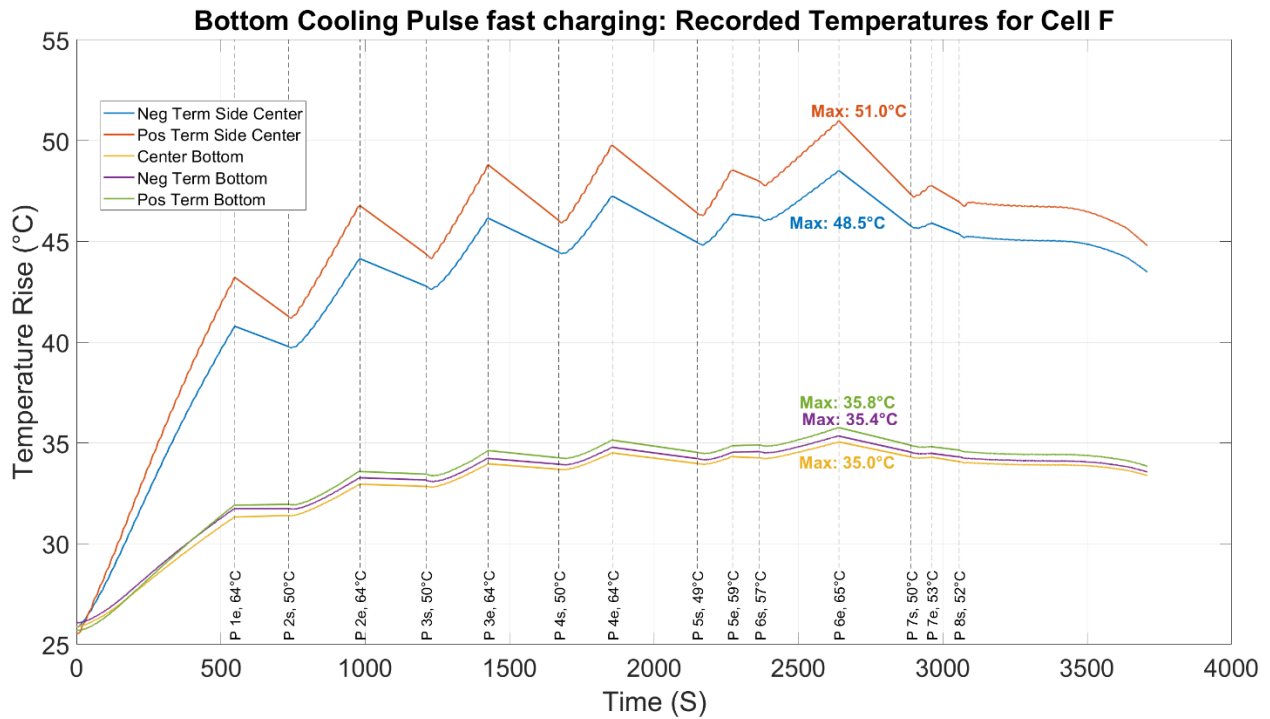


Figure 91 Bottom Cooling, Pulse fast charging cell F temperature response.

6.3 MCHP Cooling

The MCHP Cooling module introduced passive cooling through Micro-Channel Heat Pipes. Results from the Hyundai fast charging and Pulse fast charging profiles are discussed below.

6.3.1 Hyundai

The Hyundai Ioniq fast charging profile was conducted in two parts due to some cells reaching the cut-off temperature of 55°C. The voltage response curve, shown in Figure 92, illustrates the voltage behavior across both parts, including the relaxation period between them. In the first part, the voltage spiked initially and rose less steeply as the current increased. This phase lasted approximately 21 minutes, nearly completing the fast-charging region, with 80.56 Ah delivered to the cells, corresponding to a 71% SoC. This accounted for 97% of the fast-charging

region and 46% of the total charging profile. Following this, the cells required 19 minutes to cool to 50°C, while the busbars remained relatively cool throughout the test, attributable to the high thermal conductivity and smaller size of the copper busbars compared to the cells. The second part of the test concluded the fast-charging region and the CV mode, delivering a total of 107.1 Ah to the cells, slightly exceeding the test design due to potential cyclers reading errors. The total charging time was 66.14 minutes, with the module voltage increasing from 18.78 V to 25.26 V (3.13 V to 4.21 V per cell).

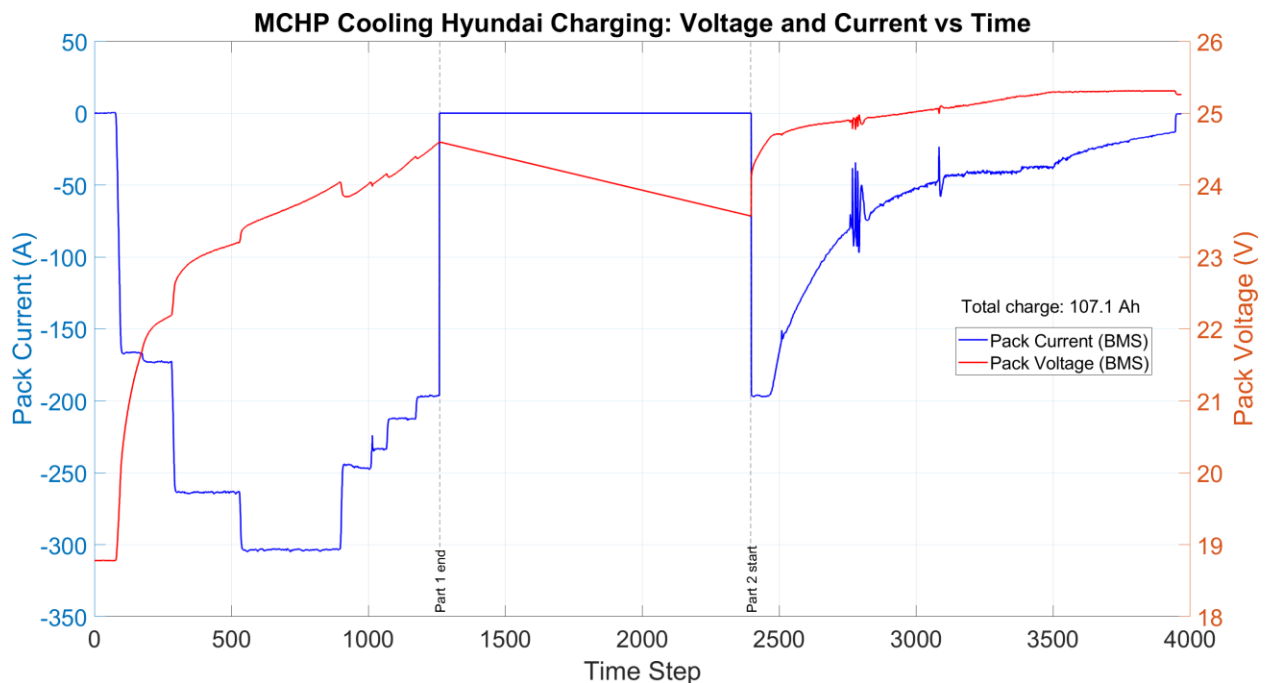


Figure 92 MCHP Cooling, Hyundai Ioniq fast charging Voltage response curve.

The cell temperature curves, shown in Figure 93 to Figure 98, reveal that the maximum temperatures for all cells occurred immediately after the first part of the test was stopped, with the highest reading around 55°C at the center bottom thermocouple of the cells. Cell C exhibited slightly higher temperatures compared to the others, followed by the positive bottom locations for

most cells, except for Cells C and D, where the upper sides near the positive terminals recorded higher values. This aligns with the cooling behavior of the MCHP, which effectively reduces temperatures along the sides, leaving the center bottom (the furthest thermocouple from the cooling sides) as the hottest location. The design of the MCHP mitigated side-to-side cell heating by physically distancing the cells from each other, though middle cells still showed slightly elevated temperatures due to localized cell-to-cell heating. Positive terminals consistently exhibited higher temperatures than negative terminals, consistent with prior single-cell tests, highlighting the higher thermal resistance of the NMC cathode compared to the graphite anode.

Unexpectedly low readings were observed on Cell E at the thermocouple near the positive terminal, suggesting either exceptionally effective MCHP performance at that location or a possible issue with the thermocouple connection, such as a loose or malfunctioning sensor. Overall, temperature variation across cells ranged from 1.31°C to 6.41°C, with only Cell B exceeding the 5°C range, reflecting the MCHP's ability to maintain a uniform temperature distribution and enhance cell stability and health.

The MCHP thermal response closely mirrored the cell patterns throughout the test. The condenser temperatures were slightly higher than those of the adiabatic region, likely due to minor natural convection at the exposed adiabatic surface. This discrepancy was generally minimal, suggesting effective phase change behavior in the adiabatic region. Optimal cooling performance requires closer temperature alignment between the adiabatic and condenser regions, with lower overall temperatures indicating better efficiency. Variations in MCHP effectiveness across cells were attributed to inconsistent surface contact between the MCHPs, cell sides, and the cold plate, which underscores the importance of proper assembly and contact pressure for maximizing cooling performance.

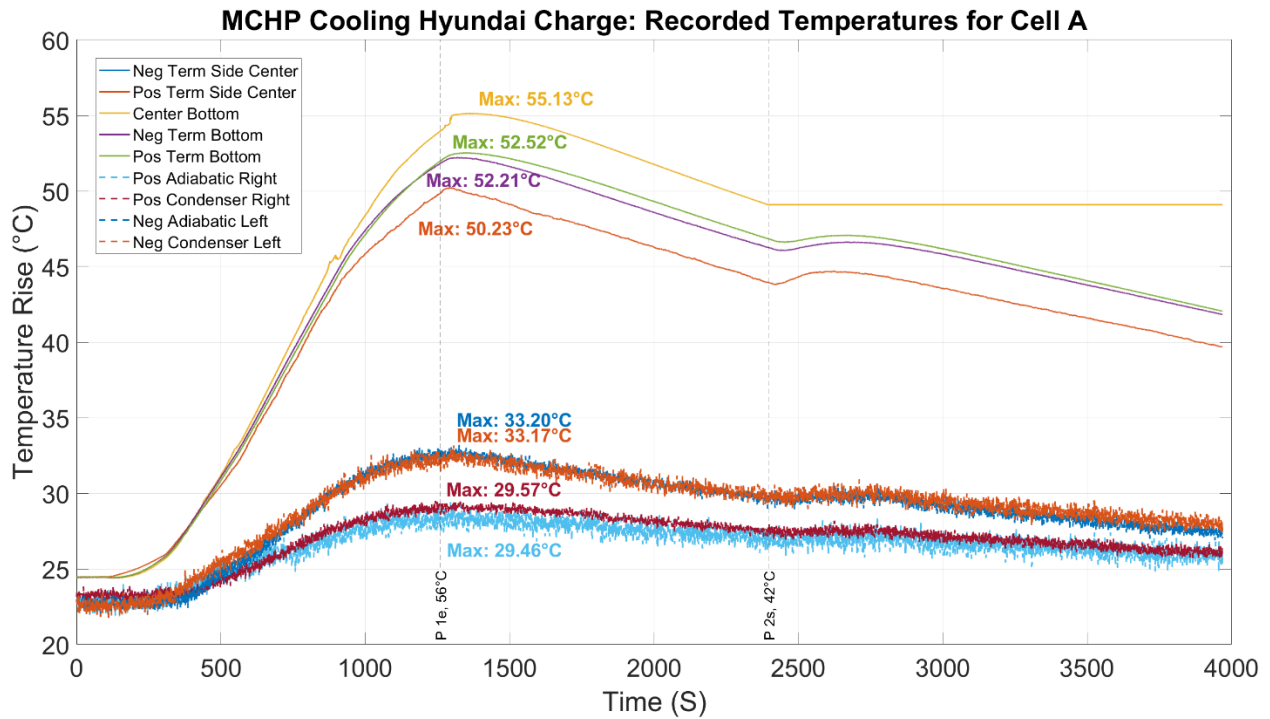


Figure 93 MCHP Cooling, Hyundai Ioniq fast charging cell A temperature response.

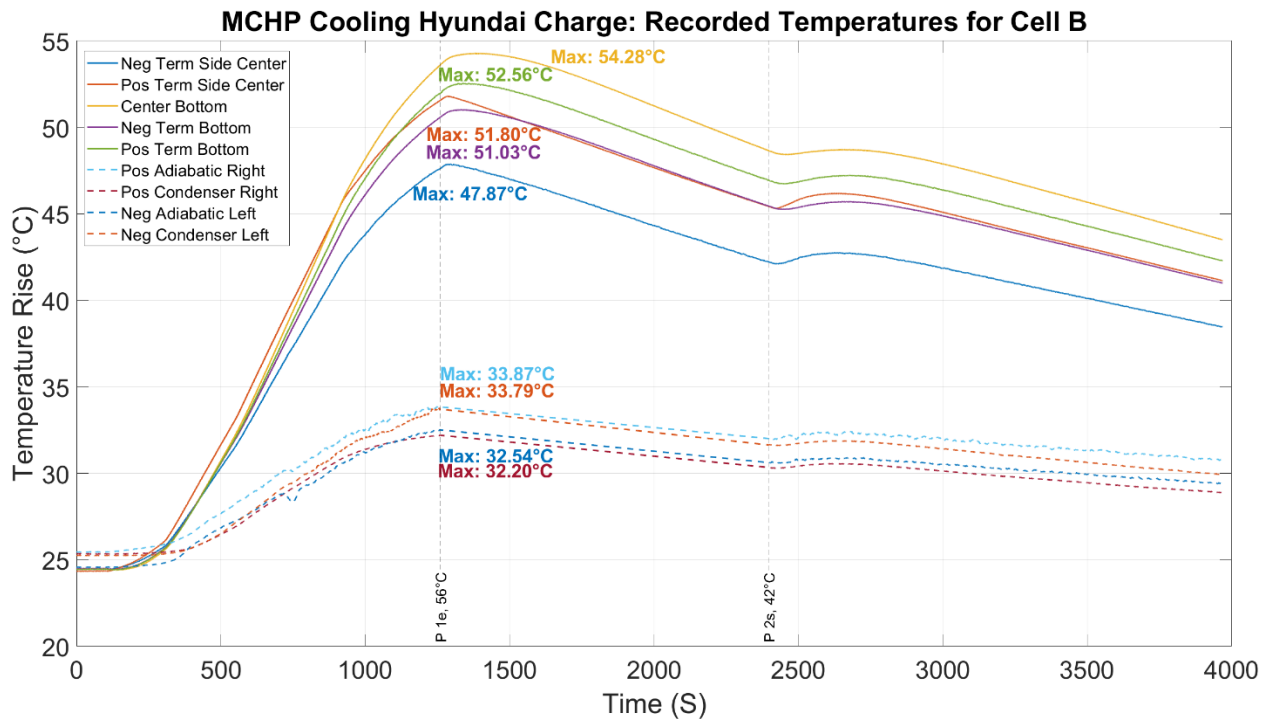


Figure 94 MCHP Cooling, Hyundai Ioniq fast charging cell B temperature response.

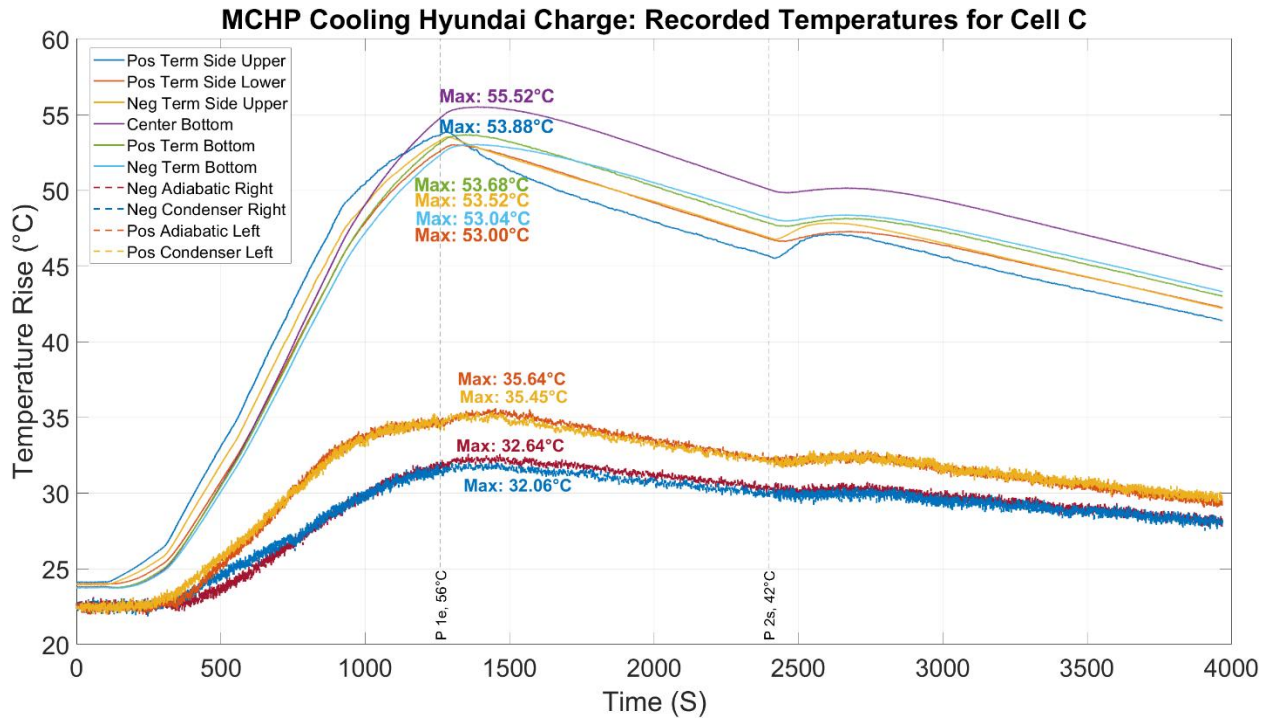


Figure 95 MCHP Cooling, Hyundai Ioniq fast charging cell C temperature response.

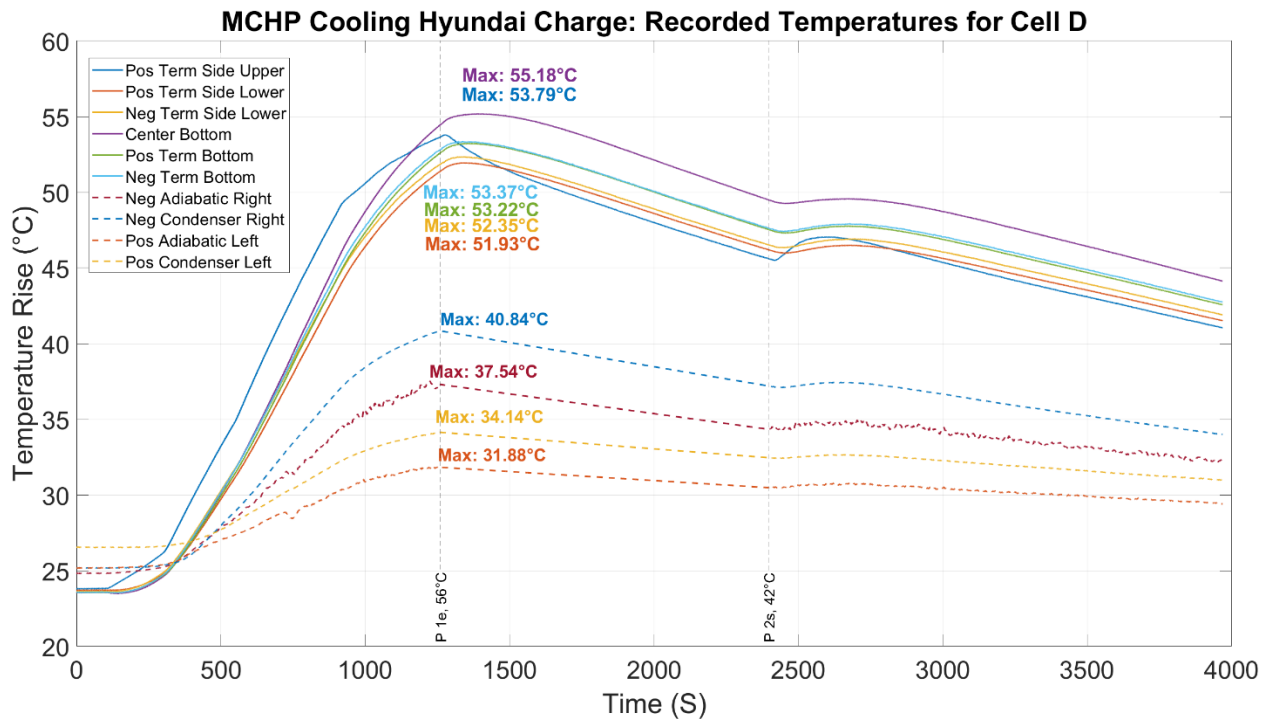


Figure 96 MCHP Cooling, Hyundai Ioniq fast charging cell D temperature response.

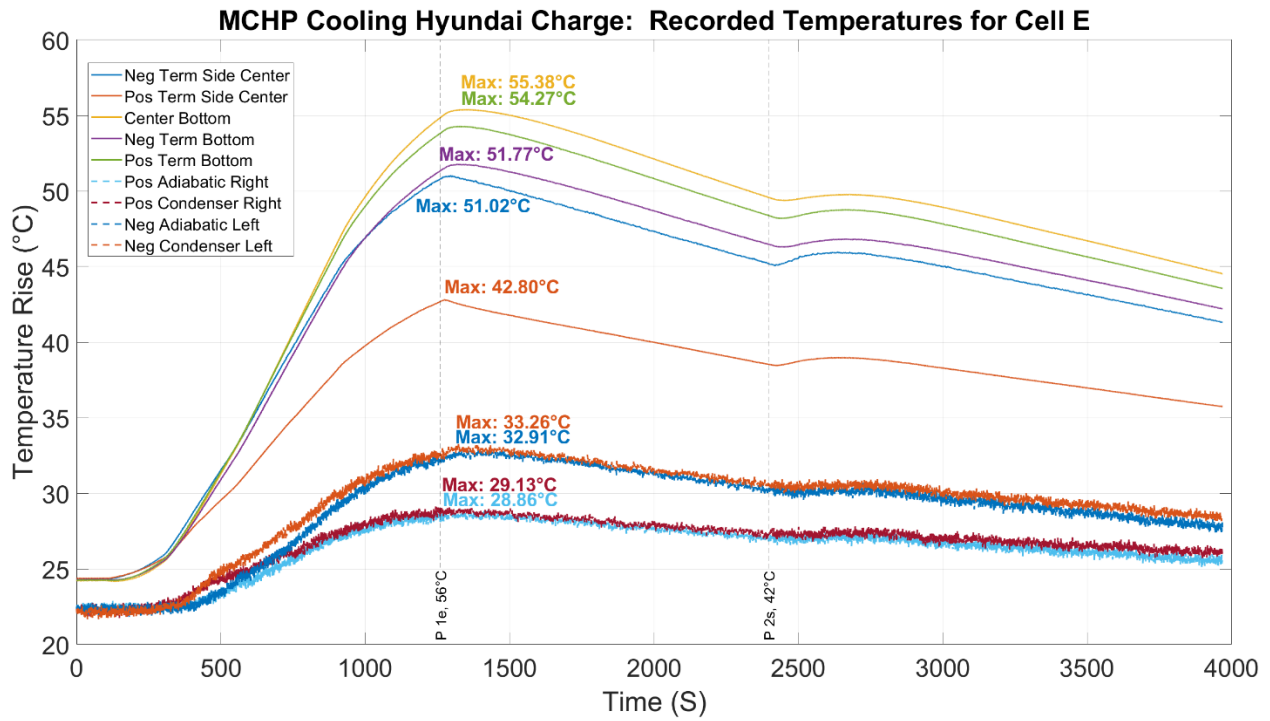


Figure 97 MCHP Cooling, Hyundai Ioniq fast charging cell E temperature response.

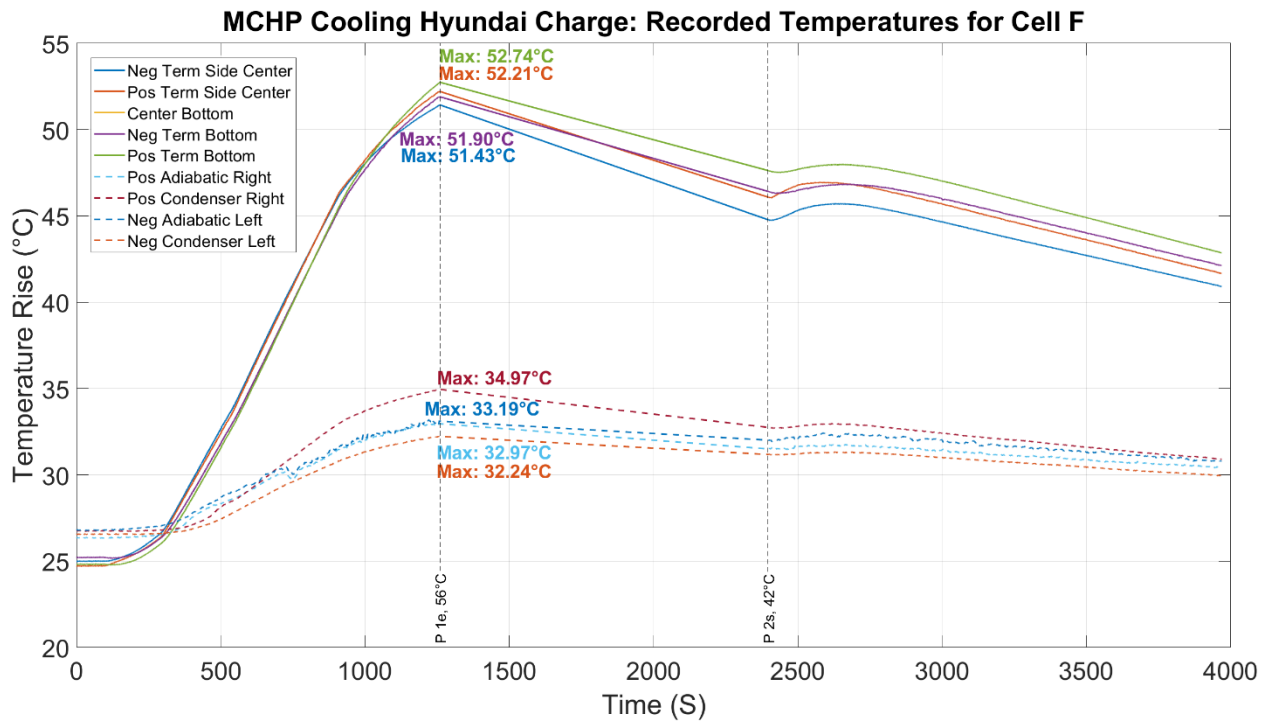


Figure 98 MCHP Cooling, Hyundai Ioniq fast charging cell F temperature response.

6.3.2 Pulse

The 10-second, 400A Pulse fast charging profile was completed in three parts, with interruptions caused first by the busbar reaching 65°C and subsequently by cells reaching the 55°C cut-off temperature. The voltage response curve, shown in Figure 99, highlights each phase of the test and the associated rest periods. During the first part, the cells were charged with 65.2Ah over 19.5 minutes, achieving approximately 57% SoC and completing 53% of the full charging profile. Following this phase, a 14.5 minutes rest period allowed the busbars to cool to 43°C and the cells to drop below 50°C.

The second charging phase lasted 8.3 minutes, delivering an additional 25.1Ah before the temperature threshold was again reached. A subsequent 16.3-minute cooling period reduced the cell temperatures to below 50°C. The third and final phase completed the charging profile, with the total test taking 67.6 minutes to deliver 106.7Ah, reaching 94% SoC. Throughout the process, the module voltage increased from 18.56V to 25.29V (3.1V to 4.2V per cell), reflecting the expected progression of cell charging.

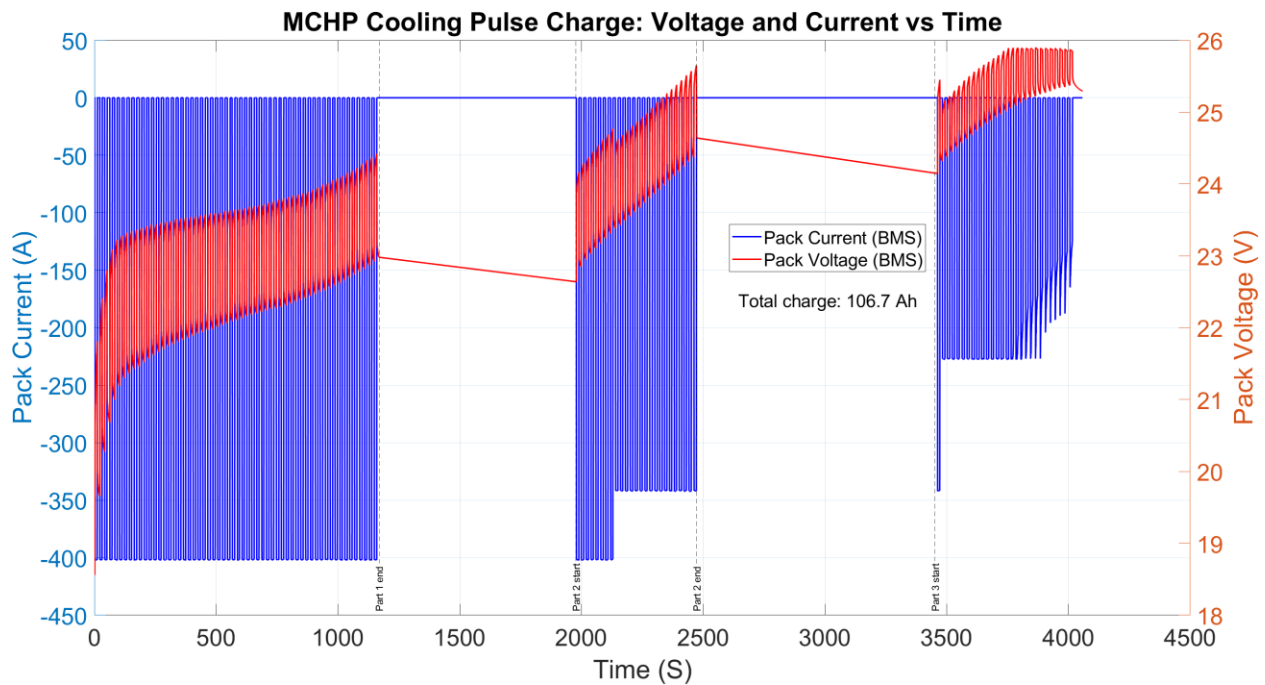


Figure 99 MCHP Cooling, Pulse fast charging Voltage response curve.

The cell temperature readings are shown in Figure 100 to Figure 105, with the maximum temperature reaching 55.23°C at the center bottom of cell C shortly after the second test stoppage. All cells reached their peak temperatures around the same time, following a consistent trend where the center bottom thermocouple recorded the highest values, except for cell D, where the upper positive side exhibited a slightly higher temperature. The effect of side-to-side cell heating was less prominent, although thermocouples near the positive terminals consistently detected higher temperatures than those near the negative terminals. Cells C and D showed more pronounced temperature elevations due to front and back cell-to-cell heating effects. Additionally, side readings near the positive terminal on cells B, C, and D exhibited rapid temperature fluctuations during current application. Cell F displayed an unusual behavior, with its temperature stabilizing after reaching a maximum at the end of the first part of the test, likely indicating a reading error from the AVL cyler. Overall, temperature readings exhibited good uniformity, ranging from 1.07°C to

5.92°C, with only cell B exceeding the 5°C threshold.

The thermal behavior of the MCHPs mirrored the cell temperature patterns, indicating proper functionality. After the first test stoppage, the MCHP temperature readings for cells B, D, and E appeared to stabilize, reinforcing the likelihood of an AVL cycler data recording error. Effective cooling was observed when the adiabatic and condenser temperature readings were closely aligned, as this reflects minimal heat transfer and efficient phase change within the MCHPs. The cooling performance was significantly influenced by the quality of surface contact between the vaporization region of the MCHP and the cell sides, as well as the contact between the condensation region and the cold plate.

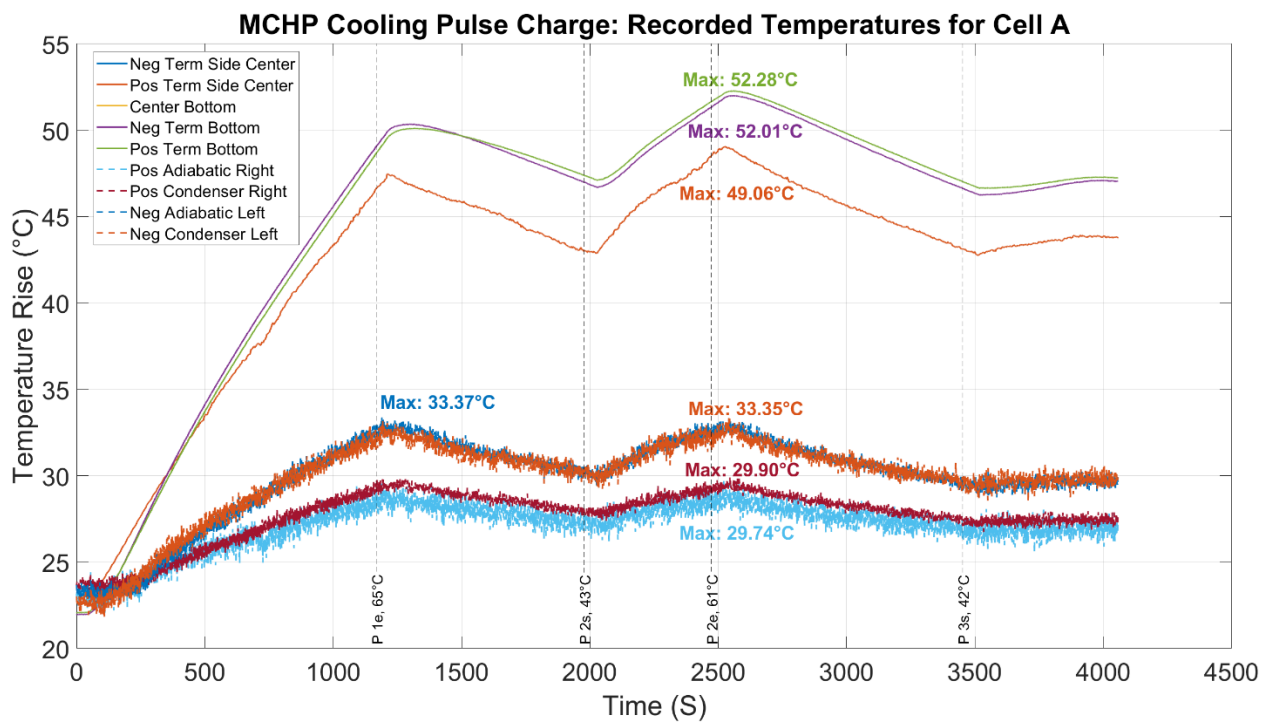


Figure 100 MCHP Cooling, Pulse fast charging cell A temperature response.

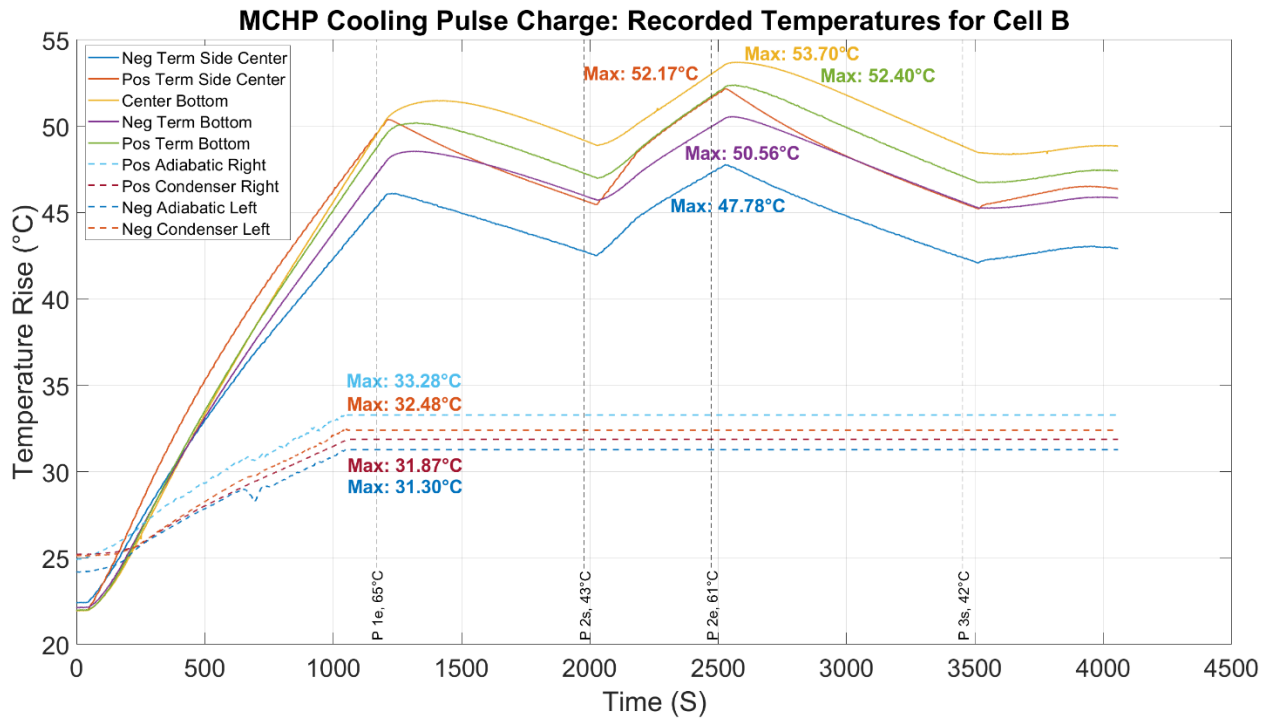


Figure 101 MCHP Cooling, Pulse fast charging cell B temperature response.

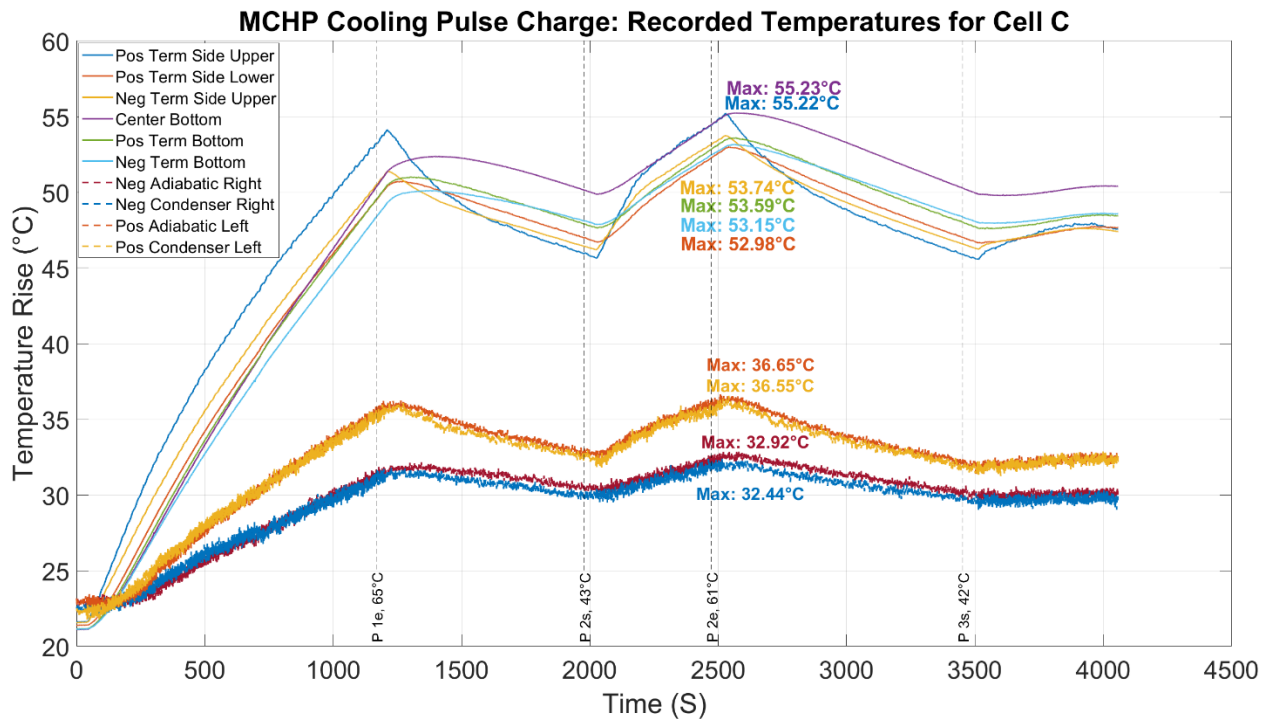


Figure 102 MCHP Cooling, Pulse fast charging cell C temperature response.

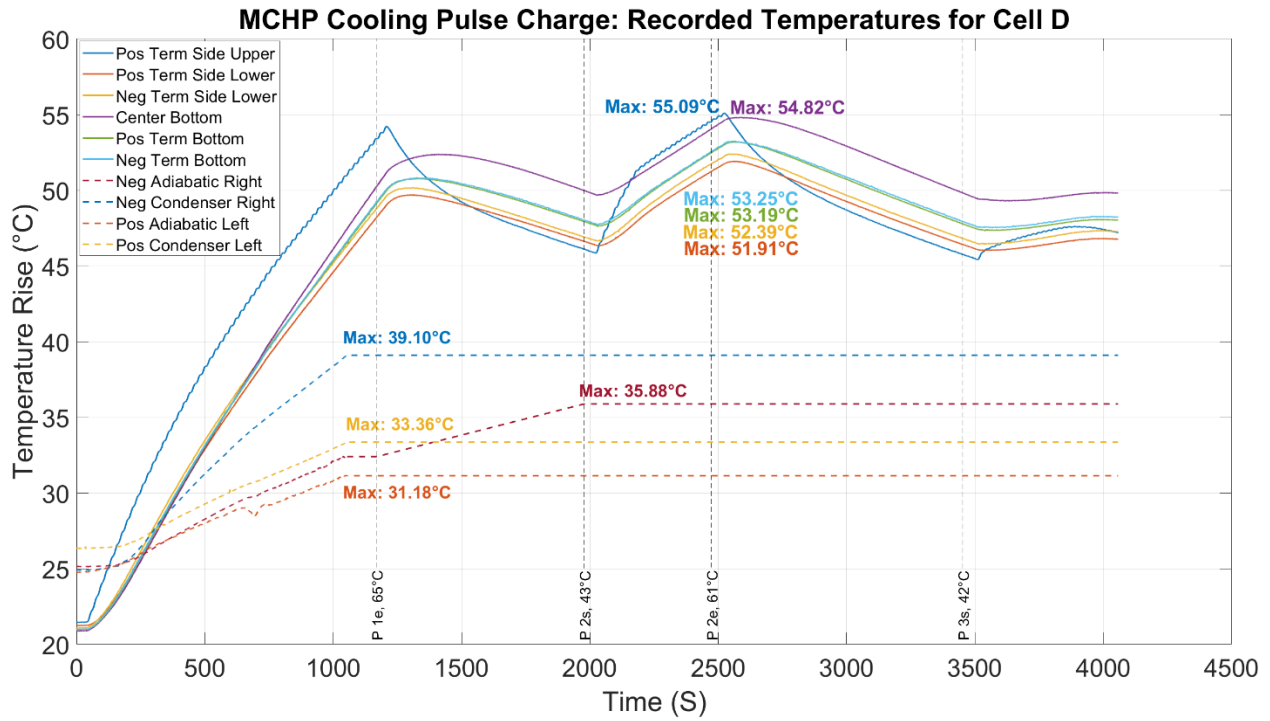


Figure 103 MCHP Cooling, Pulse fast charging cell D temperature response.

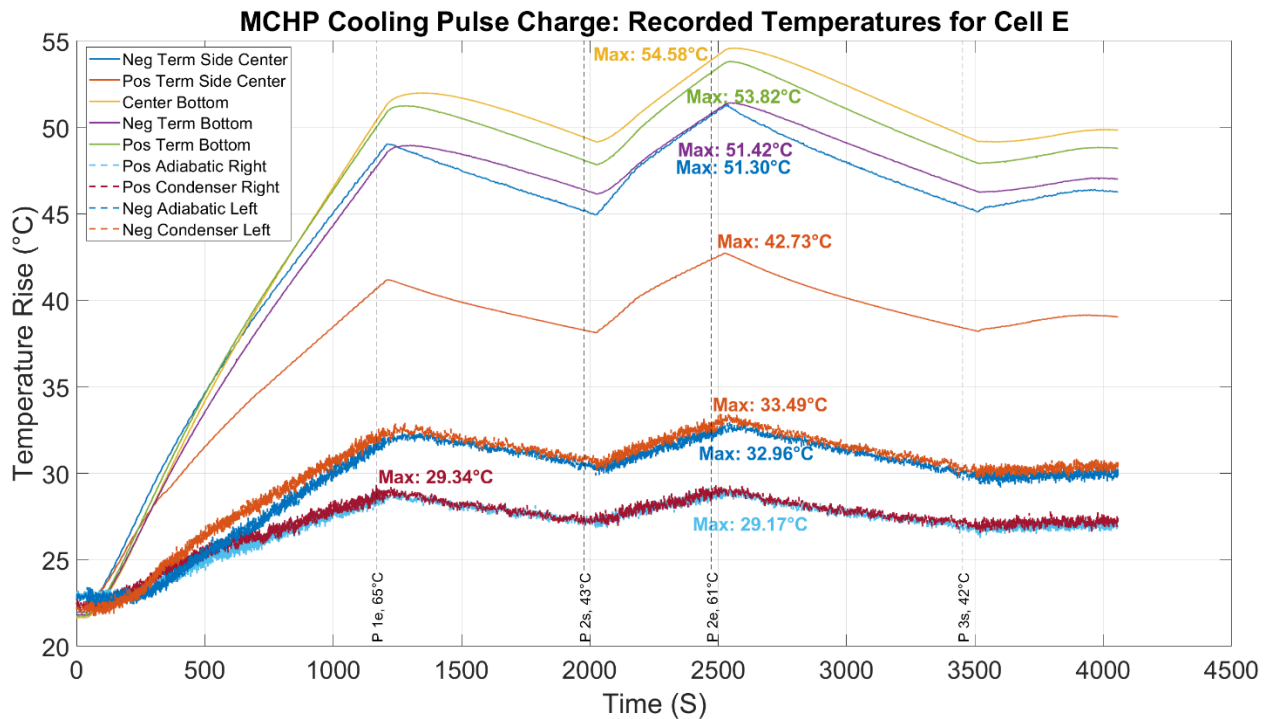


Figure 104 MCHP Cooling, Pulse fast charging cell E temperature response.

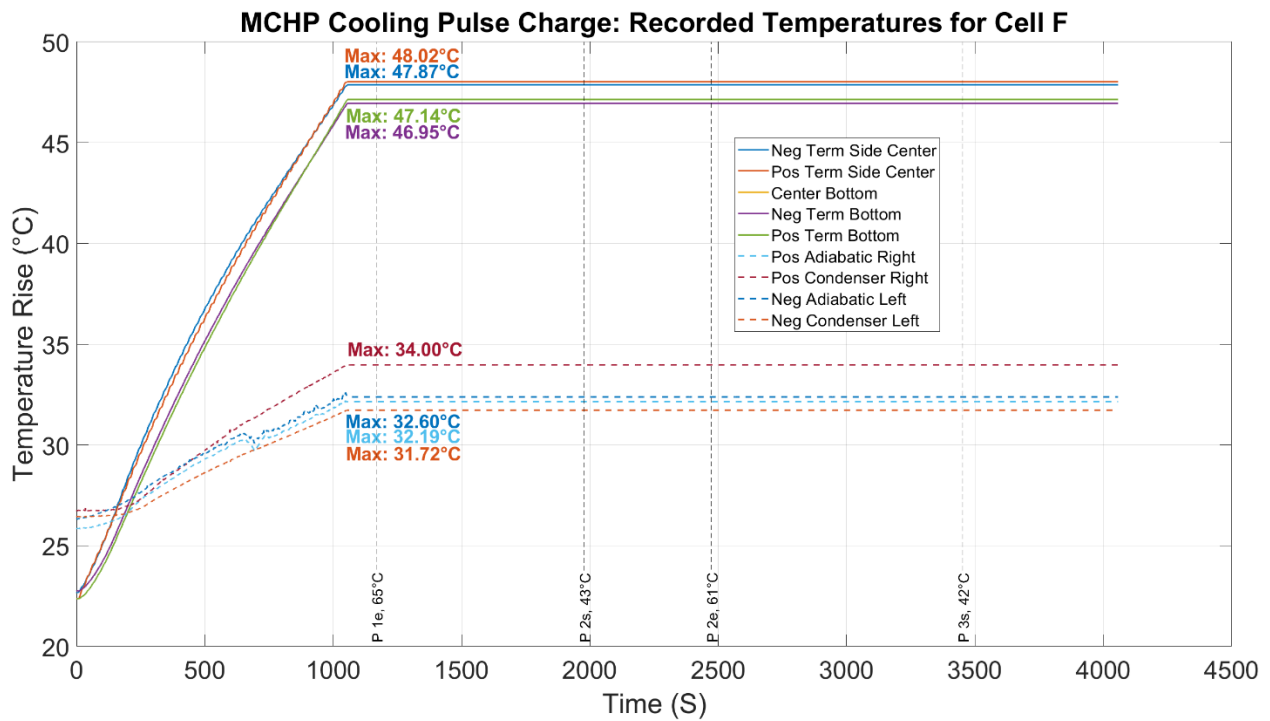


Figure 105 MCHP Cooling, Pulse fast charging cell F temperature response.

6.4 Cooling Methods Comparison Analysis

To provide a fair comparison among the three setups, the influence of busbar temperature bias must be minimized. This allows the setups to be evaluated under equivalent conditions, using the runtime of the first part of the Bottom Cooling setup as the baseline. The mutual thermocouple locations across the setups are then compared to ensure consistency. Figure 106 illustrates the thermocouple placements for cells C and D, which serve as the basis for this comparison. Thermocouples at other locations were excluded due to a lack of mutuality or missing data in one or more setups.

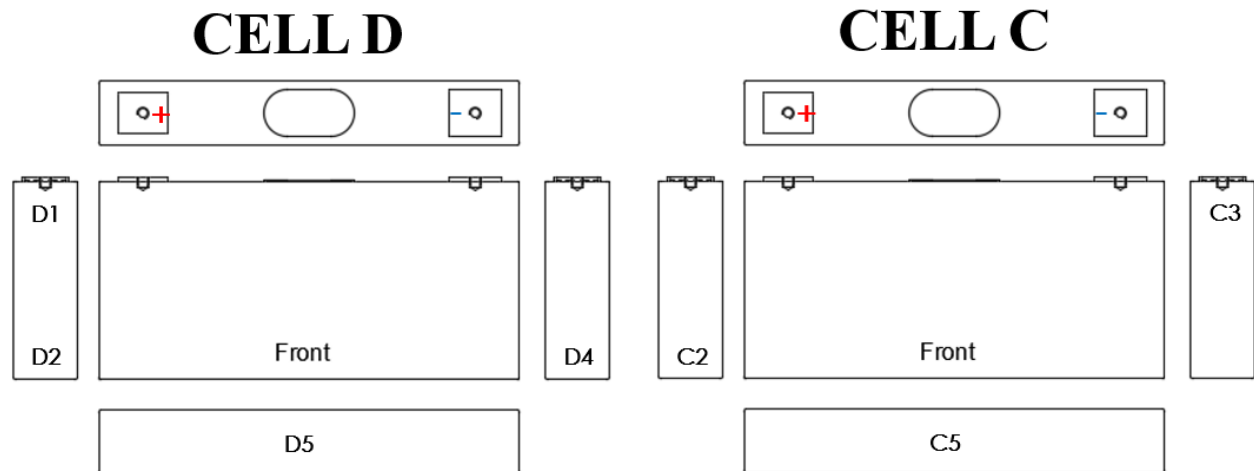


Figure 106 Cells C and D mutual thermocouple locations across the three testing setups.

6.4.1 Hyundai Fast charging

In the Hyundai fast charging test, Cells C and D exhibited consistent cooling performance trends across the methods of No Cooling, Bottom Cooling, and MCHP Cooling. Figure 107 to Figure 110 illustrate the temperature profiles for both cells during the Hyundai test, highlighting maximum temperatures and the relative effectiveness of each method compared to the no-cooling baseline.

Effectiveness is calculated using Equation (6.1) as the percentage reduction in temperature relative to the No Cooling scenario and provides a quantitative measure of how well each cooling method mitigates thermal rise.

$$Effectiveness = \frac{T_{No\ Cooling} - T_{Cooling\ Method}}{T_{No\ Cooling}} \times 100 \quad (6.1)$$

Table 7 Hyundai Fast Charging Effectiveness Values based on the last 300 S of testing.

	Bottom Cooling	MCHP Cooling

	Effectiveness (%)	Effectiveness (%)
C5 (Bottom-Centered)	20.05	7.00
D5 (Bottom-Centered)	21.02	7.66
D4 (Negative Terminal Lower)	9.82	9.50
C2 (Positive Terminal Lower)	11.82	8.80
D2 (Positive Terminal Lower)	12.39	9.67
C3 (Negative Terminal Upper)	-2.75	9.05
D1 (Positive Terminal Upper)	-2.47	1.14

Table 7 presents the average effectiveness values of both cooling methods, calculated from the last 300 seconds of testing. This approach eliminates initial thermocouple reading biases caused by sensor variability, accuracy limitations, and the time required for cells to fully reach the ambient temperature. As the test progresses and cells begin to heat up, these variations diminish, ensuring a more accurate representation of cooling performance.

At bottom-centered positions, Bottom Cooling demonstrated the highest effectiveness, achieving 20.05% for cell C and 21.02% for cell D, underscoring its strength in providing localized thermal management near the cooling plate. However, this effectiveness diminished at distant thermocouples. For example, at the upper side positions next to the negative terminal for cell C (C3) and the positive terminal for cell D (D1), Bottom Cooling yielded negative effectiveness values of -2.75% and -2.47%, indicating slight temperature increases compared to No Cooling.

Intermediate positions revealed mixed performance for Bottom Cooling. At the lower side positions near the positive terminal for cell C (C2) and cell D (D2), effectiveness values of 11.82% and 12.39% were recorded, reflecting moderate heat dissipation capabilities. Similarly, at the lower

side position next to the negative terminal for cell D (D4), Bottom Cooling achieved an average effectiveness of 9.82%, showing localized improvements but limited impact away from the cold plate.

MCHP Cooling, by contrast, delivered more consistent results across all positions. At bottom-centered locations (C5 and D5), it achieved effectiveness values of 7.00% and 7.66%, slightly lower than Bottom Cooling but indicative of uniform cooling performance. At distant positions such as C3 (Negative Terminal Side Upper) and D1 (Positive Terminal Side Upper), MCHP Cooling significantly outperformed Bottom Cooling, achieving effectiveness values of 9.05% and 1.14%, respectively. However, D1 is relatively low considered to the rest likely due to insufficient contact pressure between the MCHP and the cell. For intermediate positions (C2, D2, and D4), effectiveness ranged from 8.80% to 9.67%, highlighting MCHP Cooling's reliable and distributed heat management capabilities.

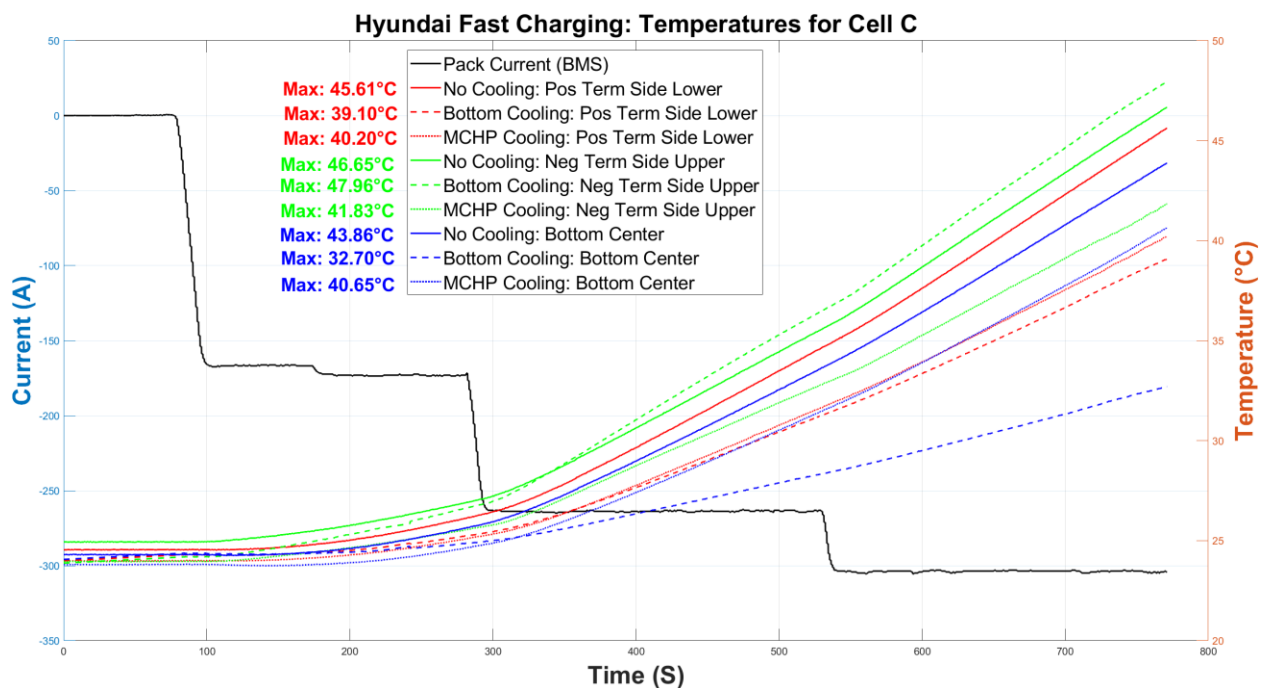


Figure 107 Mutal thermocouples, Hyundai fast charging cell C temperature response.

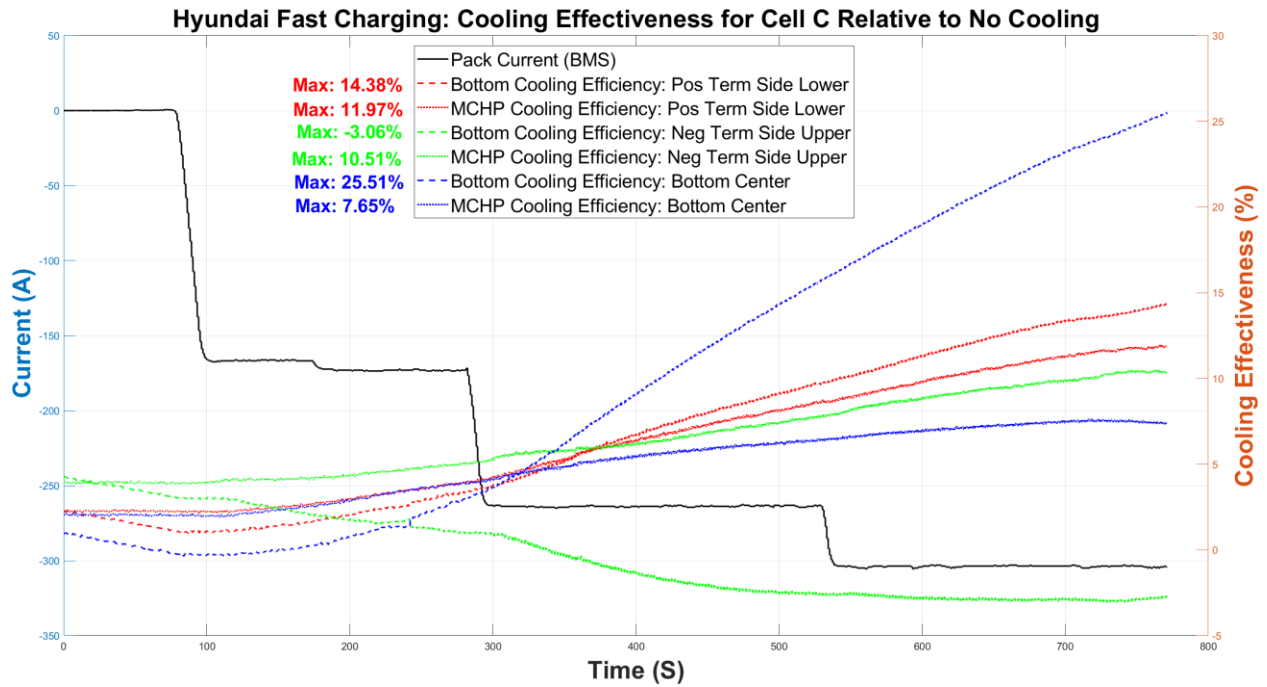


Figure 108 Mutal thermocouples, Hyundai fast charging test: Bottom and MCHP cooling cell C effectiveness relative to No Cooling.

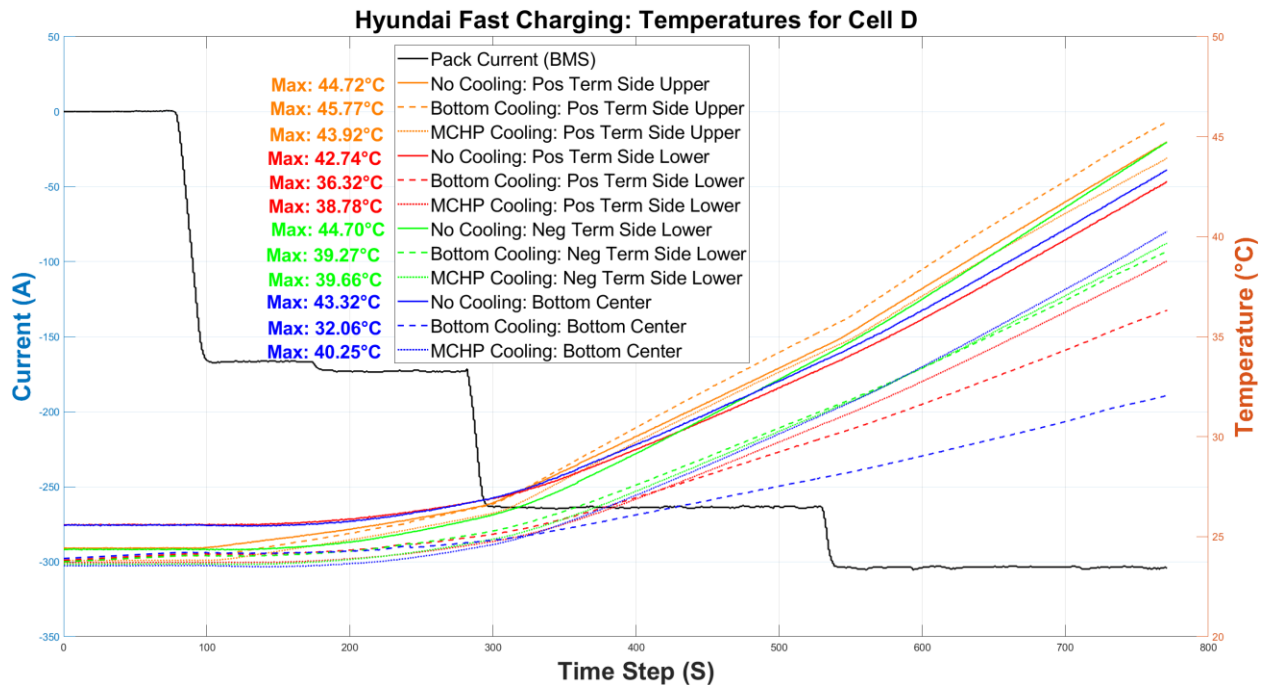


Figure 109 Mutal thermocouples, Hyundai fast charging cell D temperature response.

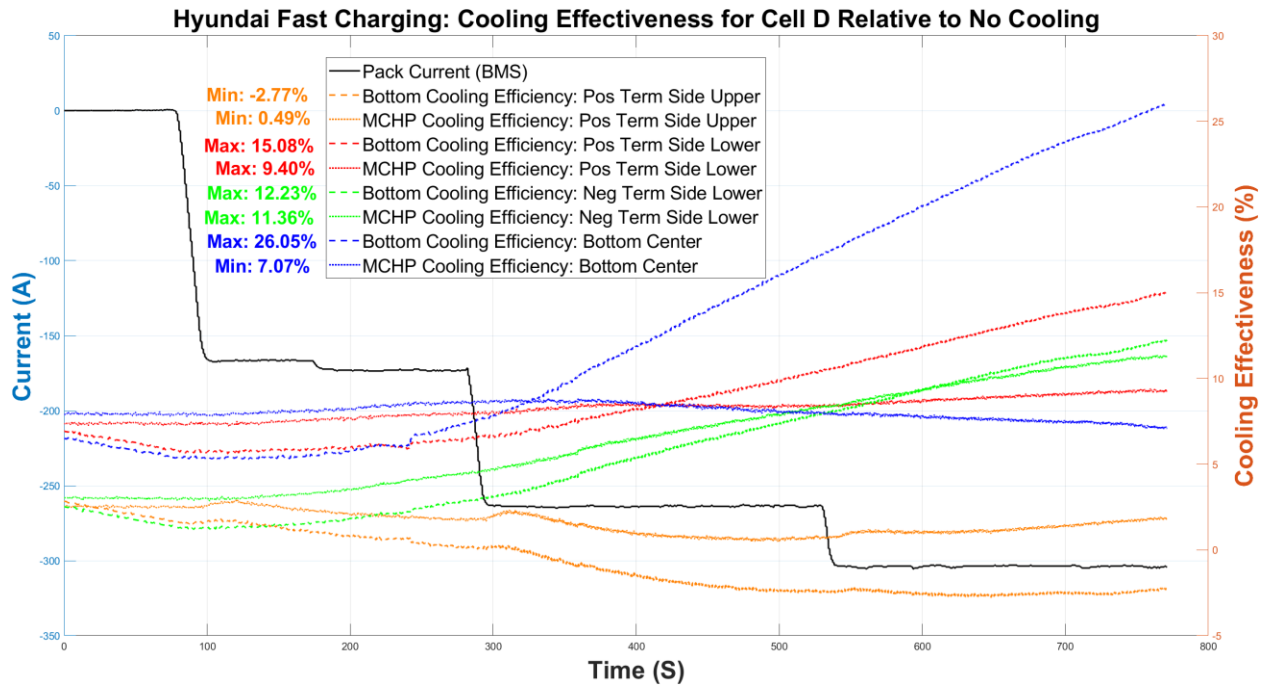


Figure 110 Mutal thermocouples, Hyundai fast charging test: Bottom and MCHP cooling cell D effectiveness relative to No Cooling.

6.4.2 Pulse

In the Pulse fast charging test, cooling effectiveness improved for both methods compared to the Hyundai test, particularly for MCHP Cooling. Figure 111 to Figure 114 present the temperature profiles and relative effectiveness for this test. Table 8 presents the average effectiveness values of both cooling methods, calculated from the last 300 seconds of testing. At bottom-centered positions (C5 and D5), Bottom Cooling achieved effectiveness values of 17.83% and 19.04%, slightly lower than in the Hyundai test but still demonstrating strong localized performance. However, distant thermocouples like C3 and D1 recorded negative effectiveness values of -3.43% and -1.84%, again reflecting Bottom Cooling's limitations in managing heat away from the cooling plate.

At intermediate positions, Bottom Cooling's performance remained moderate, with

effectiveness values of 11.64% and 12.05% at C2 and D2, and 9.55% at D4. This performance trend aligned with its focus on localized cooling near the cold plate.

MCHP Cooling consistently outperformed Bottom Cooling in terms of the cell's temperature distribution. At bottom-centered positions (C5 and D5), it achieved effectiveness values of 12.44% and 13.58%, maintaining strong localized performance. At distant positions such as C3 and D1, MCHP Cooling delivered higher effectiveness, 13.42% and 4.52%, respectively, demonstrating its capacity for uniform thermal management. The D1 location still had lower effectiveness than the rest due to the contact pressure. For intermediate positions (C2, D2, and D4), effectiveness values ranged from 13.65% to 14.00%, further emphasizing its consistent cooling performance across the entire cell.

A key observation from pulse testing is that as current increased, Bottom Cooling struggled to dissipate the additional heat, reducing its effectiveness. In contrast, MCHP Cooling improved with rising heat generation, leveraging the capillary effect, where a greater temperature gradient (ΔT) between the evaporator and condenser enhanced heat transfer efficiency.

Table 8 Pulse Fast Charging Effectiveness Values based on the last 300 S of testing.

	Bottom Cooling Effectiveness (%)	MCHP Cooling Effectiveness (%)
C5 (Bottom-Centered)	17.83	12.44
D5 (Bottom-Centered)	19.04	13.58
D4 (Negative Terminal Lower)	9.55	13.90
C2 (Positive Terminal Lower)	11.64	13.65
D2 (Positive Terminal Lower)	12.05	14.00
C3 (Negative Terminal Upper)	-3.43	13.42

D1 (Positive Terminal Upper)	-1.84	4.52
-------------------------------------	-------	------

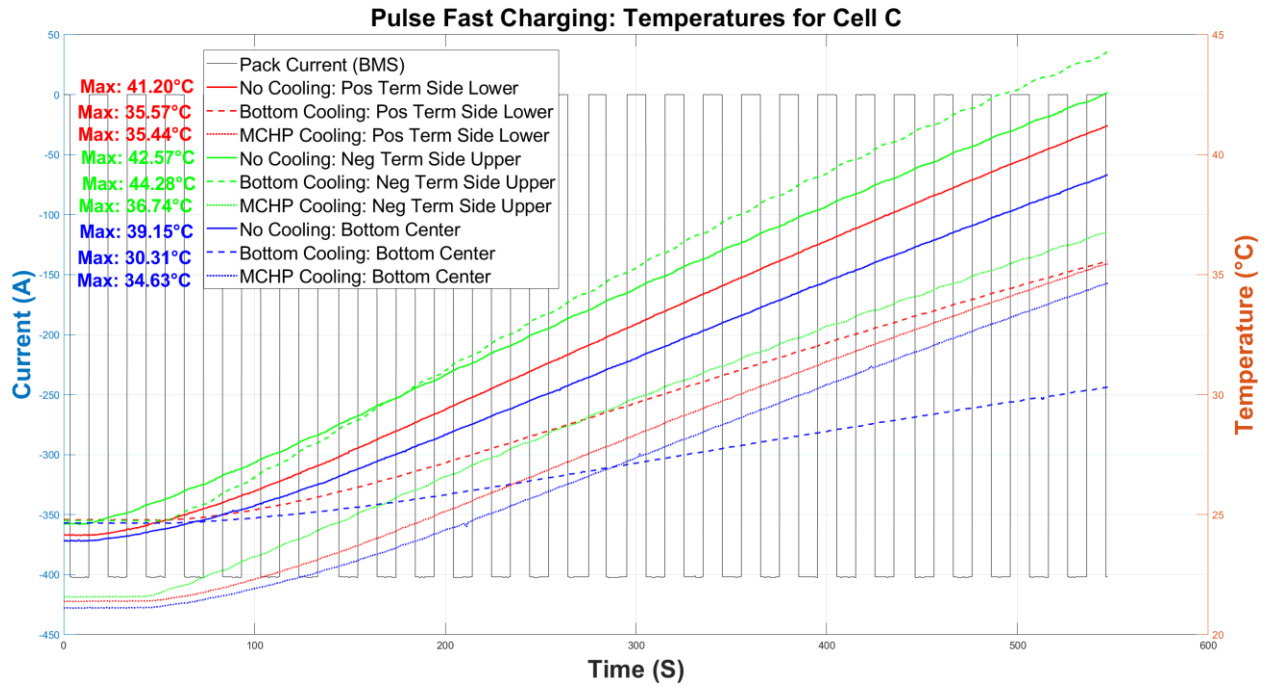


Figure 111 Mutal thermocouples, Pulse fast charging cell C temperature response.

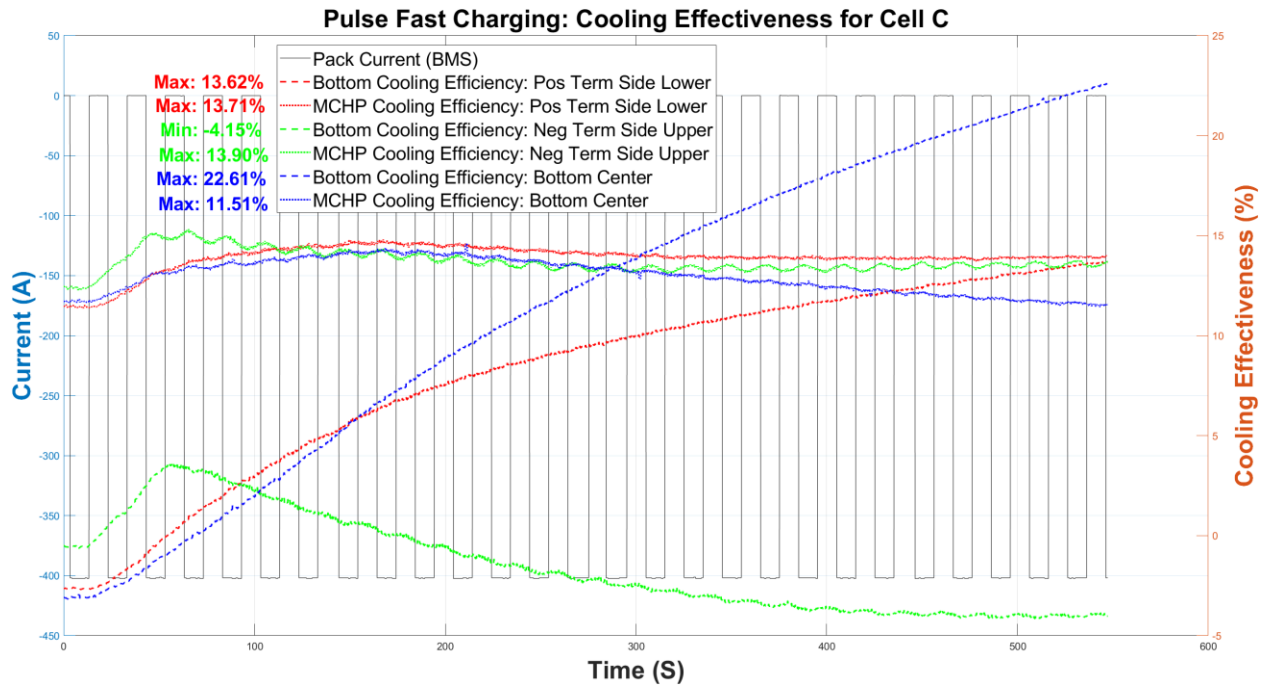


Figure 112 Mutal thermocouples, Pulse fast charging test: Bottom and MCHP cooling cell C effectiveness relative to No Cooling.

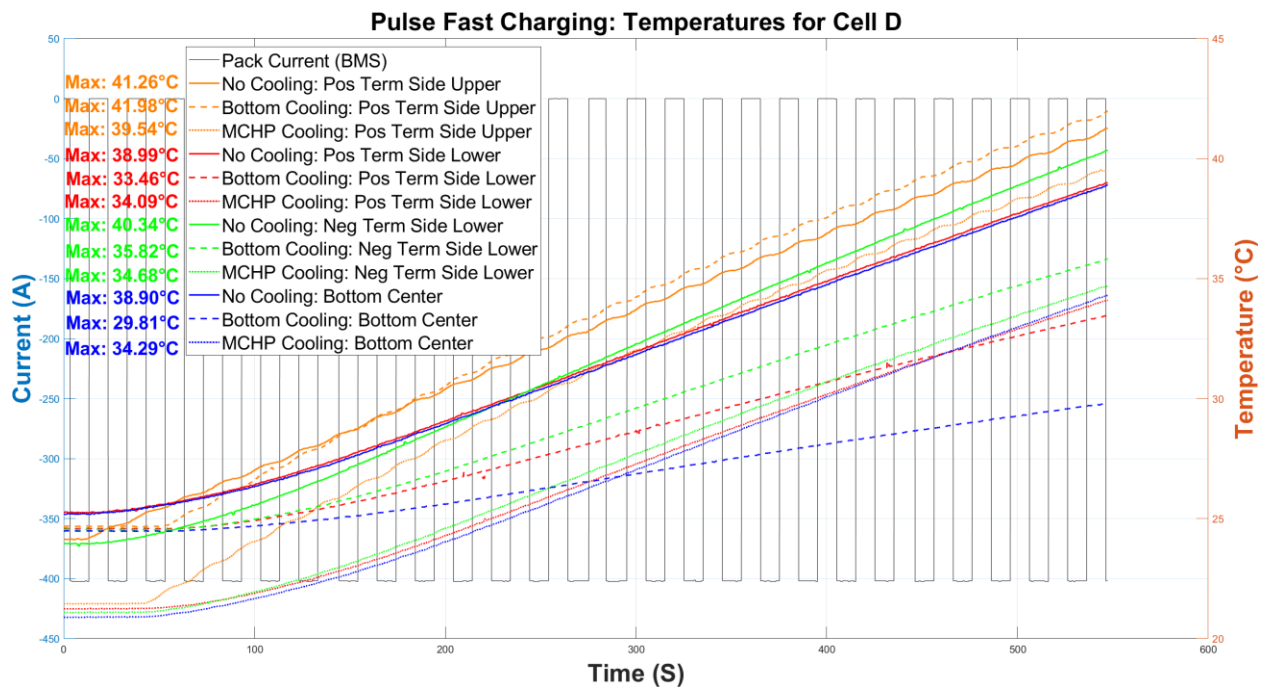


Figure 113 Mutal thermocouples, Pulse fast charging cell D temperature response.

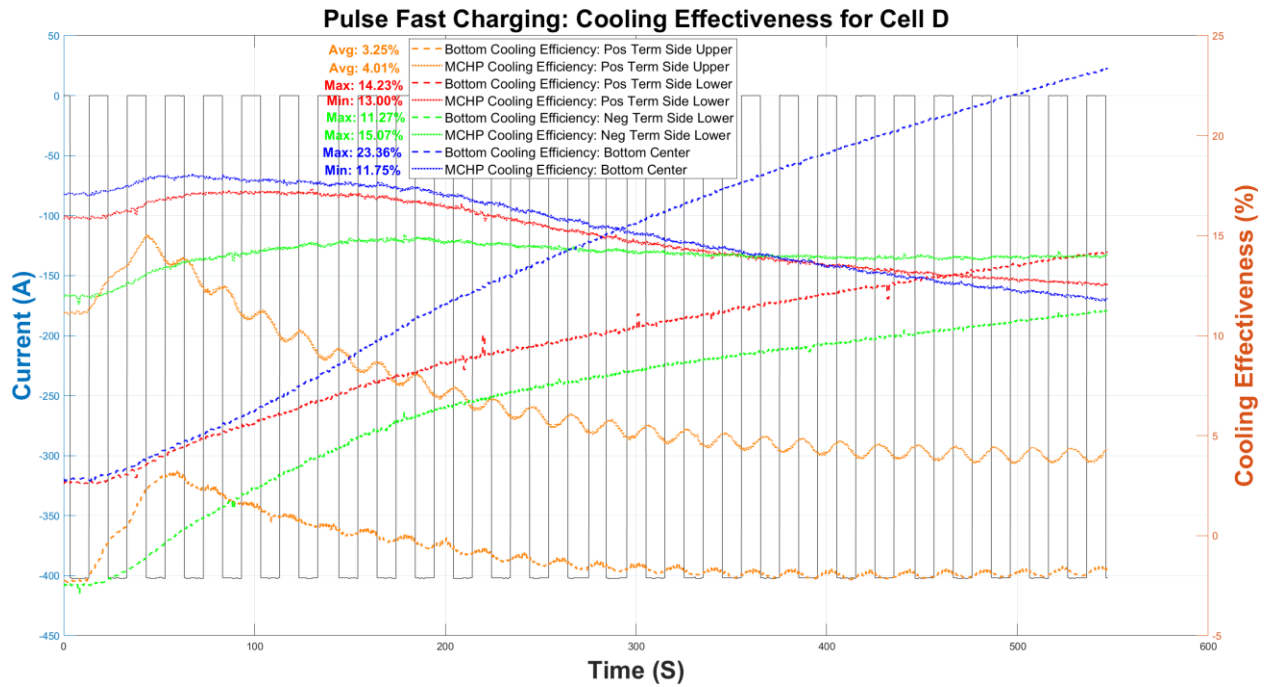


Figure 114 Mutal thermocouples, Pulse fast charging test: Bottom and MCHP cooling cell D effectiveness relative to No Cooling.

Chapter 7

Future Work

To address the design challenges faced with using three separate prototypes for each cooling configuration, a modular battery testing platform was developed. This improved design features a fixed body with interchangeable top and bottom attachments, allowing seamless transitions between four distinct testing modes: No Cooling, Bottom Cooling, MCHP Cooling, and a Combined Bottom and MCHP Cooling setup. This modular approach eliminates inconsistencies by keeping thermocouple placements, cell positioning, and the gap above the cells identical across all setups, ensuring consistent and reliable comparison of the cooling strategies. The finalized modular design is shown in Figure 115 and Figure 116. The top and bottom plates are secured to the fixed body using twelve 3/8"-16 fasteners and square nuts, allowing for precise torque settings based on the required pressures between the Cold plate, MCHP, and the bottom of the cells. The top and bottom plates are bonded to the cold plates with JB Weld Epoxy Adhesive (3900 PSI), similar to the second setup testing the bottom cooling.

On the data acquisition front, the system has been upgraded with three NI 9213 and one NI 9214 modules, capturing temperature data from all thermocouples with improved precision. The cold plate inlet and outlet are monitored using Type T thermocouples with better accuracy than the J-Type thermocouples used previously.

The Hyundai Ioniq fast charging profile and the 400A 10-second pulse fast charging profile were not designed for these cells. To optimize performance, a fast-charging profile tailored to the CALB NMC 811 cells and the MCHP cooling system can be developed to maximize charging

efficiency while preventing thermal runaway in both the cells and busbars. Given that the MCHP performs better under high heat loads, an alternative approach could involve sustaining a continuous current above 400A and dynamically reducing it once the cells reach a critical temperature threshold.

The hybrid cooling setup combining Bottom Cooling and MCHP Cooling presents an opportunity for optimized thermal management. Although the design suggests improved performance, it requires extensive experimental validation. Future studies should investigate how effectively heat is distributed, assess the system's overall thermal resistance, and determine how the coolant flow rate balance impacts performance. Proper management of the cold plate and MCHP flow paths is critical to prevent thermal interference and ensure efficient cooling.



Figure 115 New testing setup with the MCHP Top attachment to be bonded to the cold plate.

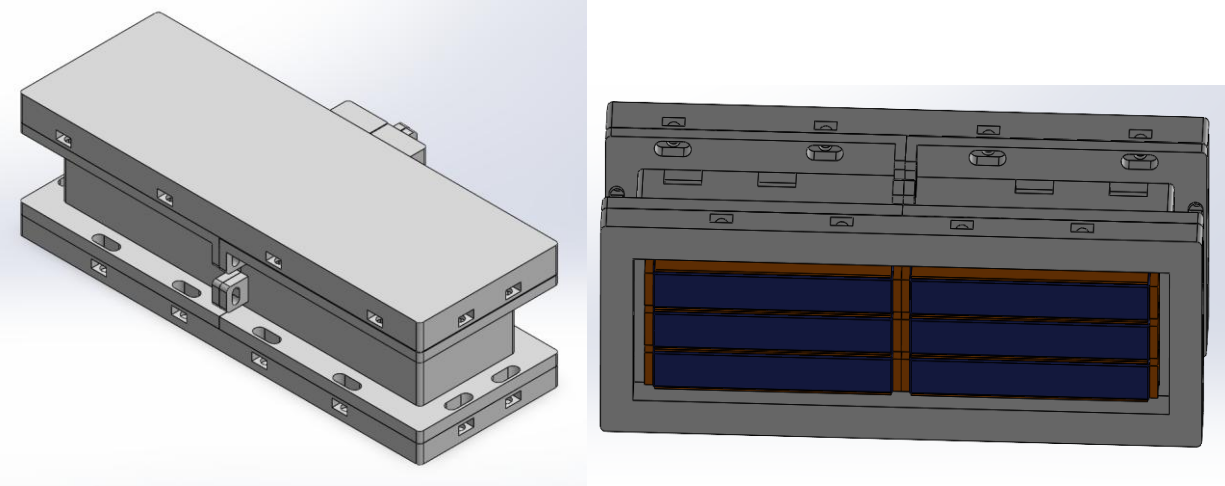


Figure 116 New testing setup with the Bottom Cooling attachment to be bonded to the cold plate.

Chapter 8

Conclusion

Effective cooling is essential for achieving fast charging. The Bottom Cooling solution demonstrated the lowest cell temperatures, excelling in localized heat management at bottom-centered positions like C5 and D5, where effectiveness values reached 21.02% and 19.04%, respectively. However, this method exhibited significant limitations, including poor temperature uniformity, with distant thermocouples often showing negative effectiveness values. Such uneven cooling is both operationally unacceptable and potentially hazardous, deeming the solution unsuitable for practical applications. Adjusting flow rates and coolant temperatures might enhance performance, but the inherent issues with temperature distribution remain a concern.

In contrast, the MCHP cooling solution provided more consistent and distributed cooling across the cells. It achieved effectiveness values of 13.42% at C3 and 4.52% at D1 during the Pulse test, and it reduced thermal gradients, with average temperature differences of 1.20°C and 1.43°C for the Hyundai and Pulse tests, respectively. This uniformity enhances cell stability and safety, making MCHP cooling a more promising approach. However, the MCHP solution did not sufficiently cool the cells to complete tests without interruptions, primarily due to inadequate contact pressure between the MCHPs, cells, and the cold plate. Optimizing contact mechanics and exploring different coolant flow rates and temperatures are necessary for further validation and performance improvement.

Busbar temperatures posed challenges across all setups, often interrupting the tests. The MCHP module's larger empty spaces and substantial terminal openings likely enhanced natural

busbar cooling, while the No Cooling setup provided moderate cooling space. In contrast, the Bottom Cooling setup, with its tightly constrained spaces and limited openings, restricted air circulation, reducing natural convection and leading to elevated busbar temperatures. Nevertheless, the impact on cell temperatures was likely minimal, as a thick thermal shield above the cells confined heat within the cell environment. Addressing these design oversights is essential to improve testing reliability and ensure consistent cooling performance.

Finally, a new modular testing platform was introduced to address the challenges of earlier prototypes, providing a consistent and repeatable framework for evaluating cooling strategies in future testing.

References

- [1] “Canada’s Zero-Emission Vehicle Sales Targets,” Dec. 2024, *Transport Canada*.
[Online]. Available: <https://tc.canada.ca/en/road-transportation/innovative-technologies/zero-emission-vehicles/canada-s-zero-emission-vehicle-sales-targets>
- [2] M. Khan, “Innovations in Battery Technology: Enabling the Revolution in Electric Vehicles and Energy Storage,” *British Journal of Multidisciplinary and Advanced Studies*, vol. 5, no. 1, pp. 23–41, Feb. 2024, doi: 10.37745/BJMAS.2022.0414.
- [3] S. Kim *et al.*, “Projecting Recent Advancements in Battery Technology to Next-Generation Electric Vehicles,” *Energy Technology*, vol. 10, no. 8, p. 2200303, Aug. 2022, doi: 10.1002/ENTE.202200303.
- [4] A. Verma, S. Shashidhara, and D. Rakshit, “A comparative study on battery thermal management using phase change material (PCM),” *Thermal Science and Engineering Progress*, vol. 11, pp. 74–83, Jun. 2019, doi: 10.1016/j.tsep.2019.03.003.
- [5] B. Chidambaranathan *et al.*, “Thermal management system in electric vehicle batteries for environmental sustainability,” *Environmental Quality Management*, vol. 33, no. 2, pp. 159–167, Dec. 2023, doi: 10.1002/TQEM.22001.
- [6] D. Worwood *et al.*, “Experimental Analysis of a Novel Cooling Material for Large Format Automotive Lithium-Ion Cells,” *Energies 2019, Vol. 12, Page 1251*, vol. 12, no. 7, p. 1251, Apr. 2019, doi: 10.3390/EN12071251.
- [7] K. P. Birke, “Modern Battery Engineering,” *Modern Battery Engineering*, Apr. 2019, doi: 10.1142/11039.

- [8] C. A. Vincent, "Primary lithium cells," *Modern Batteries*, pp. 106–141, Jan. 1997, doi: 10.1016/B978-034066278-6/50005-X.
- [9] J. Libich, J. Máca, J. Vondrák, O. Čech, and M. Sedlaříková, "Supercapacitors: Properties and applications," *J Energy Storage*, vol. 17, pp. 224–227, Jun. 2018, doi: 10.1016/j.est.2018.03.012.
- [10] A. Riaz, M. R. Sarker, M. H. M. Saad, and R. Mohamed, "Review on Comparison of Different Energy Storage Technologies Used in Micro-Energy Harvesting, WSNs, Low-Cost Microelectronic Devices: Challenges and Recommendations," *Sensors*, vol. 21, no. 15, p. 5041, Jul. 2021, doi: 10.3390/s21155041.
- [11] A. González, E. Goikolea, J. A. Barrena, and R. Mysyk, "Review on supercapacitors: Technologies and materials," *Renewable and Sustainable Energy Reviews*, vol. 58, pp. 1189–1206, May 2016, doi: 10.1016/j.rser.2015.12.249.
- [12] S. Chaudhary, M. Raja, and O. P. Sinha, "A review on the different types of electrode materials for aqueous supercapacitor applications," *Advances in Natural Sciences: Nanoscience and Nanotechnology*, vol. 12, no. 1, p. 015011, Mar. 2021, doi: 10.1088/2043-6262/abe93e.
- [13] C. Dépature, A. Macías, A. Jácome, L. Boulon, J. Solano, and J. P. Trovão, "Fuel cell/supercapacitor passive configuration sizing approach for vehicular applications," *Int J Hydrogen Energy*, vol. 45, no. 50, pp. 26501–26512, Oct. 2020, doi: 10.1016/j.ijhydene.2020.05.040.
- [14] Y. Li, Q. Wu, T. Mo, F. Chen, Y. Luo, and C. Shan, "Techno-economic analysis of a hydrogen fuel cell hybrid system and corresponding optimum matching design for

- hydrogen fuel cell forklifts,” *HKIE Transactions*, vol. 30, no. 4, pp. 33–42, Dec. 2023, doi: 10.33430/V30N4THIE-2023-0020.
- [15] X. Luo, J. Wang, M. Dooner, and J. Clarke, “Overview of current development in electrical energy storage technologies and the application potential in power system operation,” *Appl Energy*, vol. 137, pp. 511–536, Jan. 2015, doi: 10.1016/j.apenergy.2014.09.081.
- [16] G. E. Blomgren, “The Development and Future of Lithium Ion Batteries,” *J Electrochem Soc*, vol. 164, no. 1, pp. A5019–A5025, Dec. 2017, doi: 10.1149/2.0251701jes.
- [17] J. B. Quinn, T. Waldmann, K. Richter, M. Kasper, and M. Wohlfahrt-Mehrens, “Energy Density of Cylindrical Li-Ion Cells: A Comparison of Commercial 18650 to the 21700 Cells,” *J Electrochem Soc*, vol. 165, no. 14, pp. A3284–A3291, Oct. 2018, doi: 10.1149/2.0281814jes.
- [18] O. E. Bankole, C. Gong, and L. Lei, “Battery Recycling Technologies: Recycling Waste Lithium Ion Batteries with the Impact on the Environment In-View,” *Journal of Environment and Ecology*, vol. 4, no. 1, p. 14, Jun. 2013, doi: 10.5296/jee.v4i1.3257.
- [19] I. Landa-Medrano *et al.*, “Insights into the Electrochemical Performance of 1.8 Ah Pouch and 18650 Cylindrical NMC:LFP|Si:C Blend Li-ion Cells,” *Batteries*, vol. 8, no. 8, p. 97, Aug. 2022, doi: 10.3390/BATTERIES8080097/S1.
- [20] B. C. Springer, M. Frankenberger, and K. H. Pettinger, “Lamination of Separators to Electrodes using Electrospinning,” *PLoS One*, vol. 15, no. 1, Jan. 2020, doi: 10.1371/JOURNAL.PONE.0227903.
- [21] S. Shahid and M. Agelin-Chaab, “Comparison of PCM Mediums for Hybrid Thermal Management of Electric Battery Packs”, doi: 10.11159/ffhmt23.165.

- [22] M. Rabiei, A. Gharehghani, S. Saeedipour, A. M. Andwari, and J. Könnö, “Proposing a Hybrid BTMS Using a Novel Structure of a Microchannel Cold Plate and PCM,” *Energies* 2023, Vol. 16, Page 6238, vol. 16, no. 17, p. 6238, Aug. 2023, doi: 10.3390/EN16176238.
- [23] N. Soldan Cattani, E. Noronha, J. Schmied, M. Frieges, H. Heimes, and A. Kampker, “Comparative Cost Modeling of Battery Cell Formats and Chemistries on a Large Production Scale,” *Batteries* 2024, Vol. 10, Page 252, vol. 10, no. 7, p. 252, Jul. 2024, doi: 10.3390/BATTERIES10070252.
- [24] R. E. Ciez and J. F. Whitacre, “Comparison between cylindrical and prismatic lithium-ion cell costs using a process based cost model,” *J Power Sources*, vol. 340, pp. 273–281, Feb. 2017, doi: 10.1016/J.JPOWSOUR.2016.11.054.
- [25] M. Winter and R. J. Brodd, “What are batteries, fuel cells, and supercapacitors?,” *Chem Rev*, vol. 104, no. 10, pp. 4245–4269, Oct. 2004, doi: 10.1021/CR020730K/ASSET/IMAGES/MEDIUM/CR020730KF00030.GIF.
- [26] G. Lee, “Electro-Thermal Analysis of a Pouch-Type Lithium-Ion Battery with a High Discharge Rate for Urban Air Mobility,” *Batteries* 2023, Vol. 9, Page 476, vol. 9, no. 9, p. 476, Sep. 2023, doi: 10.3390/BATTERIES9090476.
- [27] Y. Liu *et al.*, “A Biomass-Based Integral Approach Enables Li-S Full Pouch Cells with Exceptional Power Density and Energy Density,” *Advanced Science*, vol. 8, no. 14, p. 2101182, Jul. 2021, doi: 10.1002/ADVS.202101182.
- [28] O. Salihoglu and R. Demir-Cakan, “Factors Affecting the Proper Functioning of a 3Ah Li-S Pouch Cell,” *J Electrochem Soc*, vol. 164, no. 13, pp. A2948–A2955, Sep. 2017, doi: 10.1149/2.0271713JES/XML.

- [29] B. Li, “Unlocking Failure Mechanisms and Improvement of Practical Li-S Pouch Cells through in Operando Pressure Study,” *ECS Meeting Abstracts*, vol. MA2022-01, no. 1, p. 109, Jul. 2022, doi: 10.1149/MA2022-011109MTGABS.
- [30] O. Leonet, Á. Doñoro, A. Fernández-Barquín, A. Kvasha, I. Urdampilleta, and J. A. Blázquez, “Understanding of Crucial Factors for Improving the Energy Density of Lithium-Sulfur Pouch Cells,” *Front Chem*, vol. 10, p. 888750, May 2022, doi: 10.3389/FCHEM.2022.888750/BIBTEX.
- [31] Y. Jie *et al.*, “Progress and Perspectives on the Development of Pouch-Type Lithium Metal Batteries,” *Angewandte Chemie*, vol. 136, no. 7, p. e202307802, Feb. 2024, doi: 10.1002/ANGE.202307802.
- [32] W. G. Lim *et al.*, “Cooperative Electronic Structure Modulator of Fe Single-Atom Electrocatalyst for High Energy and Long Cycle Li–S Pouch Cell,” *Advanced Materials*, vol. 35, no. 10, p. 2208999, Mar. 2023, doi: 10.1002/ADMA.202208999.
- [33] A. Sevarin, M. Fasching, M. Raffler, and C. Ellersdorfer, “Influence of Cell Selection and Orientation within the Traction Battery on the Crash Safety of Electric-Powered Two-Wheelers,” *Batteries 2023, Vol. 9, Page 195*, vol. 9, no. 4, p. 195, Mar. 2023, doi: 10.3390/BATTERIES9040195.
- [34] M. Tokur, “Electrochemical Performances of NMC811 Lithium-Ion Pouch Cells under Dynamic Conditions,” *Sakarya University Journal of Science*, vol. 26, no. 5, pp. 858–866, Oct. 2022, doi: 10.16984/SAUFENBILDER.1128132.
- [35] S. Badhrinathan, H. Dai, and G. P. Pandey, “Challenges and Approaches to Designing High-Energy Density Lithium-Sulfur Pouch Cells,” *Batter Supercaps*, p. e202400544, Sep. 2024, doi: 10.1002/BATT.202400544.

- [36] S. Dörfler *et al.*, “Recent Progress and Emerging Application Areas for Lithium–Sulfur Battery Technology,” *Energy Technology*, vol. 9, no. 1, p. 2000694, Jan. 2021, doi: 10.1002/ENTE.202000694.
- [37] K. C. Ndeche and S. O. Ezeonu, “Implementation of Coulomb Counting Method for Estimating the State of Charge of Lithium-Ion Battery,” *Physical Science International Journal*, pp. 1–8, Jun. 2021, doi: 10.9734/PSIJ/2021/V25I330244.
- [38] E. Chemali, P. J. Kollmeyer, M. Preindl, Y. Fahmy, and A. Emadi, “A Convolutional Neural Network Approach for Estimation of Li-Ion Battery State of Health from Charge Profiles,” *Energies 2022, Vol. 15, Page 1185*, vol. 15, no. 3, p. 1185, Feb. 2022, doi: 10.3390/EN15031185.
- [39] M. Frank, D. S. Holz, D. Klohs, C. Offermanns, H. H. Heimes, and A. Kampker, “Identification and Mitigation of Predominant Challenges in the Utilization of Aged Traction Batteries within Stationary Second-Life Scenarios,” *Energies 2024, Vol. 17, Page 988*, vol. 17, no. 5, p. 988, Feb. 2024, doi: 10.3390/EN17050988.
- [40] Y. Wang, Z. Zhou, A. Botterud, K. Zhang, and Q. Ding, “Stochastic coordinated operation of wind and battery energy storage system considering battery degradation,” *Journal of Modern Power Systems and Clean Energy*, vol. 4, no. 4, pp. 581–592, Oct. 2016, doi: 10.1007/S40565-016-0238-Z/TABLES/12.
- [41] R. P. Priya, R. Sanjay, and R. Sakile, “State of charge estimation of lithium-ion battery based on extended Kalman filter and unscented Kalman filter techniques,” *Energy Storage*, vol. 5, no. 3, Apr. 2023, doi: 10.1002/EST2.408.

- [42] T. T. D. Nguyen *et al.*, “Understanding the Thermal Runaway of Ni-Rich Lithium-Ion Batteries,” *World Electric Vehicle Journal 2019*, Vol. 10, Page 79, vol. 10, no. 4, p. 79, Nov. 2019, doi: 10.3390/WEVJ10040079.
- [43] C. Chen, Q. Zou, J. Wen, J. Liu, P. H. L. Notten, and Y. Wei, “The Operation Dependence of C – N Fatigue for Lithium-Ion Batteries,” *Adv Energy Mater*, vol. 13, no. 27, p. 2300942, Jul. 2023, doi: 10.1002/AENM.202300942.
- [44] A. R. Mandli, S. Ramachandran, A. Khandelwal, K. Y. Kim, and K. S. Hariharan, “Fast computational framework for optimal life management of lithium ion batteries,” *Int J Energy Res*, vol. 42, no. 5, pp. 1973–1982, Apr. 2018, doi: 10.1002/ER.3996.
- [45] H. Zhang, Y. Su, F. Altaf, T. Wik, and S. Gros, “Interpretable Battery Cycle Life Range Prediction Using Early Degradation Data at Cell Level,” *IEEE Transactions on Transportation Electrification*, vol. 9, no. 2, pp. 2669–2682, Apr. 2022, doi: 10.1109/tte.2022.3226683.
- [46] L. Xu *et al.*, “Giant Voltage Enhancement via Triboelectric Charge Supplement Channel for Self-Powered Electrodeposition,” *ACS Nano*, vol. 12, no. 10, pp. 10262–10271, 2018, doi: 10.1021/ACSNANO.8B05359/SUPPL_FILE/NN8B05359_SI_005.AVI.
- [47] L. Yu, L. Wang, D. Wu, Y. Zhao, and D. Sun, “Enhanced Piezoelectric Performance of Electrospun PVDF Nanofibers with Liquid Metal Electrodes,” *ECS Journal of Solid State Science and Technology*, vol. 7, no. 9, pp. N128–N131, Aug. 2018, doi: 10.1149/2.0181809JSS/XML.
- [48] L. Pei, R. Lu, and C. Zhu, “Relaxation model of the open-circuit voltage for state-of-charge estimation in lithium-ion batteries,” *IET Electrical Systems in Transportation*, vol. 3, no. 4, pp. 112–117, Dec. 2013, doi: 10.1049/IET-EST.2013.0020.

- [49] E. Kim, K. G. Shin, and J. Lee, “Real-time discharge/charge rate management for hybrid energy storage in electric vehicles,” *Proceedings - Real-Time Systems Symposium*, vol. 2015-January, no. January, pp. 228–237, Jan. 2015, doi: 10.1109/RTSS.2014.16.
- [50] S. Lv, X. Wang, W. Lu, J. Zhang, and H. Ni, “The Influence of Temperature on the Capacity of Lithium Ion Batteries with Different Anodes,” *Energies 2022, Vol. 15, Page 60*, vol. 15, no. 1, p. 60, Dec. 2021, doi: 10.3390/EN15010060.
- [51] C. Li, Z. Sun, and W. Gu, “Affection Mode of Temperature on the Lithium-Ion Battery Performance Used in Electric Vehicle,” *Adv Mat Res*, vol. 658, pp. 450–454, 2013, doi: 10.4028/WWW.SCIENTIFIC.NET/AMR.658.450.
- [52] M. F. I. M. Razi, Z. H. C. Daud, Z. Asus, I. I. Mazali, M. I. Ardani, and M. K. A. Hamid, “A Review of Internal Resistance and Temperature Relationship, State of Health and Thermal Runaway for Lithium-Ion Battery Beyond Normal Operating Condition,” *Journal of Advanced Research in Fluid Mechanics and Thermal Sciences*, vol. 88, no. 2, pp. 123–132, Oct. 2021, doi: 10.37934/ARFMTS.88.2.123132.
- [53] A. Łebkowski, “Temperature, overcharge and short-circuit studies of batteries used in electric vehicles,” *Przegląd Elektrotechniczny*, vol. 93, no. 5, pp. 67–73, 2017, doi: 10.15199/48.2017.05.13.
- [54] H. Solmaz and T. Kocakulak, “Determination of Lithium Ion Battery Characteristics for Hybrid Vehicle Models,” *International Journal of Automotive Science And Technology*, vol. 4, no. 4, pp. 264–271, Dec. 2020, doi: 10.30939/IJASTECH..723043.
- [55] “(PDF) State-of-Charge Estimation Methods for Li-ion Batteries in Electric Vehicles.” Accessed: Nov. 11, 2024. [Online]. Available:

https://www.researchgate.net/publication/351081644_State-of-Charge_Estimation_Methods_for_Li-ion_Batteries_in_Electric_Vehicles

- [56] J. Zhang, X. Yang, G. Zhang, Q. Huang, C. Xiao, and C. Yang, “Investigation on the root cause of the decreased performances in the overcharged lithium iron phosphate battery,” *Int J Energy Res*, vol. 42, no. 7, pp. 2448–2455, Jun. 2018, doi: 10.1002/ER.4025.
- [57] S. H. Ahmed, X. Kang, and S. O. B. Shrestha, “Effects of temperature on internal resistances of lithium-ion batteries,” *Journal of Energy Resources Technology, Transactions of the ASME*, vol. 137, no. 3, May 2015, doi: 10.1115/1.4028698/373140.
- [58] J. Y. Park *et al.*, “Mechanism of Degradation of Capacity and Charge/Discharge Voltages of High-Ni Cathode During Fast Long-Term Cycling Without Voltage Margin,” *Adv Energy Mater*, vol. 12, no. 29, p. 2201151, Aug. 2022, doi: 10.1002/AENM.202201151.
- [59] S. H. Hwang, Y. Chen, H. Zhang, K. Y. Lee, and D. H. Kim, “Reconfigurable hybrid resonant topology for constant current/voltage wireless power transfer of electric vehicles,” *Electronics (Switzerland)*, vol. 9, no. 8, pp. 1–13, Aug. 2020, doi: 10.3390/ELECTRONICS9081323.
- [60] Y. Xing, W. He, M. Pecht, and K. L. Tsui, “State of charge estimation of lithium-ion batteries using the open-circuit voltage at various ambient temperatures,” *Appl Energy*, vol. 113, pp. 106–115, Jan. 2014, doi: 10.1016/J.APENERGY.2013.07.008.
- [61] F. Baronti, W. Zamboni, R. Roncella, R. Saletti, and G. Spagnuolo, “Open-circuit voltage measurement of Lithium-Iron-Phosphate batteries,” *Conference Record - IEEE Instrumentation and Measurement Technology Conference*, vol. 2015-July, pp. 1711–1716, Jul. 2015, doi: 10.1109/I2MTC.2015.7151538.

- [62] Z. Ren, C. Du, Z. Wu, J. Shao, and W. Deng, “A comparative study of the influence of different open circuit voltage tests on model-based state of charge estimation for lithium-ion batteries,” *Int J Energy Res*, vol. 45, no. 9, pp. 13692–13711, Jul. 2021, doi: 10.1002/ER.6700.
- [63] D. Fu, L. Hu, X. Han, S. Chen, Z. Ren, and H. Yang, “OCV-Ah integration SOC estimation of space li-ion battery,” *Lecture Notes in Electrical Engineering*, vol. 550, pp. 291–299, 2019, doi: 10.1007/978-981-13-7123-3_35/TABLES/5.
- [64] Y. Wang, L. Zhao, J. Cheng, J. Zhou, and S. Wang, “A State of Charge Estimation Method of Lithium-Ion Battery Based on Fused Open Circuit Voltage Curve,” *Applied Sciences 2020, Vol. 10, Page 1264*, vol. 10, no. 4, p. 1264, Feb. 2020, doi: 10.3390/APP10041264.
- [65] L. K. Amifia, “Direct Comparison using Coulomb Counting and Open Circuit Voltage Method for the State of Health Li-Po Battery,” *Journal of Robotics and Control (JRC)*, vol. 3, no. 4, pp. 455–463, Jul. 2022, doi: 10.18196/JRC.V3I4.15515.
- [66] R. Zhang *et al.*, “Study on the Characteristics of a High Capacity Nickel Manganese Cobalt Oxide (NMC) Lithium-Ion Battery—An Experimental Investigation,” *Energies 2018, Vol. 11, Page 2275*, vol. 11, no. 9, p. 2275, Aug. 2018, doi: 10.3390/EN11092275.
- [67] J. P. Christophersen, “Battery Test Manual For Electric Vehicles, Revision 3,” United States, 2015. doi: 10.2172/1186745.
- [68] H. Zhang, H. W. Mu, Y. Zhang, and J. Han, “Calculation and Characteristics Analysis of Lithium Ion Batteries’ Internal Resistance Using HPPC Test,” *Adv Mat Res*, vol. 926–930, pp. 915–918, 2014, doi: 10.4028/WWW.SCIENTIFIC.NET/AMR.926-930.915.

- [69] F. Ebrahimi *et al.*, “Fault Detection for Lithium-Ion Battery Using Smooth Variable Structure Filters,” *IEEE Access*, 2024, doi: 10.1109/ACCESS.2024.3482193.
- [70] L. Cheng, A. Garg, A. K. Jishnu, and L. Gao, “Surrogate based multi-objective design optimization of lithium-ion battery air-cooled system in electric vehicles,” *J Energy Storage*, vol. 31, p. 101645, Oct. 2020, doi: 10.1016/J.EST.2020.101645.
- [71] H. Bian, Z. Wang, J. Jiang, Y. Yang, H. Wang, and S. Chen, “Thermal runaway hazard characteristics and influencing factors of Li-ion battery packs under high-rate charge condition,” *Fire Mater*, vol. 44, no. 2, pp. 189–201, Mar. 2020, doi: 10.1002/FAM.2783.
- [72] J. Xu, C. Lan, Y. Qiao, and Y. Ma, “Prevent thermal runaway of lithium-ion batteries with minichannel cooling,” *Appl Therm Eng*, vol. 110, pp. 883–890, Jan. 2017, doi: 10.1016/J.APPLTHERMALENG.2016.08.151.
- [73] X. Zhang *et al.*, “Investigation on Early-stage Internal Short Circuit Identification for Power Battery Pack,” pp. 233–235, May 2019, doi: 10.2991/SEEIE-19.2019.54.
- [74] Q. Liu, Q. Zhu, W. Zhu, and X. Yi, “Influence of Aerogel Felt with Different Thickness on Thermal Runaway Propagation of 18650 Lithium-ion Battery,” *Electrochemistry*, vol. 90, no. 8, pp. 087003–087003, Aug. 2022, doi: 10.5796/ELECTROCHEMISTRY.22-00048.
- [75] L. Zhao *et al.*, “Heat dissipation analysis of double-layer battery pack under coupling heat transfer of air, liquid, and solid,” *Int J Energy Res*, vol. 42, no. 15, pp. 4840–4852, Dec. 2018, doi: 10.1002/ER.4240.
- [76] X. Ye, Y. Zhao, and Z. Quan, “Thermal management system of lithium-ion battery module based on micro heat pipe array,” *Int J Energy Res*, vol. 42, no. 2, pp. 648–655, Feb. 2018, doi: 10.1002/ER.3847.

- [77] G. Karimi and X. Li, “Thermal management of lithium-ion batteries for electric vehicles,” *Int J Energy Res*, vol. 37, no. 1, pp. 13–24, Jan. 2013, doi: 10.1002/ER.1956.
- [78] E. S. Shrinet and L. Kumar, “Enhancing thermal management in cylindrical Li-ion battery through PCM integration with variable contact area,” *J Phys Conf Ser*, vol. 2766, no. 1, p. 012043, May 2024, doi: 10.1088/1742-6596/2766/1/012043.
- [79] Y. A. Çengel and M. A. Boles, *Thermodynamics : An Engineering Approach*. McGraw-Hill Education, 2015.
- [80] R. Mahamud and C. Park, “Reciprocating air flow for Li-ion battery thermal management to improve temperature uniformity,” *J Power Sources*, vol. 196, no. 13, pp. 5685–5696, Jul. 2011, doi: 10.1016/J.JPOWSOUR.2011.02.076.
- [81] R. Zhao, J. Liu, J. Gu, L. Zhai, and F. Ma, “Experimental study of a direct evaporative cooling approach for Li-ion battery thermal management,” *Int J Energy Res*, vol. 44, no. 8, pp. 6660–6673, Jun. 2020, doi: 10.1002/ER.5402.
- [82] L. I. Uwalaka, Q. Yao, P. Kollmeyer, and A. Emadi, “Review of Production Electric Vehicle Battery Thermal Management Systems and Experimental Testing of a Production Battery Module,” *SAE Technical Papers*, Apr. 2024, doi: 10.4271/2024-01-2672.
- [83] Rigidchill, “Lithium Battery Active Air Cooling,” Dec. 2023. [Online]. Available: <https://rigidchill.com/successful-thermal-management-to-battery-packs-of-electric-vehicle/>
- [84] “2020 Ford Fusion SE Hybrid Price & Specifications - The Car Guide,” 2020. [Online]. Available: <https://www.guideautoweb.com/en/makes/ford/fusion/2020/specifications/se-hybrid/>

- [85] “2023 Toyota Prius XLE AWD Price & Specifications - The Car Guide,” 2023. [Online]. Available: <https://www.guideautoweb.com/en/makes/toyota/prius/2023/specifications/xle-awd/>
- [86] J. M. Gitlin, “Plug-in powertrain is an efficiency win for the 2023 Toyota Prius Prime,” Dec. 2023. [Online]. Available: <https://arstechnica.com/cars/2023/10/the-2023-toyota-prius-prime-is-a-mostly-pleasant-plug-in-hybrid/>
- [87] “2025 Nissan LEAF Features: Range, Battery & Charging | Nissan Canada.” [Online]. Available: <https://www.nissan.ca/vehicles/electric-cars/leaf/features.html>
- [88] “ZOE | Renault Malaysia,” 2024. [Online]. Available: <https://www.renault.com.my/model/ZOE#PriceAndSpecifications>
- [89] Nigel, “Toyota Prius Gen 2 Battery,” Dec. 2022. [Online]. Available: <https://www.batterydesign.net/toyota-prius-gen-2-battery/>
- [90] P. Dubey, G. Pulugundla, and A. K. Srouji, “Direct Comparison of Immersion and Cold-Plate Based Cooling for Automotive Li-Ion Battery Modules,” *Energies* 2021, Vol. 14, Page 1259, vol. 14, no. 5, p. 1259, Feb. 2021, doi: 10.3390/EN14051259.
- [91] “Liquid cooling manifold with multi-function thermal interface,” Jan. 2010.
- [92] A. Ibrahim, J. Guo, Y. Wang, Y. Zheng, B. Lei, and F. Jiang, “Performance of serpentine channel based Li-ion battery thermal management system: An experimental investigation,” *Int J Energy Res*, vol. 44, no. 13, pp. 10023–10043, Oct. 2020, doi: 10.1002/ER.5599.
- [93] “Ioniq 5 N: Sophisticated Thermal Management Unlocks Performance of Hottest Hyundai – VASA,” 2024. [Online]. Available: <https://vasa.org.au/ioniq-5-n-sophisticated-thermal-management-unlocks-performance-of-hottest-hyundai/>

- [94] M. Live, "How Rivian's 7777 Batteries are packaged!," Dec. 2022. [Online]. Available: <https://www.youtube.com/watch?v=-0pmqFoQs2g>
- [95] Y. Zou, L. Wei, Z. Lu, S. Qin, and F. Cao, "An optimal study of serpentine channel with various configurations based on response surface analysis," *IOP Conf Ser Earth Environ Sci*, vol. 1074, no. 1, p. 012016, Aug. 2022, doi: 10.1088/1755-1315/1074/1/012016.
- [96] Z. Gong, H. Tang, and Y. Wang, "A study of the effects of the micro-channel cold plate on the cooling performance of battery thermal management systems," *Thermal Science*, vol. 26, no. 2 Part B, pp. 1503–1517, 2022, doi: 10.2298/TSCI210608316G.
- [97] S. A. Jayarajan and U. Azimov, "CFD Modeling and Thermal Analysis of a Cold Plate Design with a Zig-Zag Serpentine Flow Pattern for Li-Ion Batteries," *Energies 2023, Vol. 16, Page 5243*, vol. 16, no. 14, p. 5243, Jul. 2023, doi: 10.3390/EN16145243.
- [98] Y. Li *et al.*, "Numerical Simulations for Indirect and Direct Cooling of 54 V LiFePO₄ Battery Pack," *Energies 2022, Vol. 15, Page 4581*, vol. 15, no. 13, p. 4581, Jun. 2022, doi: 10.3390/EN15134581.
- [99] K. S. Garud, L. D. Tai, S. G. Hwang, N. H. Nguyen, and M. Y. Lee, "A Review of Advanced Cooling Strategies for Battery Thermal Management Systems in Electric Vehicles," *Symmetry 2023, Vol. 15, Page 1322*, vol. 15, no. 7, p. 1322, Jun. 2023, doi: 10.3390/SYM15071322.
- [100] S. H. Hong, D. S. Jang, S. Park, S. Yun, and Y. Kim, "Thermal performance of direct two-phase refrigerant cooling for lithium-ion batteries in electric vehicles," *Appl Therm Eng*, vol. 173, p. 115213, Jun. 2020, doi: 10.1016/J.APPLTHERMALENG.2020.115213.

- [101] N. P. Williams, D. Trimble, and S. M. O'Shaughnessy, "Liquid immersion thermal management of lithium-ion batteries for electric vehicles: An experimental study," *J Energy Storage*, vol. 72, p. 108636, Nov. 2023, doi: 10.1016/J.EST.2023.108636.
- [102] A. Faghri and Z. Guo, "Integration of Heat Pipe into Fuel Cell Technology," *Heat Transfer Engineering*, vol. 29, no. 3, pp. 232–238, Mar. 2008, doi: 10.1080/01457630701755902.
- [103] G. Li *et al.*, "Simulation and experiment on thermal performance of a micro-channel heat pipe under different evaporator temperatures and tilt angles," *Energy*, vol. 179, pp. 549–557, Jul. 2019, doi: 10.1016/J.ENERGY.2019.05.040.
- [104] M. Bernagozzi, A. Georgoulas, N. Miché, and M. Marengo, "Heat pipes in battery thermal management systems for electric vehicles: A critical review," *Appl Therm Eng*, vol. 219, p. 119495, Jan. 2023, doi: 10.1016/J.APPLTHERMALENG.2022.119495.
- [105] L. Liang, Y. Zhao, Y. Diao, R. Ren, and H. Jing, "Inclined U-shaped flat microheat pipe array configuration for cooling and heating lithium-ion battery modules in electric vehicles," *Energy*, vol. 235, p. 121433, Nov. 2021, doi: 10.1016/J.ENERGY.2021.121433.
- [106] J. Gou and W. Liu, "Feasibility study on a novel 3D vapor chamber used for Li-ion battery thermal management system of electric vehicle," *Appl Therm Eng*, vol. 152, pp. 362–369, Apr. 2019, doi: 10.1016/J.APPLTHERMALENG.2019.02.034.
- [107] "Press Release - Insight -SNE Research," Nov. 2024, *SNE Research*. [Online]. Available: https://www.sneresearch.com/en/insight/release_view/260/page/0
- [108] C. V. Amanchukwu, Z. Yu, X. Kong, J. Qin, Y. Cui, and Z. Bao, "A New Class of Ionically Conducting Fluorinated Ether Electrolytes with High Electrochemical Stability,"

- J Am Chem Soc*, vol. 142, no. 16, pp. 7393–7403, Apr. 2020, doi:
10.1021/JACS.9B11056/SUPPL_FILE/JA9B11056_SI_001.PDF.
- [109] CALB, “L221N113A Product Specification,” Dec. 2019.
- [110] “ARBIN BT2000 -Battery Test Equipment.” [Online]. Available: <https://slategrey.pt/wp-content/uploads/2016/06/BT-2000-Multi-Channel-Battery-Testing-System-da-ARBIN.pdf>
- [111] “ESPEC BTZ-133 Model Details.” [Online]. Available:
<https://espec.com/na/products/model/btz-133>
- [112] “AVL Compact I/O Cubes Datasheet,” AVL. [Online]. Available:
<https://www.avl.com/documents/10138/885965/Datasheet+IO+Cube.pdf>
- [113] H. Bian, Z. Wang, J. Jiang, Y. Yang, H. Wang, and S. Chen, “Thermal runaway hazard characteristics and influencing factors of Li-ion battery packs under high-rate charge condition,” *Fire Mater*, vol. 44, no. 2, pp. 189–201, Mar. 2020, doi: 10.1002/FAM.2783.
- [114] X. Huang, W. Liu, A. B. Acharya, J. Meng, R. Teodorescu, and D. I. Stroe, “Effect of Pulsed Current on Charging Performance of Lithium-Ion Batteries,” *IEEE Transactions on Industrial Electronics*, vol. 69, no. 10, pp. 10144–10153, Oct. 2022, doi: 10.1109/TIE.2021.3121726.
- [115] S. M. Bak *et al.*, “Structural changes and thermal stability of charged $\text{LiNi}_x\text{Mn}_y\text{Co}_z\text{O}_2$ cathode materials studied by combined in situ time-resolved XRD and mass spectroscopy,” *ACS Appl Mater Interfaces*, vol. 6, no. 24, pp. 22594–22601, Dec. 2014, doi: 10.1021/AM506712C/SUPPL_FILE/AM506712C_SI_001.PDF.
- [116] “Micro-channel heat pipe for batteries solution datasheet.” [Online]. Available:
<https://assets-global.website->

files.com/621d4065411a1a64851f5db1/63c8740216eae4b09ecb50b_Calyos%20MCHP-BT%20Solution%20Sheet.pdf

- [117] “Micro Channel Heat Pipes,” *Calyos*. [Online]. Available: <https://www.calyos-tm.com/technologies/micro-channel-heat-pipes>
- [118] J. William. Nilsson and S. A. . Riedel, “Electric circuits,” p. 782, 2023.
- [119] R. Javed, “Busbar Current Calculator.” [Online]. Available: <https://calculatorshub.net/electrical/busbar-current-calculator/>
- [120] H. W. Beaty and D. G. Fink, *Standard Handbook for Electrical Engineers, Sixteenth Edition*. McGraw-Hill Education, 2013. Accessed: Nov. 18, 2024. [Online]. Available: <https://www.accessengineeringlibrary.com/content/book/9780071762328>
- [121] M. Kane, “Watch Hyundai Ioniq 5 800 V Battery Pack Get Opened for First Time,” Nov. 2021. [Online]. Available: <https://insideevs.com/news/539940/hyundai-ioniq5-battery-pack-opened/>
- [122] “BMW iX Xdrive40 75kWh Battery Teardown,” Nov. 2023. [Online]. Available: <https://www.eevblog.com/forum/renewable-energy/bmw-ix-xdrive40-75kwh-battery-teardown/>
- [123] A. F. Challoob, N. A. Bin Rahmat, V. K. A/L Ramachandramurthy, and A. J. Humaidi, “Energy and battery management systems for electrical vehicles: A comprehensive review & recommendations,” *Energy Exploration and Exploitation*, vol. 42, no. 1, pp. 341–372, Jan. 2024, doi: 10.1177/01445987231211943.
- [124] “Orion 2 BMS Operation Manual.” [Online]. Available: www.orionbms.com

- [125] L. Uwalaka, “Design of Fast-Charging Profiles for the Porsche Taycan EV Battery Module Based on Electrothermal Model and Extensive Testing,” 2024, Accessed: Nov. 20, 2024. [Online]. Available: <https://macsphere.mcmaster.ca/handle/11375/30066>
- [126] “Tenney TC Cycling Test Chambers | Tenney Environmental.” [Online]. Available: <https://www.tenney.com/products/reach-in-test-chambers/tenney-tc-series-cycling-test-chambers>
- [127] “1171PD user manual.” Accessed: Nov. 20, 2024. [Online]. Available: https://us.vwr.com/assetsvc/asset/en_US/id/13563105/contents/manual_1171
- [128] “NI-9213 Specifications.” [Online]. Available: <https://www.ni.com/docs/en-US/bundle/ni-9213-specs/page/specs.html>
- [129] “NI-9214 Specifications.” [Online]. Available: <https://www.ni.com/docs/en-US/bundle/ni-9214-specs/page/specs.html>
- [130] “NI-9205 and sbRIO-9205 Specifications.” [Online]. Available: <https://www.ni.com/docs/en-US/bundle/ni-9205-specs/page/specs.html>
- [131] “Type T Thermocouples.” [Online]. Available: <https://www.thermocoupleinfo.com/type-t-thermocouple.htm>
- [132] “What is the maximum temperature that the low-voltage copper busbar can withstand during transformer operation - Knowledge,” Nov. 2024, *Jiangshan Scotech Electrical Co., Ltd.* [Online]. Available: <https://www.scotech-electrical.com/info/what-is-the-maximum-temperature-that-the-low-v-92569721.html>

Appendices

10.1 New Design Dimensioning

This section presents the future design dimensions to be 3D printed by the CMHT group, with all dimensions specified in millimeters.

10.1.1 MCHP

This is the updated MCHP dimensions by Calyos. The length of the adiabatic section was decreased based on testing results and design optimization.

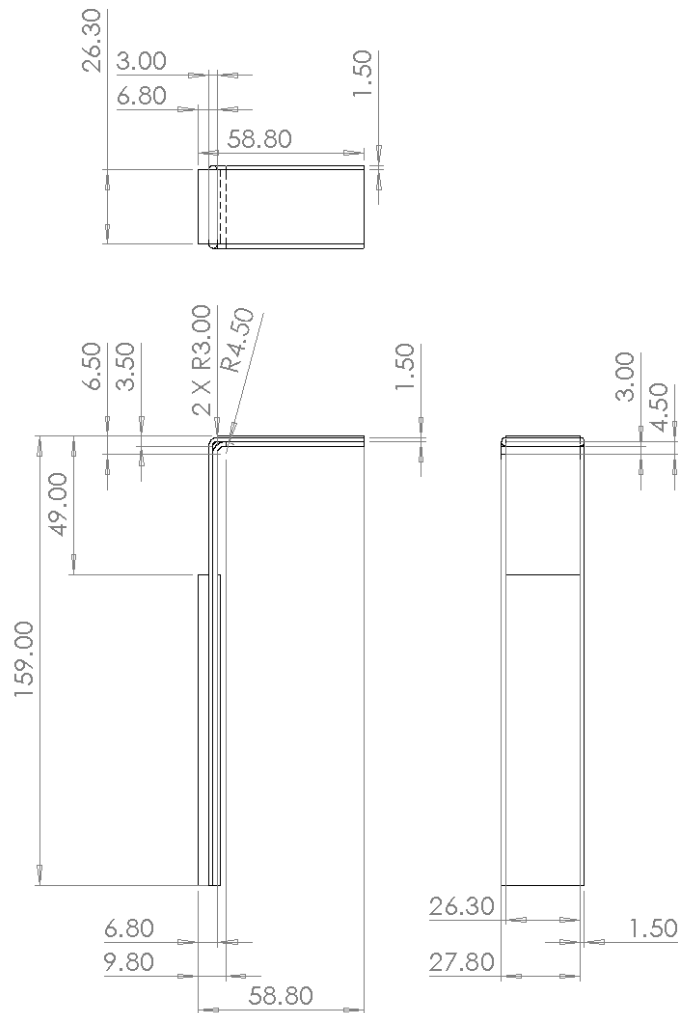


Figure 117 Optimized MCHP dimensions.

10.1.2 Body Center Part

This component is printed in duplicate, with one piece mirrored.

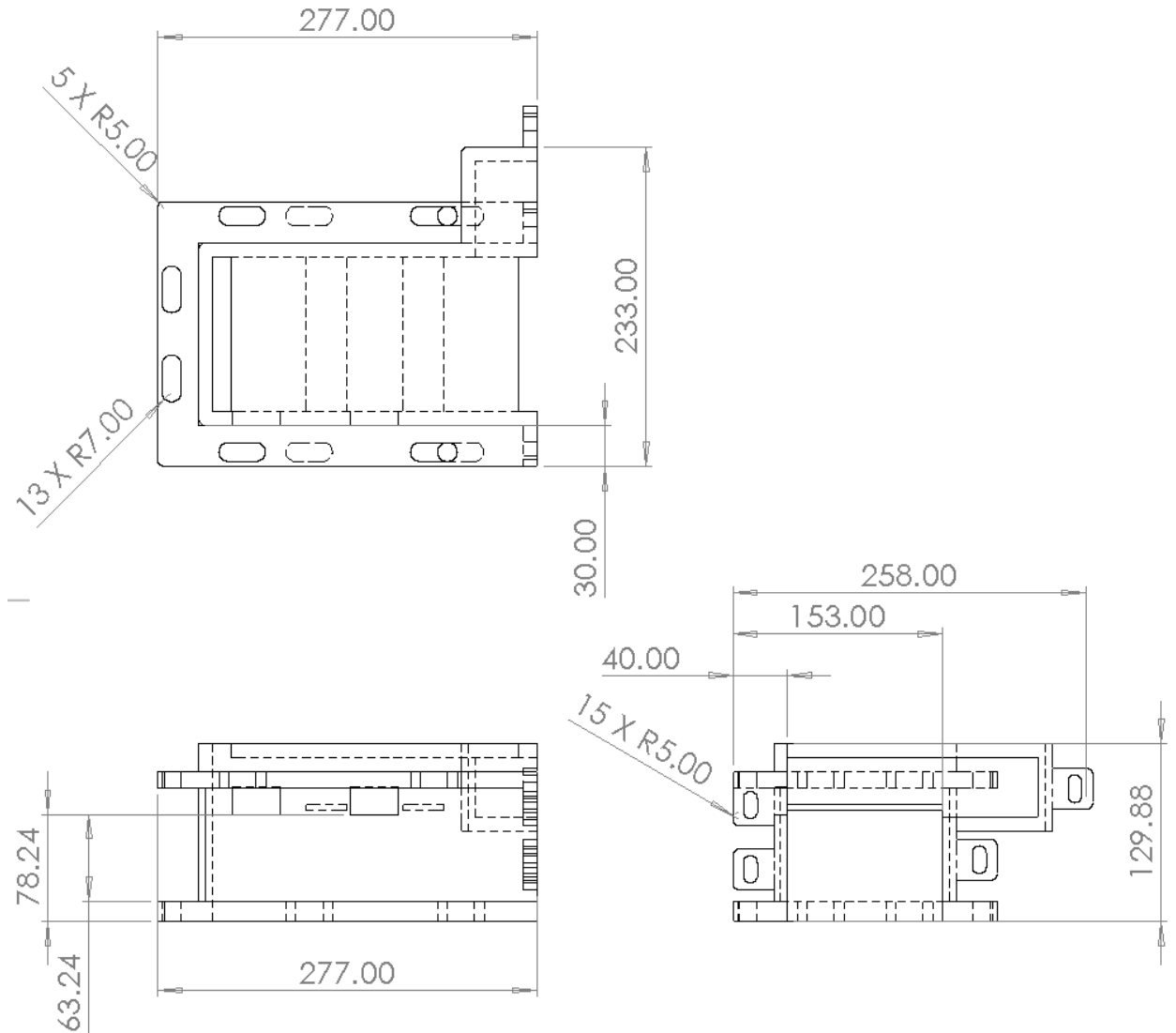


Figure 118 Body middle part left side.

10.1.3 MCHP Testing Top Part

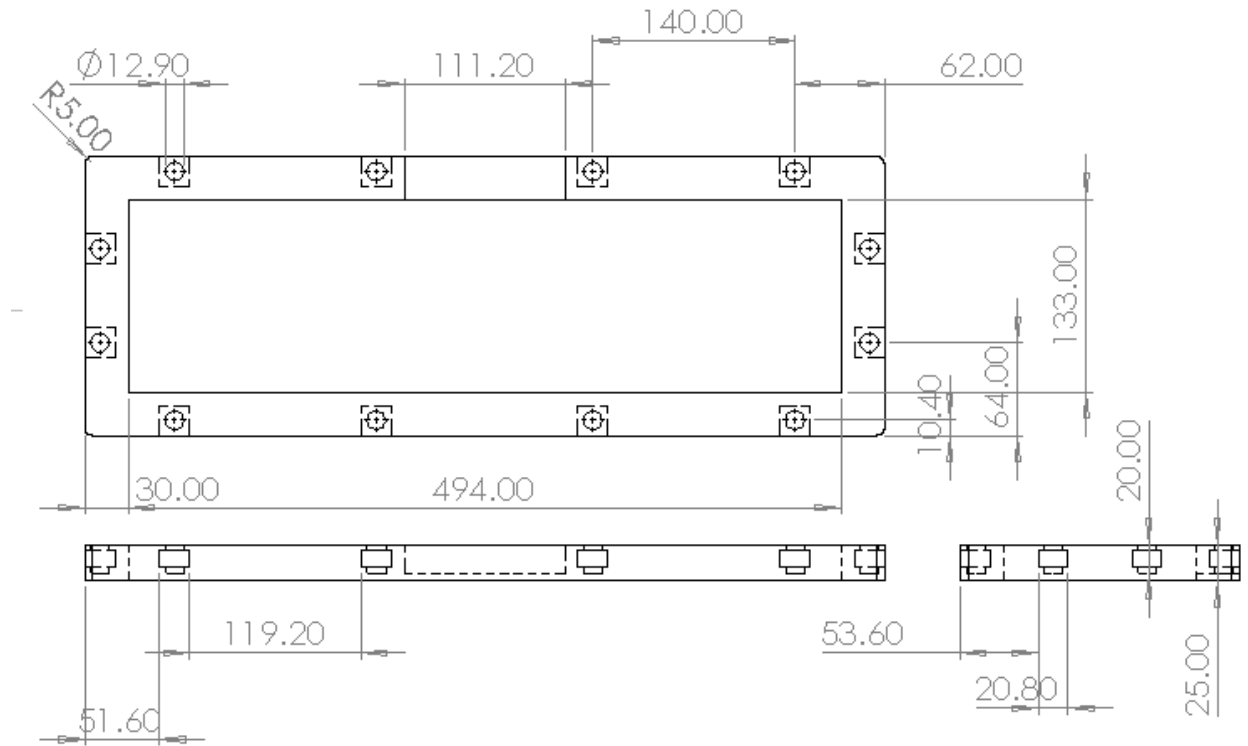


Figure 119 The MCHP testing fixture top part.

10.1.4 Enclosed Top Part

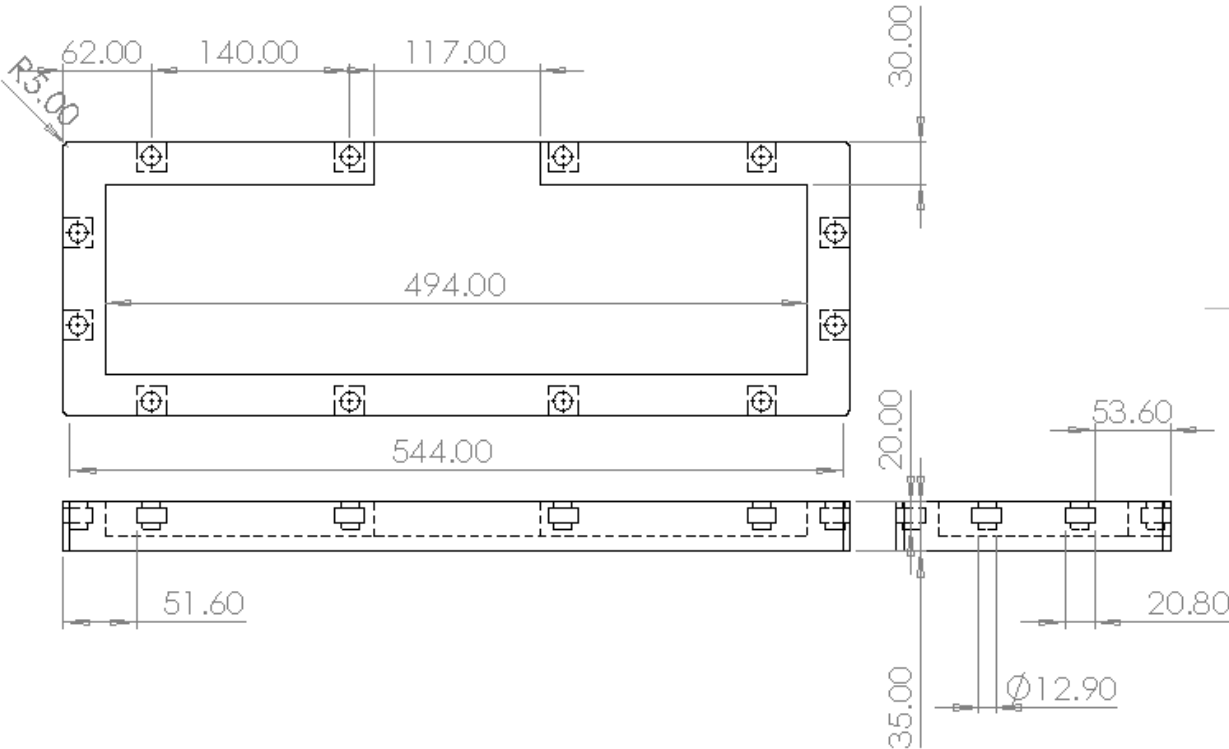


Figure 120 Enclosed top cover utilized in both No Cooling and Bottom Cooling setups.

10.1.5 Bottom Cooling Lower Part

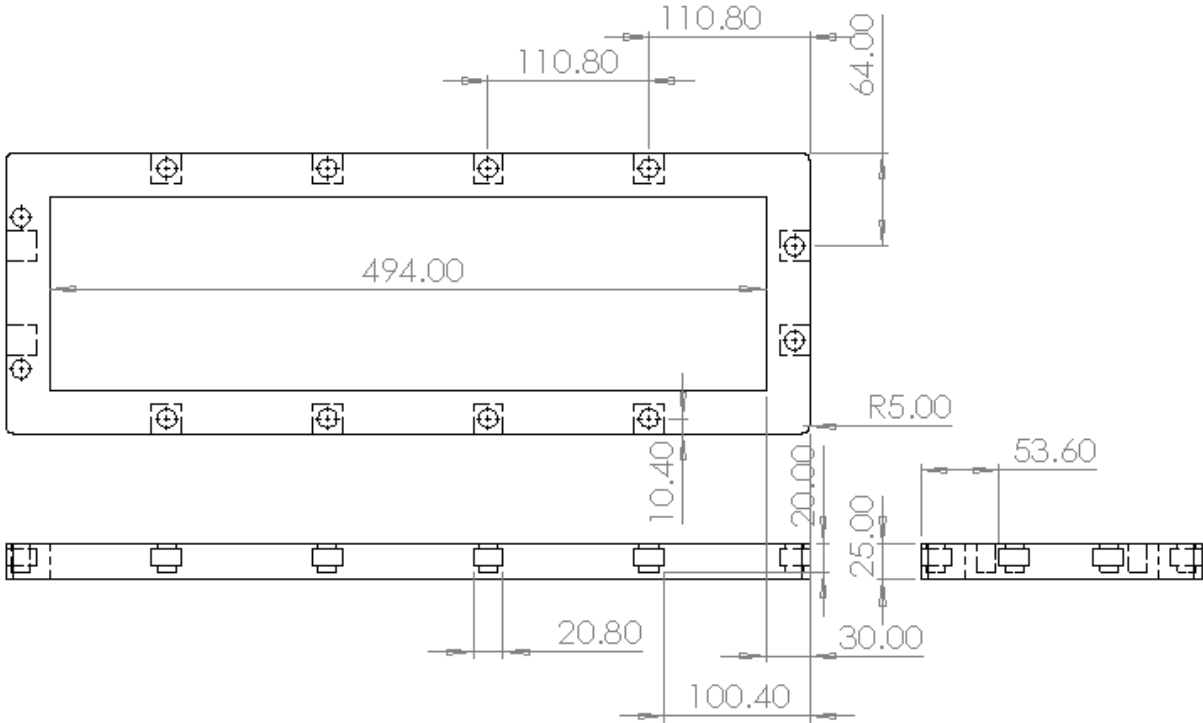


Figure 121 Bottom Cooling lower part attachment.

10.1.6 Enclosed Lower Part

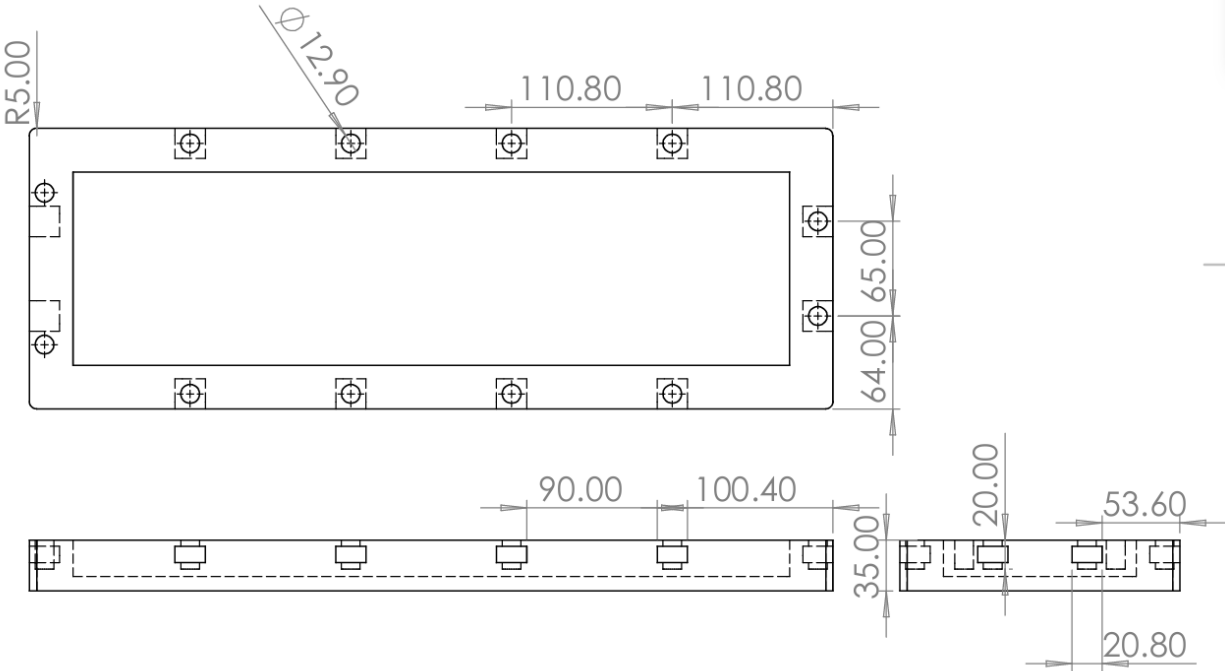


Figure 122 Enclosed Lower cover utilized in both No Cooling and MCH Cooling setups.